frontiers | Research Topics

Essential metals for plants: Uptake, transport, regulation of homeostasis and roles in plant development

Edited by
Anja Schneider, Olena Vatamaniuk and Sidsel Birkelund Schmidt

Published in
Frontiers in Plant Science

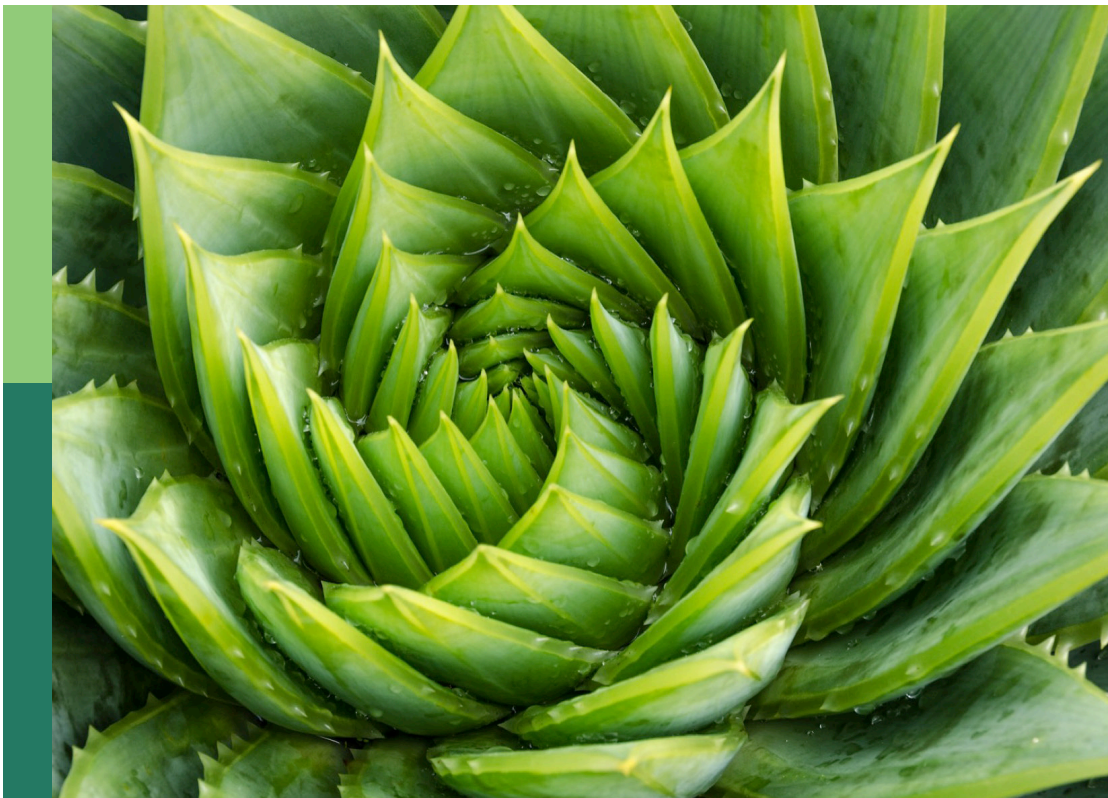

ISSN 1664-8714
ISBN 978-2-83251-796-3
DOI 10.3389/978-2-83251-796-3

About Frontiers

Frontiers is more than just an open access publisher of scholarly articles: it is a pioneering approach to the world of academia, radically improving the way scholarly research is managed. The grand vision of Frontiers is a world where all people have an equal opportunity to seek, share and generate knowledge. Frontiers provides immediate and permanent online open access to all its publications, but this alone is not enough to realize our grand goals.

Frontiers journal series

The Frontiers journal series is a multi-tier and interdisciplinary set of open-access, online journals, promising a paradigm shift from the current review, selection and dissemination processes in academic publishing. All Frontiers journals are driven by researchers for researchers; therefore, they constitute a service to the scholarly community. At the same time, the *Frontiers journal series* operates on a revolutionary invention, the tiered publishing system, initially addressing specific communities of scholars, and gradually climbing up to broader public understanding, thus serving the interests of the lay society, too.

Dedication to quality

Each Frontiers article is a landmark of the highest quality, thanks to genuinely collaborative interactions between authors and review editors, who include some of the world's best academicians. Research must be certified by peers before entering a stream of knowledge that may eventually reach the public - and shape society; therefore, Frontiers only applies the most rigorous and unbiased reviews. Frontiers revolutionizes research publishing by freely delivering the most outstanding research, evaluated with no bias from both the academic and social point of view. By applying the most advanced information technologies, Frontiers is catapulting scholarly publishing into a new generation.

What are Frontiers Research Topics?

Frontiers Research Topics are very popular trademarks of the *Frontiers journals series*: they are collections of at least ten articles, all centered on a particular subject. With their unique mix of varied contributions from Original Research to Review Articles, Frontiers Research Topics unify the most influential researchers, the latest key findings and historical advances in a hot research area.

Find out more on how to host your own Frontiers Research Topic or contribute to one as an author by contacting the Frontiers editorial office: frontiersin.org/about/contact

Essential metals for plants: Uptake, transport, regulation of homeostasis and roles in plant development

Topic editors

Anja Schneider — Ludwig Maximilian University of Munich, Germany
Olena Vatamaniuk — Cornell University, United States
Sidsel Birkelund Schmidt — The James Hutton Institute, United Kingdom

Citation

Schneider, A., Vatamaniuk, O., Schmidt, S. B., eds. (2023). *Essential metals for plants: Uptake, transport, regulation of homeostasis and roles in plant development*. Lausanne: Frontiers Media SA. doi: 10.3389/978-2-83251-796-3

Table of contents

frontiers | Frontiers in Plant Science

TYPE Editorial
PUBLISHED 15 February 2023
DOI 10.3389/fpls.2023.1156247

OPEN ACCESS

EDITED AND REVIEWED BY
Marta Wilton Vasconcelos,
Catholic University of Portugal, Portugal

*CORRESPONDENCE
Anja Schneider
anja.schneider@lrz.uni-muenchen.de

SPECIALTY SECTION
This article was submitted to Plant Nutrition, a section of the journal Frontiers in Plant Science

RECEIVED 01 February 2023
ACCEPTED 06 February 2023
PUBLISHED 15 February 2023

CITATION
Schmidt SB, Vatamaniuk O and Schneider A (2023) Editorial: Essential metals for plants: Uptake, transport, regulation of homeostasis and roles in plant development.
Front. Plant Sci. 14:1156247.
doi: 10.3389/fpls.2023.1156247

Editorial: Essential metals for plants: Uptake, transport, regulation of homeostasis and roles in plant development

Sidsel Birkelund Schmidt[1], Olena Vatamaniuk[2] and Anja Schneider[3]*

[1]Innovation Centre for Organic Farming, Aarhus, Denmark, [2]Soil and Crop Sciences Section, Cornell University, Ithaca, NY, United States, [3]Plant Science Group, Faculty of Biology, Ludwig-Maximilian University of Munich, Munich, Germany

KEYWORDS

copper, iron, zinc, stable isotope fractionation, metal deficiency, rice breeding, nutrient uptake, Arabidopsis

Editorial on the Research Topic
Essential metals for plants: Uptake, transport, regulation of homeostasis and roles in plant development

Metals are needed by all living organisms to function properly and in plants they are taken up from the soil. In both natural and anthropogenic soils, plants are exposed to a wide range of metal concentrations. Plants have therefore evolved sophisticated mechanisms to cope with fluctuating levels of metal supply from deficiency to toxicity. Metalloproteins comprise almost half of all naturally occurring proteins, which underlines the importance of a balanced and sufficient metal availability. Among the most complex reactions in a plant cell, photosynthesis, respiration, and nitrogen fixation strictly depend on metals as catalysts and cofactors. Plants can regulate the balance of metals in the cell, to ensure sufficient supply of metals to maintain substantial reactions and on the other hand, to protect the cell from damage and toxicity by allocating harmful metals. The nine articles collected for this Research Topic describe different aspects of metal homeostasis, with a special focus on the essential metals copper (Cu), iron (Fe) and zinc (Zn).

In the review by Wiggenhauser et al. recommendations are given to better exploit the information provided by varying isotope compositions, to further advance the non-traditional isotope process tracing of metals in plants. Isotope fractionation describes the small changes in relative isotope abundances during chemical reactions or physical processes. Several processes drive isotope fractionation in plants and for instance, changes in nutrient supply induced shifts in isotope fractionation patterns for Mg, Cu and Zn, suggesting that isotope process tracing can be used as a tool to provide information on acquisition mechanisms, e.g. active or passive uptake. Using this technique, Blotevogel et al. analyzed stable Cu isotope ratios in Grapevine (*Vitis vinifera*). It turned out, that there was no direct relationship between Cu contents in soils or soil solutions and Cu contents in roots, indicating a partly homeostatic control of Cu uptake. However, at low Cu supply, the Cu-isotope fractionation between soil solution and roots showed that isotopically light Cu

was preferentially taken up whereas heavy Cu isotopes were increasingly taken up at high Cu supply levels, suggesting a shift from active to passive uptake mechanisms. The authors emphasize that Cu isotope analysis is a sensitive tool to monitor differences in Cu uptake and translocation pathways even before differences in tissue contents become obvious.

The work by Mancini and Garcia-Molina describes the consequences of simultaneous Cu and Fe deficiency in *Arabidopsis thaliana* with a particular investigation of alternative splicing events on the transcriptome of rosette leaves. Functional annotation of transcript changes detected under Fe and Cu deficiency revealed that differently expressed genes belong to general stress responses and the translation machinery, while differently spliced genes belong to metabolic reactions, more specifically amino acid biosynthesis. The authors propose that during systematic reprogramming, alternative splicing could act as an independent mechanism to regulate metabolic reactions, which are not adjusted at the transcript or protein level. In a minireview by Su et al. the aspect of chromatin-based regulation in response to the plant Fe status is highlighted and involves histone modification and DNA methylation. Histone trimethylation cannot only induces chromatin condensation resulting in gene silencing during Fe sufficient conditions, but can also activate corresponding target genes in Fe deficient conditions in *Arabidopsis thaliana*. In rice plants, DNA hypermethylation, in the promotor region of corresponding downstream genes, leads to enhanced transcription during Fe deficiency, whereas the unmethylated stage confers a basal expression of Fe homeostasis genes.

A useful breeding line is described by Kandwal et al. which contain high concentrations of Fe and Zn in the rice grain, without affecting growth in a paddy field. This rice line possessed a non-sense mutation of the vacuolar localized Fe transporter OsVIT2 and thus Fe and Zn relocation changed in benefit of the grain. The line used in that study is an EMS-mutagenized rice line and therefore offers many advantages compared to transgenic approaches. It highlights the use of OsVIT2 mutations in marker-assisted breeding programs for future grain biofortification of Fe and Zn. To develop strategies for improving Zn content in legume crops, the mechanisms of response to Zn deficiency in the legume model *Medicago truncatula* was investigated by Liao et al. In legumes species, an adequate supply of Zn to the nodule-rhizobia infected cells is required to ensure optimal symbiotic nitrogen fixation. Two F-group basic region leucine-zipper (F-bZip) transcription factors were described and functionally characterized in *M. truncatula*, and MtFbZIP1 was identified as a key regulator of the Zn deficiency response related gene expression. Another approach to overcome crop Zn deficiency is described by Li et al. where the authors studied foliar Zn fertilization in sunflower leaves and subsequent translocation by transcriptome analysis combined with synchrotron-based X-ray fluorescence microscopy (XFM). It was observed that foliar Zn application caused rapid stress to the leaf, but once the stress decreased Zn was moved from the leaf epidermis to the vascular tissues. However, it was proposed that loading of Zn into the phloem, or the limited Zn mobility within the phloem itself, determine the restricted translocation of foliar applied Zn in sunflower leaves.

In terrestrial plants nutrients are mainly taken up through the roots. The Casparian strip represents a physical barrier controlling the inward flow of water and nutrients. Yang et al. reports of a novel rice mutant with delayed Casparian strip formation and ectopic suberin depositions in small lateral roots. As a consequence, the mutant showed higher concentrations of Fe, manganese (Mn) and sodium (Na) and a reduced tolerance to salt stress due to altered ion permeability. The affected gene encodes a Casparian strip membrane domain protein, which may form a transmembrane scaffold to recruit lignin biosynthetic enzymes.

In the water ecosystem nutrient uptake *via* the whole plant of submerged macrophytes is described by Xian et al. by comparing two species with different tolerances to ammonium. Ammonium uptake through the above-ground part was dominant under excess ammonium conditions, and the tolerant species possessed a higher plasticity in ammonium utilization under various concentrations and is a good candidate for applications in phytoremediation of polluted water.

Author contributions

All authors listed have made a substantial, direct and intellectual contribution to the work, and approved it for publication.

Acknowledgments

We thank all authors contributing to this Research Topic.

Conflict of interest

The authors declare that the research was conducted in the absence of any commercial or financial relationships that could be constructed as a potential conflict of interest.

Publisher's note

frontiers in Plant Science

ORIGINAL RESEARCH
published: 12 January 2022
doi: 10.3389/fpls.2021.755944

Stable Cu Isotope Ratios Show Changes in Cu Uptake and Transport Mechanisms in *Vitis vinifera* Due to High Cu Exposure

Simon Blotevogel[1]†, Priscia Oliva[1], Laurence Denaix[2], Stéphane Audry[1], Jerome Viers[1] and Eva Schreck[1]*

[1] *Géosciences Environnement Toulouse (GET), Université Paul-Sabatier Toulouse III, CNRS, IRD, Toulouse, France,*
[2] *Interactions Sol Plante Atmosphère (ISPA), Institut National de Recherche Pour l'Agriculture, l'Alimentation et l'Environnement (INRAE), Bordeaux Sciences Agro, Villenave d'Ornon, France*

Even though copper (Cu) is an essential plant nutrient, it can become toxic under certain conditions. Toxic effects do not only depend on soil Cu content, but also on environmental and physiological factors, that are not well understood. In this study, the mechanisms of Cu bioavailability and the homeostasis of *Vitis vinifera* L. cv. Tannat were investigated under controlled conditions, using stable Cu isotope analysis. We measured Cu concentrations and δ^{65}Cu isotope ratios in soils, soil solutions, roots, and leaves of grapevine plants grown on six different vineyard soils, in a 16-week greenhouse experiment. The mobility of Cu in the soil solutions was controlled by the solubility of soil organic matter. No direct relationship between Cu contents in soils or soil solutions and Cu contents in roots could be established, indicating a partly homeostatic control of Cu uptake. Isotope fractionation between soil solutions and roots shifted from light to heavy with increasing Cu exposure, in line with a shift from active to passive uptake. Passive uptake appears to exceed active uptake for soil solution concentrations higher than 270 $\mu g\ L^{-1}$. Isotope fractionation between roots and leaves was increasingly negative with increasing root Cu contents, even though the leaf Cu contents did not differ significantly. Our results suggest that Cu isotope analysis is a sensitive tool to monitor differences in Cu uptake and translocation pathways even before differences in tissue contents can be observed.

Keywords: *Vitis vinifera*, copper, metal stress response, soil solution (pore water), bioavailability, translocation, grapevine, humic acid

OPEN ACCESS

Edited by:
Anja Schneider, Ludwig Maximilian University of Munich, Germany

Reviewed by:
Szilvia Veres, University of Debrecen, Hungary
Cristina Caldelas, University of Barcelona, Spain

***Correspondence:**
Simon Blotevogel
Simon.Blotevogel@insa-toulouse.fr

†Present address:
Simon Blotevogel, Laboratoire Matériaux et Durabilité des Constructions (LMDC), Université Paul Sabatier Toulouse III, INSA, Toulouse, France

Specialty section:
This article was submitted to Plant Nutrition, a section of the journal Frontiers in Plant Science

Received: *09 August 2021*
Accepted: *03 December 2021*
Published: *12 January 2022*

Citation:
Blotevogel S, Oliva P, Denaix L, Audry S, Viers J and Schreck E (2022) Stable Cu Isotope Ratios Show Changes in Cu Uptake and Transport Mechanisms in Vitis vinifera Due to High Cu Exposure. Front. Plant Sci. 12:755944. doi: 10.3389/fpls.2021.755944

INTRODUCTION

Grapevine plants are commonly sprayed with copper (Cu) based fungicides, including the Bordeaux mixture ($CuSO_4$, combined with lime), Cu-oxides (Cu_2O, CuO), and Cu-hydroxide (Babcsanyi, 2015; Blotevogel et al., 2018). These fungicides have been used for more than 150 years and are still the only permitted treatment against downy mildew in organic viticulture. The long-term treatment of vineyards with Cu-based fungicides led to increased Cu contents, especially in topsoils (Flores-VéLez et al., 1996; Brun et al., 2001; Chaignon et al., 2003; Pietrzak and McPhail, 2004; Duplay et al., 2014). Even if copper is an essential nutrient for plants, it can become toxic if it is available in excess (Marschner and Marschner, 2012). The grapevine plant was long believed to be tolerant to high Cu exposure but reports of negative side effects are increasing and some

vineyards experience problems during replantation (Toselli et al., 2009; Anatole-Monnier, 2014; Martins et al., 2014; Miotto et al., 2014; Ambrosini et al., 2015; Brunetto et al., 2016). The mobility and phytoavailability of Cu in soils and its uptake by plants are complex and not only depending on soil or plant properties but also on their interaction (Yin et al., 2002; Kabata-Pendias, 2004; Ma et al., 2006; Wang and Staunton, 2006; Bravin et al., 2009a, 2012).

In soils, Cu shows a strong chemical affinity for the particulate phase (e.g., oxyhydroxides and organic matter) (Chaignon et al., 2003; Bradl, 2004; Pietrzak and McPhail, 2004; Strawn and Baker, 2008, 2009; Sayen et al., 2009; Sayen and Guillon, 2010; Abgottspon et al., 2015). The Cu content in soil solutions is generally low compared with the bulk soil content and is mainly controlled by the presence of soluble organic ligands and pH (Lexmond, 1980; Yin et al., 2002; Ashworth and Alloway, 2004). In the direct vicinity of roots – the rhizosphere, physico-chemical conditions as pH, Eh, and presences of organic ligands can be modified by plants to meet their mineral nutrition needs (Hinsinger et al., 2003; Kraemer, 2004; Bravin et al., 2009a, 2012). On one hand, this can be used to limit toxicity, durum wheat for example drastically reduced the Cu bioavailability in contaminated soils by rhizosphere alkalization (Hinsinger et al., 2003; Bravin et al., 2009a, 2012). On the other hand, the solubility of scarcely available nutrients such as iron (Fe) can be increased by exudation of reducing agents and phytosiderophores (Kraemer, 2004; Schenkeveld and Kraemer, 2018). Note that both strategies are not ion-specific and will affect other elements as well (Hinsinger et al., 2003; Bravin et al., 2009a; Schenkeveld and Kraemer, 2018).

The plant uptake of metal from the soil solution depends on its concentration and speciation in the rhizosphere, on the plant species and nutrition status, and the availability of other nutrients (Yin et al., 2002; Bravin et al., 2009a, 2012; Toselli et al., 2009). Driven by diffusion or mass flow, ions and small complexes (<5 nm) from the soil solution enter the pores of the cell walls and penetrate far into the plant roots (**Figure 1**) *via* the so-called apoplastic pathway (Marschner and Marschner, 2012). Metal ions can be adsorbed to pectins in the cell wall and it was reported for high Cu exposures that large fractions of root Cu are sequestered by cell wall adsorption (Shi et al., 2011; Li et al., 2016; Wan et al., 2019; Cui et al., 2020). Nevertheless, the apoplast is a dynamic compartment and it was reported that plants can adjust the number and type of metal-binding pectins as a response to metal stress (Sattelmacher, 2001; Castaldi et al., 2010; Colzi et al., 2012; Meychik et al., 2016). Some 10–20% of the apoplastic Cu was reported to be in the reduced form of Cu(I) (Cui et al., 2020). Note that *in situ* measurements of compartmentalization and speciation in roots were usually carried out on plants that received high Cu doses to overcome experimental detection limits.

From the pore solution of the apoplast, the uptake of Cu into the root cells can be mediated by several transporters (**Figure 1**). Most important under low Cu availability are high-affinity transporters of the COPT/Ctr protein family (Martins et al., 2014; Printz et al., 2016). Those highly specific Cu transporters require the reduction of Cu into Cu(I) by ferric reductase oxidase (Bernal et al., 2012; Jouvin et al., 2012; Ryan et al., 2013). This is backed by the XANES analysis that shows large proportions of Cu(I) in plant roots and implies that the homeostasis of Cu is closely linked to that of Fe (Bernal et al., 2012; Ryan et al., 2013; Printz et al., 2016; Cui et al., 2020). Besides this high-affinity transport system, Cu(II) is likely also taken up through ZIP transporters and ion channels that can carry different divalent cations (Printz et al., 2016). At very high Cu exposure levels, plants might be able to efflux Cu from the root cells (Burkhead et al., 2009; Printz et al., 2016).

The Cu can then be transported from cell to cell or within the cells by Cu-specific chaperon proteins (Mira et al., 2001; Wintz and Vulpe, 2002; Printz et al., 2016). In plant fluids,

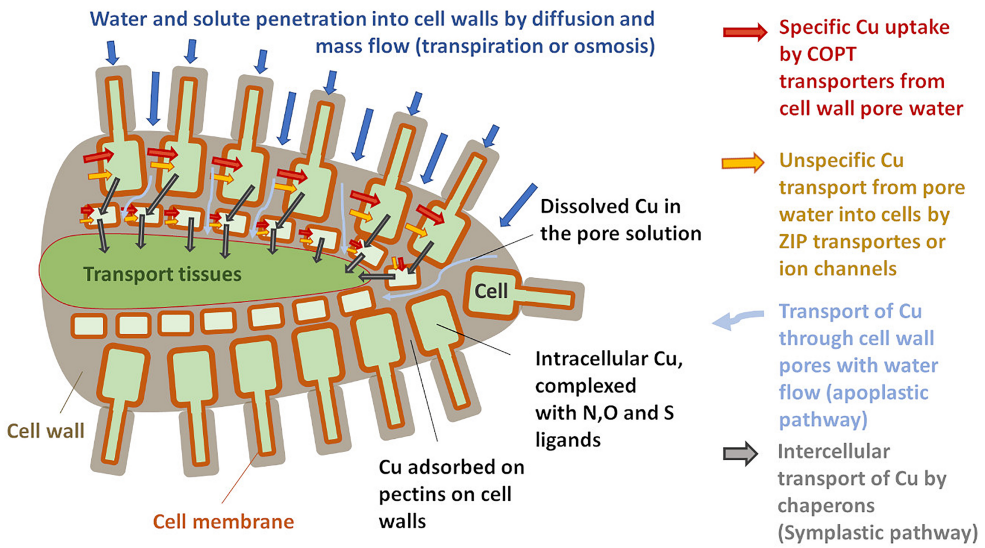

FIGURE 1 | Schematic sketch of copper (Cu) uptake and transport in roots (drawn after Printz et al., 2016; Kim et al., 2018).

Cu is likely to be present only in organometallic complexes that provide both solubility and shielding during long-distance transport (Alvarez-Fernandez et al., 2014 and references therein). Such complexes prevent toxicity as they are less reactive than free metal ions (Burkhead et al., 2009; Guigues et al., 2016). To reach the xylem that transports Cu up into the leaves, Cu coming from both symplastic and apoplastic pathways needs to be transported across the Casparian strip, a diffusion barrier for solutes (Printz et al., 2016; Kim et al., 2018). From there Cu is translocated towards the leaves *via* the xylem sap.

Meanwhile, isotope ratios of Cu have been used to trace Cu dynamics in soils (Bigalke et al., 2010b; Fekiacova et al., 2015; Babcsányi et al., 2016; Vance et al., 2016; Kusonwiriyawong et al., 2017; Blotevogel et al., 2018) and plants (Weinstein et al., 2011; Jouvin et al., 2012; Ryan et al., 2013; Li et al., 2016; Blotevogel et al., 2019). While soil processes regulating Cu mobility and speciation, as complexation with organic ligands, redox reactions, and mineral dissolution, induce limited Cu-isotopic fractionation (<1‰), Cu uptake and translocation in plants have been observed to cause large fractionations up to −1.43‰ (Bigalke et al., 2010a; Weinstein et al., 2011; Jouvin et al., 2012; Mathur et al., 2012; Ryan et al., 2013; Babcsányi et al., 2016; Li et al., 2016; Blotevogel et al., 2018, 2019). Several studies investigated Cu isotope fractionation in plants under hydroponic conditions and contributed to the understanding of redox steps during uptake by consistently reporting light isotope uptake (Jouvin et al., 2012; Ryan et al., 2013). Both studies report different fractionation patterns for root to shoot transport, which are likely due to differences in speciation of supplied Cu (ionic versus complexed) or root washing and desorption protocols (Jouvin et al., 2012; Ryan et al., 2013). Hydroponic conditions do not perfectly mimic natural systems especially they dilute root exudates and modify nutrient balance and supply mechanisms as well as Cu speciation in solution. In former studies, field-grown plants showed stronger isotope fractionation (up to −2‰) than were observed in hydroponic studies (Weinstein et al., 2011; Blotevogel et al., 2018, 2019).

Thus, to better understand the mechanisms of Cu-availability in soils, its uptake and translocation into the plant under increasing Cu-concentrations in vinyard soils, we performed a greenhouse experiment with pot-grown grapevine plants (i.e., *Vitis vinifera* L. cv. Tannat). Cu-concentrations and δ^{65}Cu isotope ratios were measured in the soils, soil solution, roots, and leaves of plants grown in six different soils presenting variable Cu pesticide background and pedological characteristics. Soil solutions were sampled every two weeks and grapevine plants were destructively harvested for analysis after 16 weeks. We thus aimed to show that the mechanisms of Cu mobility and homeostasis can be efficiently monitored by Cu stable isotope fractionation.

MATERIALS AND METHODS

Soil Description

The six selected surface soils (0–20 cm) were sampled from three winegrowing areas in France and one in Italy, presenting different soil types, physico-chemical properties, and in particular different Cu treatment histories (**Table 1**). Among the three soils coming from the "Bordeaux" area, two of them (HBN, CO) have been used for viticulture and received Cu fungicide application for over 100 years. Replantation of grapevine was reported to be problematic for these soils, likely due to Cu toxicity to young plants (details are published in Anatole-Monier in 2014). The third soil from the "Bordeaux" area (OB) was a forest soil that was recently converted to conventional viticulture including the use of Cu-based fungicide (conversion 4 years before sampling). The two soils from the "Soave" region (CI, VI) in northern Italy have received Cu fungicide applications for about a century but there was no evidence of toxicity for grapevines. The last selected soil (STM) is a vineyard soil from the Saint Mont region (STM), which did not receive any Cu treatment.

The soil samples were air-dried and sieved to 2 mm. The soil pH was measured on 1 g in 5 mL ultrapure water (18.2 MΩ) following the ISO 11464 protocol. The cation exchange capacity (CEC) was determined using cobalt hexamine. Therefore, 1 g of soil was shaken in 20 mL of a 0.017 mol L^{-1} cobalthexamine solution for 1 h, solutions were subsequently centrifuged and the supernatant filtered at 0.22 μm. Then, the cobalthexamine loss from the solution was determined by absorbance loss at 475 nm with a Varian Cary 50 spectrophotometer, Varian, Palo Alto, CA, United States. The total soil organic carbon (SOC) and total soil inorganic carbon (SIC) were calculated after subsequent measures of raw and calcined samples on a EMIA – 320 V CS automate, by Horiba Kyoto, Japan.

Experimental Design

Composite samples (100 kg) of the first 20 cm of each soil were taken during winter and spring 2016 before the first annual fungicide treatment. The soils were root-picked, dried at room temperature, and sieved with a 2-mm mesh before potting. Soil samples were then filled into 5 L PVC (polyvinyl chloride) pots and one young vine plant (*Vitis vinifera* L. cv. Tannat grafted on rootstock *V. riparia* × *V. rupestris* cv. 101.14) was planted into each pot. Five replication pots were prepared for each soil modality and a microporous cup (RHIZON® MOM 10 cm, Rhizosphere Research Products, pore size ∼0.1 μm) was inserted into each pot for sampling soil solution (**Figure 2**). After planting, pots were saturated with water and placed on heated ground until bud break (5d). Then, pots were placed in a greenhouse at the ISPA laboratory (INRAE Institute, Bordeaux, France) under artificial lighting mimicking 12 h of daily sunshine (**Figure 2**). The plants were regularly watered using demineralized water to maintain soil moisture at 80% of the water holding capacity of each soil.

Sampling of Soil Solution and Plant Tissues

Soil solution sampling began one week after potting and from then on samples were taken every two weeks. Samples were taken by applying under pressure to the suction cups for 10 min, thereby extracting between 0.5 and 10 mL of solution. The first two samples (week 0 and week 2) were

TABLE 1 | Pedological, mineralogical and physico-chemical properties of the studied vineyard soils.

Soil ID	Area	Type of viticulture	Soil type	Main mineral phases	pH	CEC	SIC	SOC
						cmol kg^{-1}	% wt	% wt
CO	Bordeaux, France	Conventional	Fluvisol	Qtz.	7.2	5.2	<0.1	0.6
HBN	Bordeaux, France	Conventional	Fluvisol	Qtz.	7.4	7.7	0.1	1.3
OB	Bordeaux, France	Conventional	Fluvisol	Qtz.	7.6	3.8	<0.1	0.5
CI	Soave, Italy	Organic	Calcaric Cambisol	Calc., Fels., Smec.	7.8	49.9	5.1	2.1
VI	Soave, Italy	Organic	Vertic Cambisol	Fels., Smec., Qtz.	7.7	59.8	0.4	2.5
STM	Saint Mont, France	Conventional (no Cu use)	Ferric Gleysol	Qtz.	6.6	5.5	<0.1	<0.1

Soil types are given according to the world reference base (WRB) (FAO, 2014), CEC, SIC, and SOC are abbreviations for cation exchange capacity, soil inorganic carbon, and soil organic carbon, respectively. Qtz. = Quartz, Calc. = Calcite, Smec. = Smectite, Fels. = Feldspar.

not included in the analysis, to let the system equilibrate. From week 4 to 16, the soil solution samples were collected and the total organic carbon (TOC) and total inorganic carbon (TIC), as well as pH, were measured promptly after sampling. Leftover solutions were acidified with ultrapure nitric acid to 2% (v/v) for later analyses of Cu concentration and isotope ratio.

Initially, five plants were grown per modality to be sure to have at least three healthy plants, as some soils were reported to be problematic for replantation. However, only three healthy plants per soil modality were destructively harvested after 16 weeks (see **Figure 2** for plants just before harvest). Five healthy fully unfolded leaves of every branch counting from the top were cut using a ceramic knife and put into plastic sample bags for Cu content and isotope ratio measurements.

Roots were extracted from soil and washed under flowing demineralized water. When no more soil particles were visible, the roots were cut from the trunk and put into sample bags. Root and leaf samples were then washed three times using demineralized water and twice using ultrapure water (18.2 MΩ). All samples were frozen at −80°C and freeze-dried. Once dried, root and leaf samples were ground to powder using a planetary mill with Zr-containers and balls.

FIGURE 2 | Picture of the grapevine plants and the soil solution sampling device, just before harvest. Plant height was about 1.2 m.

Determination of Cu Concentrations in Soil, Soil Solution, and Plant Samples

Sample digestion was carried out in the ISO 7 cleanroom laboratories of the GET Toulouse and the LEGOS Toulouse. A 100 mg sample of each ground soil was digested in a MARS 5 microwave oven (by CEM, Matthews, NC, United States) using ultrapure acids (9 mL HNO_3: 2 mL HCl: 3 mL HF), the solution was then evaporated and the samples were dissolved in double subboiled HNO_3 for analysis. Details of the digestion protocol were published elsewhere (Blotevogel et al., 2018). The plant samples were digested on hotplates in three steps. For each plant sample, 200 mg of powder were weighed into Savillex Teflon vessels. Then, 1 mL of ultrapure hydrogen (H_2O_2) was added and left to react for 2 h at room temperature. Subsequently, 5 mL of double subboiled nitric acid (HNO_3) were added in 1 mL steps to each vessel and left to react overnight. Successively, the vessels were heated to 120°C for at least 4 h and evaporated to dryness at 90°C. Once dried, 4 mL of double subboiled HCl and 2 mL of double subboiled HNO_3 were added along with 1 mL of suprapure HF. Finally, vessels were heated to 120°C for at least 4 h and evaporated to dryness at 90°C. A final digestion step was performed using 5 mL HNO_3, the samples were again heated to 120°C for at least 4 h and evaporated to dryness at 90°C.

All soil solution samples with sufficient volume (more than 100 μL) were analyzed for their Cu concentration. During the whole experiment, 1 replicate for OB, 2 for CO, 5 for CI and VI, 6 for HBN, and 9 replicates for STM could not be analyzed for their Cu content, either due to handling errors or too low sample volume (see **Supplementary Information** for details).

In soil soultions and digested soil and plant samples, total Cu concentrations were measured by inductively coupled plasmamass-spectrometry (ICP-MS) (7500ce, Agilent Technologies – Santa Clara, CA, United States) and inductively coupled plasma – optical emission spectrometry (ICP-OES) (Ultima Expert, Horiba Jobin Yvon, Kyoto, Japan) at the GET laboratory. The analytical accuracy and precision of measurements were ensured by measuring replicates of the SLRS-5 river water standard ($n = 6$). Relative standard deviations (RSD%) were <5% and Cu-recovery 100 ± 5%. The accuracy and precision of the whole sample preparation procedure were checked by determining Cu concentration in BCR-2 basalt standard [Cu recovery of 96 ± 10% ($n = 3$)] and SRM-1515 apple leaf standard [Cu recovery of 92 ± 5% ($n = 4$)].

Isotope Analyses in Soil, Soil Solution, and Plant Samples

Cu isotope measurement by multicollector-inductively coupled plasma mass spectrometer (MC-ICP-MS) (Neptune, by Thermo Fisher, Bremen, Germany) required at least 500 ng of Cu. When the amount of Cu was insufficient in a single soil solution sample, we chose to pool all replicates from a given sample week (e.g., STM and VI modalities and the late samples of OB). This allowed us to have at least one soil solution Cu isotope measurement per modality at each sample time.

Purification of digested samples was carried out under ISO1 laminar flow hoods using anionic AG MP-1 resin (Bio-Rad PolyPrep chromatographic columns – Hercules, CA, United States) (Maréchal et al., 1999). Volumes of resin and solution were adapted for the different matrices to ensure quantitative elution, as the separation procedure fractionates Cu isotopes up to ≈ 19‰, between the first and the last mL of Cu elution (Maréchal and Albarède, 2002). Soil samples were purified according to the protocol described in Blotevogel et al. (2018) and displayed in the supporting information (**Supplementary Information Table 1**). Soil solution aliquots were digested in three steps as described above for plant samples. For purification of soil solution, root, and leaf samples, the same Bio-Rad Poly Prep chromatographic columns were filled with 2 mL of AG MP-1 resin and conditioned according to Maréchal et al. (1999). After sample loading using 1 mL of a 7 M HCl solution containing 0.01% of H_2O_2, the matrix was eluted by passing 9 mL of the same 7M HCl, 0.01% H_2O_2 solution. Cu was then eluted using 24 mL of the same solution (**Supplementary Information Table 1**). This same purification procedure was carried out twice for soil solution, root, and leaf samples. Details on the method development and elution profiles can be found in Blotevogel (2017). Cu isotope ratios are expressed in ‰ relative to NIST 976 Cu standard (Eq. 1).

$$\delta^{65}Cu = \left(\frac{\left({}^{65}Cu/{}^{63}Cu\right)_{Sample}}{\left({}^{65}Cu/{}^{63}Cu\right)_{NIST976}} - 1 \right) * 1000 \qquad (1)$$

Recovery of all purified samples was checked to be 100 ± 5%. BCR-2 standards were used as precision and accuracy control of the whole procedure, the reference material was digested three times and four different purification runs were performed allowing 10 measurements. BCR-2 isotope ratios (0.26 ± 0.09‰) were slightly heavier than values from literature 0.20 ± 0.10‰ (Babcsányi et al., 2014) and 0.22 ± 0.05‰ (Bigalke et al., 2010a) but within the 2SD range of those results.

Statistical Analyses

All data analysis was carried out using the R software® in version 4.0.3. Plant biomass and Cu concentration data were analyzed using a one-way ANOVA. Except for Cu concentrations in roots ($[Cu]_{Roots}$) and in soil solutions ($[Cu]_{Solution}$) there was no departure from normality of residues within a 95% confidence interval using a Shapiro-Wilk test. To achieve normality, the $[Cu]_{Roots}$ and $[Cu]_{Solution}$ datasets were submitted to a logarithmic transformation and afterward satisfied the above-mentioned criteria. The one way ANOVAs were computed to determine if the soil type had a significant influence on the data set. Differences between means were then tested using Tukey's HSD. Differences between groups are shown in compact letter display computed using Tukey's HSD with $p < 0.05$. For soil solution samples, a one-way ANOVA was computed for each soil type to detect if there were significant differences in Cu concentration over time.

Isotope data were reported using the mean value of the three replicate samples and a 2 standard deviation (SD) error bar around this mean. Differences were considered as significant if 2SD intervals did not overlap. For isotope fractionation data the standard deviation of replicate measurements was propagated.

RESULTS

Mobility of Cu Into the Soil Solution and Its Evolution Over Time

Copper (Cu) concentrations in bulk soils ($[Cu]_{Soil}$) were between 3 and 251 mg kg^{-1} (**Table 2**). OB and STM had the lowest $[Cu]_{Soil}$ (3 and 10 mg kg^{-1}, respectively), whereas CO, CI, VI, and HBN soils had higher $[Cu]_{Soil}$ of 115, 214, 229, and 251 mg kg^{-1}, respectively.

During the experiment, for each soil modality, the $[Cu]_{Solution}$ remained in the same order of magnitude (**Figure 3**). Only for CI the one-way ANOVA showed a significant influence of the time on $[Cu]_{Solution}$ ($p < 0.0002$) and Tukey's HSD indicated that the solutions of week 16 had significantly ($p < 0.02$) higher Cu concentrations than solutions from all other time steps (**Figure 3**).

The lowest mean $[Cu]_{Solution}$ was measured in STM soils (19 μg L^{-1}), followed by CI and VI soils with mean $[Cu]_{Solution}$ of 40 and 100 μg L^{-1}, respectively (**Figure 4**). The highest $[Cu]_{Solution}$ values were measured in soils from the "Bordeaux" area with 297, 999, and 2,705 μg L^{-1} (for OB, HBN, and CO, respectively). The differences between different modalities were much larger than variations over time within the same soil (**Figure 4**). A one-way ANOVA showed a significant influence of soil type on $[Cu]_{Solution}$ ($p < 10^{-15}$) and Tukey's HSD indicated that mean $[Cu]_{Solution}$ for each soil modality was significantly ($p < 10^{-5}$) different from all other soil modalities (**Figure 4**).

There was no direct correlation between $[Cu]_{Soil}$ and $[Cu]_{Solution}$ (**Figure 5A**), also between the TOC of the soil solution and $[Cu]_{Solution}$ no direct correlation could be established, even when STM was excluded from the fit. Nevertheless, there was a positive relationship between mobile SOM (expressed as TOC/SOC) and mobile Cu (expressed $[Cu]_{Solution}/[Cu]_{Soil}$), when STM was excluded (**Figure 5B**, $R^2 = 0.92$, $p = 0.01$, $n = 5$).

Mean Cu isotope ratios in soil solutions include all measured samples with the exception of week 4 (**Table 2**). Samples of week 4 were excluded because they appeared to show transitional variations in some samples as discussed below. For STM, VI, and late OB samples all replicates were pooled for a given time step. To detect temporal variations, the evolution of one replicate is shown for CI, HBN, and CO. In STM, VI, and CI soil solutions, Cu isotope ratios are heavier than in the corresponding bulk soils ($\Delta^{65}Cu_{Solution-Soil}$ around + 0.4‰, **Figure 6**). No Cu isotope fractionation between soil and soil solution was detected in soils

TABLE 2 | Mean Cu concentrations and isotopic ratios in the different compartments (soil, soil solution, roots, and leaves) of the different soil modalities (STM, VI, CI, OB, HBN, CO). For soils also SOC values are given and in soil solutions pH and TOC.

		Type	STM	VI	CI	OB	HBN	CO
SOC	wt.%	Soil	0.1	2.5	2.1	0.5	1.3	0.6
TOC	mg L^{-1}	Solution	43	41	62	102	76	97
pH		Solution	6.4	7.9	7.7	8.0	7.8	7.9
Cu	mg kg^{-1}	Soil	10	229	214	3	251	115
Mean Cu ± SD	µg L^{-1}	Solution	19 ± 9 a	40 ± 15 b	100 ± 37 c	297 ± 247 d	999 ± 680 e	2,705 ± 1,215 f
Min-Max Cu	µg L^{-1}	Solution	11–30	28–61	66–170	21–816	469–1,671	794–6,060
Mean Cu ± SD	mg kg^{-1}	Roots	30 ± 8 a	81 ± 20 b	199 ± 27 c	25 ± 5 a	768 ± 114 d	579 ± 156 d
Min-Max Cu	mg kg^{-1}	Roots	24–39	68–103	169–220	21–31	654–883	403–701
Mean Cu ± SD	mg kg^{-1}	Leaves	5.1 ± 1.1 a	7.4 ± 2.1 ab	6.7 ± 1.1 ab	4.9 ± 2.2 ab	6.1 ± 1.2 ab	10.9 ± 3.1 b
Min-Max Cu	mg kg^{-1}	Leaves	3.9–5.9	6.0–9.8	5.4–7.5	3.4–6.5	5.1–7.4	7.8–14.0
δ^{65}Cu ± 2SD	‰	Soil	0.17 ± 0.11	0.33 ± 0.01	0.21 ± 0.04	0.27 ± 0.24	0.12 ± 0.07	0.02 ± 0.09
δ^{65}Cu* ± 2SD	‰	Solution	0.61 ± 0.08	0.56 ± 0.11	0.55 ± 0.11	0.21 ± 0.14	0.05 ± 0.11	−0.02 ± 0.11
^{65}Cu ± 2SD	‰	Roots	0.25 ± 0.04	0.30 ± 0.05	0.37 ± 0.03	0.26 ± 0.08	0.30 ± 0.20	0.24 ± 0.18
δ^{65}Cu ± 2SD	‰	Leaves	0.20 ± 0.07	0.00 ± 0.16	−0.08 ± 0.30	0.24 ± 0.01	−0.20 ± 0.17	−0.14 ± 0.25
Δ^{65}Cu* ± 2SD	‰	Solution*-Soil	0.44 ± 0.14	0.23 ± 0.11	0.34 ± 0.12	−0.06 ± 0.28	−0.07 ± 0.13	−0.04 ± 0.14
Δ^{65}Cu* ± 2SD	‰	Root-Solution*	−0.36 ± 0.09	−0.26 ± 0.12	−0.18 ± 0.11	0.05 ± 0.16	0.25 ± 0.23	0.26 ± 0.21
Δ^{65}Cu ± 2SD	‰	Leaves-Roots	−0.05 ± 0.08	−0.30 ± 0.17	−0.45 ± 0.30	−0.02 ± 0.08	−0.50 ± 0.26	−0.38 ± 0.31

Mean Cu and standard deviation (SD) values were calculated using all available Cu analyses (25 < n < 33 in soil solutions and n = 3 in plant tissues). The compact letter displays behind mean Cu values indicate significant differences between groups calculated using Tukey's HSD with an alpha of 0.05. The 2SD values in isotope analysis correspond to a 2SD interval around the mean, calculated using isotope ratio analysis of all replicates (n = 3 for plant samples and n = 1, 2, 3, 3, 8, 12, for isotope analysis in STM, VI, CI, OB, HBN, and CO soil solutions, respectively, note that STM and VI solution were pooled over multiple replicates and time steps). For the soil samples, only one sample was analyzed in the beginning of the experiment and the 2SD interval corresponds to repeated isotope measurements including sample preparation. Δ^{65}Cu values correspond to the Cu isotope fractionation between two compartments. δ^{65}Cu are mean Cu isotope composition for soil solutions calculated without samples from week 4.*

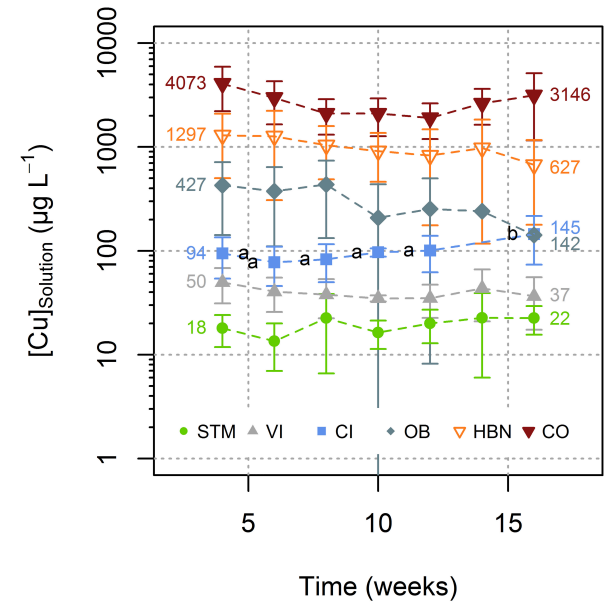

FIGURE 3 | Evolution of Cu concentration in soil solutions with time. Reported results for each time point corresponding to the mean value of Cu concentrations in all replicates for each soil type (see **Supplementary Information 1** for detailed values). Error bars correspond to the 2SD interval around the mean. Only for CI significant evolution over time was detected (Tukey's HSD, α = 0.05). Groups are displayed as letters beside the respective points.

from the Bordeaux area (**Figure 6**). Only in the first analyzed samples (week 4) of HBN and VI, δ^{65}Cu values were significantly heavier in soil solution than in bulk soil ($\Delta^{65}Cu_{Solution-Soil}$ of 0.29 ± 0.09‰ and 0.63 ± 0.03‰, respectively).

Biomass Production of Grapevine Plants

After 16 weeks of growth, the measured root biomass was between 10.1 and 20.9 g DW (**Figure 7**). A one-way ANOVA showed a significant influence of soil modality on root biomass ($p < 0.02$). Tukey's HSD showed that only the mean root biomasses of VI and OB soil were significantly different ($p < 0.04$), with 6.28 g higher root biomass in VI than in OB. For all other samples, differences were not significant (**Figure 7**).

The leaf biomass was also different according to the soil modality (one-way ANOVA $p < 0.001$). Tukey's HSD showed that CI samples had a significantly higher leaf biomass than STM (−11.3 g DW, $p < 0.04$), OB (−12.7 g DW, $p < 0.02$), and CO (−18.6 g DW, $p < 0.001$) samples, and VI samples had a higher leaf biomass than OB (−11.0 g DW, $p < 0.05$) and CO (−16.9 g DW, $p < 0.03$) samples. Furthermore, HBN samples had higher leaf biomass than CO (−12.2 g DW, $p < 0.03$) samples. Significantly different groups are shown in compact letter display in **Figure 7**.

Copper Uptake From Soil Solution to Roots

The lowest mean Cu concentrations in roots ($[Cu]_{Roots}$) were detected in STM and OB grown plants with 30 and 25 mg kg^{-1}

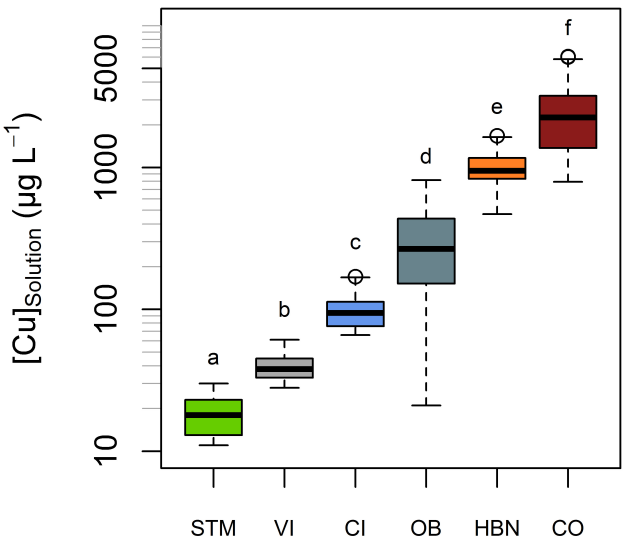

FIGURE 4 | Cu concentrations (expressed in µg L^{-1}) in solution denoted $[Cu]_{solution}$, in the six different soils. All measurements of soil solution in each soil, including different points in times and replicates, are represented in this plot. The bold line represents the median value and the boxes include values between the 25th and 75th percentile, the y-axis is in log-scale. $[Cu]_{solution}$ significantly (Tukey's HSD, $\alpha = 0.05$) differed from each soil to each soil. Groups are shown by letters above the boxes.

(**Table 2**), followed by the Italian soils CI and VI, with $[Cu]_{Roots}$ of 199 and 81 mg kg^{-1}. The highest $[Cu]_{Roots}$ were found in CO and HBN soils with, respectively, 579 and 768 mg kg^{-1}. The differences in $[Cu]_{Roots}$ were statistically significant between the soil modalities (one-way ANOVA $p < 10^{-9}$). Tukey's HSD showed that with exception of the pairs OB-STM and HBN-CO, $[Cu]_{Roots}$ significantly differed between each soil modality ($p < 0.002$, **Table 2**). The $[Cu]_{Roots}$ followed the rank of $[Cu]_{Solution}$ (**Figure 4**) for most soils, only the rank of OB decreased. Except in CI and VI, $[Cu]_{Roots}$ was higher than the $[Cu]_{Soil}$ so that significant contamination by possible leftover soil particles can be excluded. $[Cu]_{Roots}$ was not correlated to $[Cu]_{Soil}$ or $[Cu]_{Solution}$ (**Figures 8A,B**).

Copper isotope fractionation between soil solution and roots was increasingly positive with higher $[Cu]_{Solution}$ (**Figure 9A**). Negative Cu isotope fractionation between roots and soil solutions occurs in STM, VI and CI modalities ($\Delta^{65}Cu_{Roots-Solution}$ of -0.36 ± 0.09‰, -0.26 ± 0.12‰, and -0.18 ± 0.11‰, respectively). Positive isotope fractionation between roots and soil solution was observed for the Bordeaux soils OB, HBN, and OB ($\Delta^{65}Cu_{Roots-Solution}$ = 0.05 ± 0.16‰, 0.25 ± 0.23‰ and 0.26 ± 0.21‰, respectively). A logarithmic function ($\Delta^{65}Cu_{Roots-Solution}$ = 0.137 * ln ($[Cu]_{Solution}$) – 0.766) was fitted through all data points ($n = 6$, $R^2 = 0.96$, $p < 0.001$) (**Figure 9A**).

Copper Root-to-Leaf Transfer in Grapevine Plants

Given the large differences of Cu content in soil solutions, between 19 and 2,705 µg L^{-1}, the $[Cu]_{Leaves}$ were surprisingly similar in the different modalities, between 4.9 and 10.9 mg kg^{-1}. One-way ANOVA showed nevertheless a significant influence of soil modality on $[Cu]_{Leaves}$ ($p < 0.04$). Tukey's HSD indicated that $[Cu]_{Leaves}$ only differed significantly between STM and CO samples ($p < 0.04$).

When Cu content in roots was low (i.e., OB and STM), no Cu isotope fractionation between roots and leaves occurred (**Figure 9B**). Modalities with higher Cu content in roots (CI, VI, HBN, and CO) showed light Cu isotope enrichment in leaves compared to roots (**Figure 9B**).

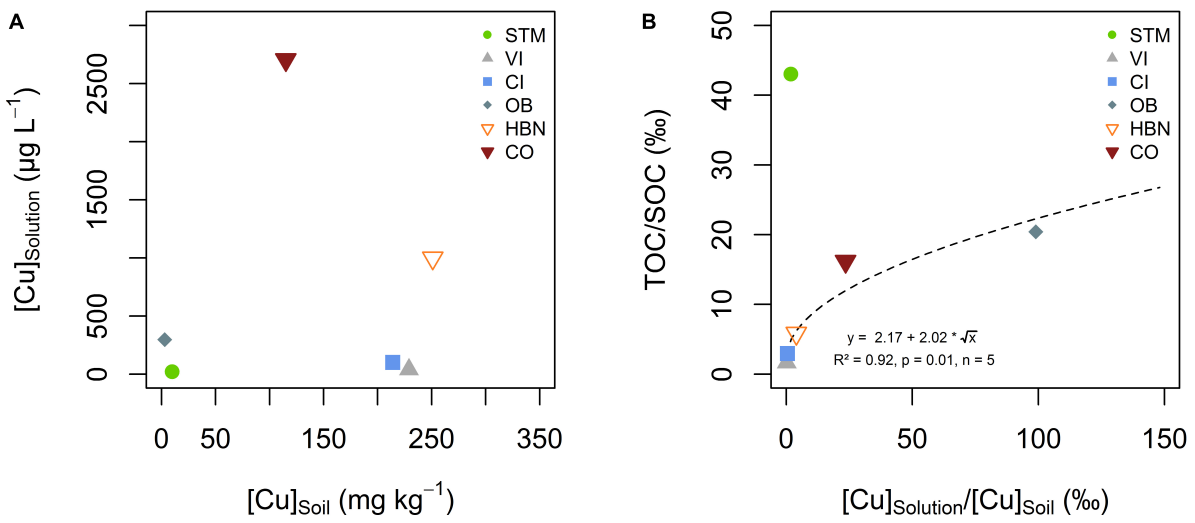

FIGURE 5 | (A) Bulk soil Cu concentration ($[Cu]_{soil}$) plotted against the arithmetic mean of soil solution Cu concentration ($[Cu]_{solution}$). **(B)** Ratios of solution total organic carbon (TOC) over SOC plotted against mean solution Cu over soil Cu content for the different soil modalities. The dashed line represents the best fit of a square root function on the data excluding STM.

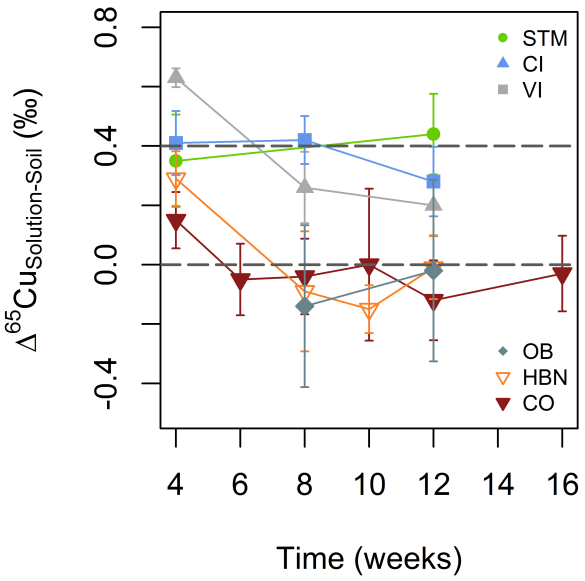

FIGURE 6 | Evolution of Cu isotope fractionation between soil solutions and bulk soil for the different soil modalities. The gray lines indicate + 0.4 and 0 (per mile) to guide the eye. Error bars correspond to the 2SD interval (see Statistical Analyses section for details).

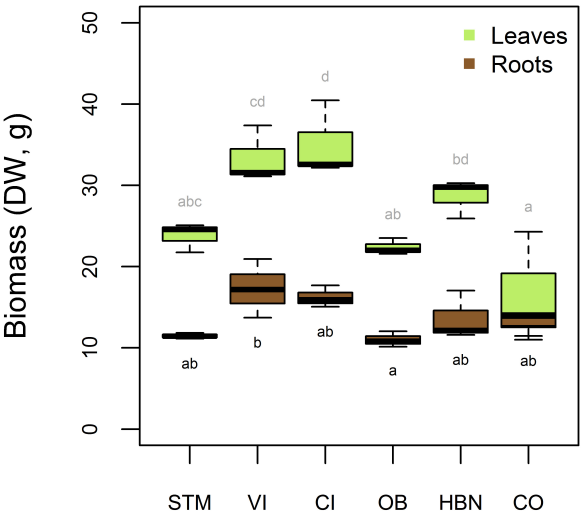

FIGURE 7 | Biomass of roots and leaves of the grapevine plants in dry weight (DW) per soil. Leaf biomasses include young leaves, that were used for Cu analysis, as well as old and senescent leaves that were not analyzed. Significantly different (Tukey's HSD, $\alpha = 0.05$) groups are displayed above the boxes for leaf masses and below for root masses.

DISCUSSION

Mobility of Cu Into the Soil Solution and Its Evolution Over Time

$[Cu]_{Soil}$ of OB and STM was below average European background concentration of about 14 mg kg^{-1}, whereas CO, CI, VI, and HBN soils showed Cu concentrations above the European background level, similar to other Cu contaminated vineyard soils (Chaignon et al., 2003; Lado et al., 2008; Reimann et al., 2018). CI, VI, and HBN exceeded the predicted no-effect concentration (PNEC) for Cu in soils (200 mg kg^{-1}) but concentrations were still two to three times less than maximum Cu contents measured in European vineyard soils (Ruyters et al., 2013; Reimann et al., 2018).

Copper mobility in soil solution appeared to be controlled by SOC mobility, rather than by the amount of TOC in the soil solution (**Figure 5B**). It has long been established that Cu in soil solution is primarily bound to organic matter, however, the role of the mobility of SOC on Cu mobility was less studied (Yin et al., 2002; Chaignon et al., 2003; Ashworth and Alloway, 2004; Ren et al., 2015). In the present study, only soil solutions from the STM soil did not fit into the trend (**Figure 5B**). This might be linked to the lower pH of STM soil solution, and thus slight differences in Cu speciation in solution or competition between Cu and protons for adsorption sites on dissolved organic matter (Yin et al., 2002; Chaignon et al., 2003; Bravin et al., 2009a, 2012). STM is also the only soil that did not receive any Cu treatment so that it is possible that only exogenic Cu is controlled by SOM mobility (Wang and Staunton, 2006). This is supported by a correlation between Fe and Cu contents in the STM soil solution (**Supplementary Information**).

A mobile Cu pool, adsorbed or complexed with organic matter is consistent with a heavy isotopic Cu signature in solution, as observed for STM, CI, and VI (**Figure 6**; Yin et al., 2002; Chaignon et al., 2003; Ashworth and Alloway, 2004; Vance et al., 2008; Bigalke et al., 2010a; Kusonwiriyawong et al., 2016). The absence of isotope fractionation between soil solution and bulk soils from the Bordeaux area suggests that the total Cu pool in soil and the mobile Cu pool have similar chemical speciation or that desorption does not fractionate Cu isotopes (**Figure 6**). No isotope fractionation between soil and soil solution would for example be observed if Cu gets into the soil solution by solubilization of the organic molecule to which Cu is bound.

The absence of a $[Cu]_{Soil} - [Cu]_{Solution}$ correlation (**Figure 5A**) is in contrast with previous studies that found correlations between bulk soil Cu, extractable Cu, or the ionic Cu^{2+} fraction and root Cu (Chaignon et al., 2003; Bravin et al., 2009a,b, 2012). Some studies reported a good correlation between bulk soil Cu and pore water Cu, especially in contaminated soils (Sauvé et al., 2000). However, our observation is perfectly in line with research showing that pH and surface adsorption control Cu mobility, not bulk soil content (Brun et al., 2001; Yin et al., 2002; Chaignon et al., 2003). There was little variation in $[Cu]_{Solution}$ over time compared to water-extractable Cu in soil incubation experiments (Wang and Staunton, 2006). The increase of $[Cu]_{Solution}$ in CI over time might reflect active processes, including rhizosphere acidification, exudation of reducing agents or phytosiderophores, implemented by plants to satisfy needs of Fe nutrition (Kraemer, 2004; Ström et al., 2005). Indeed, CI is the most calcic soil of the experiment and Fe deficiency is common in such soils (Kraemer, 2004; Ström et al., 2005).

In our setting, the offset in isotope fractionation in the first sample is likely due to the rewetting and adaptation of the soil to

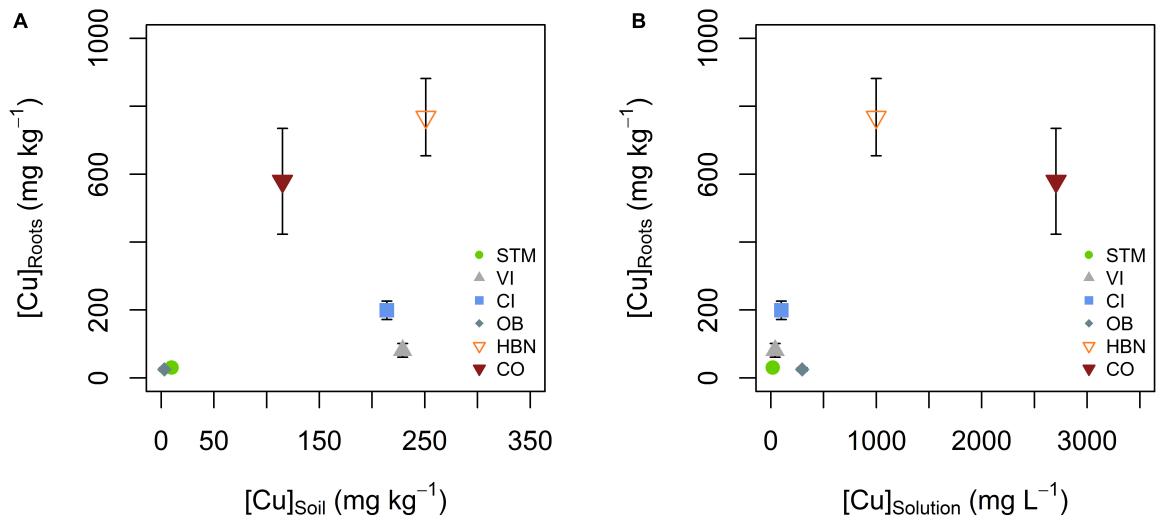

FIGURE 8 | (A) Mean root Cu concentration ($[Cu]_{Roots}$) plotted against bulk soil Cu concentration ($[Cu]_{Soil}$). **(B)** Mean root Cu concentration ($[Cu]_{Roots}$) plotted against mean soil solution Cu concentration ($[Cu]_{Solution}$). There was no apparent correlation between $[Cu]_{Roots}$ and $[Cu]_{Soil}$ or $[Cu]_{Solution}$. Error bars correspond to the SD interval around the mean of $[Cu]_{Roots}$ for three replicates per soil modality.

the new environment, accompanied by a priming effect (**Figure 6**; Miller et al., 2005). It was formerly reported that the initial DOM released from rewetted soils has a lower affinity to Cu compared to later, more humified DOM (Amery et al., 2007). Detailed interpretation of this effect without further data would be speculative but if present, it suggests that transitory effects on microbiological activity and/or soil organic matter quality can play an important role in Cu mobility and isotope fractionation.

Copper Uptake and Translocation in Grapevine Plants

Biomass Production

The observations that root biomass was not significantly different in the different soils was surprising, as one of the first symptoms of Cu toxicity in plants is reduced and abnormal root growth (Ambrosini et al., 2015). The only significant difference was detected between VI and OB, indicating that inhibition of root growth was strongest at low $[Cu]_{Roots}$. However, OB also showed very high Fe concentrations in the first solution samples, so that reductive conditions and Fe toxicity might have played a role in this modality (**Supplementary Information**). The modalities CO and HBN with high Cu contents showed lower root biomass than CI and VI samples even though this was not significant at a 95% level (**Figure 4**). Plants grown on VI and CI soils also had higher leave biomass than most other modalities, suggesting that low and high Cu supplies limited leaf growth.

Cu Concentrations in Plant Tissues

Even though soil solution concentrations varied by more than a factor ×100, grapevine leaves had only a narrow Cu concentration range (**Table 2**). The Cu concentrations reported for the leaves in our study are consistent with the value of around 6 mg kg^{-1} reported in healthy leaves (Marschner and Marschner, 2012). Moreover, despite high Cu content in soil solutions, no signs of toxicity, such as abnormal root morphology, were observed (Ambrosini et al., 2015). Significant differences in $[Cu]_{Leaves}$ were only detected between the least and most concentrated leaves. These observations are in line with former research showing a tight homeostatic control of Cu in plant tissues (Mitchell et al., 1978; Brun et al., 2001; Chaignon et al., 2003; Alaoui-Sossé et al., 2004; Chen et al., 2011; Marschner and Marschner, 2012; Ryan et al., 2013).

Relevant Mechanisms of Cu Isotope Fractionation in Plants

To interpret Cu isotope fractionation within plants it is important to consider the equilibrium fractionation of Cu isotopes during reactions that might occur within the plant. At first, the Cu isotope fractionation induced by the complexation of aqueous Cu^{2+} by organic ligands is reported to be heavy. Bigalke et al. (2010a) measured an enrichment of + 0.26 ± 0.11‰ in insolubilized humic acid with respect to solution Cu^{2+}. Ryan et al. (2014) reported increasingly heavy isotope fractionation of up to 0.84‰ with increasing complex stability. On the other hand, reactions that included the reduction of Cu(II) to Cu(I) were reported to induce a strong light isotope fractionation of -2.6 to -4 ‰ in the reduced phase (Zhu et al., 2002; Ehrlich et al., 2004; Navarrete et al., 2011). However, one needs to bear in mind that under non-equilibrium conditions, light isotopes tend to react faster than heavy isotopes leading to an enrichment of light isotopes in the reaction products – the so-called kinetic isotope fractionation. This effect can lead to isotope signatures opposite to what would be expected from equilibrium fractionation.

Mechanisms of Cu Isotope Fractionation During Root-to-Shoot Transport

Isotope fractionation between roots and leaves was light for samples with high Cu exposure (**Figure 9B**), consistent with

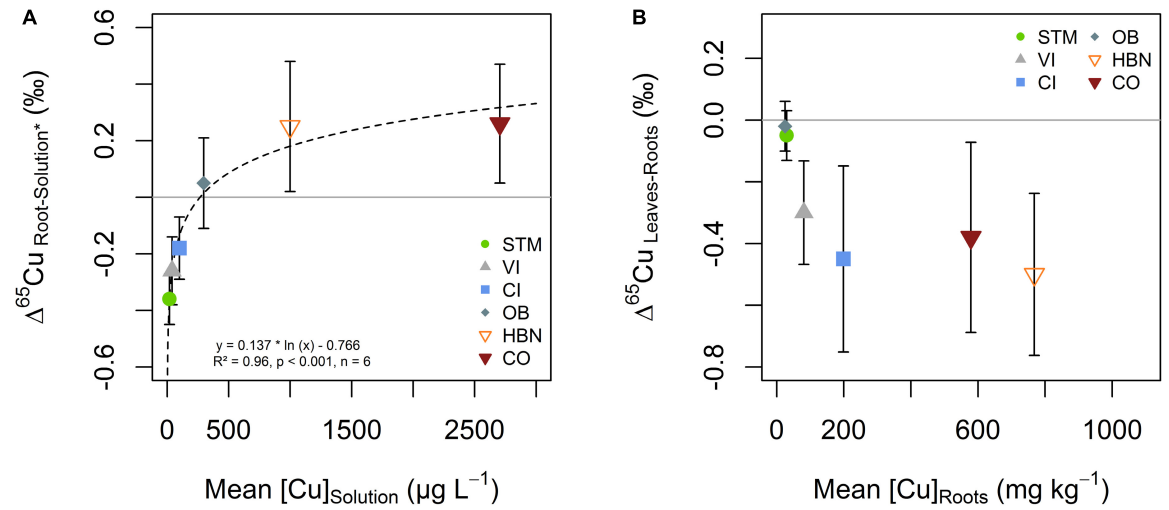

FIGURE 9 | (A) Isotope fractionation between soil solution and roots as a function Cu content in the soil solution. Isotope ratios in soil solution excluded the 4 weeks sample (Solution*), due to transient variations discussed (see section "Mobility of Cu Into the Soil Solution and Its Evolution Over Time"). The dashed line represents the fit of the logarithmic function displayed in the figure. **(B)** Cu isotope fractionation between roots and leaves plotted against Cu content in roots. The error bars in both panels correspond to the 2SD interval around the mean of three replicate plants per soil modality.

earlier studies showing light Cu isotope enrichment in aerial parts of the plant (Weinstein et al., 2011; Jouvin et al., 2012; Blotevogel et al., 2019). This effect might be due to the retention of heavy Cu in the roots, by vacuole storage or pectin binding as a response to Cu excess. This would lead to the depletion of heavy Cu isotopes in the cytoplasm so that light isotopes would be preferentially transported to the leaves. Another possibility is kinetic fractionation during Cu transport to leaves, which is increasingly negative with increasing Cu availability and transpiration rates (Ryan et al., 2013; Couder et al., 2015; Li et al., 2016). The latter is also in line with observations of very light isotope signatures in leaves of the field grow grapevine plants (Blotevogel et al., 2019).

Mechanisms Associated With Light Isotope Uptake

Isotope fractionation at the solution-root interface reveals the dynamic character of Cu uptake by the grapevine roots (**Figure 9A**). When Cu supply was low, light isotope fractionation occurred at the soil solution-root interface (STM, VI, CI). In earlier studies, light isotope fractionation was associated with active Cu uptake mechanisms including Cu(II) reduction to Cu(I) at the root surface (Jouvin et al., 2012; Ryan et al., 2013). Besides, a study on yeast cells reported a large light isotope fractionation during uptake by wild types when Cu was supplied as Cu(II) (Cadiou et al., 2017). This fractionation was absent when reductase activity was suppressed, but present when Cu(I) was supplied in solution. They concluded that active high-affinity transporters induce a strong light isotope fractionation if sufficient Cu(I) is available. This suggests, that light isotope fractionation during plant uptake is not exclusively due to Cu(II) reduction. The lighter Cu ratios might stem from kinetic fractionation due to the one-way character of high-affinity uptake (Hindshaw et al., 2013). In our setting, kinetic isotope fractionation can likely be ruled out as the light isotope fractionation between soil solution and roots does not increase with increasing Cu supply, so that the fractionation at low Cu exposure is likely due to a combination of Cu(II) reduction and active transport.

Mechanisms Associated With Heavy Isotope Uptake

The progressively positive fractionation between roots and soil solutions (**Figure 9A**) suggests that the part of Cu that is actively taken up decreases with increasing Cu content in soil solution. Preferential uptake of heavy Cu isotopes (OB, HBN, CO) is likely due to the complexation of Cu on pectin groups at the cell wall or storage mechanisms of excess Cu (Ryan et al., 2013). Furthermore, the uptake of complexed Cu from solution or unspecific uptake pathways such as ZIP transporters, YSL transporters, or ion channels could lead to higher isotope ratios in roots than in soil solution (Laurie et al., 1991; Roberts et al., 2004; Ryan et al., 2013; Caldelas and Weiss, 2017). Fitting the logarithmic function displayed in **Figure 9A** suggests that the $[Cu]_{Solution}$ for which active uptake is lower or equal to unspecific, passive uptake is 270 µg L^{-1}. This value was determined as the x-intercept of the function because from this point on negative fractionation from active uptake is completely compensated by positive fractionation from passive uptake. The limit would be reached at even lower concentrations if the fractionation of "pure" active uptake is even more negative than isotope fractionation in STM.

Cu Adsorption vs. Cu Uptake

Earlier research suggested that a large part (70%) of root Cu is adsorbed on root surfaces (Ryan et al., 2013; Li et al., 2016). In the apoplast, Cu is mainly bound to carboxyl groups of cell wall polymers or nitrogen groups of cell wall proteins, both favor heavy isotopes (Reilly, 1969; Allan and Jarrell, 1989; Sattelmacher, 2001; Colzi et al., 2012; Ryan et al., 2014; Guigues et al., 2016).

The immobilization of heavy Cu appears not to be purely due to adsorption. The absence of correlation between $[Cu]_{Solution}$ and $[Cu]_{Roots}$ shows that $[Cu]_{Roots}$ is already influenced by the plant's biological response to Cu availability rather than pure physico-chemical factors. For example, pure adsorption of Cu on roots with the same binding sites would result in an adsorption isotherm, that was not observed here. A modification of type and number of pectin molecules at the root surface as a response to Cu exposure or lowered transpiration mass transport might explain this observation (Sattelmacher, 2001; Castaldi et al., 2010; Colzi et al., 2012; Meychik et al., 2016). Further, possible plant responses to Cu exposure include immobilization of Cu *via* metallothioneins in vacuoles or efflux pumping as well as modification of physicochemical properties in the rhizosphere (Zhou et al., 2007; Bravin et al., 2009a,b; Burkhead et al., 2009; Yruela, 2009; Jouvin et al., 2012; Alvarez-Fernandez et al., 2014; Printz et al., 2016).

Conceptual Geochemical and Physiological Issues of Isotope Fractionation in Whole Plants Raised by the Data

When the overall plant isotope ratios are different from the soil solution, a heavy or a light part of the soil solution Cu either never got into the plant tissue or have been effluxed. This statement includes the cell wall pores making up the apoplastic pathway. Single organ values always present a convoluted signal of input and out into the organ. We do not present a full mass balance here, because stem Cu contents and isotopic ratios were not measured. However, in our setting we can reasonably well approximate the whole plant δ^{65}Cu:

(a) In soils, in which roots were lighter than the soil solution, the leaves had the same isotopic ratios as the roots (STM) or were lighter than the roots (CI, VI). Even though we do not have data on stems, these observations suggest that the whole plants were lighter than the soil solution.
(b) In HBN and CO, in which root Cu was heavier than soil solution Cu, the $[Cu]_{Roots}$ exceed the $[Cu]_{Leaves}$ by more than a factor ×50. Even though leave mass is about ×2–×3 higher than that of roots, only a minor fraction of the plant Cu was transported to the leaves. Therefore, the overall plant value can be approximated by the root δ^{65}Cu. This suggests that, in HBN and CO-grown plants, the overall Cu isotope ratio is heavy.

Earlier conceptual models explained only light Cu uptake by the plant, but here heavy enrichment of plants needs also to be considered. With the present data, we cannot clearly identify the responsible mechanisms but some hypotheses can be made.

Hypothesis 1: One possibility is that OM complexed Cu from the soil solution – which represents virtually all Cu in our study – might not enter the apoplastic pathway, because even basic units of humic and fulvic acids are larger (10 nm) than cell wall pores (5 nm) and the full molecules are much larger (>500 nm) (Baalousha et al., 2006; Marschner and Marschner, 2012; Klučáková, 2018). This implies

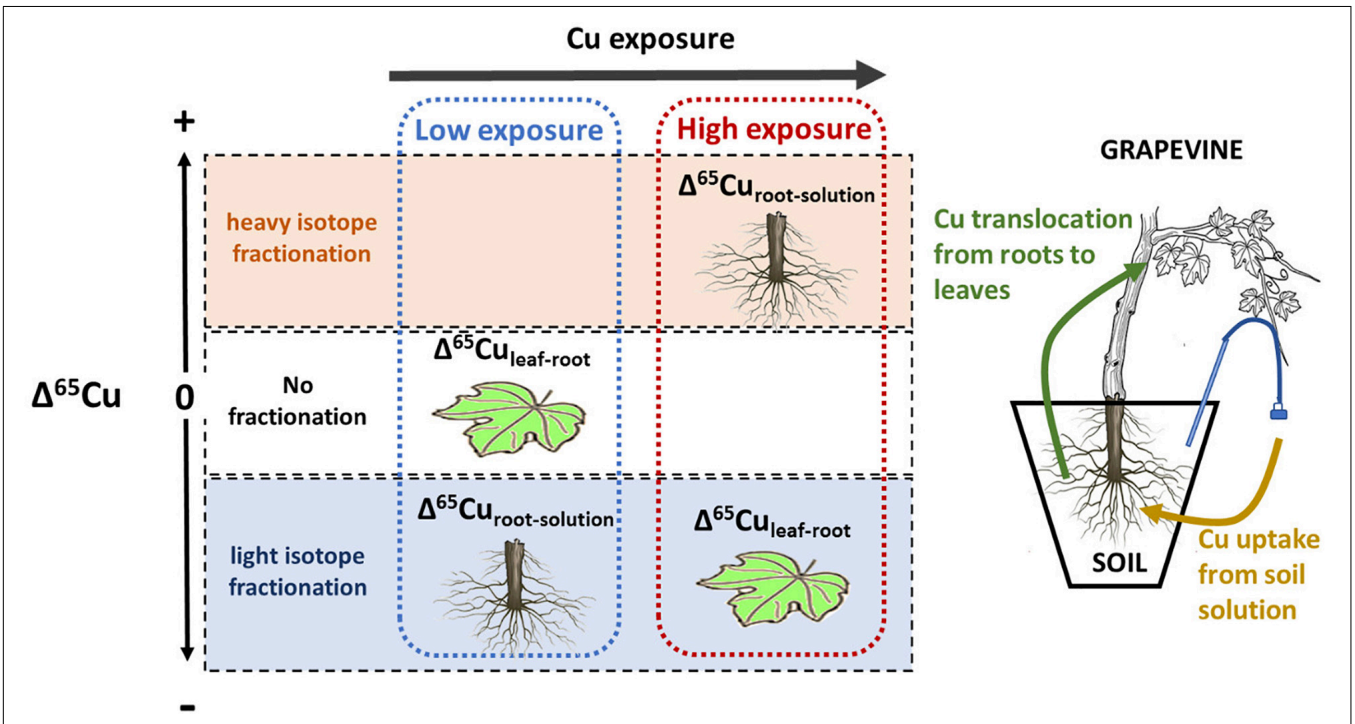

FIGURE 10 | Schematic sketch of Cu isotope fractionation depending on Cu exposure of the plant. At low exposure, Cu isotope ratios in roots are lighter than the soil solution, likely associated with active uptake. No fractionation occurs between roots and leaves. At high exposure root isotope ratios are heavier than the soil solution, likely liked to passive uptake and detoxification. In this scenario leave Cu is lighter than roots.

that a large part of the complexed heavy Cu is excluded from the apoplastic pathway. The fractionation patterns discussed in section "Relevant Mechanisms of Cu Isotope Fractionation in Plants" therefore might only happen at the root surface, and not in the apoplast. This would be consistent with our data for light isotope enrichment (transporters directly take light Cu from soil solution) and heavy enrichment (root surface is in exchange with soil solution and heavy isotopes are adsorbed). This fractionation pattern is in line with the conceptual model of Jouvin et al. (2012), only adding the constraint of non-penetration of Cu into the root cell wall pores. The apparent contradiction with studies showing large fractions of Cu in the apoplast might be due to the environmental parameters as acid pH or absence of SOM, which allowed for a significant fraction due to ionic Cu^{2+}, that was able to penetrate the apoplast in those studies (Ryan et al., 2013; Meychik et al., 2016; Cui et al., 2020).

Hypothesis 2: Another possibility for heavy isotope enrichment in plants is efflux pumping of light Cu isotopes. Cu efflux pumping is mentioned in the main reviews of Cu transport in plants, but experimental constraints remain scarce (Sattelmacher, 2001; Printz et al., 2016). Under this hypothesis, a significant fraction of the soil solution Cu could enter the root apoplast with the transpiration flow. Under high Cu exposure, light Cu would be effluxed by specific transporters against the transpiration flow, resulting in heavy Cu accumulation in the plant. This would be in line with the preferential transport of light Cu by specific transporters (Cadiou et al., 2017). Furthermore, the absence of a correlation between $[Cu]_{Root}$ and $[Cu]_{Solution}$ would be explained, because of the active regulation of Cu content by the plant. For light isotope fractionation at low Cu exposure, the fractionation might occur outside of the root, for example through exsudation of reducing agents, that preferentially mobilize light Cu from the solid soil. But light isotope fractionation might also result from the exclusion of very large, strong complexants as described under Hypothesis 1.

CONCLUSION

This study reports results of a 16-week greenhouse experiment growing grapevine plants on 6 soils with different Cu-pesticide treatment histories. The mobility and phytoavailability of Cu in the soil solution were controlled by the solubility of organic matter, not bulk soil Cu content or DOC. Root Cu concentrations showed no direct correlation with bulk soil or soil solution Cu concentration. The Cu-isotope fractionation between soil solution and roots was light for low Cu exposure and increasingly heavy for higher exposure levels, suggesting a progressive change from active to passive uptake (**Figure 10**). At around 270 $\mu g\ L^{-1}$, the isotope fractionation between soil solution and roots changed from light to heavy, indicating that from this value the passive uptake was equal to or higher than the active uptake. Isotope fractionation between leaves and roots was absent for low Cu exposure levels, and light for high exposure.

Our results show that isotope fractionation patterns in roots and leaves are linked to Cu exposure of the plants. In particular, Cu isotope fractionation between roots and soil solution can be used as a specific and sensitive tool to monitor changes in uptake mechanisms.

Besides, isotope ratios in leaves might be used to detect high Cu exposure levels before changes in Cu content occur (**Figure 10**). This is of particular importance in grapevine as physiological effects on roots are often observed before leaf Cu content increases (Toselli et al., 2009; Ambrosini et al., 2015; Brunetto et al., 2016).

DATA AVAILABILITY STATEMENT

The original contributions presented in the study are included in the article/**Supplementary Material**, further inquiries can be directed to the corresponding author.

AUTHOR CONTRIBUTIONS

SB, PO, LD, and SA did the soil sampling. SB, PO, LD, and ES participated in and supervised the greenhouse experiments and plant sampling. SB, PO, LD, JV, and ES performed and supervised chemical analysis and sample handling. SB, PO, and ES participated in writing the first draft. PO and ES acquired funding and did the project administration. All authors were involved in reviewing and editing.

FUNDING

This study was funded by the French National Institute of Sciences of the Universe (INSU) through the EC2CO-BIOHEFECT program under the project name TERVIT. SB received funding from the French Ministry of Education through a Ph.D. Grant.

ACKNOWLEDGMENTS

The authors would like to thank William Bonnet for his precious help with chemical analyses, Sylvie Bussière and Cécile Coriou for running the greenhouse experiment, Jérôme Chmeleff, Aurélie Marquet, and Philippe Besson for help with ICP analysis, and Manuel Henry and Catherine Pradoux for access and maintenance of the clean room laboratory. Finally, the authors would like to thank Cristina Caldelas and Szilvia Veres for their detailed and constructive reviews.

SUPPLEMENTARY MATERIAL

The Supplementary Material for this article can be found online at: https://www.frontiersin.org/articles/10.3389/fpls.2021.755944/full#supplementary-material

REFERENCES

Abgottspon, F., Bigalke, M., and Wilcke, W. (2015). Fast colloidal and dissolved release of trace elements in a carbonatic soil after experimental flooding. *Geoderma* 259–260, 156–163. doi: 10.1016/j.geoderma.2015.06.005

Alaoui-Sossé, B., Genet, P., Vinit-Dunand, F., Toussaint, M.-L., Epron, D., and Badot, P.-M. (2004). Effect of copper on growth in cucumber plants (*Cucumis sativus*) and its relationships with carbohydrate accumulation and changes in ion contents. *Plant Sci.* 166, 1213–1218.

Allan, D. L., and Jarrell, W. M. (1989). Proton and copper adsorption to maize and soybean root cell walls. *Plant Physiol.* 89, 823–832. doi: 10.1104/pp.89.3.823

Alvarez-Fernandez, A., Diaz-Benito, P., Abadi, A., Lopez-Millan, A.-F., and Abadia, J. (2014). Metal species involved in long distance metal transport in plants. *Front. Plant Sci.* 5:105. doi: 10.3389/fpls.2014.00105

Ambrosini, V. G., Rosa, D. J., Corredor Prado, J. P., Borghezan, M., Bastos de Melo, G. W., Fonsêca de Sousa Soares, C. R., et al. (2015). Reduction of copper phytotoxicity by liming: a study of the root anatomy of young vines (*Vitis labrusca* L.). *Plant Physiol. Biochem.* 96, 270–280. doi: 10.1016/j.plaphy.2015.08.012

Amery, F., Degryse, F., Degeling, W., Smolders, E., and Merckx, R. (2007). The copper-mobilizing-potential of dissolved organic matter in soils varies 10-fold depending on soil incubation and extraction procedures. *Environ. Sci. Technol.* 41, 2277–2281. doi: 10.1021/es062166r

Anatole-Monnier, L. (2014). *Effets De La Contamination Cuprique Des Sols Viticoles Sur La Sensibilité De La Vigne À Un Cortège De Bio-Agresseurs*. Bordeaux: Université de Bordeaux.

Ashworth, D. J., and Alloway, B. J. (2004). Soil mobility of sewage sludge-derived dissolved organic matter, copper, nickel and zinc. *Environ. Pollut.* 127, 137–144. doi: 10.1016/s0269-7491(03)00237-9

Baalousha, M., Motelica-Heino, M., and Coustumer, P. L. (2006). Conformation and size of humic substances: effects of major cation concentration and type, pH, salinity, and residence time. *Colloids Surf. A Physicochem. Eng. Aspects* 272, 48–55. doi: 10.1016/j.colsurfa.2005.07.010

Babcsanyi, I. (2015). *Copper Transport and Isotope Fractionation in an Agrosystem*. Strasbourg: Université de Strasbourg.

Babcsányi, I., Chabaux, F., Granet, M., Meite, F., Payraudeau, S., Duplay, J., et al. (2016). Copper in soil fractions and runoff in a vineyard catchment: insights from copper stable isotopes. *Sci. Total Environ.* 557–558, 154–162. doi: 10.1016/j.scitotenv.2016.03.037

Babcsányi, I., Imfeld, G., Granet, M., and Chabaux, F. (2014). Copper stable isotopes to trace copper behavior in wetland systems. *Environ. Sci. Technol.* 48, 5520–5529. doi: 10.1021/es405688v

Bernal, M., Casero, D., Singh, V., Wilson, G. T., Grande, A., Yang, H., et al. (2012). Transcriptome sequencing identifies SPL7 -regulated copper acquisition genes FRO4 / FRO5 and the copper dependence of iron homeostasis in *Arabidopsis*. *Plant Cell* 24, 738–761. doi: 10.1105/tpc.111.090431

Bigalke, M., Weyer, S., and Wilcke, W. (2010b). Stable copper isotopes: a novel tool to trace copper behavior in hydromorphic soils. *Soil Sci. Soc. Am. J.* 74:60.

Bigalke, M., Weyer, S., and Wilcke, W. (2010a). Copper isotope fractionation during complexation with insolubilized humic acid. *Environ. Sci. Technol.* 44, 5496–5502. doi: 10.1021/es1017653

Blotevogel, S. (2017). *Study of Elemental Transfers and Biogeochemical Mechanisms in the Soil-Plant-Wine Continuum Using Isotopic and Biochemical Tracers*. Bordeaux: Université de Bordeaux.

Blotevogel, S., Oliva, P., Sobanska, S., Viers, J., Vezin, H., Audry, S., et al. (2018). The fate of Cu pesticides in vineyard soils: a case study using δ 65 Cu isotope ratios and EPR analysis. *Chem. Geol.* 477, 35–46.

Blotevogel, S., Schreck, E., Audry, S., Saldi, G. D., Viers, J., Courjault-Radé, P., et al. (2019). Contribution of soil elemental contents and Cu and Sr isotope ratios to the understanding of pedogenetic processes and mechanisms involved in the soil-to-grape transfer (Soave vineyard, Italy). *Geoderma* 343, 72–85. doi: 10.1016/j.geoderma.2019.02.015

Bradl, H. B. (2004). Adsorption of heavy metal ions on soils and soils constituents. *J. Colloid Interface Sci.* 277, 1–18. doi: 10.1016/j.jcis.2004.04.005

Bravin, M. N., Garnier, C., Lenoble, V., Gérard, F., Dudal, Y., and Hinsinger, P. (2012). Root-induced changes in pH and dissolved organic matter binding capacity affect copper dynamic speciation in the rhizosphere. *Geochim. Cosmochim. Acta* 84, 256–268.

Bravin, M. N., Martí, A. L., Clairotte, M., and Hinsinger, P. (2009a). Rhizosphere alkalisation — a major driver of copper bioavailability over a broad pH range in an acidic, copper-contaminated soil. *Plant Soil* 318, 257–268.

Bravin, M. N., Tentscher, P., Rose, J., and Hinsinger, P. (2009b). Rhizosphere pH gradient controls copper availability in a strongly acidic soil. *Environ. Sci. Technol.* 43, 5686–5691. doi: 10.1021/es900055k

Brun, L. A., Maillet, J., Hinsinger, P., and Pépin, M. (2001). Evaluation of copper availability to plants in copper-contaminated vineyard soils. *Environ. Pollut.* 111, 293–302. doi: 10.1016/s0269-7491(00)00067-1

Brunetto, G., Bastos de Melo, G. W., Terzano, R., Del Buono, D., Astolfi, S., Tomasi, N., et al. (2016). Copper accumulation in vineyard soils: rhizosphere processes and agronomic practices to limit its toxicity. *Chemosphere* 162, 293–307. doi: 10.1016/j.chemosphere.2016.07.104

Burkhead, J. L., Gogolin Reynolds, K. A., Abdel-Ghany, S. E., Cohu, C. M., and Pilon, M. (2009). Copper homeostasis: tansley review. *New Phytol.* 182, 799–816.

Cadiou, J.-L., Pichat, S., Bondanese, V. P., Soulard, A., Fujii, T., Albarède, F., et al. (2017). Copper transporters are responsible for copper isotopic fractionation in eukaryotic cells. *Sci. Rep.* 7:44533. doi: 10.1038/srep44533

Caldelas, C., and Weiss, D. J. (2017). Zinc Homeostasis and isotopic fractionation in plants: a review. *Plant Soil* 411, 17–46.

Castaldi, P., Lauro, G., Senette, C., and Deiana, S. (2010). Role of the Ca-pectates on the accumulation of heavy metals in the root apoplasm. *Plant Physiol. Biochem.* 48, 1008–1014. doi: 10.1016/j.plaphy.2010.09.017

Chaignon, V., Sanchez-Neira, I., Herrmann, P., Jaillard, B., and Hinsinger, P. (2003). Copper bioavailability and extractability as related to chemical properties of contaminated soils from a vine-growing area. *Environ. Pollut.* 123, 229–238. doi: 10.1016/s0269-7491(02)00374-3

Chen, C.-C., Chen, Y.-Y., Tang, I.-C., Liang, H.-M., Lai, C.-C., Chiou, J.-M., et al. (2011). *Arabidopsis* SUMO E3 ligase SIZ1 is involved in excess copper tolerance. *Plant Physiol.* 156, 2225–2234. doi: 10.1104/pp.111.178996

Colzi, I., Arnetoli, M., Gallo, A., Doumett, S., Del Bubba, M., Pignattelli, S., et al. (2012). Copper tolerance strategies involving the root cell wall pectins in *Silene paradoxa* L. *Environ. Exp. Bot.* 78, 91–98. doi: 10.1016/j.envexpbot.2011.12.028

Couder, E., Mattielli, N., Drouet, T., Smolders, E., Delvaux, B., Iserentant, A., et al. (2015). Transpiration flow controls Zn transport in *Brassica napus* and *Lolium multiflorum* under toxic levels as evidenced from isotopic fractionation. *Comptes Rendus Geosci.* 347, 386–396. doi: 10.1016/j.crte.2015.05.004

Cui, J., Zhao, Y., Chan, T., Zhang, L., Tsang, D. C. W., and Li, X. (2020). Spatial distribution and molecular speciation of copper in indigenous plants from contaminated mine sites: implication for phytostabilization. *J. Hazard. Mater.* 381:121208. doi: 10.1016/j.jhazmat.2019.121208

Duplay, J., Semhi, K., Errais, E., Imfeld, G., Babcsanyi, I., and Perrone, T. (2014). Copper, zinc, lead and cadmium bioavailability and retention in vineyard soils (Rouffach, France): the impact of cultural practices. *Geoderma* 230–231, 318–328.

Ehrlich, S., Butler, I., Halicz, L., Rickard, D., Oldroyd, A., and Matthews, A. (2004). Experimental study of the copper isotope fractionation between aqueous Cu(II) and covellite, CuS. *Chem. Geol.* 209, 259–269.

FAO (2014). *World Reference Base for Soil Resources 2014: International Soil Classification System for Naming Soils and Creating Legends for Soil Maps*. Rome: FAO.

Fekiacova, Z., Cornu, S., and Pichat, S. (2015). Tracing contamination sources in soils with Cu and Zn isotopic ratios. *Sci. Total Environ.* 517, 96–105. doi: 10.1016/j.scitotenv.2015.02.046

Flores-VéLez, L. M., Ducaroir, J., Jaunet, A. M., and Robert, M. (1996). Study of the distribution of copper in an acid sandy vineyard soil by three different methods. *Eur. J. Soil Sci.* 47, 523–532. doi: 10.1111/j.1365-2389.1996.tb01852.x

Guigues, S., Bravin, M. N., Garnier, C., Masion, A., Chevassus-Rosset, C., Cazevieille, P., et al. (2016). Involvement of nitrogen functional groups in high-affinity copper binding in tomato and wheat root apoplasts:

spectroscopic and thermodynamic evidence. *Metallomics* 8, 366–376. doi: 10.1039/c5mt00298b

Hindshaw, R. S., Reynolds, B. C., Wiederhold, J. G., Kiczka, M., Kretzschmar, R., and Bourdon, B. (2013). Calcium isotope fractionation in alpine plants. *Biogeochemistry* 112, 373–388.

Hinsinger, P., Plassard, C., Tang, C., and Jaillard, B. (2003). Origins of root-mediated pH changes in the rhizosphere and their responses to environmental constraints: a review. *Plant Soil* 248, 43–59.

Jouvin, D., Weiss, D. J., Mason, T. F. M., Bravin, M. N., Louvat, P., Zhao, F., et al. (2012). Stable isotopes of Cu and Zn in higher plants: evidence for Cu reduction at the root surface and two conceptual models for isotopic fractionation processes. *Environ. Sci. Technol.* 46, 2652–2660. doi: 10.1021/es202587m

Kabata-Pendias, A. (2004). Soil–plant transfer of trace elements—an environmental issue. *Geoderma* 122, 143–149.

Kim, Y. X., Ranathunge, K., Lee, S., Lee, Y., Lee, D., and Sung, J. (2018). Composite transport model and water and solute transport across plant roots: an update. *Front. Plant Sci.* 9:193. doi: 10.3389/fpls.2018.00193

Klučáková, M. (2018). Size and charge evaluation of standard humic and fulvic acids as crucial factors to determine their environmental behavior and impact. *Front. Chem.* 6:235. doi: 10.3389/fchem.2018.00235

Kraemer, S. M. (2004). Iron oxide dissolution and solubility in the presence of siderophores. *Aquat. Sci.* 66, 3–18.

Kusonwiriyawong, C., Bigalke, M., Abgottspon, F., Lazarov, M., and Wilcke, W. (2016). Response of Cu partitioning to flooding: a δ65Cu approach in a carbonatic alluvial soil. *Chem. Geol.* 420, 69–76.

Kusonwiriyawong, C., Bigalke, M., Cornu, S., Montagne, D., Fekiacova, Z., Lazarov, M., et al. (2017). Response of copper concentrations and stable isotope ratios to artificial drainage in a French Retisol. *Geoderma* 300, 44–54.

Lado, L. R., Hengl, T., and Reuter, H. I. (2008). Heavy metals in European soils: a geostatistical analysis of the FOREGS Geochemical database. *Geoderma* 148, 189–199. doi: 10.1016/j.geoderma.2008.09.020

Laurie, S. H., Tancock, N. P., Mcgrath, S. P., and Sanders, J. R. (1991). Influence of complexation on the uptake by plants of iron, manganese, copper and zinc: I. effect of edta in a multi-metal and computer simulation study. *J. Exp. Bot.* 42, 509–513.

Lexmond, T. H. M. (1980). The effect of soil pH on copper toxicity to forage maize grown under field conditions. *Netherlands J. Agric. Sci.* 28, 164–184. doi: 10.18174/njas.v28i3.17030

Li, S.-Z., Zhu, X.-K., Wu, L.-H., and Luo, Y.-M. (2016). Cu isotopic compositions in *Elsholtzia splendens*: influence of soil condition and growth period on Cu isotopic fractionation in plant tissue. *Chem. Geol.* 444, 49–58. doi: 10.1016/j.chemgeo.2016.09.036

Ma, Y., Lombi, E., Oliver, I. W., Nolan, A. L., and McLaughlin, M. J. (2006). Long-term aging of copper added to soils. *Environ. Sci. Technol.* 40, 6310–6317. doi: 10.1021/es060306r

Maréchal, C., and Albarède, F. (2002). Ion-exchange fractionation of copper and zinc isotopes. *Geochim. Cosmochim. Acta* 66, 1499–1509. doi: 10.1016/s0016-7037(01)00815-8

Maréchal, C. N., Télouk, P., and Albarède, F. (1999). Precise analysis of copper and zinc isotopic compositions by plasma-source mass spectrometry. *Chem. Geol.* 156, 251–273. doi: 10.1016/s0009-2541(98)00191-0

Marschner, H., and Marschner, P. (eds) (2012). *Marschner's Mineral Nutrition of Higher Plants*. Amsterdam: Elsevier.

Martins, V., Teixeira, A., Bassil, E., Blumwald, E., and Gerós, H. (2014). Metabolic changes of *Vitis vinifera* berries and leaves exposed to Bordeaux mixture. *Plant Physiol. Biochem.* 82, 270–278. doi: 10.1016/j.plaphy.2014.06.016

Mathur, R., Jin, L., Prush, V., Paul, J., Ebersole, C., Fornadel, A., et al. (2012). Cu isotopes and concentrations during weathering of black shale of the Marcellus Formation, Huntingdon County, Pennsylvania (USA). *Chem. Geol.* 304–305, 175–184. doi: 10.1016/j.chemgeo.2012.02.015

Meychik, N., Nikolaeva, Y., Kushunina, M., and Yermakov, I. (2016). Contribution of apoplast to short-term copper uptake by wheat and mung bean roots. *Funct. Plant Biol.* 43:403. doi: 10.1071/FP15356

Miller, A., Schimel, J., Meixner, T., Sickman, J., and Melack, J. (2005). Episodic rewetting enhances carbon and nitrogen release from chaparral soils. *Soil Biol. Biochem.* 37, 2195–2204.

Miotto, A., Ceretta, C. A., Brunetto, G., Nicoloso, F. T., Girotto, E., Farias, J. G., et al. (2014). Copper uptake, accumulation and physiological changes in adult grapevines in response to excess copper in soil. *Plant Soil* 374, 593–610. doi: 10.1007/s11104-013-1886-7

Mira, H., Martínez-García, F., and Peñarrubia, L. (2001). Evidence for the plant-specific intercellular transport of the *Arabidopsis* copper chaperone CCH: *Arabidopsis* copper chaperone functions intercellularly. *Plant J.* 25, 521–528. doi: 10.1046/j.1365-313x.2001.00985.x

Mitchell, G. A., Bingham, F. T., and Page, A. L. (1978). Yield and metal composition of lettuce and wheat grown on soils amended with sewage sludge enriched with cadmium, copper, nickel, and zinc. *J. Environ. Qual.* 7, 165–171. doi: 10.2134/jeq1978.00472425000700020002x

Navarrete, J. U., Borrok, D. M., Viveros, M., and Ellzey, J. T. (2011). Copper isotope fractionation during surface adsorption and intracellular incorporation by bacteria. *Geochim. Cosmochim. Acta* 75, 784–799. doi: 10.1016/j.gca.2010.11.011

Pietrzak, U., and McPhail, D. C. (2004). Copper accumulation, distribution and fractionation in vineyard soils of Victoria, Australia. *Geoderma* 122, 151–166. doi: 10.1016/j.geoderma.2004.01.005

Printz, B., Lutts, S., Hausman, J.-F., and Sergeant, K. (2016). Copper trafficking in plants and its implication on cell wall dynamics. *Front. Plant Sci.* 7:601. doi: 10.3389/fpls.2016.00601

Reilly, C. (1969). The uptake and accumulation of copper by becium homblei (de wild.) duvig. & plancke. *New Phytol.* 68, 1081–1087. doi: 10.1111/j.1469-8137.1969.tb06509.x

Reimann, C., Fabian, K., Birke, M., Filzmoser, P., Demetriades, A., Négrel, P., et al. (2018). GEMAS: establishing geochemical background and threshold for 53 chemical elements in European agricultural soil. *Appl. Geochem.* 88, 302–318.

Ren, Z.-L., Tella, M., Bravin, M. N., Comans, R. N. J., Dai, J., Garnier, J.-M., et al. (2015). Effect of dissolved organic matter composition on metal speciation in soil solutions. *Chem. Geol.* 398, 61–69. doi: 10.1016/j.chemgeo.2015.01.020

Roberts, L. A., Pierson, A. J., Panaviene, Z., and Walker, E. L. (2004). Yellow Stripe1. Expanded roles for the maize iron-phytosiderophore transporter. *Plant Physiol.* 135, 112–120. doi: 10.1104/pp.103.037572

Ruyters, S., Salaets, P., Oorts, K., and Smolders, E. (2013). Copper toxicity in soils under established vineyards in Europe: a survey. *Sci. Total Environ.* 443, 470–477. doi: 10.1016/j.scitotenv.2012.11.001

Ryan, B. M., Kirby, J. K., Degryse, F., Harris, H., McLaughlin, M. J., and Scheiderich, K. (2013). Copper speciation and isotopic fractionation in plants: uptake and translocation mechanisms. *New Phytol.* 199, 367–378.

Ryan, B. M., Kirby, J. K., Degryse, F., Scheiderich, K., and McLaughlin, M. J. (2014). Copper isotope fractionation during equilibration with natural and synthetic ligands. *Environ. Sci. Technol.* 48, 8620–8626. doi: 10.1021/es500764x

Sattelmacher, B. (2001). The apoplast and its significance for plant mineral nutrition. *New Phytol.* 149, 167–192. doi: 10.1046/j.1469-8137.2001.00034.x

Sauvé, S., Hendershot, W., and Allen, H. E. (2000). Solid-solution partitioning of metals in contaminated soils: dependence on pH, total metal burden, and organic matter. *Environ. Sci. Technol.* 34, 1125–1131. doi: 10.1021/es9907764

Sayen, S., and Guillon, E. (2010). X-ray absorption spectroscopy study of Cu2+ geochemical partitioning in a vineyard soil. *J. Colloid Interface Sci.* 344, 611–615. doi: 10.1016/j.jcis.2009.12.028

Sayen, S., Mallet, J., and Guillon, E. (2009). Aging effect on the copper sorption on a vineyard soil: column studies and SEM–EDS analysis. *J. Colloid Interface Sci.* 331, 47–54. doi: 10.1016/j.jcis.2008.11.049

Schenkeveld, W., and Kraemer, S. (2018). Constraints to synergistic fe mobilization from calcareous soil by a phytosiderophore and a reductant. *Soil Syst.* 2:67. doi: 10.3390/soilsystems2040067

Shi, J., Yuan, X., Chen, X., Wu, B., Huang, Y., and Chen, Y. (2011). Copper uptake and its effect on metal distribution in root growth zones of *Commelina communis* revealed by SRXRF. *Biol. Trace Elem. Res.* 141, 294–304. doi: 10.1007/s12011-010-8710-5

Strawn, D. G., and Baker, L. L. (2008). Speciation of Cu in a contaminated agricultural soil measured by XAFS, μ-XAFS, and μ-XRF. *Environ. Sci. Technol.* 42, 37–42. doi: 10.1021/es071605z

Strawn, D. G., and Baker, L. L. (2009). Molecular characterization of copper in soils using X-ray absorption spectroscopy. *Environ. Pollut.* 157, 2813–2821. doi: 10.1016/j.envpol.2009.04.018

Ström, L., Owen, A. G., Godbold, D. L., and Jones, D. L. (2005). Organic acid behaviour in a calcareous soil implications for rhizosphere nutrient cycling. *Soil Biol. Biochem.* 37, 2046–2054.

Toselli, M., Baldi, E., Marcolini, G., Malaguti, D., Quartieri, M., Sorrenti, G., et al. (2009). Response of potted grapevines to increasing soil copper concentration. *Austral. J. Grape Wine Res.* 15, 85–92.

Vance, D., Archer, C., Bermin, J., Perkins, J., Statham, P. J., Lohan, M. C., et al. (2008). The copper isotope geochemistry of rivers and the oceans. *Earth Planet. Sci. Lett.* 274, 204–213. doi: 10.1016/j.epsl.2008.07.026

Vance, D., Matthews, A., Keech, A., Archer, C., Hudson, G., Pett-Ridge, J., et al. (2016). The behaviour of Cu and Zn isotopes during soil development: controls on the dissolved load of rivers. *Chem. Geol.* 445, 36–53.

Wan, H., Du, J., He, J., Lyu, D., and Li, H. (2019). Copper accumulation, subcellular partitioning and physiological and molecular responses in relation to different copper tolerance in apple rootstocks. *Tree Physiol.* 39, 1215–1234. doi: 10.1093/treephys/tpz042

Wang, G., and Staunton, S. (2006). Evolution of water-extractable copper in soil with time as a function of organic matter amendments and aeration. *Eur. J. Soil Sci.* 57, 372–380. doi: 10.1111/j.1365-2389.2005.00748.x

Weinstein, C., Moynier, F., Wang, K., Paniello, R., Foriel, J., Catalano, J., et al. (2011). Isotopic fractionation of Cu in plants. *Chem. Geol.* 286, 266–271.

Wintz, H., and Vulpe, C. (2002). Plant copper chaperones. *Biochem. Soc. Trans.* 30, 732–735. doi: 10.1042/bst0300732

Yin, Y., Impellitteri, C. A., You, S.-J., and Allen, H. E. (2002). The importance of organic matter distribution and extract soil:solution ratio on the desorption of heavy metals from soils. *Sci. Total Environ.* 287, 107–119. doi: 10.1016/s0048-9697(01)01000-2

Yruela, I. (2009). Copper in plants: acquisition, transport and interactions. *Funct. Plant Biol.* 36, 409–430. doi: 10.1071/FP08288

Zhou, Z., Zhou, J., Li, R., Wang, H., and Wang, J. (2007). Effect of exogenous amino acids on Cu uptake and translocation in maize seedlings. *Plant Soil* 292, 105–117. doi: 10.1007/s11104-007-9206-8

Zhu, X. K., Guo, Y., Williams, R. J. P., O'Nions, R. K., Matthews, A., Belshaw, N. S., et al. (2002). Mass fractionation processes of transition metal isotopes. *Earth Planet. Sci. Lett.* 200, 47–62. doi: 10.1016/s0012-821x(02)00615-5

Conflict of Interest: The authors declare that the research was conducted in the absence of any commercial or financial relationships that could be construed as a potential conflict of interest.

The reviewer CC declared a past co-authorship with one of the authors JV to the handling editor.

frontiers in Plant Science

ORIGINAL RESEARCH
published: 31 January 2022
doi: 10.3389/fpls.2022.827828

Analysis of Alternative Splicing During the Combinatorial Response to Simultaneous Copper and Iron Deficiency in Arabidopsis Reveals Differential Events in Genes Involved in Amino Acid Metabolism

Estefania Mancini[1] *and Antoni Garcia-Molina*[2]*

[1] Centre for Genomic Regulation, Barcelona, Spain, [2] Centre for Research in Agricultural Genomics (CRAG), CSIC-IRTA-UAB-UB, Barcelona, Spain

OPEN ACCESS

Edited by:
Anja Schneider,
Ludwig Maximilian University of Munich, Germany

Reviewed by:
Marion Eisenhut,
Heinrich Heine University of Düsseldorf, Germany
Torsten Möhlmann,
University of Kaiserslautern, Germany

***Correspondence:**
Antoni Garcia-Molina
antoni.garcia@cragenomica.es

Specialty section:
This article was submitted to Plant Nutrition, a section of the journal Frontiers in Plant Science

Received: 02 December 2021
Accepted: 11 January 2022
Published: 31 January 2022

Citation:
Mancini E and Garcia-Molina A (2022) Analysis of Alternative Splicing During the Combinatorial Response to Simultaneous Copper and Iron Deficiency in Arabidopsis Reveals Differential Events in Genes Involved in Amino Acid Metabolism. Front. Plant Sci. 13:827828. doi: 10.3389/fpls.2022.827828

Copper (Cu) and iron (Fe) constitute fundamental nutrients for plant biology but are often limited due to low bioavailability. Unlike responses to single Cu or Fe deprivation, the consequences of simultaneous Cu and Fe deficiency have not yet been fully deciphered. Previously, it was demonstrated that Cu and Fe deficiency applied in combination imposes transcriptome, proteome, and metabolome changes different from those triggered under each deficiency individually. Here, we evaluated the effect of alternative splicing (AS) on the transcriptome of rosette leaves under single and simultaneous Cu and Fe deficiency. Differentially spliced genes (DSGs) and differentially expressed genes (DEGs) coincided in number (2,600 approx.) although the overlapping fraction was minimal (15%). Functional annotation of changes exclusively detected under simultaneous Cu and Fe deficiency revealed that DEGs participated in general stress responses and translation, while DSGs were involved in metabolic reactions, especially amino acid biosynthesis. Interestingly, transcripts encoding central features for tryptophan (Trp) and asparagine (Asn) synthesis – two significantly altered metabolites under simultaneous Cu and Fe deficiency – underwent exclusive intron retention events under the double deficiency. However, transcript and protein amounts for these enzymes did not correlate with Trp and Asn concentration. In consequence, we propose that AS might act as a regulatory mechanism to modify the stability and/or functionality of the enzymes and therefore fine-tune amino acid production during the combinatorial response to simultaneous Cu and Fe deficiency.

Keywords: alternative splicing, copper deficiency, iron deficiency, combinatorial stress, systems biology, *Arabidopsis thaliana*

INTRODUCTION

Copper (Cu) and iron (Fe) are essential nutrients for plants because they possess suitable redox properties to sustain fundamental processes such as photosynthesis, respiration, and antioxidative defense reactions, among others (Puig et al., 2007; Ravet and Pilon, 2013; Zhang, 2015). However, the same redox properties lead to cytotoxicity when Cu and Fe are present in excess (Puig et al., 2007; Ravet and Pilon, 2013). In consequence, plants require fine-tuned mechanisms to keep Cu and Fe levels within balanced ranges. Despite being abundant in soils, Cu and Fe bioavailability is often restricted due to the chelating effect of organic matter, low insolubility in alkaline soils, or overexploitation of farmlands for agricultural purposes (Morrissey and Guerinot, 2009; Puig and Penarrubia, 2009).

Plant responses to individual Cu or Fe scarcity have been extensively investigated, especially in the model plant *Arabidopsis thaliana* (hereafter Arabidopsis). The transcription factors SQUAMOSA PROMOTER BINDING PROTEIN-LIKE 7 (SPL7) and FER-LIKE IRON DEFICIENCY INDUCED TRANSCRIPTION FACTOR (FIT1) orchestrate the transcriptional reprogramming under Cu and Fe limitation (Colangelo and Guerinot, 2004; Yamasaki et al., 2009; Bernal et al., 2012). SPL7 and IRT1 promote high-affinity uptake systems consisting of FERRIC REDUCTION OXIDASE (FRO) metalloreductases to reduce Cu^{2+} and Fe^{3+} to Cu^{+} and Fe^{2+} prior to transport via COPPER TRANSPORT PROTEINS (COPTs) and IRON-REGULATED TRANSPORTER 1 (IRT1), respectively. In addition, the dissection of the mechanism of action of SPL7 and FIT1 unveiled points of cross-talk between Cu and Fe homeostatic networks. For instance, SPL7 triggers the replacement of Cu/Zn-depending SUPEROXIDE DISMUTASE by the Fe-depending isoform to prioritize Cu ions in chloroplasts for PLASTOCYANINE and, thus, preserve photosynthesis under Cu deficient conditions (Yamasaki et al., 2009; Bernal et al., 2012). On the other hand, FIT1 promotes FRO4/5 and COPT2 to rely on Cu-depending proteins when Fe is limiting (Colangelo and Guerinot, 2004).

However, our understanding of the molecular mechanisms involved in combinatorial responses to simultaneous Cu and Fe deficiency is still limited. This fact is of special relevance as molecular responses to combinatorial stress trigger patterns that largely differ from those activated under each stressor individually (Atkinson et al., 2013; Prasch and Sonnewald, 2013; Rasmussen et al., 2013; Suzuki et al., 2014; Gupta et al., 2016). Recently, a systems biology study provided a holistic picture of transcriptome, proteome, and metabolome changes under single and simultaneous Cu and Fe deficiencies in Arabidopsis adult leaves (Garcia-Molina et al., 2020). Quantitatively, the combinatorial response caused half of all detected transcripts and proteins that significantly changed in abundance. Conditional networks on molecular changes under single and double Cu and Fe deficiencies displayed important divergences in topology and detection of communities, revealing substantial differences in co-expression of biological processes. Indeed, data mining on changing transcripts and proteins as a result of the interaction between Cu and Fe deficiencies uncovered specific expression patterns for transcripts related to ribosome subunit conformation and translation activities, and for proteins assisting protein folding and degradation. At the metabolome level, the combinatorial response to double Cu and Fe deficiency provoked decreases in the total fraction of sugars and organic acids from the tricarboxylic acid cycle in comparison with single deficiencies, and limited the increase in amino acids observed under single Fe deficiency. Further analysis of metabolome profiles explained such trends by significant drops in the concentration of phenylalanine (Phe), asparagine (Asn), tryptophan (Trp), and the organic acid fumarate. Moreover, loss-of-function lines of the cytosolic fumarase FUMARASE2 displayed improved growth and photosynthesis performance in seedlings cultivated under Cu and Fe deficient conditions, which was accompanied by balanced levels of amino acids (Garcia-Molina et al., 2021). This finding confirmed the existence of specific mechanisms exclusively operating in plants under simultaneous Cu and Fe deficiency and posed fumaric acid as a central modulator of the combinatorial response.

Alternative splicing (AS) is a post-transcriptional mechanism specific to eukaryotic organisms consisting in the differential processing of the exons and introns in precursor mRNAs to generate different isoforms of the same transcript. In plants, it is estimated that AS affects up to 70% of all precursor mRNAs, encompassing multiple exons with intron retention being the most predominant event (Filichkin et al., 2010; Marquez et al., 2012). The resulting transcript isoforms can display altered stability, translational efficiency, or subcellular retention, or can be translated into protein variants with divergent structures and functions. Thus, AS acts as a central regulatory strategy to sustain plant growth and development under different conditions (Reddy et al., 2013; Laloum et al., 2018; Szakonyi and Duque, 2018; Chaudhary et al., 2019). Moreover, recent studies in the field contributed in demonstrating the relevance of AS events in transcriptome responses to abiotic stress conditions as well as part of the so-called "memory stress" program (Ding et al., 2014; Calixto et al., 2018; Kannan et al., 2018; Ling et al., 2018; Huang et al., 2019).

How AS is involved in the combinatorial response to simultaneous Cu and Fe deficiency still remains an open question. Therefore, in this work we aimed to extend the holistic picture of molecular changes in response to the double Cu and Fe deficiency with the contribution of AS in transcript regulation. Our analysis of the transcriptome data generated in Garcia-Molina et al. (2020) uncovered a specific cohort of genes exclusively undergoing AS during the combinatorial response. These genes were related to biosynthetic pathways for amino acids changing under this condition, especially Asn and Trp. Further integration of transcriptome, proteome, and metabolome profiles revealed lack of correlation between transcripts and proteins for enzymes synthesizing Trp and Asn and metabolite concentration when both Cu and Fe are limiting. Accordingly, we propose that AS events might act as a potential regulatory mechanism to adjust metabolic composition to plant demands during the combinatorial response to double Cu and Fe deficit.

MATERIALS AND METHODS

Data Collection

Transcriptome (GEO ID: GSE125894), proteome (Pride ID: PXD013598), and metabolome (**Supplementary Table 1**) profiles of adult rosette leaves reported by Garcia-Molina et al. (2020) were used in this study. Briefly, 12-day-old *A. thaliana* (ecotype Col0) seedlings grown on soil were transferred to hydroponic cultures with full 1/10 Hoagland medium (Hermans et al., 2004) for 12 days and then treated with the same medium or without Cu and/or Fe salts for 10 days. RNA-seq libraries (n = 2 independent replicates per treatment) were sequenced using standard Illumina HiSeq 2500 (Illumina, San Diego, CA, United States) protocols. Proteomes (n = 4 independent replicates per treatment) were profiled by means of liquid chromatography-tandem mass spectrometry (LC-MS/MS) and processed with MAXQUANT (Cox and Mann, 2008). Metabolite concentration (n = 4 and 7 independent replicates per treatment at 5 and 10 days, respectively) was determined by targeted gas chromatograph coupled to a time-of-flight mass spectrometer (GC-TOF-MS) according to the Golm Metabolome Database (Kopka et al., 2005) using ribitol and ^{13}C-sorbitol as internal standards for relative quantification.

Analysis of Alternative Splicing

The analysis of alternative splicing was conducted in *R* using the *ASpli* package (Mancini et al., 2021). Sequencing reads derived from RNA-Seq files were mapped to the *A. thaliana* genome (TAIR10) using the aligner tool STAR (Dobin et al., 2012) with default parameters, except for maximum intron length set at 5,000 nucleotides. Then, the transcriptome was partitioned into subgenic regions named "bins" as proposed on DEXseq (Anders et al., 2012). Read counts in each bin region were recorded. Null values (NA) representing lack of coverage of bins were manually replaced by 0. Splice junction information was employed to compute the Percent of Inclusion (PSI) and Percent of Intron Retention (PIR) for each bin.

Significant changes in alternative splicing events were calculated from differences in PSI or PIR using a two-way ANOVA (p-value $\leq$ 0.05) for the interaction between Cu and Fe deficiencies. Subsequently, significant changes in alternative splicing events among conditions were declared using an absolute $\log_2$ fold-change for PSI or PIR $\geq$ 1 in pair-wise comparisons (adjusted-p-value $\leq$ 0.05, Tukey's *post hoc* test).

Bioinformatic Tools

Data analysis and statistical treatments were conducted in *R*. Data transformation, Pearson correlations, and ANOVA were computed using the *stats* and *agricolae* package (available at The Comprehensive *R* Archive Network, CRAN).[1] Heatmaps with hierarchical clustering were elaborated using the *pheatmap* package (available at CRAN; see text footnote 1). Significant enrichment in Gene Ontology terms (adjusted-p-value $\leq$ 0.05, Fisher's exact test) was carried out in *Thalemine*[2] and redundant terms were removed in *REVIGO*[3] to obtain a small list (0.5) (Supek et al., 2011). Benjamini-Hochberg's method was applied for multiple testing correction in all cases. To identify metabolic reactions targeted by alternative splicing events, differentially spliced genes were loaded onto *Mapman* v.3.5.1[4] and the bins for amino acid reactions in the category "metabolism overview" extracted (Thimm et al., 2004). Alternative splicing events were visualized in *Integrative Genome Viewer* (Robinson et al., 2011) according to the coverage in the RNA-Seq experiments using $\log_{10}$-transformed read counts.

RESULTS

Alternative Splicing Events During the Combinatorial Copper and Iron Deficiency Target a Fraction of Genes That Are Not Differentially Expressed

High-throughput profiling and systemic analysis of the transcriptome, proteome, and metabolome of adult rosette leaves grown under double Cu and Fe deficiency for 10 days uncovered an array of molecular changes that were not triggered under single Cu or Fe deficiencies (Garcia-Molina et al., 2020). To complete this picture with the contribution of AS in the combinatorial response to simultaneous Cu and Fe deficiency, the transcriptome profiles generated in Garcia-Molina et al. (2020) were analyzed using the *ASpli* package (Mancini et al., 2021). Reads spanning intronic and exonic bins as well as junctions were used to estimate the PIR or PSI (Mancini et al., 2021) under each of the conditions. Differential alternative splicing events (DASs) were declared based on significant changes in PIR or PSI for the interaction between Cu and Fe deficiencies (p-value $\leq$ 0.05, two-way ANOVA). In total, 3,917 DASs were identified −27.7% of these corresponded to annotated exon skipping (ES) events, whereas 57.8% were intron retention (IR) events and 14.40% were other minoritarian forms of AS events. Moreover, DASs were located in 2,806 different genes that were further considered differentially spliced genes (DSGs) (**Figures 1A,B**).

Interestingly, although the DSG fraction represented 33.56% of all potential DSGs annotated in *ASpli*, however, only 428 DSGs (15.25% of all DSGs) were previously reported as differentially expressed genes (DEGs) in Garcia-Molina et al. (2020; **Supplementary Table 2**) using the same cut-off for significance. Similarly, only 16.23% of the reported DEGs underwent significant AS events (**Figure 1B**). This observation indicates that transcriptome rewiring by AS during single and simultaneous Cu and Fe deficiency targets a coreset of transcripts unchanged as regards of abundance.

To identify expression patterns in the effect of AS on the transcriptome, DAS were used to elaborate a heatmap with hierarchical clustering. As depicted in **Figure 1C**, seven main clusters of DASs were detected using the Ward D2 method. With

[1] https://cran.r-project.org/

[2] https://bar.utoronto.ca/thalemine/

[3] http://revigo.irb.hr/

[4] https://mapman.gabipd.org/es_ES/home

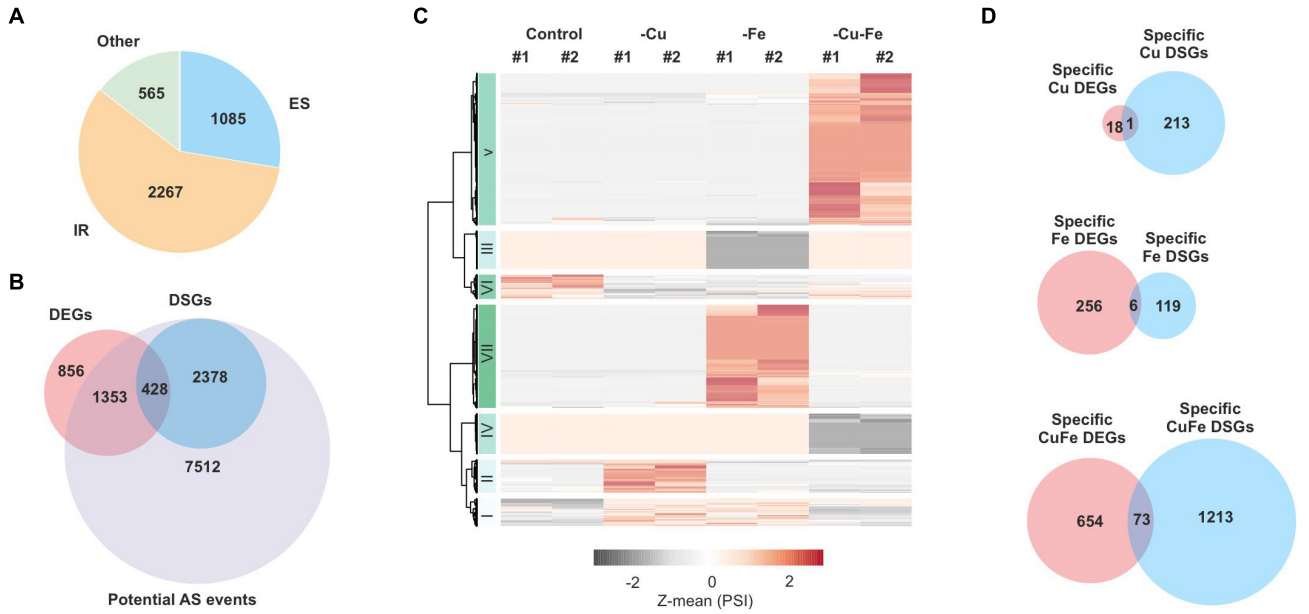

FIGURE 1 | Analysis of differential splicing events under individual and simultaneous copper and iron deficiency. RNA-Seq read counts covering exonic and intronic regions from the transcriptome profiles of rosette leaves treated for single and double copper and iron deficiency reported in Garcia-Molina et al. (2020) were obtained with the *ASpli* package (see "Materials and Methods"). **(A)** Classification of AS events into intron retention (IR), exon skipping (ES) or other events (Other). **(B)** Euler diagram comparing the fraction of all genes potentially affected by AS, the differentially spliced genes (DSGs) detected and differentially expressed genes (DEGs) reported in Garcia-Molina et al. (2020). **(C)** Heatmap with hierarchical clustering according to the Ward D2 method with Z-mean for significant changes in percentage of intron retention or bin inclusion (represented as PSI) (p-value ≤ 0.05, two-way ANOVA) under standard conditions (control), copper (–Cu) and iron (–Fe) deficiency or double deficiency (–Cu–Fe). **(D)** Euler diagrams comparing the fraction of specific DEGs in Garcia-Molina et al. (2020) and specific DSGs for each treatment. Specific DEGs and DSGs were defined as the common fraction in multiple comparisons among significant changes in each of the conditions (absolute fold-change ≥ 2 in pair-wise comparisons, adjusted-p-value ≤ 0.05, Tukey's test; **Supplementary Figure 1**).

the exception of the two minor clusters I and VI (486 AS events, 12.04%) that represented DAS under both single deficiencies, the rest of the clusters included AS events specific to each of the conditions, i.e., cluster II (311 AS events, 7.93%) contained changes mainly taking place during Cu deficiency, clusters III and VII (1,323 AS events, 33.77%) changes only occurring under Fe deficiency, and clusters IV and V (1,801 AS events, 45.97%) changes specific to double Cu and Fe deficiency. Another remarkable trend was that the main fraction of all identified DAS (68.94%) was motivated by increases in AS rates (**Figure 1C**).

Since our analysis unveiled that DAS was mainly treatment-specific, the fraction of genes that specifically underwent AS events under each of the treatments was captured by means of multiple comparisons of DAS that displayed an absolute fold-change of at least two in pair-wise comparisons (adjusted-p-value ≤ 0.05, Tukey's test; **Supplementary Figure 1** and **Supplementary Table 3**). Thus, 214 specific Cu-DSGs, 125 specific Fe-DSGs, and 1,286 specific CuFe–DSGs were identified. Although Cu deficiency alone had a low impact on transcriptome changes, the number of Cu–DSGs was twice that of Fe–DSGs (**Supplementary Figure 1**). The existence of a combinatorial effect in simultaneous Cu and Fe deficiency was also demonstrated at the AS level since the number of specific CuFe–DSGs was four-fold higher than the sum of those found under both single deficiencies. Again, a small overlap between specific DSGs and specific DEGs per condition – quantified as less than 10% of DEGs being DSGs – was found (**Figure 1D**), further confirming that changes in transcript abundance were not motivated by significant splicing events.

Specific Alternative Splicing Events Under the Combinatorial Response to Copper and Iron Deficiency Target Biosynthetic Pathways for Changing Amino Acids

Given the divergence in the coreset of genes that experienced changes in AS and transcript abundance, we interrogated whether different biological processes would be regulated in each case. To this end, functional annotation of specific DEGs and DSGs was conducted by significant enrichment of non-redundant gene ontology (GO) terms (adjusted-p-value ≤ 0.05, Fisher's exact test, and filter 0.5 in REVIGO, Supek et al., 2011). Cu deficiency did not lead to significant enrichments of neither DSGs nor DEGs, due to the low impact of the treatment, whereas Fe-DEGs rendered enrichment in 12 terms mainly related to Fe homeostasis ("Iron ion homeostasis," "Iron ion transport," or "Regulation of iron ion import"), hypoxia ("Response to oxygen levels," "Response to decreased oxygen levels"), and abiotic stress response ("Response to abiotic stimulus") (**Figure 2**). However, 26 and four non-redundant terms were found for

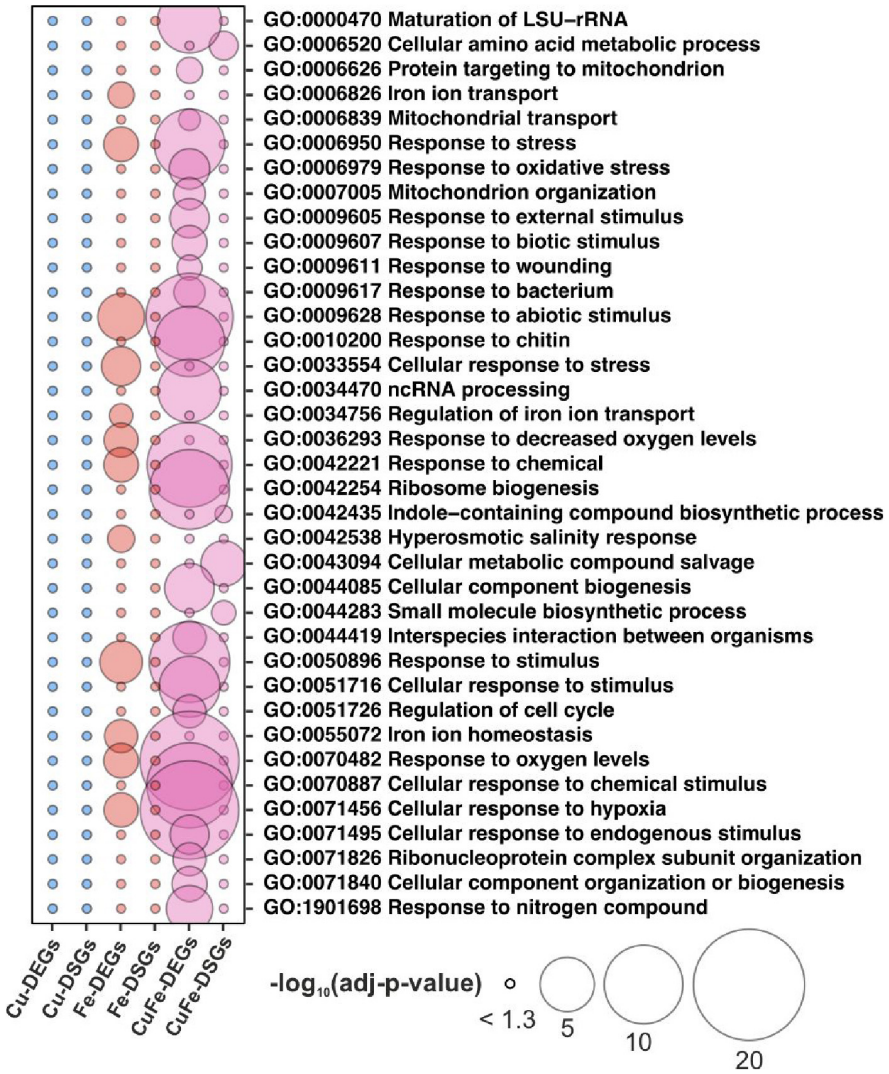

FIGURE 2 | Functional annotation of specific changes in transcriptome and alternative splicing under single and simultaneous copper and iron deficiency. Bubble plot depicting differences in specific DEGs and DSGs detected under single and double copper and iron deficiency treatments (Cu, Fe, and CuFe, respectively). Specific DEGs and DSGs were analyzed for significant gene ontology (GO) term enrichment (adjusted-*p*-value $\leq$ 0.05, Fisher's test) and filtered for redundancy by REVIGO (filter 0.5). The size of the bubble is proportional to the –log10-transformation of the adjusted-*p*-value in the Fisher's test.

CuFe–DEGs and CuFe-DSGs, respectively (**Figure 2**). CuFe–DEGs were related to general responses to both biotic and abiotic stress, ("Response to stress," "Response to abiotic stimulus," "Response to biotic stimulus," "Response to bacterium"), translation ("Ribosome biogenesis," "Maturation of LSU-rRNA", "Ribonucleoprotein complex subunit organization"), nitrogen homeostasis ("Response to nitrogen compound"), mitochondrion biology ("Mitochondrion organization," "Mitochondrial transport"), or cell cycle ("Regulation of cell cycle"). On the other hand, CuFe-DSGs participate in pathways for compound salvage and amino acid metabolism, among others (**Figure 2**). These observations indicate that the reprogramming of the majority of biological processes involved in the response to single Fe and double Cu and Fe deficiencies takes place via changes in transcript abundance. Furthermore, our data suggest that DSGs detected under single Cu and Fe deficiencies might be the consequence of either the necessity to fine-tune isolated sets of transcripts, or aberrant splicing events due to stress imposed by the treatments. In contrast, AS events under simultaneous Cu and Fe deficiency might rather obey a more general regulatory strategy aimed at adjusting plant amino acid composition.

Previously, it was shown that coincident Cu and Fe limitation imposed a particular reconfiguration of the amino acid fraction in adult leaves, and how seedlings tolerant to the double deficiency via suppression of the cytosolic *FUMARASE2* restored amino acid levels to those under standard conditions (Garcia-Molina et al., 2020, 2021). Due to the potential prevalence of targeting pathways related to amino acid metabolism and the relevance of amino acids in plant homeostasis during simultaneous Cu

TABLE 1 | Identified Mapman bins related to amino acid metabolism.

Description of the bin	DEG	Description of the gene
Amino acid metabolism.synthesis		
Aspartate.aspartate aminotransferase	AT5G19550	ASPARTATE AMINOTRANSFERASE 2 (ASN2)
Aspartate.aspartate aminotransferase	AT1G72330	ALANINE AMINOTRANSFERASE 2 (ALAAT2)
Serine-glycine-cysteine group.serine.phosphoserine aminotransferase	AT3G19030	Unknown
Serine-glycine-cysteine group.cysteine	AT5G65720	Alanine-glyoxylate aminotransferase, putative
Serine-glycine-cysteine group.cysteine.OASTL	AT4G14880	*O*-ACETYLSERINE (THIOL) LYASE ISOFORM A1 (OASA1)
Amino acid metabolism.degradation		
Glutamate family.glutamine	AT5G13780	*N*-TERMINAL ACETYLTRANSFERASE 10 (NAA10)
Description of the bin	**DSG**	**Description of the gene**
Amino acid metabolism.synthesis		
GABA.Glutamate decarboxylase	AT1G65960	GLUTAMATE DECARBOXYLASE 2 (GAD2)
Aspartate.aspartate aminotransferase	AT5G19550	ASPARTATE AMINOTRANSFERASE 2 (ASP2)
Alanine.alanine aminotransferase	AT1G70580	ALANINE-2-OXOGLUTARATE AMINOTRANSFER. 2 (AOAT2)
Alanine.alanine-glyoxylate aminotransferase	AT2G13360	ALANINE:GLYOXYLATE AMINOTRANSFERASE (AGT)
Glutamate family.proline.d 1-pyrroline-5-carboxylate synt	AT2G39800	DELTA1-PYRROLINE-5-CARBOXYLATE SYNTH. 1 (P5CS1)
Aspartate family.asparagine.asparagine synthetase	AT5G65010	ASPARAGINE SYNTHETASE 2 (ASN2)
Aspartate family.methionine	AT4G34840	METHYLADENOSINE NUCLEOSIDASE 2 (MTN2)
Aspartate family.methionine.homocysteine S-methyl	AT3G22740	HOMOCYSTEINE S-METHYLTRANSFERASE 3 (HMT3)
Aspartate family.methionine.homocysteine S-methyl	AT1G78140	Methyltransferase-related
Aspartate family.lysine.diaminopimelate epimerase	AT3G53580	Diaminopimelate epimerase family protein
Aspartate family.misc.homoserine.bifunctional aspartate kinase/homoserine dehydrogenase	AT4G19710	Aspartate kinase/homoserine dehydrogenase, putative
Aspartate family.misc.homoserine.aspartate semialdehyde dehydrogenase	AT1G14810	Semialdehyde dehydrogenase family protein
Branched chain group.leucine specific.3-isopropylmalate dehydrogenase	AT5G14200	3-Isopropylmalate dehydrogenase, putative
Serine-glycine-cysteine group.glycine.glycine transamin	AT1G70580	ALANINE-2-OXOGLUTARATE AMINOTRANSFER. 2 (AOT2)
Serine-glycine-cysteine group.glycine.serine glyoxylate aminotransferase	AT2G13360	ALANINE:GLYOXYLATE AMINOTRANSFERASE (AGT)
Serine-glycine-cysteine group.cysteine.OASTL	AT3G22460	O-ACETYLSERINE (THIOL) LYASE ISOFORM A2 (OASA2)
Serine-glycine-cysteine group.cysteine.SAT	AT2G17640	SERINE O-ACETYLTRANSFERASE (ATSERAT3;1)
Aromatic aa.tryptophan.phosphoribosyanthranilate isom	AT5G05590	PHOSPHORIBOSYLANTHRANILATE ISOMERASE 2 (PAI2)
Aromatic aa.tryptophan.phosphoribosyanthranilate isom	AT1G07780	PHOSPHORIBOSYLANTHRANILATE ISOMERASE 1 (PAI1)
Aromatic aa.tryptophan.indole-3-glycerol phosphate synt	AT5G48220	Indole-3-glycerol phosphate synthase, putative (InGPS)
Aromatic aa.tryptophan.tryptophan synthase	AT5G54810	TRYPTOPHAN SYNTHASE BETA-SUBUNIT 1 (TSB1)
Aromatic aa.tryptophan.tryptophan synthase	AT4G02610	Tryptophan synthase, alpha subunit, putative (TSA1)
Histidine.glutamine amidotransferase/cyclase	AT4G26900	IMIDAZOLEGLYCEROL-PHOSPHATE SYNTAHSE (HISN4)
Amino acid metabolism.degradation		
Aspartate family.asparagine.L-asparaginase	AT5G08100	L-Asparaginase/L-asparagine amidohydrolase (ASPGA1)
Branched-chain group.shared	AT3G08860	Alanine-glyoxylate aminotransferase, putative (PYD4)
Branched-chain group.leucine	AT4G34030	3-METHYLCROTONYL-COA CARBOXYLASE (MCCB)
Branched chain group.isoleucine	AT5G48880	PEROXISOMAL 3-KETO-ACYL-COA THIOLASE 2 (KAT5)
Aromatic aa.tryptophan	AT5G65940	BETA-HYDROXYISOBUTYRYL-COA HYDROLASE 1 (CHY1)

Specific differentially expressed genes (DEGs) and differentially spliced genes (DSGs) detected in the double deficiency were mapped onto the category "central metabolism" in Mapman. Bins were sorted for synthesis or degradation and presented with the bin description, the gene ID, and the description of the gene.

and Fe deficiency, CuFe–DSGs were mapped into *Mapman* bins for the category "central metabolism" (Thimm et al., 2004) to gain more insight as to which amino acid reactions were affected by AS events. In this way, 28 of the 175 bins (**Supplementary Table 4**) for central metabolism mapped by specific CuFe–DSGs were involved in biosynthetic reactions for the aromatic amino acid Trp, for the group of serine-glycine-cysteine, or for the Asp family, as well as catabolic reactions for the branched-chained amino acids leucine and isoleucine (**Table 1**). On the other hand, CuFe–DEGs mapped into five bins related to amino acid metabolism and only overlapped with CuFe–DSGs for *ASPARTATE AMINOTRANSFERASE 2* (*ASP2*) (**Table 1**).

To address the relevance of AS changes in the amino acid composition of plants, we recovered the metabolome profiles in response to Cu, Fe, and the double Cu and Fe deficiency treatments after 5 and 10 days described in Garcia-Molina et al. (2020). Data were filtered for compounds with unknown mass and metabolites that were not present in all replicates. In this way, 76 metabolites were retained (**Supplementary Table 1**), and the median of normalized abundance was used to draw

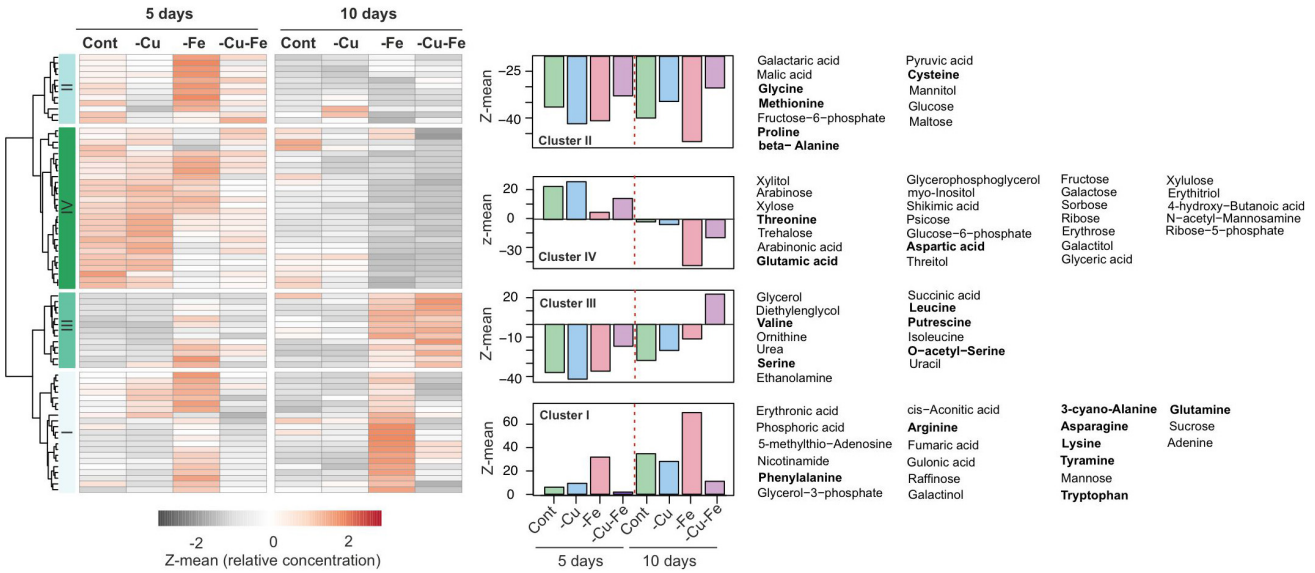

FIGURE 3 | Metabolome profiles in response to single and double deficiency of copper and iron. Heatmap with hierarchical clustering according to the Ward method with Z-means for the median of the relative concentration of metabolites from rosette leaves exposed to standard conditions (control, Cont), copper (–Cu), and iron (–Fe) deficiency or double deficiency (–Cu–Fe) for 5 (n = 4) or 10 days (n = 7) in Garcia-Molina et al. (2020; **Supplementary Table 1**). For each cluster in the heatmap the trend is depicted as the average of the Z-mean of the compounds along with the name of the metabolites. Amino acids are highlighted in bold.

a heatmap with hierarchical clustering. Accordingly, four main patterns were identified (**Figure 3**). Metabolites in cluster I (22 metabolites) accumulated under control and Cu deficient conditions overtime and displayed a pronounced increase under Fe deficiency at both 5 and 10 days of treatment, while being decreased under simultaneous Cu and Fe deficiency (**Figure 3**). This pattern is of special relevance as it recapitulates the behavior of fumaric acid, adenine, the amino acids Asn, Phe, Trp and the Trp-derivative tyramine, which were previously identified as significantly altered metabolites (SAMs) in the combinatorial response to double Cu and Fe deficiency (Garcia-Molina et al., 2020). Compounds in cluster II (13 metabolites) rose in content after 5 days of Fe deficient treatment, but then remained steady under all conditions after 10 days. Cluster III (14 metabolites) included metabolites that increased under both Fe deficient and double Cu and Fe deficient treatments, with a more remarkable increase under double Cu and Fe deficiency (**Figure 3**). Finally, cluster IV (29 metabolites) contains, above all, sugars (trehalose, fructose, galactose, and sorbose) and sugar-alcohols (myo-inositol, xylitol, and galactitol), which decrease in content after 10 days under all treatments, with a more pronounced drop under both treatments lacking Fe (**Figure 3**).

Interestingly, cluster I – which contains the SAMs under simultaneous Cu and Fe deficiency as mentioned above – included the main fraction of amino acids that are end products of the metabolic reactions identified by *Mapman* bins using CuFe-DSGs, namely glutamine (Gln), Asn, and Trp, as well as the rest of the aromatic amino acids (Phe and tyrosine, Tyr), and tyramine (**Figure 3**). Consequently, we hypothesized that AS could operate as a new layer in the combinatorial response to refine transcriptome changes in order to adjust amino acid composition to plant necessities under the double Cu and Fe deficiency.

Transcripts Encoding Enzymes Central to Tryptophan and Asparagine Biosynthesis Display Intron Retention Events Under Simultaneous Copper and Iron Deficiency

With the aim of dissecting the effect of AS on metabolic pathways for amino acids exclusively changing under the combinatorial Cu and Fe deficiency, we focused on those for Trp and Asn since they are two SAMs and the *Mapman* bins mapped by CuFe-DSGs allowed us to extract central features in their biosynthesis. This is the case of PHOSPHORIBOSYLANTHRANILATE ISOMERASE 1 and 2 (PAI1/2), INDOLE-3-GLYCEROL PHOSPHATE SYNTHASE (InGPS), TRYPTOPHAN SYNTHASE A (TSA1), and TRYPTOPHAN SYNTHASE BETA-SUBUNIT 1 (TBS1) for Trp (**Table 1**). For Asp, we found ASP2, the enzyme catalyzing the conversion of oxaloacetate to Asp in the first step of Asn biosynthesis, ASPARAGINE SYNTHETASE 2 (ASN2), the main enzyme mediating the condensation of Asp and Gln to render Asn, and L-ASPARAGINASE (ASPGA1), an enzyme that can degrade Asn to render Asp again (**Table 1**).

To first infer potential molecular mechanisms regulating Trp and Asn biosynthetic pathways, the transcriptome, proteome, and metabolome data generated in Garcia-Molina et al. (2020) were integrated as depicted in **Figure 4**. Regarding Trp biosynthesis, PAI1 and 2 showed antagonistic trends in transcript abundance under both Fe and double Cu and Fe deficient conditions, as *PAI1* levels dropped under both treatments,

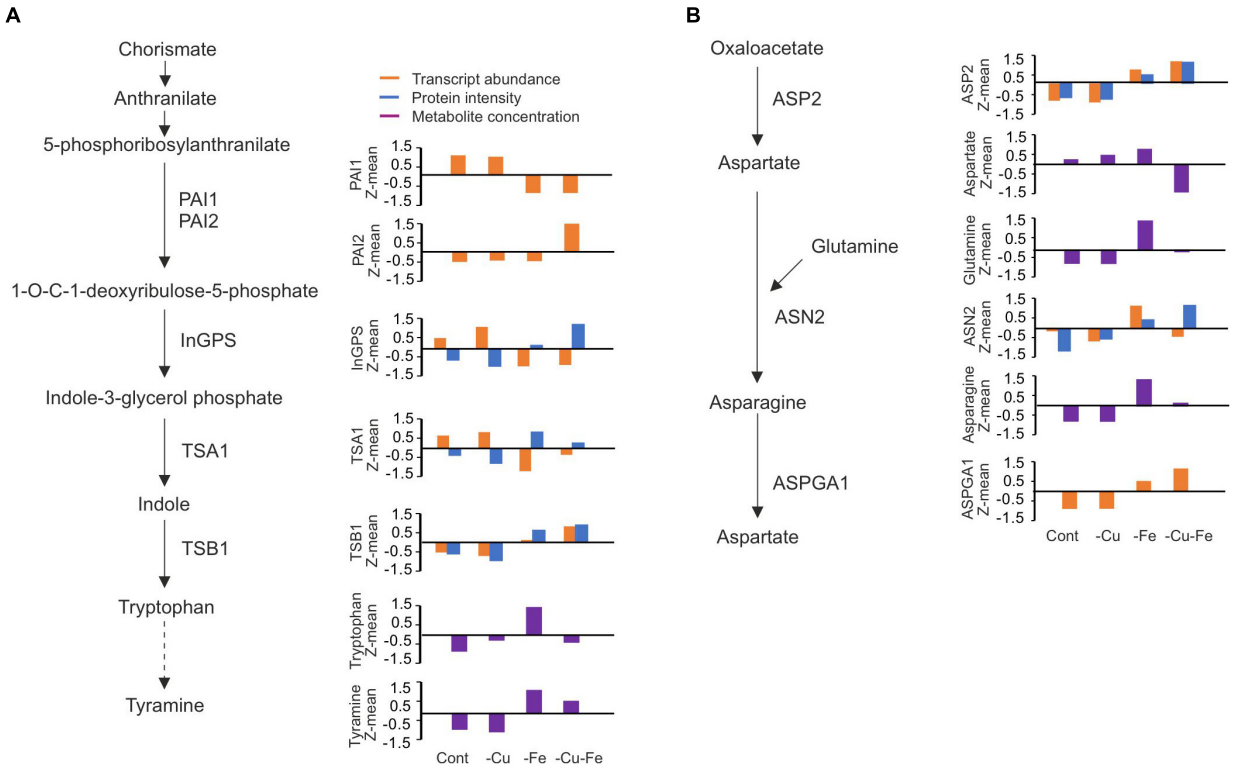

FIGURE 4 | Molecular changes in tryptophan and asparagine biosynthetic pathways in response to single and double deficiency of copper and iron. **(A,B)** Overview of the metabolic reactions involved in tryptophan (Trp, **A**) and asparagine (Asn, **B**) biosynthesis. Depicted are the metabolic intermediates and the enzymes catalyzing each of the reactions. Z-means of transcript counts (Fragments Per Kilobase Million, FPKM), proteins (LC-MS chromatography peak intensity), and metabolite (normalized concentration to ^{13}C-sorbitol and fresh weight) for each condition at 10 days, as reported in Garcia-Molina et al. (2020), were plotted. PAI1,2, PHOSPHORIBOSYLANTHRANILATE ISOMERASE 1 AND 2; InGPS, INDOLE-3-GLYCEROL PHOSPHATE SYNTHASE; TBS1, TRYPTOPHAN SYNTHASE BETA-SUBUNIT 1; TSA1, TRYPTOPHAN SYNTHASE A; ASP2, ASPARTATE AMINOTRANSFERASE 2; ASN2, ASPARAGINE SYNTHETASE 2; ASPGA1, L-ASPARAGINASE.

TABLE 2 | Correlation among transcriptome, proteome and metabolome changes in the tryptophan and asparagine biosynthesis pathways.

	RNA Prot	Trp (RNA/Prot)	Tyramine (RNA/Prot)		RNA Prot	Asp (RNA/Prot)	Gln (RNA/Prot)	Asn (RNA/Prot)
PAI1	NA	−0.64/NA	**−0.97**/NA	**ASP2**	**0.99**	−0.55/−0.65	**0.67**/0.57	**0.79**/**0.70**
PAI2	NA	−0.23/NA	0.39/NA	**ASN2**	0.22	0.48/−0.61	**0.93**/0.54	**0.86**/**0.67**
InGPS	**−0.87**	−0.58/0.18	**−0.97**/NA	**ASPGA1**	NA	−0.62/NA	0.60/NA	**0.73**/NA
TSA1	**−0.96**	**−0.84**/**0.76**	**−0.99**/**0.98**					
TSB1	**0.95**	0.24/0.49	0.24/0.49					

Pearson correlation for pair-wise comparisons among transcript (RNA) and protein (Prot) abundance or metabolite content as indicated. Pearson correlation coefficients $r > 0.65$ in absolute value are highlighted in bold as relevant.

whereas those for *PAI2* increased (**Figure 4A**) – proteome profiles did not provide information at the protein level. Transcript and protein amounts of the remaining intermediate enzymes, InGPS, TSA1, and TBS1, displayed changes under both treatments lacking Fe, though not always coincident in trend (absolute $r > 0.85$; **Table 2**). Indeed, all changes at the protein level represented increases in abundance, whereas the InGPS and TSA1 transcript amounts decreased ($r = -0.87$ and -0.96) and those for TSB1 increased ($r = 0.95$; **Figure 4A** and **Table 2**). However, the pattern of transcript and protein amounts of the intermediate enzymes could not explain changes in Trp concentration ($r < 0.65$) due to the drop experienced under double Cu and Fe deficient conditions, except for TSA1 ($r = -0.99$ for the transcript and 0.76 for the protein; **Figure 4A** and **Table 2**). However, a better correlation between transcripts and proteins of intermediate enzymes and tyramine concentration – the degradative product of Trp – was found. This finding suggests that treatments limiting Fe as well as Cu and Fe impose the accumulation of protein for the enzymes mediating Trp biosynthesis, regardless of transcript levels, although this response does not allow Trp accumulation in the double Cu and Fe deficiency. On the other hand, both ASP2 transcript and protein levels showed perfect synchronization ($r = 0.99$), increasing under both Fe and double Cu and Fe deficient

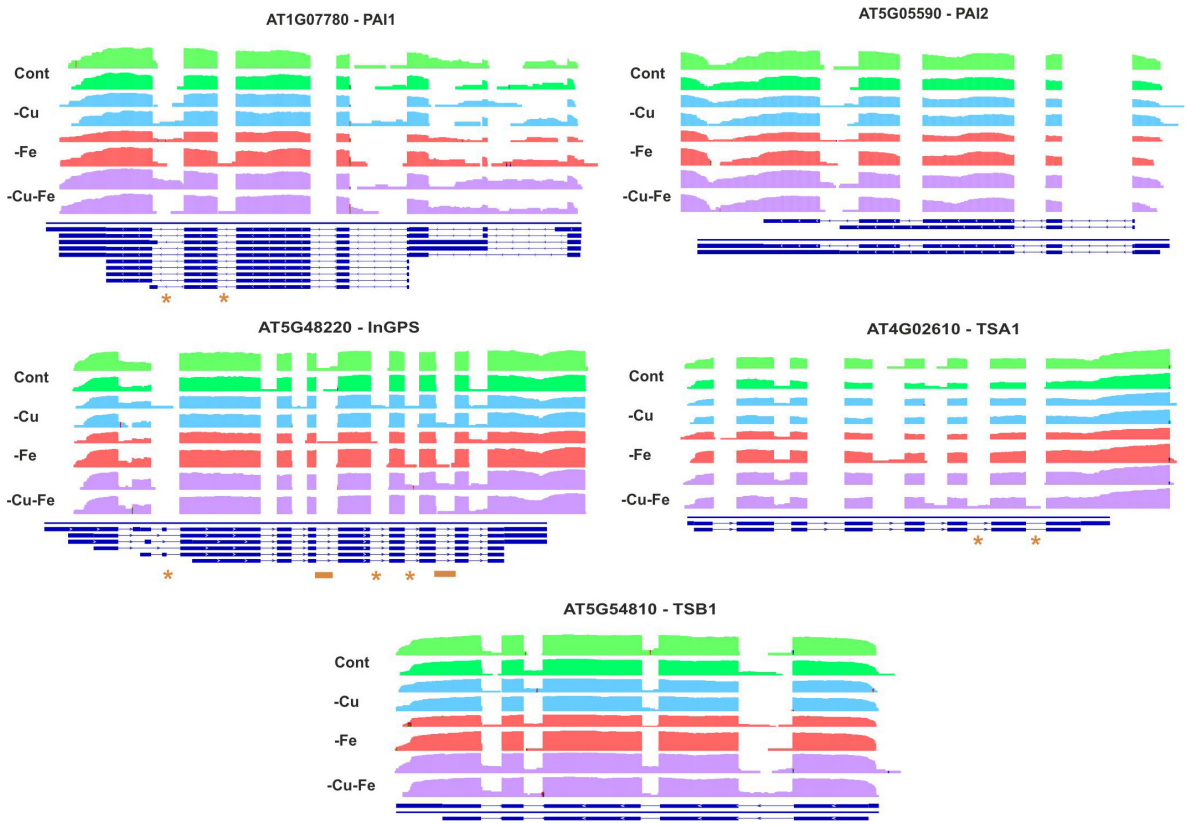

FIGURE 5 | Visualization of alternative splicing events in the transcripts involved in tryptophan biosynthesis under single and simultaneous copper and iron deficiency. Log_{10}-transformed read counts were used to represent the RNA-Seq coverage of intronic and exonic regions of PHOSPHORIBOSYLANTHRANILATE ISOMERASE 1 AND 2 (PAI1, 2), INDOLE-3-GLYCEROL PHOSPHATE SYNTHASE (InGPS), TRYPTOPHAN SYNTHASE BETA-SUBUNIT 1 (TBS1), TRYPTOPHAN SYNTHASE A (TSA1) under standard conditions (Cont) and single and double copper and iron deficiencies (–Cu, –Fe, and –Cu–Fe). Differences in the presence of intronic regions are depicted as asterisks (for changes in one replicate under –Fe or –Cu–Fe), or as orange lines (changes exclusive to –Cu–Fe conditions). Blue lines represent the gene model in TAIR10.

conditions, although it did not explain the drop in Asp under the double deficiency ($r = -0.55$ and -0.65, respectively; **Figure 4B** and **Table 2**). Transcript levels of ASN2 exhibited the same pattern as Gln and Asn ($r = 0.93$ and 0.86, respectively), although protein levels tended to increase under single and double Cu and Fe deficiencies (**Figure 4B** and **Table 2**). Finally, ASPGA1 could only be investigated for transcript levels, which showed a good correlation with Asn concentration ($r = 0.73$; **Figure 4B** and **Table 2**). Collectively, our molecular analysis confirms that the specific drop in Trp and Asn concentration during simultaneous Cu and Fe deficient conditions cannot be explained by fluctuations in transcript or protein abundance of the enzymes participating in the biosynthesis of these amino acids.

To further investigate the regulation of Trp and Asn biosynthesis, density plots were elaborated to visualize the RNA-Seq coverage of intronic and exonic regions of the transcripts of the above-investigated genes (**Figures 5**, **6**). Intron bins harbored 1–12% of total coverage, depending on the gene and condition (**Supplementary Figure 2**). To track the most extreme differences, coverage maps were then manually curated to filter changes in AS events motivated by differential intron and exon composition from those due to differences in count abundance. As a general trend, Fe and double Cu and Fe deficiency led to differential coverage of intronic regions in at least one of the replicates. This is the case of *PAI1* (introns 5 and 6), *InGPS* (intron 8), *ASP2* (introns 1, 3, 7, and 10), and *ASN2* (intron 10) (see asterisks in **Figures 5**, **6**). In three genes, the presence of additional introns was observed in only one replicate for the double Cu and Fe deficiency treatment, namely *TSA1* (introns 6 and 7), *ASN2* (intron 3), and *ASPGA1* (intron 2) (see asterisks in **Figures 5**, **6**). Furthermore, we detected consistent IR events exclusively taking place under simultaneous Cu and Fe deficiency for *InGPS* (intron 6 and 9, **Figure 5**) in the Trp biosynthesis pathway and for all three selected enzymes for Asn biosynthesis, i.e., *ASP2* (intron 9), *ASN2* (intron 9), and *ASPGA1* (intron 3) (**Figure 6**). This observation suggests that the detrimental consequences related to Fe removal and, especially, the double Cu and Fe deficiency causes misfunctions in the AS machinery, which increases the frequency of different transcript isoforms due to IR events. Thus, the incapacity to increase Trp and Asn concentrations, albeit the high levels of biosynthetic enzymes under the double Cu and Fe deficiency, could, in part, be attributed to the accumulation of non-functional protein isoforms under this condition.

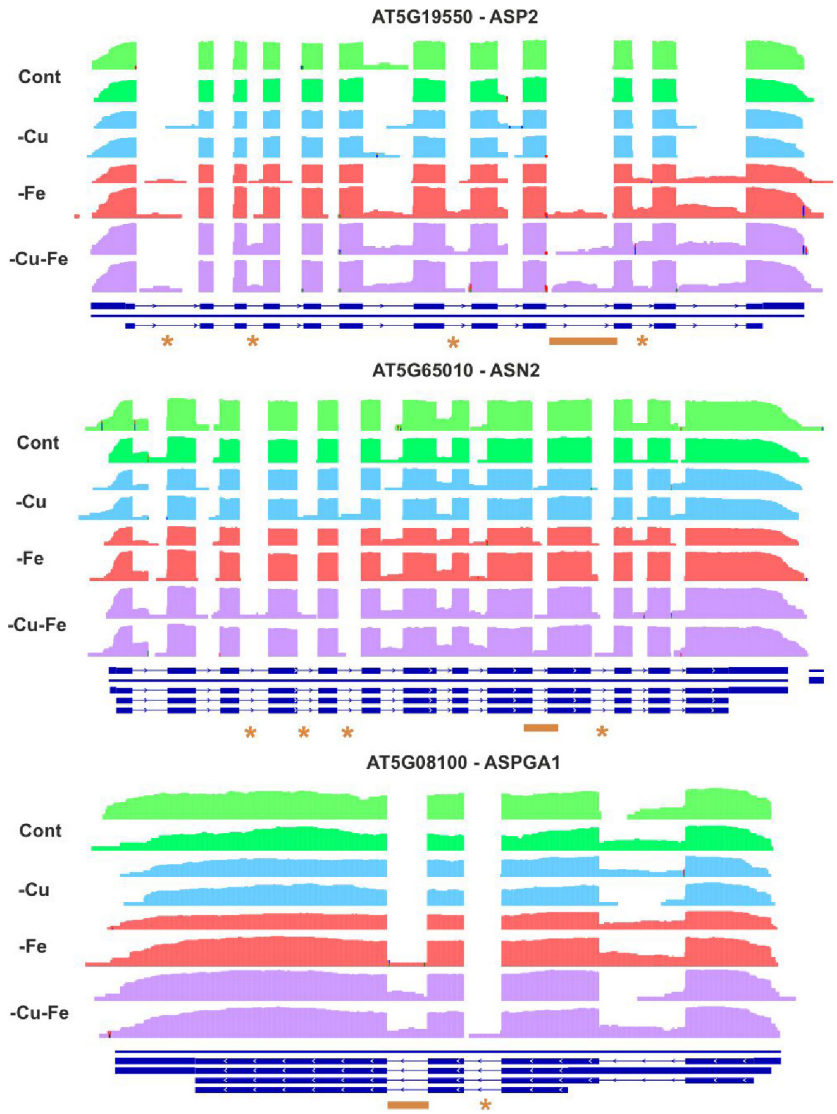

FIGURE 6 | Visualization of alternative splicing events in the transcripts involved in asparagine biosynthesis under single and simultaneous copper and iron deficiency. Log_{10}-transformed read counts were used to represent the RNA-Seq coverage of intronic and exonic regions of ASPARTATE AMINOTRANSFERASE 2 (ASP2), ASPARAGINE SYNTHETASE 2 (ASN2), and L-ASPARAGINASE (ASPGA1) under standard conditions (Cont) and single and double copper and iron deficiencies (–Cu, –Fe, and –Cu–Fe). Differences in the presence of intronic regions are depicted as asterisks (for changes in one replicate under –Fe or –Cu–Fe) or as orange lines (changes exclusive to –Cu–Fe conditions). Blue lines represent the gene model in TAIR10.

DISCUSSION

Transcriptome changes due to AS events in Arabidopsis adult rosette leaves exposed to single and double Cu and Fe deficiency for 10 days are not coincident with the fraction of transcripts changing in abundance. Even if 67.53% of the 2,637 DEGs reported in Garcia-Molina et al. (2020) could be potentially affected by AS, our analyses revealed that only 428 DEGs classified as DSGs for the interaction between Cu and Fe deficiencies (p-value $\leq$ 0.05, two-way ANOVA; **Figure 1B**). Previous studies also uncovered minimal overlap fractions between DEGs and DSGs in response to multiple nutrient deficiencies for 4 days, high salt, heat, or elevated CO_2 levels (Ding et al., 2014; Nishida et al., 2017; Kannan et al., 2018; Huang et al., 2019), while Calixto et al. (2018) reported that almost half of the DEGs detected in plants cold-treated for 4 days underwent AS. Therefore, AS operates as an independent mechanism to refine plant responses to detrimental conditions beyond regulating gene expression.

In addition, changes in AS and transcript amounts resulting from the interaction between Cu and Fe deficiencies occurred according to different patterns. On the one hand, AS is a condition-dependent response mainly detected under Fe and double Cu and Fe deficiencies (**Figure 1C**). On the other hand, although specific changes in transcripts under Fe and simultaneous Cu and Fe deficiencies were found, the major

fraction of transcript levels displayed an increase under Fe limitation that was more prominent during the double deficiency (Garcia-Molina et al., 2020). Per treatments, despite that Cu shortage for 10 days minimally impacted adult plants, we detected 200 transcripts exclusively undergoing AS under Cu deficiency, which is 10-fold the number of transcripts changing in abundance under this condition (**Figure 1D**). Fe deprivation provokes more profound physiological and molecular changes than Cu, but only imposed twice the number of Fe-specific DSGs than DEGs (262 *vs.* 125) (**Figure 1D**). However, Cu and Fe deficiencies applied simultaneously led to the major fraction of significant changes in AS events. Quantitatively, CuFe–DSGs were 2-fold the number of CuFe–DEGs (1,286 *vs.* 727) and 6- to 10-fold the number of DSGs found under single deficiencies, respectively (1,286 *vs.* 214 and 125) (**Figure 1D**). This finding provides more evidence supporting that combinatorial responses to simultaneous Cu and Fe deficiency trigger molecular mechanisms absent under single deficiencies.

In line with this, functional annotation of specific transcriptome changes related Fe-DEGs to Fe homeostasis and abiotic stress responses, whereas no significant terms for biological processes emerged when considering Cu–DEGs, Cu–DSGs, and Fe–DSGs. CuFe–DEGs enriched multiple terms, such as ribosome biogenesis, maturation of rRNA, response to cell cycle, oxidative stress, and both biotic and abiotic stimulus (**Figure 2**). However, CuFe–DSGs were involved in metabolic reactions, more precisely in amino acid biosynthesis. This fact indicates that general stress responses and adjustment in translational components during simultaneous Cu and Fe deficiency would be achieved by changes in transcript abundance, while certain aspects of plant metabolism might be systematically refined by AS.

Amino acids play a central role in the combinatorial response to simultaneous Cu and Fe deficiency in Arabidopsis. Compared with standard and Cu deficient conditions, amino acid pools tend to rise under Fe deficiency, already after 5 days of treatment, whereas under the double deficiency, this increase is more attenuated (Garcia-Molina et al., 2020). Metabolome profiling of Arabidopsis seedlings under double Cu and Fe deficiency uncovered a significant 2-fold increase in the amino acid fraction as a result of growth impairments and chloroplast misfunction. However, abrogation of Arabidopsis cytosolic fumarase FUMARASE2 (FUM2) conferred improved growth and photosynthesis rates under simultaneous Cu and Fe deficiency, and led to a barely unaltered amino acid composition in comparison with standard conditions (Garcia-Molina et al., 2021). Considering the interplay of Cu and Fe in sustaining antioxidant activities mediated by superoxide dismutases and electron transport chains in chloroplast and mitochondrion (Kliebenstein et al., 1998; Abdel-Ghany et al., 2005; Yamasaki et al., 2009; Bernal et al., 2012), the detrimental consequences of the simultaneous limitation of Cu and Fe would prevent the proper function of photosynthesis and respiration to obtain energy based on carbon skeletons. Given the potentiality of amino acids as energy sources (Hildebrandt et al., 2015), it could be likely that protein catabolism might act as a compensatory mechanism to fulfill plant energetic demands and, therefore, amino acid synthesis would be unnecessary under this scenario.

Having *Mapman* bins for central metabolism as a reference (Thimm et al., 2004), CuFe–DSGs retrieved genes coding for enzymes involved in Gln, Asp, Leu, Ser, Gly, Leu anabolism, and most of the central features in the Asn and Trp biosynthesis pathways (**Table 1**). Interestingly, Gln, Asn, and Trp appeared in the group of amino acids that rose in concentration under Fe deficient conditions and decreased or minimally increased during the double deficiency (cluster I, **Figure 3**). Moreover, Trp and Asn, as well as the Trp-derivative tyramine, Phe, fumaric acid, and adenine, were previously categorized as significantly altered metabolites in Garcia-Molina et al. (2020). To address regulatory mechanisms in the biosynthesis of metabolites changing in response to the combinatorial deficiency, the transcriptome, proteome and metabolome profiles previously reported were analyzed in combination. Single Fe and double Cu and Fe deficiency imposed similar changes in transcript and protein amounts for the selected enzymes involved in Trp and Asn biosynthesis, though not always coincident in trend (absolute $r > 0.85$; **Figure 4** and **Table 2**). This indicates that the enzyme levels are not linearly dependent on the expression of the coding transcript. Indeed, enzyme amounts always increased under Fe and double Cu and Fe deficiency, regardless of the trend displayed by the coding transcript. However, the increase in enzyme levels could explain the increase in Trp and Asn concentration under Fe deficiency, but this is contradictory with the drop observed under simultaneous Cu and Fe deficiency. This observation could be attributed to either protein dysfunctionality, lack of intermediate availability, or faster consumption of the end products. Further analysis of the Trp pathway showed that tyramine – a degradative product of Trp – displayed a less dramatic decay under the double Cu and Fe condition in comparison with Trp. In that case, better correlations between tyramine concentration and enzyme amounts were found ($r > 0.75$), suggesting that tyramine would accumulate under the double deficiency as result of increased Trp degradation (**Figure 4** and **Table 2**). On the other hand, Gln and Asp decreased in the same proportion as Asn under the combinatorial deficiency (**Figure 4** and **Table 2**), ruling out the overaccumulation of metabolic intermediates caused by the drop in Asn.

Mechanistically, AS regulates gene expression either by the generation of transcript isoforms with altered stability, or by the production of modified protein versions with different functionality (Kelemen et al., 2013). In plants, IR is the most frequent AS event and has been well described as a phenomenon occurring during unfavorable conditions (Kalyna et al., 2011; Drechsel et al., 2013; Kwon et al., 2014; Filichkin et al., 2015; Ling et al., 2018). Although we found differences in AS motivated by differential count accumulation in introns, we described IR events in the Trp and Asn biosynthesis pathways under Fe and, especially, under double Cu and Fe deficiency (**Figures 5**, **6**) that we attributed to misfunction of the splicing machinery due to the stress conditions imposed by the treatments. IR has been proposed to act as a strategy to promote transcript decay via the interruption of the reading frame (Kalyna et al., 2011; Drechsel et al., 2013), however, the biosynthetic enzymes for

Trp and Asn that we analyzed increased at the protein level, regardless of the behavior of the coding transcript (**Figure 4**). Consequently, we proposed that the IR events taking place in the Trp and Asn biosynthesis pathways during the combinatorial response result in the codification of protein isoforms that are more stable, though less efficient in function. Nevertheless, we are not aware of any comprehensive study addressing the functional consequences of AS for the enzyme isoforms that we have described here. Similarly, the necessity of a specific regulation of Trp and Asn concentration during the double Cu and Fe deficiency remains elusive. Therefore, the role of such AS events as well as the changes in Asn and Trp concentration under the combinatorial Cu and Fe deficiency are open questions that deserve further investigation.

Taken together, our analysis sheds some new light on the systemic reprogramming of molecular changes that plants undergo during the combinatorial response to simultaneous Cu and Fe deficiency by including AS as an independent mechanism to regulate metabolic reactions that are not adjusted at either the transcript nor the protein level.

DATA AVAILABILITY STATEMENT

The original contributions presented in the study are included in the article/**Supplementary Material**, further inquiries can be directed to the corresponding author.

AUTHOR CONTRIBUTIONS

EM and AG-M designed the project, conducted the bioinformatic analysis, wrote the manuscript, and approved the submitted version.

FUNDING

This work was also supported by grant CEX2019-000902-S funded by MCIN/AEI/10.13039/501100011033 and by the CERCA Programme/Generalitat de Catalunya.

ACKNOWLEDGMENTS

Marcelo Yanovsky (Instituto de Investigaciones Bioquímicas de Buenos Aires - Fundación Instituto Leloir, Argentina) was acknowledged for encouraging comments in the design and interpretation of the analysis carried out. Helena Kruyer was acknowledged for critically reading and proof-editing the manuscript.

SUPPLEMENTARY MATERIAL

The Supplementary Material for this article can be found online at: https://www.frontiersin.org/articles/10.3389/fpls.2022.827828/full#supplementary-material

Supplementary Figure 1 | Analysis of differential splicing events under individual and simultaneous deficiency of copper and iron. Venn diagrams for multiple comparisons among differentially splicing events per treatment according to an absolute fold-change of at least 2 in pair-wise comparisons (adjusted-p-value ≤ 0.05, two-way ANOVA with *post hoc* Tukey's test).

Supplementary Figure 2 | Primary analysis of intron retention in transcripts involved in tryptophan and asparagine biosynthesis under single and simultaneous copper and iron deficiency. The average of read counts per exon or intron bins for the selected genes under standard conditions (Cont) and single and double copper and iron deficiencies (–Cu, –Fe, and –Cu–Fe) was calculated using the *ASpli* package. Bars represent the percentage of reads detected in intronic bins over the total reads in the whole genic region (introns plus exons bins).

REFERENCES

Abdel-Ghany, S. E., Muller-Moule, P., Niyogi, K. K., Pilon, M., and Shikanai, T. (2005). Two P-type ATPases are required for copper delivery in *Arabidopsis thaliana* chloroplasts. *Plant Cell* 17, 1233–1251. doi: 10.1105/tpc.104.030452

Anders, S., Reyes, A., and Huber, W. (2012). Detecting differential usage of exons from RNA-seq data. *Genome Res.* 22, 2008–2017. doi: 10.1101/gr.133744.111

Atkinson, N. J., Lilley, C. J., and Urwin, P. E. (2013). Identification of genes involved in the response of *Arabidopsis* to simultaneous biotic and abiotic stresses. *Plant Physiol.* 162, 2028–2041. doi: 10.1104/pp.113.222372

Bernal, M., Casero, D., Singh, V., Wilson, G. T., Grande, A., Yang, H., et al. (2012). Transcriptome sequencing identifies SPL7-regulated copper acquisition genes FRO4/FRO5 and the copper dependence of iron homeostasis in *Arabidopsis*. *Plant Cell* 24, 738–761. doi: 10.1105/tpc.111.090431

Calixto, C. P. G., Guo, W., James, A. B., Tzioutziou, N. A., Entizne, J. C., Panter, P. E., et al. (2018). Rapid and dynamic alternative splicing impacts the *Arabidopsis* cold response transcriptome. *Plant Cell* 30, 1424–1444. doi: 10.1105/tpc.18.00177

Chaudhary, S., Jabre, I., Reddy, A. S. N., Staiger, D., and Syed, N. H. (2019). Perspective on alternative splicing and proteome complexity in plants. *Trends Plant Sci.* 24, 496–506. doi: 10.1016/j.tplants.2019.02.006

Colangelo, E. P., and Guerinot, M. L. (2004). The essential basic helix-loop-helix protein FIT1 is required for the iron deficiency response. *Plant Cell* 16, 3400–3412. doi: 10.1105/tpc.104.024315

Cox, J., and Mann, M. (2008). MaxQuant enables high peptide identification rates, individualized p.p.b.-range mass accuracies and proteome-wide protein quantification. *Nat. Biotechnol.* 26, 1367–1372. doi: 10.1038/nbt.1511

Ding, F., Cui, P., Wang, Z., Zhang, S., Ali, S., and Xiong, L. (2014). Genome-wide analysis of alternative splicing of pre-mRNA under salt stress in *Arabidopsis*. *BMC Genomics* 15:431. doi: 10.1186/1471-2164-15-431

Dobin, A., Davis, C. A., Schlesinger, F., Drenkow, J., Zaleski, C., Jha, S., et al. (2012). STAR: ultrafast universal RNA-seq aligner. *Bioinformatics* 29, 15–21. doi: 10.1093/bioinformatics/bts635

Drechsel, G., Kahles, A., Kesarwani, A. K., Stauffer, E., Behr, J., Drewe, P., et al. (2013). Nonsense-mediated decay of alternative precursor mRNA splicing variants is a major determinant of the *Arabidopsis* steady state transcriptome. *Plant Cell* 25, 3726–3742. doi: 10.1105/tpc.113.115485

Filichkin, S., Priest, H. D., Megraw, M., and Mockler, T. C. (2015). Alternative splicing in plants: directing traffic at the crossroads of adaptation and environmental stress. *Curr. Opin. Plant Biol.* 24, 125–135. doi: 10.1016/j.pbi.2015.02.008

Filichkin, S. A., Priest, H. D., Givan, S. A., Shen, R., Bryant, D. W., Fox, S. E., et al. (2010). Genome-wide mapping of alternative splicing in *Arabidopsis thaliana*. *Genome Res.* 20, 45–58. doi: 10.1101/gr.093302.109

Garcia-Molina, A., Lehmann, M., Schneider, K., Klingl, A., and Leister, D. (2021). Inactivation of cytosolic FUMARASE2 enhances growth and photosynthesis under simultaneous copper and iron deprivation in *Arabidopsis*. *Plant J.* 106, 766–784. doi: 10.1111/tpj.15199

Garcia-Molina, A., Marino, G., Lehmann, M., and Leister, D. (2020). Systems biology of responses to simultaneous copper and iron deficiency in *Arabidopsis*. *Plant J.* 103, 2119–2138. doi: 10.1111/tpj.14887

Gupta, A., Sarkar, A. K., and Senthil-Kumar, M. (2016). Global transcriptional analysis reveals unique and shared responses in *Arabidopsis thaliana* exposed to combined drought and pathogen stress. *Front. Plant Sci.* 7:686. doi: 10.3389/fpls.2016.00686

Hermans, C., Johnson, G. N., Strasser, R. J., and Verbruggen, N. (2004). Physiological characterisation of magnesium deficiency in sugar beet: acclimation to low magnesium differentially affects photosystems I and II. *Planta* 220, 344–355. doi: 10.1007/s00425-004-1340-4

Hildebrandt, T. M., Nunes Nesi, A., Araujo, W. L., and Braun, H. P. (2015). Amino acid catabolism in plants. *Mol. Plant* 8, 1563–1579. doi: 10.1016/j.molp.2015.09.005

Huang, W., Chen, X., Guan, Q., Zhong, Z., Ma, J., Yang, B., et al. (2019). Changes of alternative splicing in *Arabidopsis thaliana* grown under different CO_2 concentrations. *Gene* 689, 43–50. doi: 10.1016/j.gene.2018.11.083

Kalyna, M., Simpson, C. G., Syed, N. H., Lewandowska, D., Marquez, Y., Kusenda, B., et al. (2011). Alternative splicing and nonsense-mediated decay modulate expression of important regulatory genes in *Arabidopsis*. *Nucleic Acids Res.* 40, 2454–2469. doi: 10.1093/nar/gkr932

Kannan, S., Halter, G., Renner, T., and Waters, E. R. (2018). Patterns of alternative splicing vary between species during heat stress. *AoB Plants* 10:ply013. doi: 10.1093/aobpla/ply013

Kelemen, O., Convertini, P., Zhang, Z., Wen, Y., Shen, M., Falaleeva, M., et al. (2013). Function of alternative splicing. *Gene* 514, 1–30. doi: 10.1016/j.gene.2012.07.083

Kliebenstein, D. J., Monde, R. A., and Last, R. L. (1998). Superoxide dismutase in *Arabidopsis*: an eclectic enzyme family with disparate regulation and protein localization. *Plant Physiol.* 118, 637–650. doi: 10.1104/pp.118.2.637

Kopka, J., Schauer, N., Krueger, S., Birkemeyer, C., Usadel, B., Bergmuller, E., et al. (2005). GMD@CSB.DB: the Golm metabolome database. *Bioinformatics* 21, 1635–1638. doi: 10.1093/bioinformatics/bti236

Kwon, Y.-J., Park, M.-J., Kim, S.-G., Baldwin, I. T., and Park, C.-M. (2014). Alternative splicing and nonsense-mediated decay of circadian clock genes under environmental stress conditions in *Arabidopsis*. *BMC Plant Biol.* 14:136. doi: 10.1186/1471-2229-14-136

Laloum, T., Martin, G., and Duque, P. (2018). Alternative splicing control of abiotic stress responses. *Trends Plant Sci.* 23, 140–150. doi: 10.1016/j.tplants.2017.09.019

Ling, Y., Serrano, N., Gao, G., Atia, M., Mokhtar, M., Woo, Y. H., et al. (2018). Thermopriming triggers splicing memory in *Arabidopsis*. *J. Exp. Bot.* 69, 2659–2675. doi: 10.1093/jxb/ery062

Mancini, E., Rabinovich, A., Iserte, J., Yanovsky, M., and Chernomoretz, A. (2021). ASpli: integrative analysis of splicing landscapes through RNA-Seq assays. *Bioinformatics* 37, 2609–2616. doi: 10.1093/bioinformatics/btab141

Marquez, Y., Brown, J. W., Simpson, C., Barta, A., and Kalyna, M. (2012). Transcriptome survey reveals increased complexity of the alternative splicing landscape in *Arabidopsis*. *Genome Res.* 22, 1184–1195. doi: 10.1101/gr.134106.111

Morrissey, J., and Guerinot, M. L. (2009). Iron uptake and transport in plants: the good, the bad, and the ionome. *Chem. Rev.* 109, 4553–4567. doi: 10.1021/cr900112r

Nishida, S., Kakei, Y., Shimada, Y., and Fujiwara, T. (2017). Genome-wide analysis of specific alterations in transcript structure and accumulation caused by nutrient deficiencies in *Arabidopsis thaliana*. *Plant J.* 91, 741–753. doi: 10.1111/tpj.13606

Prasch, C. M., and Sonnewald, U. (2013). Simultaneous application of heat, drought, and virus to *Arabidopsis* plants reveals significant shifts in signaling networks. *Plant Physiol.* 162, 1849–1866. doi: 10.1104/pp.113.221044

Puig, S., Andres-Colas, N., Garcia-Molina, A., and Penarrubia, L. (2007). Copper and iron homeostasis in *Arabidopsis*: responses to metal deficiencies, interactions and biotechnological applications. *Plant Cell Environ.* 30, 271–290. doi: 10.1111/j.1365-3040.2007.01642.x

Puig, S., and Penarrubia, L. (2009). Placing metal micronutrients in context: transport and distribution in plants. *Curr. Opin. Plant Biol.* 12, 299–306. doi: 10.1016/j.pbi.2009.04.008

Rasmussen, S., Barah, P., Suarez-Rodriguez, M. C., Bressendorff, S., Friis, P., Costantino, P., et al. (2013). Transcriptome responses to combinations of stresses in *Arabidopsis*. *Plant Physiol.* 161, 1783–1794. doi: 10.1104/pp.112.210773

Ravet, K., and Pilon, M. (2013). Copper and iron homeostasis in plants: the challenges of oxidative stress. *Antioxid. Redox Signal.* 19, 919–932. doi: 10.1089/ars.2012.5084

Reddy, A. S. N., Marquez, Y., Kalyna, M., and Barta, A. (2013). Complexity of the alternative splicing landscape in plants. *Plant Cell* 25, 3657–3683. doi: 10.1105/tpc.113.117523

Robinson, J. T., Thorvaldsdóttir, H., Winckler, W., Guttman, M., Lander, E. S., Getz, G., et al. (2011). Integrative genomics viewer. *Nat. Biotechnol.* 29, 24–26. doi: 10.1038/nbt.1754

Supek, F., Bosnjak, M., Skunca, N., and Smuc, T. (2011). REVIGO summarizes and visualizes long lists of gene ontology terms. *PLoS One* 6:e21800. doi: 10.1371/journal.pone.0021800

Suzuki, N., Rivero, R. M., Shulaev, V., Blumwald, E., and Mittler, R. (2014). Abiotic and biotic stress combinations. *New Phytol.* 203, 32–43. doi: 10.1111/nph.12797

Szakonyi, D., and Duque, P. (2018). Alternative splicing as a regulator of early plant development. *Front. Plant Sci.* 9:1174. doi: 10.3389/fpls.2018.01174

Thimm, O., Bläsing, O., Gibon, Y., Nagel, A., Meyer, S., Krüger, P., et al. (2004). mapman: a user-driven tool to display genomics data sets onto diagrams of metabolic pathways and other biological processes. *Plant J.* 37, 914–939. doi: 10.1111/j.1365-313X.2004.02016.x

Yamasaki, H., Hayashi, M., Fukazawa, M., Kobayashi, Y., and Shikanai, T. (2009). SQUAMOSA promoter binding protein-like7 is a central regulator for copper homeostasis in *Arabidopsis*. *Plant Cell* 21, 347–361. doi: 10.1105/tpc.108.060137

Zhang, C. (2015). Involvement of iron-containing proteins in genome integrity in *Arabidopsis thaliana*. *Genome Integr.* 6:2. doi: 10.4103/2041-9414.155953

Conflict of Interest: The authors declare that the research was conducted in the absence of any commercial or financial relationships that could be construed as a potential conflict of interest.

Publisher's Note: All claims expressed in this article are solely those of the authors and do not necessarily represent those of their affiliated organizations, or those of the publisher, the editors and the reviewers. Any product that may be evaluated in this article, or claim that may be made by its manufacturer, is not guaranteed or endorsed by the publisher.

frontiers in Plant Science

ORIGINAL RESEARCH
published: 02 March 2022
doi: 10.3389/fpls.2022.757048

Translocation of Foliar Absorbed Zn in Sunflower (*Helianthus annuus*) Leaves

Cui Li[1], Linlin Wang[1], Jingtao Wu[2], F. Pax C. Blamey[3], Nina Wang[1], Yanlong Chen[1], Yin Ye[1], Lei Wang[1], David J. Paterson[4], Thea L. Read[5], Peng Wang[6], Enzo Lombi[5], Yuheng Wang[1]* and Peter M. Kopittke[3]*

[1] School of Ecology and Environment, Northwestern Polytechnical University, Xi'an, China, [2] Key Laboratory of Vegetation Restoration and Management of Degraded Ecosystems, South China Botanical Garden, Chinese Academy of Sciences, Guangzhou, China, [3] School of Agriculture and Food Sciences, The University of Queensland, Brisbane, QLD, Australia, [4] Australian Synchrotron, Clayton, VIC, Australia, [5] Future Industries Institute, University of South Australia, Mawson Lakes, SA, Australia, [6] College of Resources and Environmental Sciences, Nanjing Agricultural University, Nanjing, China

OPEN ACCESS

Edited by:
Sidsel Birkelund Schmidt, The James Hutton Institute, United Kingdom

Reviewed by:
Pedro Humberto Castro, Centro de Investigacao em Biodiversidade e Recursos Geneticos (CIBIO-InBIO), Portugal
Adalberto Benavides-Mendoza, Universidad Autónoma Agraria Antonio Narro, Mexico

***Correspondence:**
Cui Li
cui.li@nwpu.edu.cn
Yuheng Wang
yuheng.wang@nwpu.edu.cn

Specialty section:
This article was submitted to Plant Nutrition, a section of the journal Frontiers in Plant Science

Received: *11 August 2021*
Accepted: *17 January 2022*
Published: *02 March 2022*

Citation:
Li C, Wang L, Wu J, Blamey FPC, Wang N, Chen Y, Ye Y, Wang L, Paterson DJ, Read TL, Wang P, Lombi E, Wang Y and Kopittke PM (2022) Translocation of Foliar Absorbed Zn in Sunflower (Helianthus annuus) Leaves. Front. Plant Sci. 13:757048. doi: 10.3389/fpls.2022.757048

Foliar zinc (Zn) fertilization is an important approach for overcoming crop Zn deficiency, yet little is known regarding the subsequent translocation of this foliar-applied Zn. Using synchrotron-based X-ray fluorescence microscopy (XFM) and transcriptome analysis, the present study examined the translocation of foliar absorbed Zn in sunflower (*Helianthus annuus*) leaves. Although bulk analyses showed that there had been minimal translocation of the absorbed Zn out of the leaf within 7 days, *in situ* analyses showed that the distribution of Zn in the leaf had changed with time. Specifically, when Zn was applied to the leaf for 0.5 h and then removed, Zn primarily accumulated within the upper and lower epidermal layers (when examined after 3 h), but when examined after 24 h, the Zn had moved to the vascular tissues. Transcriptome analyses identified a range of genes involved in stress response, cell wall reinforcement, and binding that were initially upregulated following foliar Zn application, whereas they were downregulated after 24 h. These observations suggest that foliar Zn application caused rapid stress to the leaf, with the initial Zn accumulation in the epidermis as a detoxification strategy, but once this stress decreased, Zn was then moved to the vascular tissues. Overall, this study has shown that despite foliar Zn application causing rapid stress to the leaf and that most of the Zn stayed within the leaf over 7 days, the distribution of Zn in the leaf had changed, with Zn mostly located in the vascular tissues 24 h after the Zn had been applied. Not only do the data presented herein provide new insight for improving the efficiency of foliar Zn fertilizers, but our approach of combining XFM with a transcriptome methodological system provides a novel approach for the study of element translocation in plants.

Keywords: foliar fertilizers, translocation, sunflower, XFM, Zn nutrition

INTRODUCTION

Zinc (Zn) is a micronutrient for both plants and humans. However, Zn deficiency ranks as the third most common micronutrient deficiency in humans (Menguer et al., 2018), with more than 30% of the global human population suffering from Zn deficiency (Xia et al., 2020). This deficiency in the global human population is primarily due to the low dietary Zn supply caused by widespread crop

Zn deficiency (Zhang et al., 2018). Foliar fertilization with Zn is an efficient approach to overcome crop Zn deficiency and to fortify foods with Zn, thus alleviating human Zn deficiency, especially for soils that limit the root uptake of Zn (Joy et al., 2015; Fu et al., 2016). However, much remains unknown regarding the translocation of the Zn in crops following its initial movement across the leaf surface.

We have previously examined the absorption of foliar-applied Zn in sunflower (*Helianthus annuus*), finding that Zn is absorbed through the base of non-glandular trichomes (NGTs) and the general cuticular area (i.e., leaf areas covered by the cuticle without stomata and trichomes) (Li et al., 2019). However, following its absorption, the subsequent movement of Zn (i.e., translocation) is considered to be limited in sunflower (Li et al., 2017) and also in other plant species (Zhang and Brown, 1999; Du et al., 2015). How Zn moves within the leaf following its absorption, and the factors regulating this movement, remain unclear. This lack of knowledge hinders the optimal use of Zn foliar fertilizers and the development of new and more efficient Zn foliar fertilizers.

Theoretically, the translocation of foliar absorbed Zn involves three processes: (1) movement of the Zn from the apoplast of the leaf epidermal cells to the leaf vascular tissues (phloem and xylem); (2) long-distance translocation within the vascular tissues; and (3) unloading from the vascular tissues and translocation into the destination tissues. It has been proposed that the limited translocation of foliar-absorbed Zn could be due to several factors, including the strong binding of Zn within the leaf epidermal cell wall (Du et al., 2015), low mobility within the phloem (Wu et al., 2010; Xue et al., 2015), the use of different Zn fertilizer types that differ in their properties (Doolette et al., 2018), or differences in the phenological stages of the plant that alter the translocation of the Zn (Fernández and Brown, 2013). Furthermore, it has been reported that Zn deficiency promotes the redistribution of Zn from old leaves to young leaves (Xie et al., 2019). However, few studies have utilized molecular biology to investigate the foliar translocation of Zn in order to understand the mechanisms that regulate its translocation.

In the present study, we use two broad approaches for improving our understanding of the translocation of foliar absorbed Zn. Firstly, it is useful to examine progressive changes in the distribution of elements in plants. In this regard, synchrotron-based X-ray fluorescence microscopy (XFM) is a valuable tool that can be used for obtaining maps showing the real-time element distribution in living plants (Blamey et al., 2018; Kopittke et al., 2020). Secondly, RNA-sequence analysis is a powerful technique for understanding gene expression. The present study combined these two approaches, allowing us to relate the changes in Zn distribution in the leaf to the underlying gene expression. Using sunflower, we first examined the *in situ* distribution of Zn in the leaf in a time-resolved manner using synchrotron-based XFM in living plants. Next, based upon the distribution of Zn, RNA-sequence analysis was employed to show the leaf gene expression at different Zn translocation stages. This study provides novel information on the movement of foliar absorbed Zn within the leaf and corresponding changes in leaf gene expression during this process. It is expected that the results will increase our understanding of the translocation of foliar Zn fertilizers and provide new insight in improving the efficiency of Zn foliar fertilizers, thus assisting to alleviate the health problems caused by Zn deficiency in 30% of the global human population.

MATERIALS AND METHODS

General Conditions for Plant Growth

Sunflower (cv. Hyoleic 41) seeds were germinated in rolled paper towels covered with a plastic bag placed vertically in a beaker filled with tap water for 4 days. Thereafter, four seedlings were transferred to black buckets (11 L) using the same method and nutrient solution composition as described in Li et al. (2018a). Briefly, the plants were grown at a temperature of 25°C and with artificial light (photon flux density of 1,500 μmol m^{-2} s^{-1}) for 12 h d^{-1}. Nutrient solutions were continuously aerated and changed weekly. Aliquots (5 ml) of 44 mM KH_2PO_4 were supplied to each bucket every other day after 10 days of growth to replace the phosphorus (P) being removed by plant growth.

Fertilizer Application and Bulk Leaf Zn Concentrations

The Zn foliar fertilizer used in the study was 1,000 mg Zn L^{-1} (15.4 mM, pH 5.2) with 0.05% Tween 20 (Reuveni et al., 1994), with the solution prepared using $ZnSO_4$. $7H_2O$. Using 2-week-old sunflower plants, Zn was applied using a pipette as 5 μL droplets onto the youngest fully expanded leaf (YFEL) surface, with each leaf having a total of 30 droplets. The Zn was always applied to the adaxial leaf surface. After 0.5 h, all the droplets were removed by blotting dry using filter paper, with the leaf still attached to the plants. Then, the leaf blades were cut from the petioles at 0, 6, 24, 60, and 168 h after removing the droplets. Leaves to which no Zn was applied were also harvested at 0 and 168 h as controls. All the leaves were then rinsed thoroughly using (sequentially) deionized water, 3% ethanol, 2% HNO_3, and then deionized water (Vu et al., 2013). Then the leaves were dried at 60°C and digested using a 5:1 mixture of nitric acid and perchloric acid. We measured Zn concentrations using atomic absorption spectrometry, with blanks and reference standards included to ensure accuracy. Three replicates were utilized.

Tracing Zn Distribution in Sunflower Leaf Using X-ray Fluorescence Microscopy

This experiment was conducted at the XFM beamline of the Australian Synchrotron (Clayton, Australia) (Paterson et al., 2011; Howard et al., 2020). The excitation energy was 12,900 eV, the X-rays were selected using a Si (111) monochromator, and the beam size was 2 × 2 μm. The total photon flux was ca. 2.9×10^9 photons s^{-1} on the sample. A 384-element Maia detector system in a backscatter position of the sample was used to collect the X-ray fluorescence emitted by the specimen (Kopittke et al., 2011). Two types of analyses were conducted using XFM: (1) Repeated, time-resolved scans using living plants to examine changes in Zn distribution in leaves following the foliar application of Zn (Blamey et al., 2018); and (2) scans

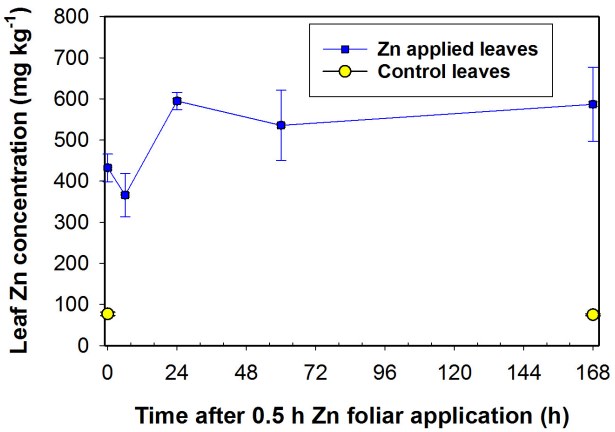

FIGURE 1 | Bulk concentration of zinc (Zn) in sunflower leaves to which Zn had been foliar-applied. The Zn was applied for 0.5 h before then being removed, leaves were then harvested after growing for a further 0, 6, 24, 60, and 168 h. For the control leaves, no Zn was applied and the leaves were harvested after 0 and 168 h. Data are mean ± SD (n = 3).

using freeze-dried cross-sections harvested at various times after applying the Zn (Li et al., 2018a).

For the first analysis (time-resolved scans in living plants), 2-week-old sunflower plants were transferred to the Australian Synchrotron and individual plants were placed in a 50 ml centrifuge tube with the stem held firmly in place using foam. The tube (and plant) was placed in a customized sample holder, with the YFEL mounted flat onto a sample window with the adaxial surface of the leaf (i.e., the surface to which the Zn had been applied) facing the incident beam and the detector. The tube was filled with nutrient solution and the plant was maintained in artificial light (as described above) unless being scanned. A 5 μL droplet of the Zn fertilizer solution was applied to the YFEL using a pipette. After 0.5 h, the droplet was removed by blotting dry using filter paper. From the time when the Zn was removed from the leaf surface, the leaf was scanned repeatedly at 0.25, 2.2, 4, 6, 20, 45, and 60 h. Two replicate leaves were examined (the leaves being on different plants), with the second leaf scanned after 1, 3, 5, 7, 21, 46, and 61 h. For each scan, a coarse scan was first conducted to locate the area where the Zn had initially been applied and to ensure that each scan was performed on the same area. After this initial coarse scan, a fine scan was conducted to obtain a higher resolution map. The coarse scan was conducted at a step size of 30 μm and a horizontal stage velocity of 5 mm s^{-1}, resulting in a pixel transit time of 6 ms. The fine scan was done at a step size of 2 μm and horizontal stage velocity of 1.5 mm s^{-1}, resulting in a pixel transit time of 1.33 ms. The XFM data were analyzed using GeoPIXE (Ryan and Jamieson, 1993; Ryan, 2000). Following completion of the experimental period, the leaves were visually examined and showed no damage.

For the second type of analysis, the freeze-dried leaf sections were prepared in advance. To provide a larger area that could be sectioned, a 100 μL Zn droplet was applied to the YFELs of 40-day-old sunflower plants for 0.5 h and then removed by blotting dry using filter paper. Once the droplet had been removed, the leaves were then excised after 0, 0.5, 3, and 24 h. YFELs that had not received any Zn were used as the control. Following excision, the YFELs were rinsed thoroughly using deionized water, 3% ethanol, 2% HNO_3, and deionized water (Vu et al., 2013). The area where Zn had been applied was excised, embedded in 4% agar and sections (150 μm in thickness) prepared using a vibratome (Leica VT 1000s) (Li et al., 2018b). The sections were then freeze-dried after sealing between Ultralene films (holes were punched in the film to aid the freeze-drying process) which were held using XRF sample cups (SC-8047, Premier Lab Supply). The freeze-dried samples were then transferred to the Australian Synchrotron with the sample cup for analysis. At the Australian Synchrotron, the sections were placed between Ultralene films (4 μm thickness) on the sample holder (**Supplementary Figure 1**). Two replicates were examined. A rapid coarse scan was first used to locate the samples before a fine scan was performed at a higher resolution. The parameters of the scans were the same as indicated earlier.

Transcriptome Analysis of Leaf During Different Zn Translocation Stages

Based on the XFM analyses (see section "Results"), the Zn distribution in the leaf cross-sections differed markedly for the samples examined 0 and 24 h after the initial 0.5 h application period, with the overall Zn translocation rate increasing at ca. 20 h. Therefore, the following samples were collected for transcriptome analysis: (1) The YFELs without Zn treatment as control (L0); (2) the YFELs to which Zn applied for 0.5 h before being removed and then harvested immediately as L1 (i.e., 0 h after removing the Zn); and (3) the YFELs to which Zn applied for 0.5 h and grown for 24 h after fertilizer removal as L2 (i.e., 24 h after removing the Zn). For this experiment, Zn was sprayed over the entire leaf surface. The leaves were excised at the required harvest time and rinsed using deionized water. The samples were placed into RNase-free tubes and immediately frozen in liquid nitrogen and placed in a freezer (–80°C) until further analysis. Three biological replicates were examined.

Total RNA was extracted using the RNAprep pure plant kit (DP441, Tiangen) following the manufacturer's instructions. The RNA quantification and quality were examined using 1% agarose gels, a NanoPhotometer spectrophotometer (IMPLEN, CA, United States), and the RNA Nano 6000 Assay Kit of the Bioanalyzer 2100 system (Agilent Technologies, CA, United States). Next, 1 μg RNA per sample was used to generate the RNA sequencing libraries using NEBNext Ultra RNA Library Prep Kit for Illumina (Novogene, Beijing, China) following the manufacturer's instructions. The clustering of the samples was performed using a cBot Cluster Generation System with TruSeq PE Cluster Kit v3-cBot-HS (Illumina). The sequencing analysis was then conducted on an Illumina NovaSeq platform after cluster generation and 150 bp paired-end reads were generated. After obtaining the raw reads, the reads of low quality and containing adapter or poly-N were removed to get the clean reads, with the Q20, Q30, and guanine and cytosine (GC) content of the clean reads calculated. All analyses were performed using the processed clean reads. The clean reads were aligned to the

genome of the sunflower using Hisat2 v2.0.5 (Badouin et al., 2017).

For the gene expression quantification, the read numbers of each gene were counted using featureCounts v1.5.0-p3, and the fragments per kilobase of transcript per million mapped reads (FPKM) of each gene were calculated for comparison among different samples (Nautiyal et al., 2020). The DESeq2 R package was employed for analyzing the differentially expressed genes (DEGs) between the three samples, i.e., genes with an adjusted *p*-value (*p*adj) ≤ 0.05 and $|\log2(\text{FoldChange})| \geq 0$ were assigned as differentially expressed. Gene Ontology (GO) and Kyoto Encyclopedia of Genes and Genomes (KEGG) analyses were used to classify the functions of the DEGs by using the clusterProfiler R package (3.4.4), with *p*adj < 0.05 identified as significantly enriched GO terms and *p*-value < 0.05 as KEGG pathways.

Quantitative Reverse Transcription PCR Validation

To validate the transcriptome results, 15 genes were selected for Quantitative Reverse Transcription PCR (RT-qPCR) analysis. The total RNA was extracted as described above. The first-strand complementary DNA (cDNA) was synthesized using the Prime Script® RT reagent Kit (Takara, Japan). The primers were designed using Primer3 (v. 0.4.0) (**Supplementary Table 1**). RT-qPCR was performed using an SYBR Premix EX Taq Kit (Takara) in a 20 μL reaction mixture on an ABI7300 (Applied Biosystems, United States). The Actin (gene ID: 110903735) and Ubiquitin (gene ID: 110936586) were used as the internal controls (Fernandez et al., 2008; Ramu et al., 2016). The relative expression was assessed using the $2^{-\Delta\Delta CT}$ method (Livak and Schmittgen, 2001).

RESULTS

Changes in Leaf Bulk Zn Concentration After Foliar Zn Application

Following the initial application of Zn for 0.5 h, the concentration of Zn within the bulk leaf tissue (ca. 400–600 mg kg^{-1}) was substantially higher than for the control (ca. 100 mg kg^{-1}) (**Figure 1**). For the leaves to which Zn had been applied, the slight increase in the leaf Zn concentration from 0 to 24 h was possibly due to the continued absorption of Zn from the residual Zn on the leaf surface given that the Zn was only removed using a filter paper after 0.5 h. It is noteworthy that there was no notable decrease in the bulk leaf tissue Zn concentration over time, suggesting that there was not a pronounced translocation of Zn out of the Zn applied leaf.

In situ Analyses of Foliar Absorbed Zn in Sunflower Leaves

To allow for *in situ* analyses of the changes in the distribution of Zn following its foliar absorption, time-resolved XFM analyses using living plants were used to examine the leaf areas where the Zn had been applied for 0.5 h and then removed (**Figure 2** and **Supplementary Figure 2**). Importantly, when examining

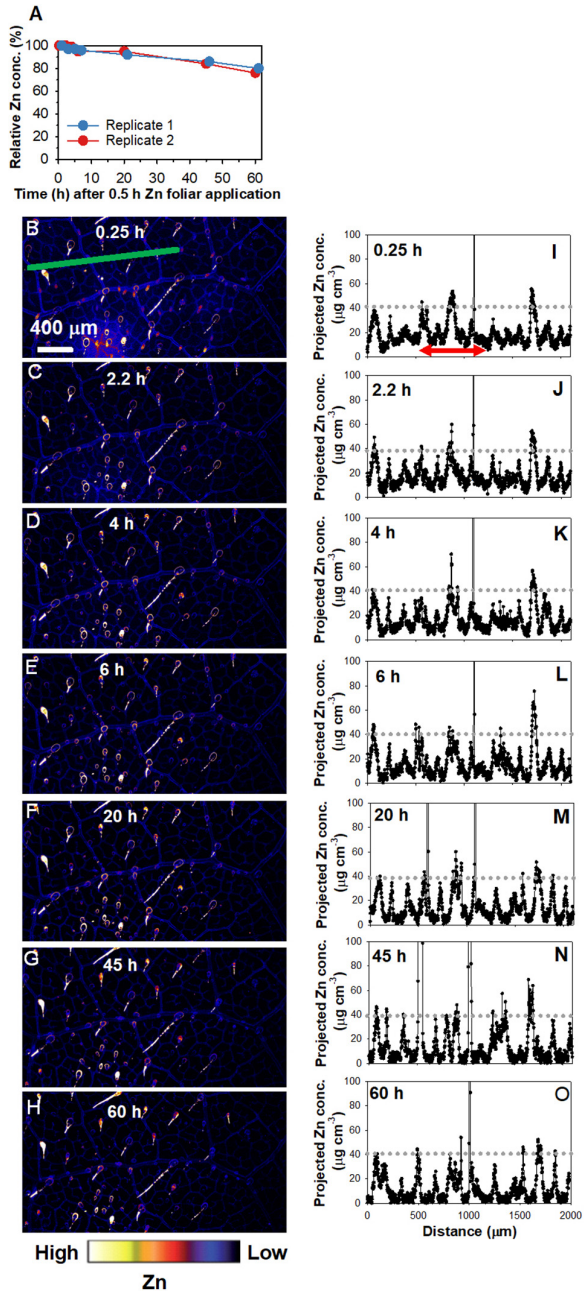

FIGURE 2 | Repeated X-ray fluorescence microscopy (XFM) scans of the same leaf area of sunflower over 60 h showing the changes in the Zn concentration under the area previously exposed to a 5 μL droplet of 1,000 mg Zn L^{-1} (15.4 mM, pH 5.2) with 0.05% Tween for 0.5 h. Note that the entire area in the images shown was from the area beneath the area to which the Zn had been applied. **(A)** Changes in the relative Zn concentrations with time, calculated using the average Zn concentrations of the areas in **(B–H)** and **Supplementary Figure 2**. (i.e., two replicates). **(B–H)** Maps showing the Zn distribution for Replicate 2, with the scans conducted at 0.25 h **(B)**, 2.2 h **(C)**, 4 h **(D)**, 6 h **(E)**, 20 h **(F)**, 45 h **(G)**, and 60 h **(H)** following 0.5 h foliar application. Part of **(B–H)** is from Li et al. (2021) with using permission. **(I–O)** showing the projected Zn concentration along the green line in **(B–H)**, respectively. The red arrow in **(I)**, which applies to **(J–O)** also, allows a comparison of Zn concentration in the veins and interveinal area. Colors are comparable in **(B–H)**. The scale in B applies to **(C–H)**.

these elemental distribution maps, it must be noted that the Zn was applied as a single droplet and that the entire area is shown in **Figure 2** and **Supplementary Figure 2** is from an area originally under droplet. Firstly, changes in the relative average Zn concentrations of the area were analyzed (**Figure 2A**). It was found that the two replicates had a similar trend, with the relative Zn concentration decreasing by ca. 5% after 20 h, and then decreasing by ca. 20% after 60 h. Indeed, when comparing the same leaf scanned repeatedly over time, the decreased brightness of colors from 0.25 to 60 h showed that the concentration of Zn in the leaf tissues underlying the area where the Zn had been applied gradually decreased over time (**Figures 2B–H** and **Supplementary Figure 2**). Particularly, the roles of NGTs in absorption and translocation of foliar-applied Zn are not discussed here as it has been discussed previously in Li et al. (2019, 2021).

Next, the transect indicated by the green line in **Figures 2B–H** was used to examine the Zn concentration at a finer scale over time (**Figures 2I–O**). The initial peaks at ca. 40 $\mu g\ cm^{-3}$ in **Figures 2I–O** showed that the highest concentration of Zn along this linear transect corresponded to the veins. In contrast, the interveinal areas had ca. 10 $\mu g\ cm^{-3}$ Zn—a concentration that decreased as time progressed to typically $< 5\ \mu g\ cm^{-3}$ after 20 h, and continued decrease thereafter (**Figures 2I–O**). This suggests that the Zn in the interveinal areas was gradually translocated away, most likely to the veins.

To further assess the changes in Zn concentrations in the leaf over time, we examined the Zn distribution in leaf cross-sections that were collected 0, 0.5, 3, and 24 h following the initial 0.5 h Zn application (**Figure 3**). Light microscopy showed that bundle sheath extensions (BSEs) connected the leaf tissues both vertically and horizontally, with the vertical BSEs generally connecting with NGTs on adaxial and abaxial surfaces and the horizontal BSEs connecting to the leaf veins (**Figure 3A**). In this regard, it is known that the BSEs play an important role in the translocation of foliar absorbed Zn (Li et al., 2019). As expected, XFM analysis showed that Zn concentration within the leaf tissues was higher for all treated leaves than for the control in both replicates. However, the distribution of the Zn within the leaf cross-sections changed over time (**Figures 3B,C** and **Supplementary Figure 3**). We examined average Zn concentrations along a linear transect that was ca. 500 μm wide across the five treatments as shown by the white box in **Figure 3B**, with these average values shown in **Figure 3C**. For the control leaf, the highest Zn concentration was in the middle (inner) tissues of the leaf. Immediately after Zn application (i.e.,0.5 + 0 h), the highest Zn concentration was found in the adaxial epidermal layer (Zn having been applied to the adaxial leaf surface). It was interesting that in as little as 0.5 h since the initial application of foliar Zn, some of the Zn that had been absorbed was already located in the inner leaf tissues and in the abaxial epidermal layer. This raises the possibility of Zn being translocated from the adaxial surface to the abaxial surface by the vertical BSEs (Li et al., 2019). After 3 h (0.5 + 3 h), there was a pronounced movement of Zn across the entire cross-section, including in the BSEs and the NGT bases. After 24 h (0.5 + 24 h), Zn was mostly presented in the vascular tissues (**Figure 3**).

Overall, these results demonstrate that the changes in the concentration and distribution of foliar absorbed Zn occurs quickly, with the Zn initially located in the adaxial epidermal layers (0–3 h) but later also moving to the middle (inner) vascular tissues of the leaf (24 h) which appear to correspond to the horizontal BSEs (**Figure 3A**). These observations for the cross-sections are in agreement with the data obtained from the repeated scanning of living leaves (**Figure 2**) which showed that the Zn translocation rate was limited in the first 6 h, with this stage likely corresponding to Zn accumulating in the epidermal layers, whereas after 24 h, the Zn had begun moving to the BSEs and thus the translocation rate increased thereafter.

Identification of Differentially Expressed Genes in Sunflower Leaves at Different Zn Translocation Stages

Based on the XFM analyses, the following leaf samples were selected for transcriptome analysis: (i) L0, leaves without any treatment as the control; (ii) L1, leaves to which Zn had foliar applied for 0.5 h, representing the stage when Zn is mainly located in the epidermal layers; and (iii) leaves to which had kept growing for 24 h after 0.5 h of foliar Zn application, representing the stage when Zn is mainly located in the middle layer of the leaf. High-throughput Illumina sequencing yielded an average of 45.5 million clean reads from L0, 46.3 million from L1, and 46.3 million from L2 (**Supplementary Table 2**). Aligning to the genome of sunflower, L0 had a unique alignment rate of 86.1%, L1 of 85.7%, and L2 of 85.4% (**Supplementary Table 3**). The Spearman correlation coefficient (SCC) between the biological replicates of the three samples varied from 0.90 to 0.98 (**Supplementary Table 4**). The RT-qPCR analysis of the 15 randomly selected genes all showed a similar gene expression pattern with the transcriptome analysis (**Supplementary Figure 4**). Together, these findings indicate the good quality of the sequential data and replicates.

To compare gene expression among the three samples (L0, L1, and L2), the genes of the unique map libraries were all normalized to the FPKM value (**Supplementary Additional File 1**). Principal component analysis using the FPKM value showed that the leaf gene expression was significantly different among the three samples (**Figure 4A**). Specifically, L1 had 12,417 DEGs, with 6,924 genes upregulated and 5,475 downregulated compared to L0. Compared to L1, L2 had 2,850 genes upregulated and 3,582 genes downregulated (**Figures 4B,C** and **Supplementary Additional File 2**).

Gene Ontology and Kyoto Encyclopedia of Genes and Genomes Enrichment Analysis of the Differentially Expressed Genes

The GO enrichment analysis was conducted for the DEGs of L1 vs. L0 and L2 vs. L1, with the most significantly enriched GO terms shown in **Table 1** (full list in **Supplementary Additional File 3**). Comparing L1 to L0, the GO terms of "hydrolase activity: acting on glycosyl bonds," "transferase activity: transferring acyl groups other than amino-acyl groups," "cell periphery," and

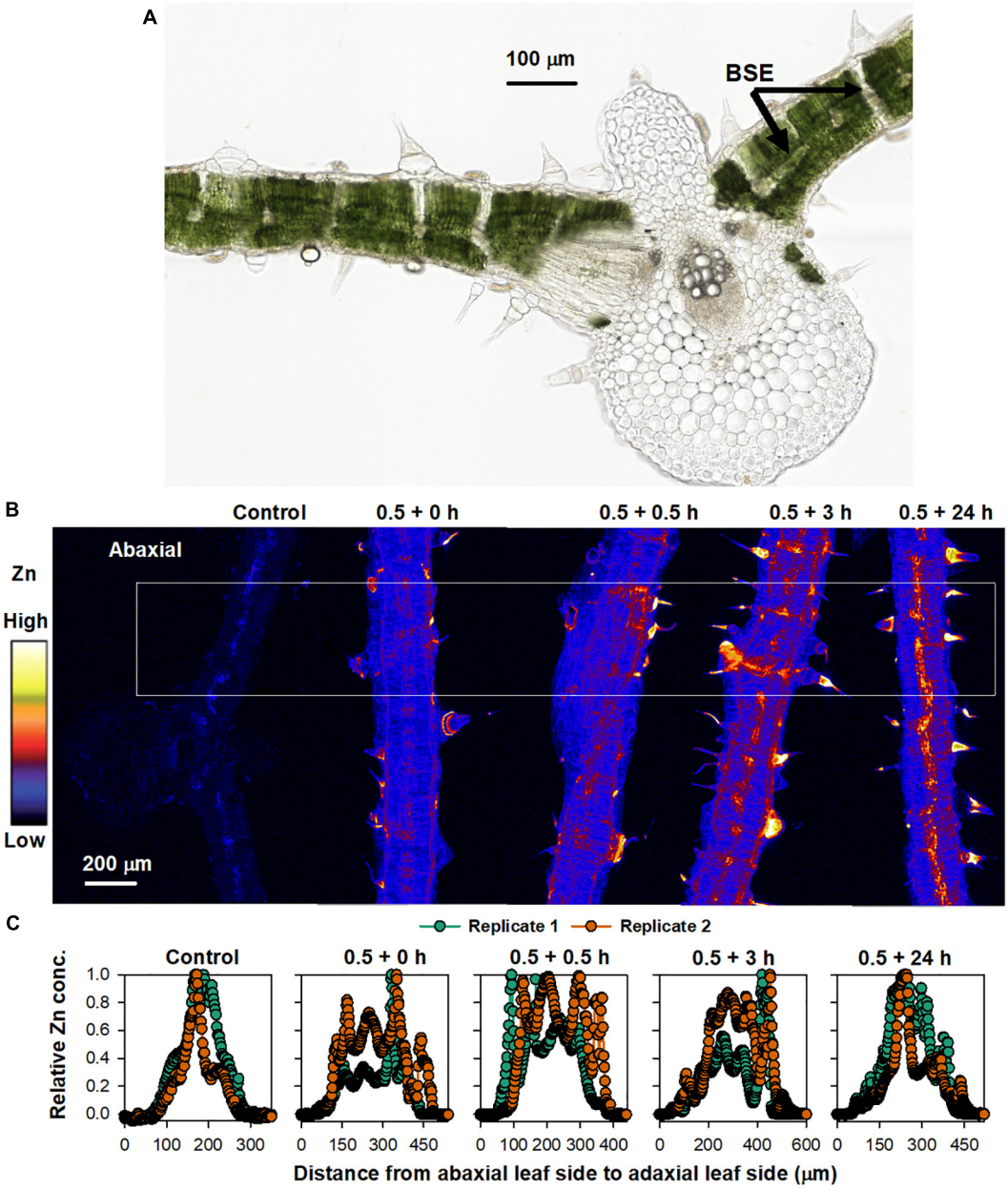

FIGURE 3 | Sunflower leaves to which Zn had been applied. **(A)** Light micrograph of sunflower leaf cross-section, showing the bundle sheath extension (BSE) (from Li et al., 2018b with permission). **(B)** XFM images showing Zn distribution in cross-sections of a control leaf, and leaves to which Zn had been applied for 0.5 h before the Zn was removed and the plant then grown for a further 0 (0.5 + 0 h), 0.5 (0.5 + 0.5 h), 3 (0.5 + 3 h), and 24 h (0.5 + 24 h) (all leaf tissues shown were sampled from underneath where the Zn had applied). The colors are comparable in **(B)**. **(C)** Relative average Zn concentration along each leaf area from the white box in **(B)**. Two replicates were examined, with Replicate 1 shown here and Replicate 2 shown in **Supplementary Figure 3**.

"cell wall" were found to be upregulated, with these four GO terms all relevant to cell wall construction (Lopez-Casado et al., 2008). The GO terms of "carbohydrate binding" and "iron ion binding" were also upregulated, with these potentially relevant for the binding of the absorbed Zn^{2+}. In addition, "response to wounding" was also significantly upregulated, suggesting that abiotic stress was induced by the foliar $ZnSO_4$ application. In contrast, genes involved in "structural constituent of ribosome" and "protein transport" were downregulated. Comparing L2 to L1, the GO terms which were downregulated in L1 compared to L0, such as "structural constituent of ribosome" and "translation" were actually upregulated in L2. The reverse was also found, that some terms that were upregulated in L1 (compared to L0) such as "transferase activity: transferring acyl groups other than amino-acyl groups" and "response to wounding" were actually downregulated in L2 compared to L1. These observations suggest

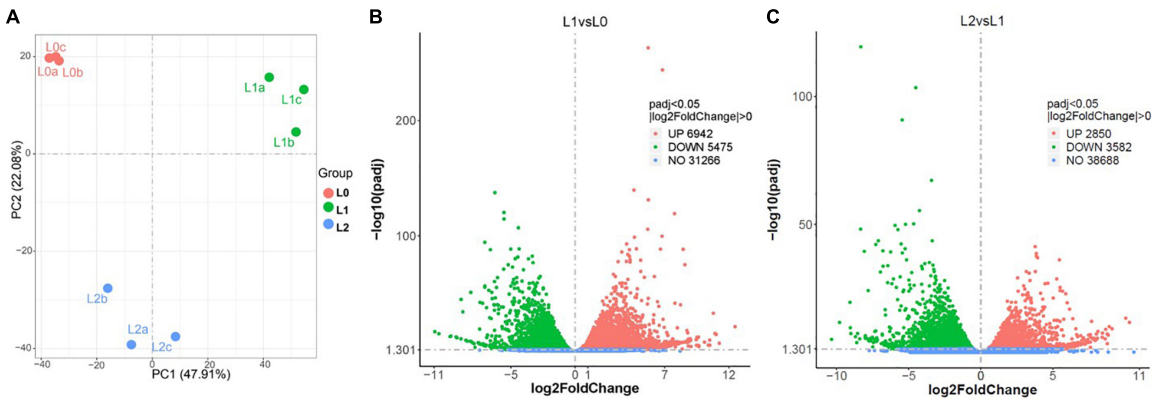

FIGURE 4 | Overview of the sunflower leaf transcriptome analysis results. **(A)** Principal component analysis using the fragments per kilobase of transcript per million (FPKM) value of L0 (the leaves without Zn treatment), L1 (the leaves to which Zn applied for 0.5 h before being removed and then harvested immediately), and L2 (the leaves harvested 24 h after Zn applied for 0.5 h and removed), with a, b, and c referring to three replicates. **(B,C)** DEGs between L1 vs. L0 **(B)** and L2 vs. L1 **(C)**.

TABLE 1 | Selected significantly enriched GO terms of the DEGs in L0 (control leaves without Zn), L1 (leaves to which Zn was applied for 0.5 h before being removed and then harvested immediately), and L2 (leaves to which Zn was applied for 0.5 h before being removed and then left for 24 h before being harvested).

Category	GO ID	Description	*p*adj	Count
Up-regulated in L1 vs. L0				
MF	GO:0016798	Hydrolase activity: acting on glycosyl bonds	2.67E-07	120
MF	GO:0016747	Transferase activity: transferring acyl groups other than amino-acyl groups	1.39E-05	77
MF	GO:0030246	Carbohydrate binding	0.000204	59
CC	GO:0071944	Cell periphery	0.000738	51
MF	GO:0004857	Enzyme inhibitor activity	0.000946	42
CC	GO:0005618	Cell wall	0.003643	30
BP	GO:0009611	Response to wounding	0.003779	9
MF	GO:0005506	Iron ion binding	0.019931	102
Down-regulated in L1 vs. L0				
BP	GO:0006412	Translation	1.20E-67	240
MF	GO:0003735	Structural constituent of ribosome	1.02E-72	201
BP	GO:0006082	Organic acid metabolic process	0.00024	99
BP	GO:0051188	Cofactor biosynthetic process	0.001849	39
BP	GO:0015031	Protein transport	0.01952	45
MF	GO:0003723	RNA binding	5.53E-17	131
Up-regulated in L2 vs. L1				
MF	GO:0003735	Structural constituent of ribosome	7.07E-27	101
BP	GO:0006412	Translation	1.99E-18	114
CC	GO:0048046	Apoplast	0.015166	12
MF	GO:0016762	Xyloglucan: xyloglucosyl transferase activity	0.017901	12
MF	GO:0043565	Sequence-specific DNA binding	0.001219	52
down-regulated in L2 vs. L1				
CC	GO:0098796	Membrane protein complex	0.00011	40
MF	GO:0030414	Peptidase inhibitor activity	0.001209	12
MF	GO:0016747	Transferase activity: transferring acyl groups other than amino-acyl groups	0.002933	42
BP	GO:0009611	Response to wounding	0.0052	7
BP	GO:0016567	Protein ubiquitination	0.0052	22
MF	GO:0022803	Passive transmembrane transporter activity	0.02162	17

Terms of padj < 0.05 as significantly enriched; Category refers to the functional classification of the Gene Ontology (GO) terms: biological process (BP), cellular component (CC), and molecular function (MF); Count means the number of the DEGs assigned to this GO term.

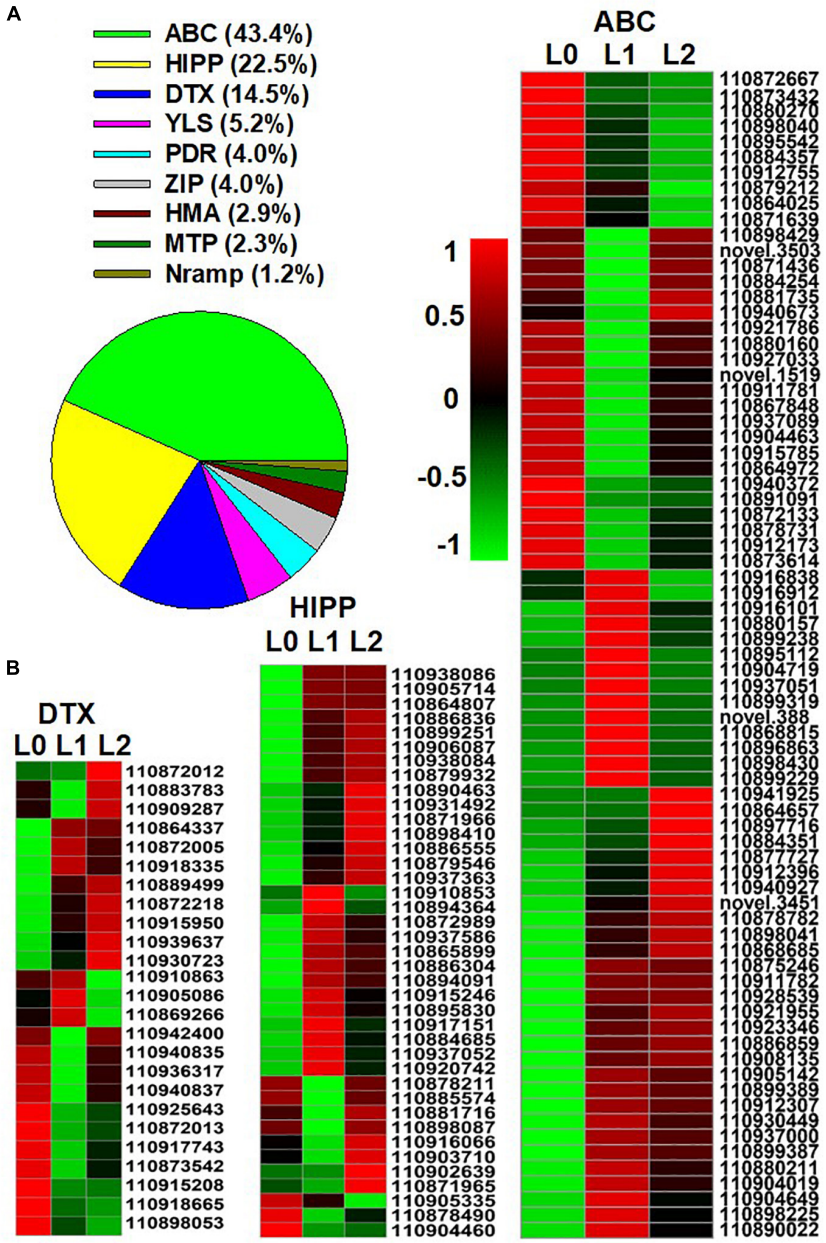

FIGURE 5 | Genes of Zn transporters identified from the differentially expressed genes (DEGs) of the sunflower leaves. L0 = control leaves without Zn, L1 = leaves to which Zn was applied for 0.5 h before being removed and then harvested immediately, and L2 = leaves to which Zn was applied for 0.5 h before being removed and then left for 24 h before being harvested. **(A)** The proportion of the nine groups' Zn transporters in the DEGs of the three samples. **(B)** Gene expression heatmap of the DEGs in the three Zn transporter families. ABC, ATP binding cassette transporters; HIPP, heavy metal-associated isoprenylated protein; DTX, protein DETOXIFICATION. Scale bar in B indicates a normalized FPKM value of genes.

that the stresses that were induced immediately following the foliar application of $ZnSO_4$ for 0.5 h had then subsided after 24 h.

The significantly enriched KEGG pathways from the DEGs of L1 vs. L0 and L2 vs. L1 are shown in **Supplementary Additional File 4**. Firstly, the most significantly upregulated pathways in L1 compared to L0 are "glycerolipid metabolism," "alpha-Linolenic acid metabolism," "fatty acid degradation," "cutin, suberine and wax biosynthesis," and "plant-pathogen interaction." The former four pathways belong to lipid metabolism which is likely relevant to the cuticular lipids biosynthesis of the cell wall (Reina-Pinto and Yephremov, 2009). In contrast, the most significantly downregulated pathways in L1 compared to L0 are ribosome and ribosome biogenesis in eukaryotes. Secondly, compared with L1, the pathways of the ribosome and ribosome biogenesis in eukaryotes were upregulated in L2, whereas pathways such as alpha-Linolenic acid metabolism,

glycerolipid metabolism, and plant hormone signal transduction were downregulated in L2.

Differentially Expressed Genes Related to Zn Transporters and Metal Chelating Ligands

After entering the leaf, the transmembrane transport of Zn is regulated by Zn transporters. A total of 173 genes belonging to the following nine groups of Zn transporters were found in the DEGs: ATP binding cassette (ABC) transporters, heavy metal-associated isoprenylated protein (HIPP), protein DETOXIFICATION (DTX), yellow stripe-like transporter (YSL), the ZRT/IRT-like protein (ZIP), pleiotropic drug resistance protein (PDR), metal tolerance proteins (MTP), heavy metal ATPase (HMA), and natural resistance-associated macrophage protein (NRAMP) (**Figure 5A**; the full list appears in **Supplementary Additional File 5**). Of the nine groups, ABC (43.3%), HIPP (22.5%), and DTX (14.5%) accounted for 80.3%, as shown by the expression heatmap (**Figure 5B**).

Previous studies have shown that when $ZnSO_4$ is applied, the Zn is absorbed as Zn^{2+} (Li et al., 2018b). In contrast, Zn is present mainly in chelated forms within plant tissues given that high concentrations of Zn^{2+} are harmful to the plant's normal metabolism (Sinclair and Krämer, 2012). In this regard, the present study identified eight groups of metal chelating ligand genes in the DEGs among the three samples, including genes related to cysteine, glutathione, heat shock protein (HSP), histidine, pectin, methionine, citrate, and metallothionein (MT) (**Figure 6A** and **Supplementary Additional File 6**). There was a total of 216 DEGs, of which genes related to cysteine accounted for 30.6%, while genes related to glutathione and heat shock protein (HSP) both accounted for 23.7%, suggesting that these three groups of chelating ligand played important roles in chelating the foliar absorbed Zn^{2+} in the leaf. The gene expression heatmap of the three groups is shown in **Figure 6B**.

DISCUSSION

Distribution of Zn in Sunflower Leaves Following Foliar Zn Application

To explore the translocation of Zn following its foliar absorption in sunflower, the present study initially examined changes in the concentration and distribution of Zn within sunflower leaves following its foliar application. Firstly, bulk analyses of leaf Zn concentrations showed that foliar application of Zn for 0.5 h before being removed increased the leaf Zn concentration from ca. 90 mg kg^{-1} to ca. 600 mg kg^{-1}, with no marked changes in these concentrations in subsequent 7 days (**Figure 1**). Next, to examine changes in the distribution of the Zn within the sunflower leaf, synchrotron-based XFM was used for *in situ* analyses. It was found that the Zn within the interveinal leaf areas was gradually translocated into the veins, especially during the first 6 h (**Figure 2**). Furthermore, XFM analysis of the Zn distribution in leaf cross-sections showed that the Zn in the upper epidermal layer was quickly moved to the lower epidermis, with these epidermal layers being the main site for Zn accumulation within the first 3 h following foliar Zn application. Combining these observations with the findings in Li et al. (2019), who showed that foliar-absorbed Zn was located in the apoplast of the epidermal cells and that the BSEs are important in Zn translocation in sunflower leaves, it is likely that this Zn that is accumulating in the epidermal cells is also likely to be in the apoplast, and that the movement of the Zn between the epidermal layers is likely *via* the BSEs. When examined at a period of 24 h after the foliar application of the Zn, much of the Zn had moved from the epidermal layers to the inner vascular tissues, especially the horizontal BSEs (**Figure 3**). Our observation that the majority of the Zn remained within the leaf over a period of 7 days (as opposed to being translocated to other tissues) is in accordance with previous studies which found that the foliar absorbed Zn has limited mobility in plants (Zhang and Brown, 1999; Du et al., 2015). Regardless, we show here that although there is only limited translocation out of the leaf, the distribution of the Zn within the leaf changes markedly following its absorption—the absorbed Zn initially moved from the upper epidermis to the lower epidermis, before gradually moving to the horizontal BSEs and veins (**Figures 2**, **3**).

Leaf Gene Expression During Zn Translocation Process and Implications for Foliar $ZnSO_4$ Application

Not only did we examine changes in Zn distribution in leaves following its foliar application, but we also examined corresponding changes in leaf gene expression. It was found that genes related to stress response were upregulated rapidly following the 0.5 h foliar $ZnSO_4$ application, including GO terms of response to wounding and protein ubiquitination (Dametto et al., 2015) and the KEGG pathway of plant-pathogen interaction. Furthermore, the mitogen-activated protein kinase (MAPK) signaling pathway was upregulated, and stress-related responses including leaf cell wall reinforcement and lipid metabolism were also significantly upregulated (**Supplementary Additional Files 3**, **4**). In contrast, GO terms of translation, structural constituent of ribosome, and protein transport, were downregulated in L1 compared to L0, suggesting that the essential metabolic activity of the leaf had been impaired. These various observations suggest that the foliar application of Zn caused a stress reaction to the leaf. We have previously found that when $ZnSO_4$ is applied to the leaf surface, the Zn enters the leaf as Zn^{2+} (Li et al., 2018a), but it is known that high concentrations of free Zn^{2+} within the leaf can cause toxicity due to the high affinity of Zn^{2+} for numerous proteins, with this resulting in metabolic disorders (Hessels and Merkx, 2015). Hence, it is likely that the stress observed in the present study following the foliar application of Zn likely resulted from the sudden fourfold increase in leaf Zn concentration following foliar application (**Figure 1**). Indeed, similar results were reported by Li et al. (2021) who found that the genes relevant to "response to wounding" in the NGTs of sunflower leaf were also significantly upregulated after foliar Zn application, suggesting that the foliar Zn application caused abiotic stress to the plant. This finding

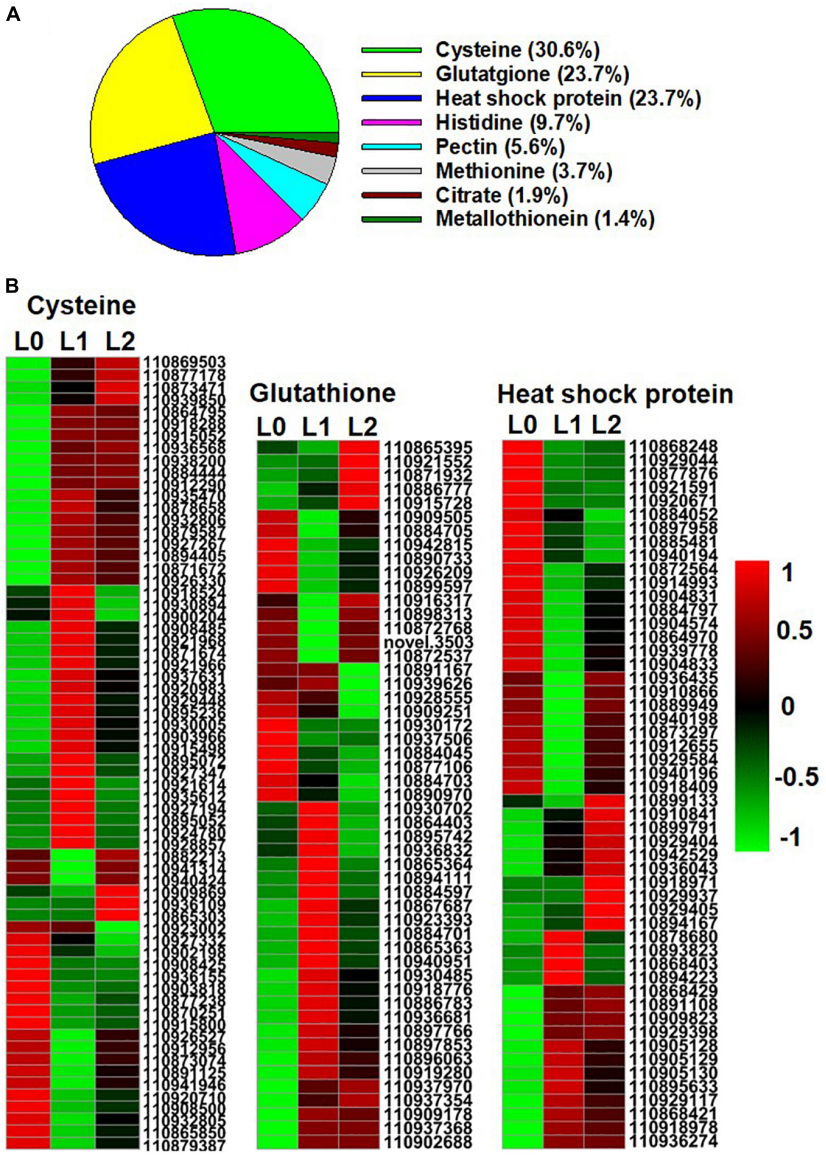

FIGURE 6 | Genes of Zn metal chelating ligands identified from the DEGs of the sunflower leaves. L0 = control leaves without Zn, L1 = leaves to which Zn was applied for 0.5 h before being removed and then harvested immediately, and L2 = leaves to which Zn was applied for 0.5 h before being removed and then left for 24 h before being harvested. **(A)** The proportion of genes of the eight group metal chelating ligands in the DEGs of the three samples. **(B)** Gene expression heatmap of the DEGs in cysteine, glutathione, and heat shock protein. Scale bar in B indicates a normalized FPKM value of genes.

is also in agreement with previous studies that have reported that lower Zn application rates can result in higher efficiencies and that higher application rates can cause localized toxicity (Doolette et al., 2020).

Although the foliar application of Zn caused a toxic response, this stress was only temporary—the stress-relevant GO terms which were upregulated rapidly after Zn application (L1) were subsequently downregulated after 24 h (L2), while those that were downregulated in L1 were upregulated in L2 (**Supplementary Additional File 3**). Accordingly, Zn was found mainly in the epidermal layers (including the NGTs) in the first 3 h (**Figure 3**), with this likely being a detoxification strategy (Frey et al., 2000; Tappero et al., 2007; Horeth et al., 2020; Li et al., 2021). In contrast, after 24 h, much of the Zn had moved to the horizontal BSEs and the veins. This stress alleviation was also related to Zn transporters and chelating ligands. For example, the ABC transporters (43.4%), HIPP (22.5%), and DTX (14.5%) have been previously reported to be related to the alleviation of Zn and Cd stress (Moons, 2003; Dong et al., 2019; Manara et al., 2020), with ABC transporters playing a role in the compartmentalization of excess metals in vacuoles (Sharma et al., 2016). Furthermore, of the eight groups of chelating ligands, heat shock protein (23.7%) is also related to metal stress alleviation (Hasan et al., 2017). However, it must be noted that in the

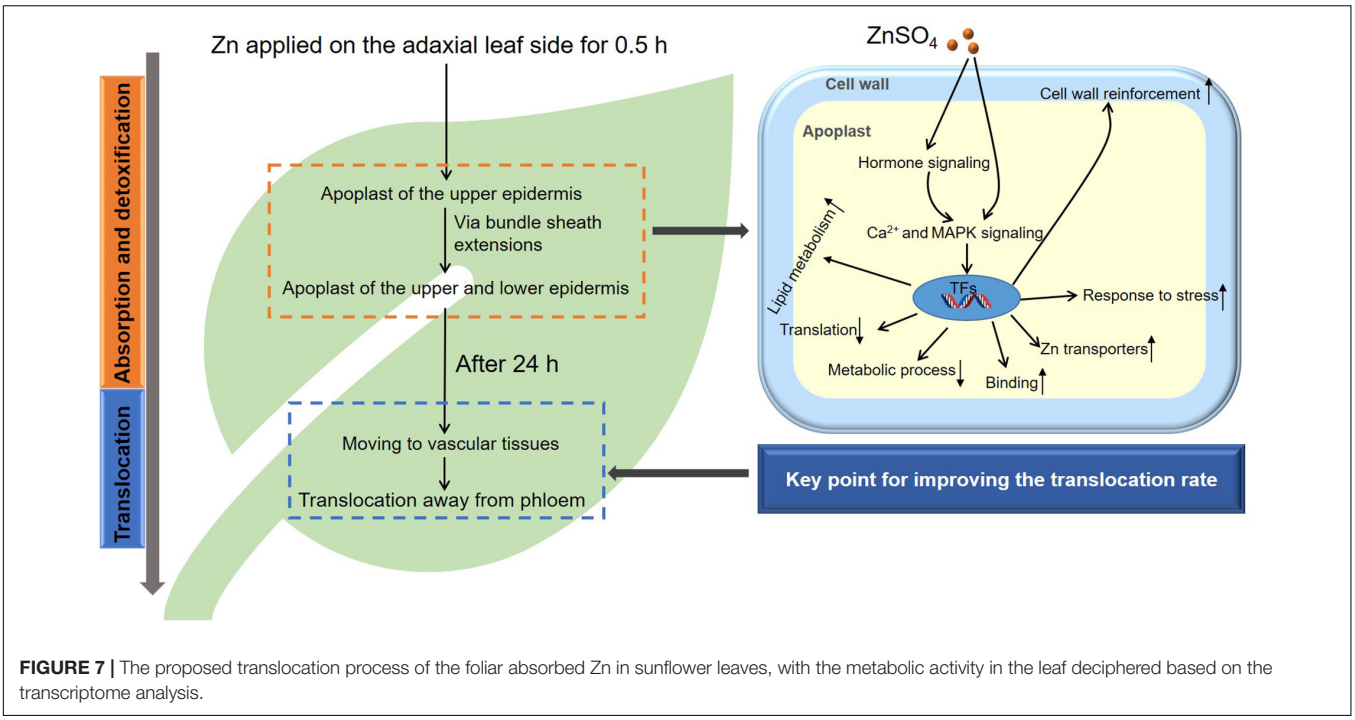

FIGURE 7 | The proposed translocation process of the foliar absorbed Zn in sunflower leaves, with the metabolic activity in the leaf deciphered based on the transcriptome analysis.

present study, Zn was applied to the leaves for only 0.5 h, and it is likely that a longer application time would result in increased absorption of Zn, and hence the resulting stress would presumably be prolonged. Therefore, care must be taken when devising a foliar fertilization regime to avoid causing severe leaf stress.

Given that the Zn was applied as $ZnSO_4$, it is likely that the SO_4^{2-} also entered the leaves. In this regard, it is known that S that is foliar-applied can be metabolized into cystine, methionine, and glutathione (Legris-Delaporte et al., 1987; Landry et al., 1991), and it is known that foliar application of S can be helpful for plant tolerance against heat stress (Waraich et al., 2022) and that root uptake of S can mitigate Cd toxicity (Adhikari et al., 2018). Hence, in the present study, changes in the leaf gene expression are due to both the Zn^{2+} and the SO_4^{2-}, although the effects of SO_4^{2-} are unclear (i.e., whether it contributed to the stress or whether it assisted in alleviating the stress caused by Zn).

Reasons for Limited Translocation of the Foliar Absorbed Zn and New Insights for Improving the Efficiency of Foliar Zn Fertilizer

The present study found that little of the foliar absorbed Zn moved out of the leaf to which it has been applied, even within 7 days (**Figure 1**), *in situ* analyses showed that the Zn appears to be mobile within the leaf, with the Zn found within the vascular tissues after 24 h (**Figures 1–3**). It has previously been hypothesized that the limited translocation of Zn out of the leaf is due to the binding of Zn to the epidermal cell wall, with this restricting further redistribution (Du et al., 2015). However, our results demonstrate that the main reason for the limited mobility of Zn is related to the translocation of Zn in vascular tissues. In this regard, the xylem is unlikely to be involved in Zn translocation from the leaf given that the xylem is for the upward movement of water and nutrients from roots to shoots, while the phloem is responsible for both the upwards and downwards movement of solutes. Indeed, it was found in wheat (*Triticum aestivum*) (Haslett et al., 2001) and citrus (*Citrus reticulatus*) (Du et al., 2020) that the translocation of the foliar absorbed nutrients occurred *via* the phloem. Tian et al. (2015) also reported for sunflower that foliar absorbed Zn was translocated within the phloem. Thus, it seems likely that the loading of Zn into the phloem, or the low mobility of Zn within the phloem itself, are responsible for the limited translocation of the foliar absorbed Zn in plants.

In this regard, the loading of Zn into the phloem requires Zn transporters, with the mobility of Zn within the phloem being influenced by Zn speciation (Ricachenevsky et al., 2015; Nozoye, 2018). The Zn transporters in sunflowers have not received much attention, with Huang et al. (2021) reporting that some HMA and MTP genes are involved in the Zn translocation in seeds of sunflowers. Of the DEGs related to Zn transporters in sunflower leaves, *HMA3* (gene ID: 110878461) was significantly upregulated in L1 and L2 compared to L0, and hence it could potentially play a role in the translocation of Zn into the vacuoles for detoxification, as discussed for other plant species (Cai et al., 2019); In contrast, *NRAMP3* (gene ID: 110889223) was downregulated in L1 compared to L0 which could be involved in the Zn translocation out of the vacuoles (Thomine et al., 2003); and *YSL1* (gene ID: 110924134) was downregulated in L1 while upregulated in L2 which could be related to Zn loading into the vascular tissues (Sinclair and Krämer, 2012; **Supplementary Additional File 5**). In addition,

of the eight groups of metal-chelating ligands identified from the DEGs among L0, L1, and L2, cysteine and glutathione were the two main groups (**Figure 6**). This observation suggests that cysteine and glutathione may be important in chelating Zn^{2+} in sunflower leaves and that their increase in the leaf might enhance the translocation of the foliar absorbed Zn (Palmer and Stangoulis, 2018; Nakamura et al., 2019; Wongkaew et al., 2019). In order to improve the efficiency of foliar Zn fertilizers, future studies should investigate which Zn transporters are involved in the Zn translocation in leaves and what Zn speciation favors Zn translocation in the leaves.

A New Methodological System for Studying Element Translocation in Plant

Our combined use of XFM together with transcriptome analysis illustrates the ability of this methodological platform to allow the systemic study of nutrient translocation in plants. Given that changes in gene expression can be rapid and XFM can provide *in situ* elemental imaging at high temporal and spatial resolutions, this system can provide information on the physiological behavior coupled with molecular activity. Such information is important in bridging the phenotype to the genotype gap.

Translocation of the Foliar Absorbed Zn in Sunflower Leaves

In conclusion, we found that foliar application of Zn caused rapid stress to the sunflower leaf, with the foliar Zn absorption process accompanied by the detoxification process (**Figure 7**). Correspondingly, Zn was initially presented in the apoplast of the upper and lower epidermal layers (including in the NGTs) as a detoxification strategy, and genes within the leaves involved in cell wall reinforcement, response to stress, and Zn transporters were upregulated to address this stress (**Figures 2**, **3**, **7** and **Table 1**). After this stress receded, Zn was gradually moved to the vascular tissues, and the further translocation was likely *via* the phloem. It seems that the limited translocation of Zn in the phloem (for example, limited loading into the phloem, or limited mobility in the phloem) was the key reason for the restricted translocation of the foliar absorbed Zn in leaves of sunflower.

DATA AVAILABILITY STATEMENT

All data supporting the findings of this study are available within the paper, the supplementary information and additional file published online. The RNA sequencing data can be found in NCBI database (accession: PRJNA723486).

AUTHOR CONTRIBUTIONS

CL: conceptualization, data curation, formal analysis, investigation, methodology, writing—original draft, review and editing, and funding acquisition. LiW: formal analysis, investigation, and methodology. JW and FB: investigation, methodology, and writing—review and editing. NW, YC, YY, and LeW: methodology. DP: resources and methodology. TR, PW, and EL: writing—review and editing. YW: funding acquisition, supervision, and writing—review and editing. PK: conceptualization, data curation, formal analysis, investigation, methodology, writing original draft and review and editing, funding acquisition, and supervision. All authors contributed to the article and approved the submitted version.

FUNDING

This work was supported by the China Postdoctoral Science Foundation Grant (2019M663825), the National Natural Science Foundation of China (NSFC, 32101838), and the Science Foundation for Youths of Shaanxi Province (2021JQ-097). Support was also provided to CL through the International Postdoctoral Exchange Fellowship Program (YJ20190217, Talent-Introduction Program) and the Fundamental Research Funds for the Central Universities (D5000210898).

ACKNOWLEDGMENTS

Part of the experiment was undertaken on the XFM beamline at the Australian Synchrotron, part of ANSTO. We thank the Australian Synchrotron for the beamtime and technical assistance. We also acknowledge the use of the facilities and technical assistance of the Analytical & Testing Centre of Northwestern Polytechnical University. We also would like to thank the reviewers for their valuable suggestions and careful reading of the manuscript.

SUPPLEMENTARY MATERIAL

The Supplementary Material for this article can be found online at: https://www.frontiersin.org/articles/10.3389/fpls.2022.757048/full#supplementary-material

Supplementary Additional File 5 | List of the zinc (Zn) transporter genes identified from the DEGs.

Supplementary Additional File 6 | List of the metal-chelating ligand genes identified from the DEGs.

REFERENCES

Adhikari, S., Ghosh, S., Azahar, I., Adhikari, A., Shaw, A. K., Konar, S., et al. (2018). Sulfate improves cadmium tolerance by limiting cadmium accumulation, modulation of sulfur metabolism and antioxidant defense system in maize. *Environ. Exp. Bot.* 153, 143–162. doi: 10.1016/j.envexpbot.2018.05.008

Badouin, H., Gouzy, J., Grassa, C. J., Murat, F., Staton, S. E., Cottret, L., et al. (2017). The sunflower genome provides insights into oil metabolism, flowering and Asterid evolution. *Nature* 546, 148–152. doi: 10.1038/nature22380

Blamey, F. P. C., Paterson, D. J., Walsh, A., Afshar, N., McKenna, B. A., Cheng, M., et al. (2018). Time-resolved X-ray fluorescence analysis of element distribution and concentration in living plants: an example using manganese toxicity in

cowpea leaves. *Environ. Exp. Bot.* 156, 151–160. doi: 10.1016/j.envexpbot.2018.09.002

Cai, H., Huang, S., Che, J., Yamaji, N., and Ma, J. F. (2019). The tonoplast-localized transporter OsHMA3 plays an important role in maintaining Zn homeostasis in rice. *J. Exp. Bot.* 70, 2717–2725. doi: 10.1093/jxb/erz091

Dametto, A., Buffon, G., dos Reis Blasi, E. A., and Sperotto, R. A. (2015). Ubiquitination pathway as a target to develop abiotic stress tolerance in rice. *Plant Signal. Behav.* 10:e1057369. doi: 10.1080/15592324.2015.1057369

Dong, B., Niu, L., Meng, D., Song, Z., Wang, L., Jian, Y., et al. (2019). Genome-wide analysis of MATE transporters and response to metal stress in *Cajanus cajan*. *J. Plant Interact.* 14, 265–275. doi: 10.1080/17429145.2019.1620884

Doolette, C. L., Read, T. L., Howell, N. R., Cresswell, T., and Lombi, E. (2020). Zinc from foliar-applied nanoparticle fertiliser is translocated to wheat grain: a ^{65}Zn radiolabelled translocation study comparing conventional and novel foliar fertilisers. *Sci. Total Environ.* 749:142369. doi: 10.1016/j.scitotenv.2020.142369

Doolette, C. L., Read, T. L., Li, C., Scheckel, K. G., Donner, E., Kopittke, P. M., et al. (2018). Foliar application of zinc sulphate and zinc EDTA to wheat leaves: differences in mobility, distribution, and speciation. *J. Exp. Bot.* 69, 4469–4481. doi: 10.1093/jxb/ery236

Du, W., Pan, Z. Y., Hussain, S. B., Han, Z. X., Peng, S. A., and Liu, Y. Z. (2020). Foliar Supplied Boron Can Be Transported to Roots as a Boron-Sucrose Complex via Phloem in Citrus Trees. *Front. Plant Sci.* 11:250. doi: 10.3389/fpls.2020.00250

Du, Y., Kopittke, P. M., Noller, B. N., James, S. A., Harris, H. H., Xu, Z. P., et al. (2015). *In situ* analysis of foliar zinc absorption and short-distance movement in fresh and hydrated leaves of tomato and citrus using synchrotron-based X-ray fluorescence microscopy. *Ann. Bot.* 115, 41–53. doi: 10.1093/aob/mcu212

Fernandez, P., Di Rienzo, J., Fernandez, L., Hopp, H. E., Paniego, N., and Heinz, R. A. (2008). Transcriptomic identification of candidate genes involved in sunflower responses to chilling and salt stresses based on cDNA microarray analysis. *BMC Plant Biol.* 8:11. doi: 10.1186/1471-2229-8-11

Fernández, V., and Brown, P. H. (2013). From plant surface to plant metabolism: the uncertain fate of foliar-applied nutrients. *Front. Plant Sci.* 4:289. doi: 10.3389/fpls.2013.00289

Frey, B., Keller, C., and Zierold, K. (2000). Distribution of Zn in functionally different leaf epidermal cells of the hyperaccumulator *Thlaspi caerulescens*. *Plant Cell Environ.* 23, 675–687. doi: 10.1046/j.1365-3040.2000.00590.x

Fu, X. Z., Xing, F., Cao, L., Chun, C. P., Ling, L. L., Jiang, C. L., et al. (2016). Effects of Foliar Application of Various Zinc Fertilizers with Organosilicone on Correcting Citrus Zinc Deficiency. *Hortscience* 51, 422–426. doi: 10.21273/HORTSCI.51.4.422

Hasan, M. K., Cheng, Y., Kanwar, M. K., Chu, X.-Y., Ahammed, G. J., and Qi, Z.-Y. (2017). Responses of Plant Proteins to Heavy Metal Stress—A Review. *Front. Plant Sci.* 8:1492. doi: 10.3389/fpls.2017.01492

Haslett, B. S., Reid, R. J., and Rengel, Z. (2001). Zinc mobility in wheat: uptake and distribution of Zinc applied to leaves or roots. *Ann. Bot.* 87, 379–386. doi: 10.1006/anbo.2000.1349

Hessels, A. M., and Merkx, M. (2015). Genetically-encoded FRET-based sensors for monitoring Zn^{2+} in living cells. *Metallomics* 7, 258–266. doi: 10.1039/c4mt00179f

Horeth, S., Pongrac, P., van Elteren, J. T., Debeljak, M., Vogel-Mikus, K., Weber, M., et al. (2020). *Arabidopsis halleri* shows hyperbioindicator behaviour for Pb and leaf Pb accumulation spatially separated from Zn. *New Phytol.* 226, 492–506. doi: 10.1111/nph.16373

Howard, D. L., de Jonge, M. D., Afshar, N., Ryan, C. G., Kirkham, R., Reinhardt, J., et al. (2020). The XFM beamline at the Australian Synchrotron. *J. Synchrotron Radiat.* 27, 1447–1458. doi: 10.1107/S1600577520010152

Huang, Y. T., Cai, S. Y., Ruan, X. L., Chen, S. Y., Mei, G. F., Ruan, G. H., et al. (2021). Salicylic acid enhances sunflower seed germination under Zn^{2+} stress via involvement in Zn^{2+} metabolic balance and phytohormone interactions. *Sci. Hortic.* 275:109702. doi: 10.1016/j.scienta.2020.109702

Joy, E. J., Stein, A. J., Young, S. D., Ander, E. L., Watts, M. J., and Broadley, M. R. (2015). Zinc-enriched fertilisers as a potential public health intervention in Africa. *Plant Soil* 389, 1–24. doi: 10.1007/s11104-015-2430-8

Kopittke, P. M., Lombi, E., van der Ent, A., Wang, P., Laird, J. S., Moore, K. L., et al. (2020). Methods to Visualize Elements in Plants. *Plant Physiol.* 182, 1869–1882. doi: 10.1104/pp.19.01306

Kopittke, P. M., Menzies, N. W., de Jonge, M. D., McKenna, B. A., Donner, E., Webb, R. I., et al. (2011). *In situ* distribution and speciation of toxic copper, nickel, and zinc in hydrated roots of cowpea. *Plant Physiol.* 156, 663–673. doi: 10.1104/pp.111.173716

Landry, J., Legris-Delaporte, S., and Ferron, F. (1991). Foliar application of elemental sulphur on metabolism of sulphur and nitrogen compounds in leaves of sulphur-deficient wheat. *Phytochemistry* 30, 729–732. doi: 10.1016/0031-9422(91)85242-R

Legris-Delaporte, S. P., Ferron, F. O., Landry, J., and Costes, C. (1987). Metabolization of elemental sulfur in wheat leaves consecutive to its foliar application. *Plant Physiol.* 85, 1026–1030. doi: 10.1104/pp.85.4.1026

Li, C., Wang, P., Lombi, E., Cheng, M., Tang, C., Howard, D. L., et al. (2018a). Absorption of foliar-applied Zn fertilizers by trichomes in soybean and tomato. *J. Exp. Bot.* 69, 2717–2729. doi: 10.1093/jxb/ery085

Li, C., Wang, P., Lombi, E., Wu, J., Blamey, F. P. C., Fernández, V., et al. (2018b). Absorption of foliar applied Zn is decreased in Zn deficient sunflower (*Helianthus annuus*) due to changes in leaf properties. *Plant Soil* 433, 309–322. doi: 10.1007/s11104-018-3841-0

Li, C., Wang, P., Menzies, N. W., Lombi, E., and Kopittke, P. M. (2017). Effects of changes in leaf properties mediated by methyl jasmonate (MeJA) on foliar absorption of Zn, Mn and Fe. *Ann. Bot.* 120, 405–415. doi: 10.1093/aob/mcx063

Li, C., Wang, P., van der Ent, A., Cheng, M., Jiang, H., Lund Read, T., et al. (2019). Absorption of foliar-applied Zn in sunflower (*Helianthus annuus*): importance of the cuticle, stomata and trichomes. *Ann. Bot.* 123, 57–68. doi: 10.1093/aob/mcy135

Li, C., Wu, J., Blamey, F. P. C., Wang, L., Zhou, L., Paterson, D. J., et al. (2021). Non-glandular trichomes of sunflower are important in the absorption and translocation of foliar-applied Zn. *J. Exp. Bot.* 72, 5079–5092. doi: 10.1093/jxb/erab180

Livak, K. J., and Schmittgen, T. D. (2001). Analysis of relative gene expression data using real-time quantitative PCR and the $2^{-\Delta\Delta CT}$ method. *Methods* 25, 402–408. doi: 10.1006/meth.2001.1262

Lopez-Casado, G., Urbanowicz, B. R., Damasceno, C. M. B., and Rose, J. K. C. (2008). Plant glycosyl hydrolases and biofuels: a natural marriage. *Curr. Opin. Plant Biol.* 11, 329–337. doi: 10.1016/j.pbi.2008.02.010

Manara, A., Fasani, E., Molesini, B., DalCorso, G., Pennisi, F., Pandolfini, T., et al. (2020). The Tomato Metallocarboxypeptidase Inhibitor I, which Interacts with a Heavy Metal-Associated Isoprenylated Protein, Is Implicated in Plant Response to Cadmium. *Molecules* 25:700. doi: 10.3390/molecules25030700

Menguer, P. K., Vincent, T., Miller, A. J., Brown, J. K. M., Vincze, E., Borg, S., et al. (2018). Improving zinc accumulation in cereal endosperm using HvMTP1, a transition metal transporter. *Plant Biotechnol. J.* 16, 63–71. doi: 10.1111/pbi.12749

Moons, A. (2003). *Ospdr9*, which encodes a PDR-type ABC transporter, is induced by heavy metals, hypoxic stress and redox perturbations in rice roots. *FEBS Lett.* 553, 370–376. doi: 10.1016/s0014-5793(03)01060-3

Nakamura, S. I., Wongkaew, A., Nakai, Y., Rai, H., and Ohkama-Ohtsu, N. (2019). Foliar-applied glutathione activates zinc transport from roots to shoots in oilseed rape. *Plant Sci.* 283, 424–434. doi: 10.1016/j.plantsci.2018.10.018

Nautiyal, A. K., Gani, U., Sharma, P., Kundan, M., Fayaz, M., Lattoo, S. K., et al. (2020). Comprehensive transcriptome analysis provides insights into metabolic and gene regulatory networks in trichomes of *Nicotiana tabacum*. *Plant Mol. Biol.* 102, 625–644. doi: 10.1007/s11103-020-00968-2

Nozoye, T. (2018). The nicotianamine synthase gene is a useful candidate for improving the nutritional qualities and Fe-deficiency tolerance of various crops. *Front. Plant Sci.* 9:340. doi: 10.3389/fpls.2018.00340

Palmer, L. J., and Stangoulis, J. C. R. (2018). Changes in the elemental and metabolite profile of wheat phloem sap during grain filling indicate a dynamic between plant maturity and time of day. *Metabolites* 8:53. doi: 10.3390/metabo8030053

Paterson, D., De Jonge, M., Howard, D., Lewis, W., McKinlay, J., Starritt, A., et al. (2011). "The X-ray fluorescence microscopy beamline at the Australian Synchrotron," in *The 10th International Conference on X-ray Microscopy*, (New York: AIP Publishing), 219–222. doi: 10.1063/1.3625343

Ramu, V. S., Paramanantham, A., Ramegowda, V., Mohan-Raju, B., Udayakumar, M., and Senthil-Kumar, M. (2016). Transcriptome analysis of sunflower genotypes with contrasting oxidative stress tolerance reveals individual-

and combined- biotic and abiotic stress tolerance mechanisms. *PLoS One* 11:e0157522. doi: 10.1371/journal.pone.0157522

Reina-Pinto, J. J., and Yephremov, A. (2009). Surface lipids and plant defenses. *Plant Physiol. Biochem.* 47, 540–549. doi: 10.1016/j.plaphy.2009.01.004

Reuveni, R., Agapov, V., Reuveni, M., and Raviv, M. (1994). Effects of foliar sprays of phosphates on powdery mildew (*Sphaerotheca pannosa*) of roses. *J. Phytopathol.* 142, 331–337. doi: 10.1111/j.1439-0434.1994.tb04547.x

Ricachenevsky, F. K., Menguer, P. K., Sperotto, R. A., and Fett, J. P. (2015). Got to hide your Zn away: molecular control of Zn accumulation and biotechnological applications. *Plant Sci.* 236, 1–17. doi: 10.1016/j.plantsci.2015.03.009

Ryan, C. (2000). Quantitative trace element imaging using PIXE and the nuclear microprobe. *Int. J. Imaging Syst. Technol.* 11, 219–230. doi: 10.1002/ima.1007

Ryan, C., and Jamieson, D. (1993). Dynamic analysis: on-line quantitative PIXE microanalysis and its use in overlap-resolved elemental mapping. *Nucl. Instrum. Methods Phys. Res. B* 77, 203–214. doi: 10.1016/0168-583X(93)95545-G

Sharma, S. S., Dietz, K.-J., and Mimura, T. (2016). Vacuolar compartmentalization as indispensable component of heavy metal detoxification in plants. *Plant Cell Environ.* 39, 1112–1126. doi: 10.1111/pce.12706

Sinclair, S. A., and Krämer, U. (2012). The zinc homeostasis network of land plants. *Biochim. Biophys. Acta* 1823, 1553–1567. doi: 10.1016/j.bbamcr.2012.05.016

Tappero, R., Peltier, E., Graefe, M., Heidel, K., Ginder-Vogel, M., Livi, K. J. T., et al. (2007). Hyperaccumulator Alyssum murale relies on a different metal storage mechanism for cobalt than for nickel. *New Phytol.* 175, 641–654. doi: 10.1111/j.1469-8137.2007.02134.x

Thomine, S., Lelièvre, F., Debarbieux, E., Schroeder, J. I., and Barbier-Brygoo, H. (2003). AtNRAMP3, a multispecific vacuolar metal transporter involved in plant responses to iron deficiency. *Plant J.* 34, 685–695. doi: 10.1046/j.1365-313X.2003.01760.x

Tian, S., Lu, L., Xie, R., Zhang, M., Jernstedt, J., Hou, D., et al. (2015). Supplemental macronutrients and microbial fermentation products improve the uptake and transport of foliar applied zinc in sunflower (*Helianthus annuus* L.) plants. Studies utilizing micro X-ray florescence. *Front. Plant Sci.* 5:808. doi: 10.3389/fpls.2014.00808

Vu, D. T., Huang, L., Nguyen, A., Du, Y., Xu, Z., Hampton, M. A., et al. (2013). Quantitative methods for estimating foliar uptake of zinc from suspension-based Zn chemicals. *J. Plant Nutr. Soil Sci.* 176, 764–775. doi: 10.1002/jpln.201200407

Waraich, E. A., Hussain, A., Ahmad, Z., Ahmad, M., and Barutcular, C. (2022). Foliar application of sulfur improved growth, yiled and physiological attributes of canola (*brassica napus* L.) under heat stress conditions. *J. Plant Nutr.* 45, 369–379. doi: 10.1080/01904167.2021.1985138

Wongkaew, A., Nakamura, S.-I., Suzui, N., Yin, Y.-G., Ishii, S., Kawachi, N., et al. (2019). Elevated glutathione synthesis in leaves contributes to zinc transport from roots to shoots in *Arabidopsis*. *Plant Sci.* 283, 416–423. doi: 10.1016/j.plantsci.2018.11.003

Wu, C.-Y., Lu, L.-L., Yang, X.-E., Feng, Y., Wei, Y.-Y., Hao, H.-L., et al. (2010). Uptake, translocation, and remobilization of zinc absorbed at different growth stages by rice genotypes of different zn densities. *J. Agric. Food Chem.* 58, 6767–6773. doi: 10.1021/jf100017e

Xia, H., Wang, L., Qiao, Y., Kong, W., Xue, Y., Wang, Z., et al. (2020). Elucidating the source-sink relationships of zinc biofortification in wheat grains: a review. *Food Energy Secur.* 9:e243. doi: 10.1002/fes3.243

Xie, R., Zhao, J., Lu, L., Ge, J., Brown, P. H., Wei, S., et al. (2019). Efficient phloem remobilization of Zn protects apple trees during the early stages of Zn deficiency. *Plant Cell Environ.* 42, 3167–3181. doi: 10.1111/pce.13621

Xue, Y.-F., Xia, H.-Y., McGrath, S. P., Shewry, P. R., and Zhao, F.-J. (2015). Distribution of the stable isotopes ^{57}Fe and ^{68}Zn in grain tissues of various wheat lines differing in their phytate content. *Plant Soil* 396, 73–83. doi: 10.1007/s11104-015-2582-6

Zhang, Q., and Brown, P. H. (1999). Distribution and transport of foliar applied zinc in pistachio. *J. Am. Soc. Hortic. Sci.* 124, 433–436. doi: 10.21273/JASHS.124.4.433

Zhang, T., Sun, H., Lv, Z., Cui, L., Mao, H., and Kopittke, P. M. (2018). Using synchrotron-based approaches to examine the foliar application of $ZnSO_4$ and ZnO nanoparticles for field-grown winter wheat. *J. Agric. Food Chem.* 66, 2572–2579. doi: 10.1021/acs.jafc.7b04153

Conflict of Interest: The authors declare that the research was conducted in the absence of any commercial or financial relationships that could be construed as a potential conflict of interest.

Publisher's Note: All claims expressed in this article are solely those of the authors and do not necessarily represent those of their affiliated organizations, or those of the publisher, the editors and the reviewers. Any product that may be evaluated in this article, or claim that may be made by its manufacturer, is not guaranteed or endorsed by the publisher.

frontiers | Frontiers in Plant Science

REVIEW
published: 19 April 2022
doi: 10.3389/fpls.2022.840941

Stable Isotope Fractionation of Metals and Metalloids in Plants: A Review

Matthias Wiggenhauser[1]†, Rebekah E. T. Moore[2]*†, Peng Wang[3], Gerd Patrick Bienert[4], Kristian Holst Laursen[5] and Simon Blotevogel[6]*

[1]Group of Plant Nutrition, Department of Environmental System Science, Institute of Agricultural Sciences, ETH Zurich, Zurich, Switzerland, [2]MAGIC Group, Department of Earth Science and Engineering, Imperial College London, London, United Kingdom, [3]College of Resources and Environmental Sciences, Nanjing Agricultural University, Nanjing, China, [4]Crop Physiology, Molecular Life Sciences, Technical University of Munich, Freising, Germany, [5]Plant Nutrients and Food Quality Research Group, Plant and Soil Science Section and Copenhagen Plant Science Centre, Department of Plant and Environmental Sciences, Faculty of Science, University of Copenhagen, Copenhagen, Denmark, [6]Laboratoire Matériaux et Durabilité des Constructions (LMDC), UPS/INSA, Université Paul Sabatier - Toulouse III, Toulouse, France

OPEN ACCESS

Edited by:
Marc Hanikenne, University of Liège, Belgium

Reviewed by:
Stephan Clemens, University of Bayreuth, Germany
Maria Bernal, Ruhr University Bochum, Germany

***Correspondence:**
Matthias Wiggenhauser
matthias.wiggenhauser@usys.ethz.ch
Rebekah E. T. Moore
r.moore13@imperial.ac.uk

[†]These authors share first authorship

Specialty section:
This article was submitted to Plant Nutrition, a section of the journal Frontiers in Plant Science

Received: *21 December 2021*
Accepted: *17 February 2022*
Published: *19 April 2022*

Citation:
Wiggenhauser M, Moore RET, Wang P, Bienert GP, Laursen KH and Blotevogel S (2022) Stable Isotope Fractionation of Metals and Metalloids in Plants: A Review. Front. Plant Sci. 13:840941. doi: 10.3389/fpls.2022.840941

This work critically reviews stable isotope fractionation of essential (B, Mg, K, Ca, Fe, Ni, Cu, Zn, Mo), beneficial (Si), and non-essential (Cd, Tl) metals and metalloids in plants. The review (i) provides basic principles and methodologies for non-traditional isotope analyses, (ii) compiles isotope fractionation for uptake and translocation for each element and connects them to physiological processes, and (iii) interlinks knowledge from different elements to identify common and contrasting drivers of isotope fractionation. Different biological and physico-chemical processes drive isotope fractionation in plants. During uptake, Ca and Mg fractionate through root apoplast adsorption, Si through diffusion during membrane passage, Fe and Cu through reduction prior to membrane transport in strategy I plants, and Zn, Cu, and Cd through membrane transport. During translocation and utilization, isotopes fractionate through precipitation into insoluble forms, such as phytoliths (Si) or oxalate (Ca), structural binding to cell walls (Ca), and membrane transport and binding to soluble organic ligands (Zn, Cd). These processes can lead to similar (Cu, Fe) and opposing (Ca vs. Mg, Zn vs. Cd) isotope fractionation patterns of chemically similar elements in plants. Isotope fractionation in plants is influenced by biotic factors, such as phenological stages and plant genetics, as well as abiotic factors. Different nutrient supply induced shifts in isotope fractionation patterns for Mg, Cu, and Zn, suggesting that isotope process tracing can be used as a tool to detect and quantify different uptake pathways in response to abiotic stresses. However, the interpretation of isotope fractionation in plants is challenging because many isotope fractionation factors associated with specific processes are unknown and experiments are often exploratory. To overcome these limitations, fundamental geochemical research should expand the database of isotope fractionation factors and disentangle kinetic and equilibrium fractionation. In addition, plant growth studies should further shift toward hypothesis-driven experiments, for example, by integrating contrasting nutrient supplies, using established model plants, genetic approaches, and by combining isotope analyses

with complementary speciation techniques. To fully exploit the potential of isotope process tracing in plants, the interdisciplinary expertise of plant and isotope geochemical scientists is required.

Keywords: stable isotopes, fractionation, plant uptake, translocation, process tracing, multiple-collector-ICP-MS, metals, metalloids

INTRODUCTION

Stable isotopes are atoms with the same number of protons and electrons but a different number of neutrons and are considered stable if they do not undergo a measurable nuclear decay. Isotope fractionation describes small changes in the isotope composition (i.e., relative isotope abundances) during chemical reactions or physical processes. Isotope compositions of plant organs can provide a record of biological and physico-chemical processes that control an element's journey from their source to different organs, such as roots, leaves, and fruits. This information is complementary to organ-specific concentrations that provide information on element availability and utilization. This complementary information has been widely used for so-called "traditional isotopes" of, for example, H, C, N, O, and S to investigate for example water and fertilizer utilization, as well as nutrient assimilation (O'Leary et al., 1992; Tcherkez and Tea, 2013; Novak et al., 2019, 2021). Analytical advances during the past two decades now also allow the detection of naturally occurring variations of isotope compositions in plants for other, usually heavier elements (Hoefs, 2018), known as "non-traditional isotopes." Here, we critically review the fractionation of non-traditional stable isotopes to identify biological and physico-chemical processes that control the uptake and transport of these elements within plants (i.e., stable isotope process tracing). To this end, we: (i) provide interdisciplinary fundamentals on plant physiology and stable isotope process tracing, (ii) compile available data on isotope process tracing of B, Mg, Si, K, Ca, Fe, Ni, Cu, Zn, Mo, Cd, and Tl, (iii) interlink and discuss findings and approaches from the individual element reviews, and (iv) highlight best practices for data acquisition and interpretation, and define future research priorities. This review does not cover the use of non-traditional stable isotopes to trace the origin of elements (i.e., "source tracing") and to decipher complexation processes of elements onto soil components and thereby isotope fractionation between soil pools. Both topics have been reviewed recently (Komárek et al., 2021; Wang et al., 2021). Also beyond the scope of this review is the use of enriched stable isotopes as tracers to, for example, identify pathways of elements in plants (e.g., Yan et al., 2018). Finally, this review contributes to bridge plant science and isotope geochemistry by harmonizing nomenclature and working models of plant-based isotope studies to encourage interdisciplinary research and collaboration.

Non-traditional Isotopes: The Basics

In plants, isotope fractionation is usually mass-dependent (**Table 1**). Mass-dependent isotope effects are induced by slight differences of masses of distinct isotopes. Properties affected by the mass difference are velocities and diffusivities, as well as vibrational and rotational frequencies and thermodynamic energies (Dauphas and Schauble, 2016). Differences in vibrational frequencies are the most important factor, as they determine isotope fractionation during chemical reactions. The general theory of isotope fractionation has been extensively reviewed elsewhere (Fry, 2006; Hoefs, 2018). We use Ca as an example in the following paragraphs to illustrate the basics of non-traditional isotope fractionation in plants. Isotope compositions are governed by equilibrium and kinetic isotope fractionation (**Table 1**). Equilibrium fractionation can occur when, for example, Ca ions in the soil or nutrient solution sorb to the negatively charged root apoplast (Cobert et al., 2011). In this case, thermodynamic equilibrium is reached when the adsorption and desorption of Ca ions are equally likely and occur at the same rate. Importantly, at isotope equilibrium, the individual Ca isotope ratios (e.g., $^{44}Ca/^{40}Ca$) of the adsorbed and desorbed (i.e., dissolved) phase remain the same over time. At equilibrium conditions, the isotope fractionation depends on the mass difference of the isotopes and the stiffness of the bonds involved. Heavier isotopes preferentially go into stiffer bonds (higher spring constant of the bond, Bigeleisen, 1965). This effect is due to the larger mass-dependent difference in zero-point energy in stiffer bonds. In applied sciences, the stiffness of a bond is often approximated by the bond length or the thermodynamic stability of a chemical species.

If a system is not in thermodynamic equilibrium, kinetic processes control the isotope fractionation. For example, during the precipitation of Ca oxalate in plants (Cobert et al., 2011). Precipitation can induce kinetic isotope fractionation as long as the quantity of mineral Ca oxalate is increasing. At this stage, the forward reaction is quicker than the backward reaction (i.e., the dissolution of Ca oxalate) and favorably light isotopes precipitate into Ca oxalate. This is due to the slightly lower activation energy of lighter isotopes. When the amount of Ca oxalate remains constant, an (isotope) equilibrium between mineral and solution will be reached and the resulting isotope fractionation is governed by equilibrium fractionation. Note that chemical equilibrium is usually established faster than isotope equilibrium.

Isotope fractionation differs in closed and open systems, which can be defined using Rayleigh modeling (Fry, 2006). In closed systems, only negligible quantities of reactants or reaction products are added or removed from a system. For instance, a plant that preferentially takes up light Ca isotopes from a nutrient solution will deplete the nutrient solution of Ca and light Ca isotopes if the nutrient solution is not frequently replenished. As the plant will continue to preferentially remove light isotopes from the nutrient solution, the nutrient solution will become enriched with heavy isotopes while the isotopes taken up by the plant

TABLE 1 | Glossary of terms relevant to isotope composition analysis.

Analytical precision	Usually expressed as the 2× standard deviation (2sd) of repeat measurements of a primary/bracketing standard or matrix-matched reference material (**Supplementary Tables S1, S2**), or the 2sd of repeated sample measurements. Gives a good estimate of the isotope composition resolvability. Often referred to as "external precision."
Analyte purification	Isolation of analyte from the matrix of a digested sample. Most common method is ion exchange chromatography: percolation of acids of different molarities through resin-filled columns.
Digestion	Breakdown of molecules to allow liberation of individual elements. Uses hotplate or microwave oven-assisted acid digestion using nitric acid (and hydrogen peroxide) /aqua-regia /perchloric acid /hydrofluoric acid. For Si analysis, alkaline fusion (e.g., using NaOH) is more appropriate, since SiF_6 is volatile after HF digestion.
Double spike	A mass bias correction technique for elements with ≥ 4 stable isotopes. A mixture of 2 enriched isotope solutions with known concentration and isotope composition is equilibrated with samples. An iterative procedure is used to deconvolute the data.
Equilibrium fractionation	Occurs when two or more substrates are in chemical (isotope) equilibrium. Heavier isotopes are preferentially incorporated into stiffer bonds in equilibrium reactions.
External normalization	A mass bias correction technique using a second element that is close in atomic mass and ionization potential to the analyte.
Isobaric interference	When isotopes of different elements have similar mass, mass spectrometry may be unable to distinguish between them, for example, ^{40}Ca, ^{40}Ar.
Isotope fractionation	Changes in proportions of isotopes that occur during chemical reactions or physical processes.
Kinetic (isotope) fractionation	In chemical reactions that are not at equilibrium, light isotopes accumulate in reaction products as they have slightly lower activation energies and therefore react faster.
Mass bias	Isotope fractionation that occurs inside mass spectrometers due to differences in transmission efficiencies between isotopes. This can induce large isotope fractionations, so post-measurement mathematical correction is required. Mass bias is much stronger in ICP than in TIMS.
Mass-dependent fractionation (MDF)	Fractionation scales with the difference in isotopic mass. for example, the mass difference between ^{68}Zn and ^{64}Zn is ~double that of ^{66}Zn and ^{64}Zn, so fractionations of ~2 and ~1‰ are expected (Maréchal et al., 1999).
Molecular interference	Also known as poly-atomic interferences. These occur within mass spectrometers when the mass of a molecule (e.g., $^{40}Ar^{16}O$) overlaps with an isotope of the analyte (e.g., ^{56}Fe).
Multiple collector inductively coupled plasma mass spectrometry	Use an Ar ICP source, magnetic sector analyzer, and Faraday collector array to simultaneously measure isotope abundances at precisions higher than attainable by single-collector ICP-MS. Enables analysis of a large variety of elements, including those with high ionization potentials, such as Zn. Samples are introduced as a solution or aerosol and even solid when laser ablation is used.
Procedural blank	A sample taken through every preparation step to enable the quantification of any contamination that can alter a samples' true isotope composition.
Sample-standard bracketing	A mass bias correction technique. Samples are analyzed between standards. Post-measurement, a correction is made relative to the standard before and after the sample.
Thermal ionization mass spectrometry (TIMS)	More traditional devices for isotope analysis. Samples are deposited on a filament that is heated by an electric current to ionize the analyte. Isotopes are separated using a magnetic sector and an array of faraday cups. TIMS measurements involve lower mass bias and interferences than MC-ICP-MS, however they are slower and accurate mass bias correction mostly relies on the double spike technique, drastically limiting the amount of possible analytes.

become successively heavier. Finally, when the entire Ca is taken up from the solution, the plant will have the same Ca isotope ratio as the solution initially had. In contrast, if the solution is frequently replenished, the plant is virtually exposed to an infinite Ca source and the system is considered open. In such a system, the plant will continuously take up light Ca isotopes from the nutrient solution and the Ca isotope ratios in the plant and in the solution do not change over time.

Isotope ratio analyses are more meaningful when mass balances are calculated. To calculate such "isotope mass balances" in plants, the dry weights, the plant organs (e.g., roots, leaves) concentrations, and isotope ratios of both the plant organs and the nutrient source need to be determined. For instance, the weighted mean of Ca isotope ratios in different plant organs provide the isotope ratio of the whole plant and thereby the isotope fractionation associated with Ca uptake from soil to plant can be calculated. Note, these calculations consider that there is no significant efflux of Ca from the plant into the soil.

Metals and Metalloids in Plants: The Basics

Plants require 17 elements in order to complete their life cycle (**Table 2**). Besides hydrogen (H), carbon (C), and oxygen (O), which are the main building blocks of plant tissues, the remaining 14 elements are the macronutrients: nitrogen (N), magnesium (Mg), phosphorus (P), sulfur (S), potassium (K), calcium (Ca) and the micronutrients: boron (B), chlorine (Cl), manganese (Mn), iron (Fe), nickel (Ni), copper (Cu), zinc (Zn) and molybdenum (Mo) (Marschner and Marschner, 2012).

TABLE 2 | Overview of elements found in plant tissue that have been studied using stable isotope fractionation (listed according to atomic weight)**.

Element	Symbol (atomic weight)	Main plant available form(s)	Normal/sufficient content (in dry matter*)	Phloem mobility	Functional roles in plants
Boron	B (10.81)	$B(OH)_4^-$ $B(OH)_3$	5–60 µg/g	Low	***Essential*** plant nutrient: Stabilization of cell walls, nucleotide biosynthesis, translocation, pollen germination
Magnesium	Mg (24.305)	Mg^{2+}	0.1–1%	High	***Essential*** plant nutrient: Photosynthesis (central atom of chlorophyll), enzyme activation
Silicon	Si (28.085)	H_4SiO_4	0.1–10%	Low	***Beneficial*** plant nutrient: Alleviates abiotic and biotic stresses (salt, heavy metal, fungal disease, osmotic, drought)
Potassium	K (39.098)	K^+	1–6%	High	***Essential*** plant nutrient: Translocation, osmoregulation, pH homeostasis, enzyme activation
Calcium	Ca (40.078)	Ca^{2+}	0.2–3%	Low	***Essential*** plant nutrient: Cell wall synthesis and stabilization, signal transduction
Iron	Fe (55.845)	Fe^{3+} Fe^{2+}	30–300 µg/g	Conditional	***Essential*** plant nutrient: Enzyme activation, electron transport, chlorophyll biosynthesis, oxidative stress protection
Nickel	Ni (58.693)	Ni^{2+}	0.1–1 µg/g	Conditional	***Essential*** plant nutrient: Enzyme activation, urea metabolism
Copper	Cu (63.546)	Cu^+ Cu^{2+}	4–25 µg/g	Conditional	***Essential*** plant nutrient: Enzyme activation, synthesis of cell wall components, electron transport, oxidative stress protection
Zinc	Zn (65.38)	Zn^{2+}	15–80 µg/g	Conditional	***Essential*** plant nutrient: Gene expression, enzyme activation, hormone and nucleic acid synthesis, oxidative stress protection
Molybdenum	Mo (95.95)	MoO_4^{2-}	0.1–1 µg/g	Conditional	***Essential*** plant nutrient: Enzyme activation, nitrogen fixation, nitrate reduction
Cadmium	Cd (112.41)	Cd^{2+}	0.01–1 µg/g	Conditional	***Non-essential, non-beneficial***
Thallium	Tl (204.38)	Tl^+	site dependent	NA	***Non-essential, non-beneficial***

*Main plant available form(s) of each element, normal or sufficient content, phloem mobility, functional roles in plants and selected additional information of relevance for interpretation of element-specific isotope fractionations. NA = information not available. *Dependent on the developmental stage of the plant, the plant species, the plant genotype, and the plant organ. **Adapted from Pilon-Smits et al. (2009); Husted et al. (2011); Marschner and Marschner (2012); de Bang et al. (2020); www.iupac.org. For element-specific information on uptake, functional roles and utilization in plants, we refer to recent reviews for: B (Yoshinari and Takano, 2017), Ca (Thor, 2019), Mg (Chen et al., 2018), K (Wang and Wu, 2017), Si (Ma, 2015), Cu, Fe, Ni, Zn, and Cd (Andresen et al., 2018), Mo (Tejada-Jimenez et al., 2018).*

Besides the essential plant nutrients, many other elements of the periodic table are also found in plants. Some elements, such as silicon (Si), are considered beneficial for certain plant species. Others with no functional role are present in plant organs as a result of their environmental abundance and due to non-specific uptake by plants. Some of these elements represent a threat to plant growth and performance, for example, cadmium (Cd). Most elements are acquired as inorganic ions from the soil solution and are subsequently translocated in plant organs and utilized in a plethora of biochemical functions (**Table 2**).

Physiological Processes and Isotope Compositions in Plants

Physiological processes, such as root uptake, short and long-distance transport (in xylem or phloem), storage (e.g., vacuolar), metabolic functionalization, and compartmentalization (**Figure 1A**), are a series of physico-chemical processes that potentially change isotope compositions of a given element. Physico-chemical processes comprise water mass flow, sorption, ligand exchange, redox changes, precipitation, dissolution, and diffusion.

Plant Root Uptake of Elements

Plants take up most elements in specific, phytoavailable, chemical forms from the soil solution (**Tables 2, 3**). These are transported in roots *via* the apoplastic, symplastic, or transcellular pathways (**Figure 1B**; **Table 3**). Elements enter the root apoplast with water mass flow, mainly driven by the transpiration stream or by diffusion along an electrochemical gradient. The apoplastic mobility of elements is determined by the number and affinity of available adsorption, complexation, and exchange sites within cell walls for the specific element (Meychik et al., 2021). When a physico-chemical barrier restricts further apoplastic transport, elements have to cross a cell membrane to take the symplastic and transcellular pathways, which may require metabolic energy (**Figure 1C**; **Table 3**). One such barrier during root-to-shoot transport is the endodermis. It forms the boundary between the cortex and the stele and contains a lignin- and suberin-based hydrophobic radial cell wall "impregnation" called the "Casparian strip" (Geldner, 2013). To cross the endodermis, all elements have to enter the intracellular space at least

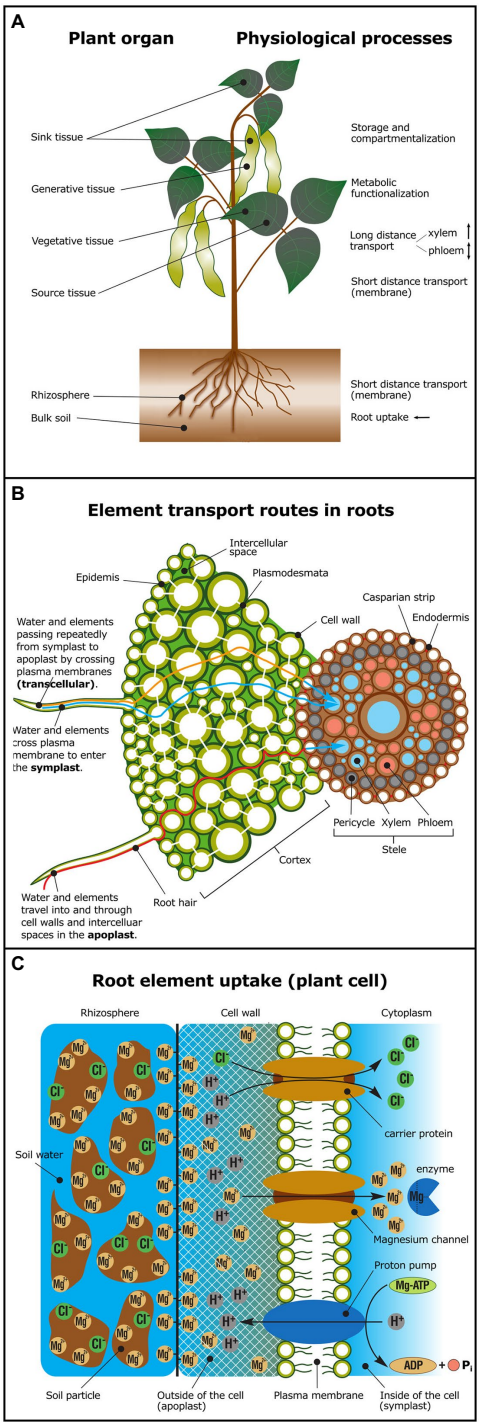

FIGURE 1 | Overview of physiological processes potentially causing isotope fractionation. **(A)** In shoots, isotope fractionation may occur during short distance transport across membranes, during long-distance transport in xylem (unidirectional transport) or in the phloem (bidirectional transport), due to metabolic functionalization (e.g., enzyme activation, ligand exchange), element storage or compartmentalization. Major physiological processes in roots are nutrient uptake and short distance transport across membranes. Elements are taken up from the rhizosphere and translocated *via* the xylem to sink tissue (young leaves or generative tissue, such as fruits, grains, or pods). Elements may also be re-translocated *via* the phloem from source tissue (e.g., old leaves) to sink tissue. **(B)** Simplified model of symplastic (blue), apoplastic (red) versus transcellular (orange) element transport routes in plant roots. Cell-to-cell transport in the symplastic pathway occurs *via* plasmodesmata. In the apoplastic pathway elements travel in the cell wall and the intercellular space. The plasma membrane must be crossed to exit the root cortex and enter the stele and the vasculature system. **(C)** Elements may be bound to soil particles in the rhizosphere or to the negatively charged cell wall prior to uptake across the plasma membrane mediated by transport proteins (e.g., *via* carriers and channels). In the cytoplasm, elements may form complexes with enzymes and substrates—for example, ATP activation through Mg-ATP complexation (Adapted from *Marschner and Marschner, 2012*; Taiz et al., 2015). For glossary of terms and processes see **Table 3**.

temporarily (**Figure 1B**). After crossing the endodermis, an element is loaded into the vascular system (**Table 3**) for further root-to-shoot transport.

Cross-Membrane Transport of Elements

Elements are transported across membranes either by passive diffusion through the phospholipid bilayer or *via* an armada of specialized membrane transport proteins (**Figure 1C**; **Table 3**). Passive diffusion is negligible for charged molecules due to their restricted membrane permeability while passive channels, secondary active carriers, and active transporters generate an element-specific and rapidly controllable pathway through various membranes (Stein and Litman, 2015; Tang et al., 2020). Each transport protein has a unique activity. The subcellular localization of each membrane protein is mostly restricted to one cellular membrane system (e.g., plasma membrane, tonoplast, mitochondrial or chloroplastic membrane) or even a spatially targeted fraction of a membrane system. For instance, certain transporters that control the uptake of nutrients, such as B and Si, are polarly localized solely at the distal side of root rhizodermis cells, while transporters responsible for the further translocation of nutrients into the cortex are localized to the proximal side (Ma and Yamaji, 2015; Yoshinari and Takano, 2017). Similar to animal epithelial cells, where the mechanisms for polar localization of nutrient transporters at the apical or basolateral membrane were intensively studied (Mellman and Nelson, 2008), many plant nutrient transporters that are either responsible for rhizodermal uptake or xylem loading, have been demonstrated to be polarly localized (Łangowski et al., 2010 and references therein).

The main driving force for protein-mediated membrane transport is an electrochemical gradient (**Table 3**) which depends on differences in element concentrations and electrical potential inside and outside of the cell. The electrochemical gradient is established by membrane proteins (H^+-ATPases), which pump protons out of cells against an inward directed proton gradient (**Figure 1C**). This process requires metabolic energy from ATP hydrolysis and generates an electrical gradient (positive outside, negative inside) and a pH gradient (acidic outside vs. neutral/alkaline inside) across the membrane. As a consequence, there is a permanent driving force (proton motive force) for cations into plant cells and anions out of plant cells (Falhof et al., 2016). These energetic downhill transport processes can be used to energize uphill transport processes that are mainly facilitated by carrier-type transport proteins (Stein and Litman, 2015; Tang et al., 2020).

TABLE 3 | Glossary of terms and processes relevant for understanding isotope fractionation in plants (in alphabetical order).

Active transport – cellular influx and efflux – short distance transport	Movement of an ion/molecule across the membrane against the concentration gradient of the transported atom/molecule and/or against the electrochemical gradient. Requires metabolic energy to pump molecules across a membrane (transport direction = uniport; transport rates = 1–10^2 molecules per sec; energization = ATP/PPi -hydrolysis; protein types mediating the active transport = pumps, ATPases, which demands structural changes of the protein; examples = Ca, Zn, Mn, Cd, Co P-type ATPases, Cd, Pb, As, Hg (II), Sb ATP-Binding-Cassette (ABC)-transporters).
Apoplastic transport (extracellular)	Transport of an ion/molecule in the apoplast, which comprises the entirety of plant cell wall and the intercellular space, without entering the cell. Note, elements that fulfill functions in the apoplast, like Ca (cell wall stabilization), can be considered as taken up by the plant although they have not entered the symplast.
Bulk Soil	Soil outside of the rhizosphere and neither penetrated nor influenced by plant roots.
Compartmentalization	Separation of ion/molecule into isolated subcellular compartments (organelles, cell wall, etc.) or cells.
Dual-affinity transport proteins	Transport proteins which are suggested to transport efficiently at high or low nutrient concentrations due to their ability to switch their structural or biochemical protein properties *via* post-translational modifications (e.g., the potassium transporter AtKUP1).
Electrochemical Gradient	A difference in 1) charge and 2) the chemical concentration of a compound across the plasma membrane.
High-affinity transport proteins	Transport proteins which are suggested to dominantly transport at low nutrient concentrations; transport can be saturated (e.g., the iron transporter AtIRT1).
Ligand	A group, ion or molecule coordinated to a central atom or molecule in a complex. For example nicotianamine, phytate, citrate and malate.
Long-distance transport (*via* mass flow)	Transport of ion/molecule within the vasculature at the level of the whole plant linking a multitude of roots with branches and leaves *via* the specialized tissues called xylem (unidirectional transport, up in a plant ↑) and phloem (bidirectional transport, up and down in a plant ↕). Driven by pressure flow (hydrostatic or osmotic).
Low-affinity transport proteins	Transport proteins which are suggested to dominantly transport at high nutrient concentrations; transport seems non-saturable (e.g., the cation Cd transporter OsLCT1).
Passive transport – cellular influx and efflux – short distance transport	Movement of an ion/molecule across the membrane along the concentration gradient of the transported atom/molecule and/or along the electrochemical gradient. Protein-mediated or *via* sole diffusion across the membrane (transport direction = uniport; transport rates = 10^6–10^8 molecules per sec; energization = electrochemical potential gradient; protein types mediating the passive transport = channels; examples = K, B, Si, Cl, Ca channels).
Phytoavailability	Plant availability - i.e., elements are available to plants for uptake. Most commonly used when referring to essential plant nutrients that are in the right chemical form at sufficient concentrations in the soil solution.
Rhizosphere	The soil around living roots, which is influenced by root activity. The radial extension of the rhizosphere can range from sub-µm to supra-cm scales.
Secondary active transport – cellular influx and efflux – short distance transport	Movement of an ion/molecule across the membrane against the concentration gradient of the transported molecule and/or against the electrochemical gradient (transport direction = uniport, symport, antiport; transport rates = 10^2–10^4 molecules per sec; energization = proton (H^+) gradient established by active transport processes; protein types mediating the active transport = carriers, which demands structural changes of the protein; examples = K, Na, Fe, Zn, Mg, B, Cl transporters).
Selectivity of a transporter	Each individual transport protein, irrespective of whether it is a channel (passive transporter), a carrier (a secondary active transporter) or an active transporter (pump) has a specific transport selectivity allowing for selective passage of (a) specific atom(s)/molecule(s). This transporter-intrinsic specificity does neither depend on the type of transport process (active vs. passive) nor on the transported atom/molecule (ionic versus polar molecule).
Short distance transport	Transport that occurs within, into and out of cells including a membrane crossing in the process. Includes diffusion and mass flow.
Symplastic (intracellular) transport	Cell-to-cell transport of an ion/molecule *via* plasmodesmata which has once entered the symplast *via* passive diffusion or a transport protein.
Transcellular (intracellular/extracellular) transport	Transport protein-mediated transport of an ion/molecule from one cell to the other, passing repeatedly from symplast to apoplast, independent of the water mass flow but depending on a non-overlapping localization of influx and efflux transporters in the plasma membrane to allow a directional flow.

Specific uptake and efflux transport proteins have been identified for mineral nutrients in the rhizodermis and root hairs at the plant–soil interface (Bienert et al., 2021), as well as in the cortex cells which have to be passed before nutrients enter the vasculature of the stele (**Figure 1B**). Although transport proteins have often developed a high selectivity for their substrate-of-interest, most are not fully element-specific and can accommodate a range of substrates simply due to physico-chemical similarities. The selectivity of transport proteins is mostly determined by 3D physico-electrochemical properties of the amino acid residues constituting the surface of and the transport pathway through the protein (Chan and Shukla, 2021). While some transporters are ubiquitously expressed, others are only found at certain developmental stages, times of day, or only in response to stimuli (e.g., nutrient deficiency, mineral toxicity).

In the absence of knowledge on transport proteins, nutrient uptake fluxes have been historically differentiated into low- and high-affinity uptake systems (**Table 3**). Low-affinity uptake systems

act at higher phytoavailable nutrient concentrations while high-affinity uptake systems act at low phytoavailable nutrient concentrations. In addition, dual-affinity transport systems act under a wide concentration range of phytoavailable nutrient concentrations. The high-low-dual-affinity terminology is sometimes confusingly used as it is often extended to the binding affinity of a substrate to a transport protein that also determines nutrient uptake kinetics. However, underlying experimental transporter characteristics have not been determined and environmental parameters might determine transport rates by the respective protein (Dreyer and Michard, 2020).

Long-Distance Transport of Elements

From the root cortex, elements are transported into the stele and the vasculature system for long-distance, unidirectional transport toward the shoot (translocation, **Figure 1A**; **Table 3**). The xylem transports elements with the transpirational flow of water toward the leaves and generative tissues. Re-translocation of elements and bidirectional transport occurs in the phloem where high concentrations of assimilates (mainly sucrose) are loaded from source tissues (e.g., leaves) and are unloaded in sink tissues (e.g., fruits) by transport proteins. This generates a diffusion or osmotic gradient which induces a flow in the phloem and thereby long-distance transport of elements. The unloading of elements from the xylem and phloem as well as the distribution to physiological sink cells and organs again requires membrane transport proteins (see Cross-Membrane Transport of Elements). All these transport processes may cause isotope fractionation and change depending on physiological status, developmental stage, nutritional status, and the environmental condition at which a plant grows.

Binding of Elements to Organic Molecules

While elements are transported to their physiological destination they are exposed to a variety of non-transport related reactions. For instance, B readily forms ester bonds in many metabolites of primary and secondary metabolism while Cu can be retained in prosthetic bonds or as a cofactor in enzymes (Brdar-Jokanović, 2020; Li et al., 2020; Mir et al., 2021). Sorption, chelation, and complexation of elements to and with various organic and inorganic molecules is ubiquitous in plants. Some of these interactions are developmentally or physiologically targeted, others occur solely due to their chemical reactivity (Hanikenne et al., 2021). Noteworthy, in a quantitative sense, is the binding of, for example, Mg in chlorophyll, Fe in ferritin or heme, Zn in zinc finger proteins or nicotianamine, and trace metals to a plethora of thiols. In addition, the affinity of Ca to cell wall components contributes to the stability of cell walls (Thor, 2019).

METHODS FOR ISOTOPE ANALYSES OF PLANTS

Analyzing non-traditional stable isotope compositions of plants requires cautious sample handling, compared to traditional isotope analyses, and additional preparation steps, such as sample purification. In the following sections, the analytical procedures are listed chronologically.

Sample Preparation

For all post-harvest processes, such as plant sample cleaning, drying, and homogenization, sample contamination should be kept to a minimum since it can significantly bias isotope compositions. For guidelines on post-harvest sample preparation, we recommend Hansen et al. (2013). A crucial step for isotope analyses in plants is the cleaining of the roots of hydroponically and soil grown plants. To remove soil particles, weak salt solutions, ultrapure, and ice-cold water (18.2 MΩ.cm) are used (Tang et al., 2016). Salt solutions or weak acids can be further used to extract the apoplastic root pool prior to isotope ratio analysis (e.g., Tang et al., 2016; Garnier et al., 2017). However, both the washing procedure and the extractant used may significantly impact the isotope ratios of the different root pools.

Wet Chemistry

Wet chemistry sample preparation comprises two steps: sample digestion and analyte purification. To minimize sample contamination, these steps need to be conducted in "clean labs" (i.e., laboratories with non-metal fixtures, filtered air, ideally certified), ultra-clean reagents (e.g., distilled acids), and acid-cleaned PTFE/PFA containers (see also Section Quality Control). For most elements, digestion of plants requires strong acids (e.g., HNO_3) and a microwave oven or a hotplate (**Table 1**). Silicon analyses represent a special case, where alkaline fusion procedures are more common than acid digestions (Frick et al., 2020). After digestion, the samples are "purified" by anion/cation exchange and extraction chromatography (**Table 1**; **Supplementary Table S1**) which is the most common technique to separate pure analyte fractions. Often more than one of these "column chemistry" procedures are required to separate residual matrix elements. It is important that the chromatographic yields are close to 100%, as any loss of element on the column can result in isotope fractionation and thereby bias results. For example, Cu isotopes can significantly fractionate between the first and last milliliter of elution from a commonly used column chemistry, and even not collecting the final 5% of Cu can induce a significant isotope fractionation (Maréchal and Albarède, 2002). For some elements, quantitative yields are less important if the double spike technique is used (**Table 1**; **Supplementary Table S1**).

Isotope Analyses and Notation

To resolve differences in stable isotope composition in the per mil range, the use of multiple collector inductively coupled plasma mass spectrometry (MC-ICP-MS) or thermal ionization mass spectrometry (TIMS) is required (**Table 1**; Hoefs, 2018). Sample purification is necessary to avoid isobaric or poly-atomic/molecular interferences on the target element (**Table 1**). However, due to residual impurities or molecular interferences with elements present in the solution or the plasma (like N, O, H, Ar), it is often still challenging to perform precise isotope ratio analysis. Common problems include the formation of argides and those associated with analyzing isotopes that have very low natural abundances. For instance, ^{56}Fe overlaps with the argide $^{40}Ar^{16}O$. This problem is resolved by, for example, performing analyses at high-resolution modes, which is able to distinguish between Fe and argon oxides (Schoenberg and von Blanckenburg, 2005).

Mass bias during analyses needs to be corrected (**Table 1**). The simplest method adopted is "sample-standard bracketing" (**Table 1**). If a mass bias is non-linear, this method will not produce accurate results but can be improved by the addition of external normalization and mass fractionation laws (**Table 1**; Rehkämper et al., 2001). Such normalization, or "doping" uses the assumption that a dopant will undergo similar instrumental mass bias to the analyte, based on mass and ionization potential (e.g., Ni or Zn as doping element for Cu analyses). For elements with at least four stable isotopes, mass bias can be corrected by the double spike technique (**Table 1**; Rudge et al., 2009).

Stable isotope compositions are usually reported relative to an internationally recognized primary standard material and as a δ notation, exemplified for Ca (Hoefs, 2018):

$$\delta^{44/40}\mathrm{Ca}\,(‰) = \left[\frac{\left(^{44}\mathrm{Ca}/^{40}\mathrm{Ca}\right)_{\mathrm{sample}}}{\left(^{44}\mathrm{Ca}/^{40}\mathrm{Ca}\right)_{\mathrm{standard}}} - 1\right] 1000 \qquad (1)$$

Values are most often presented in per mil, but are also occasionally given as ε (10,000 times instead of 1,000 times multiplication). The isotopes used for reporting the isotope composition and the internationally accepted primary reference standard of each reviewed element are listed in **Supplementary Table S1**. For several elements, it is conventional that only the heavier isotope is included in the δ notation (e.g., $\delta^{44/40}$Ca is written as δ^{44}Ca).

The isotope fractionation between two compartments of soil–plant system is expressed as:

$$\Delta^{44}\mathrm{Ca}_{a-b}\,(‰) = \delta^{44}\mathrm{Ca}_a - \delta^{44}\mathrm{Ca}_b \qquad (2)$$

In plants, Δ can refer to the isotope fractionation (i) between the whole plant, a, and its source, b, resulting in $\Delta^{44}\mathrm{Ca}_{\text{plant-source}}$ to determine the isotope fractionation during the root uptake of an element or (ii) within a plant (e.g., $\Delta^{44}\mathrm{Ca}_{\text{shoot-root}}$). In isotope studies where full mass balances are difficult to calculate (e.g., for trees), often $\Delta^{44}\mathrm{Ca}_{\text{root-source}}$ is given. This notation is not equal to the isotope fractionation during uptake as the root isotope ratios result from both uptake and further transport of the element.

Quality Control

To assure the quality of the non-traditional stable isotope ratio measurements, two principle quality control measures are necessary. First, the concentration of a "procedural blank" (**Table 1**) needs to be determined to ensure that the unintended addition of an analyte, for example, Zn, from acids, plastics, and dust, to a sample is kept to a minimum. As a general rule, a procedural blank that contains less than 1% of the analyte mass in a sample creates no significant artificial effect on isotope ratios. Second, reference samples need to be analyzed to show that the sample preparation and analyses are robust and reproducible. The quality of the isotope ratio measurement is commonly reported using the reproducibility of the primary reference standards (**Supplementary Table S1**). Furthermore, interlaboratory comparisons of certified reference materials (CRMs) enable the recovery of an element during sample digestion and purification to be calculated (**Supplementary Table S2**). There are published (although not certified) isotope ratios for some of these materials and we highly recommend their use, since they better match the composition of plant samples and enable the validation of the whole analytical process from sample preparation to isotope analyses.

ISOTOPE FRACTIONATION IN PLANTS

In this section, isotope fractionation in plants is reviewed for individual elements. Where element mass balances were available mass balances were available, isotope fractionation upon uptake by plants (e.g., $\Delta^{44}\mathrm{Ca}_{\text{plant-source}}$) is reported, along with any within-plant isotope fractionation (e.g., $\Delta^{44}\mathrm{Ca}_{\text{shoot-root}}$, $\Delta^{44}\mathrm{Ca}_{\text{grains-leaves}}$). Interpretations on distinct isotope compositions of plants are reviewed when data-driven and well-substantiated hypotheses were provided. Elements that have been analyzed in exploratory studies, without detailed process tracing discussions (K, Mo, and Tl) are reviewed briefly at the end.

Boron

Only a few studies have systematically investigated B isotope fractionation in plants. As full mass balances were not available, only semi-quantitative information on isotope fractionation between source and plant ($\Delta^{11}\mathrm{B}_{\text{plant-source}}$), and within the plant ($\Delta^{11}\mathrm{B}_{\text{within.plant}}$) can be extracted from these data. Nevertheless, B isotope analyses in B sources, such as hydroponic nutrient solutions and plants indicated that $\Delta^{11}\mathrm{B}_{\text{plant-source,}}$ may differ between plant species or between cultivars of the same species, as demonstrated for different grapevine cultivars (Marentes et al., 1997; Coetzee et al., 2010; **Figure 2**). These differences are possibly linked to distinct B demand at similar B supply. In bell pepper, heavy B isotopes were preferentially transported from roots to leaves ($\Delta^{11}\mathrm{B}_{\text{leaves-roots}}$ +0.8 to +27‰, Geilert et al., 2015, 2019). Within the shoots, leaves were isotopically heavier than stems and fruits were in most cases lighter than leaves.

A main driver of B isotope fractionation within the plant may be changes of the B species boric acid ($B(OH)_3$) and borate ($B(OH)_4^-$, Geilert et al., 2019; **Figure 2**). At equilibrium, boric acid ($B(OH)_3$) is enriched in heavy isotopes compared to borate ($B(OH)_4^-$, Zeebe, 2005). Boron is transported into the root cytoplasm under B-deficient growth conditions as boric acid by the so-called Nodulin26-like Intrinsic Protein (NIP)-type membrane channels (Yoshinari and Takano, 2017). In the cytoplasm, boric acid is partially transformed to borate, which is effluxed by borate transporter proteins (BORs) membrane transporters to the xylem (Parker and Boron, 2013). Hence, the transport of B from root-to-shoot may favor the transport of light B isotopes. However, this was not the case (Geilert et al., 2019), indicating that isotope fractionation between boric acid and borate was masked by other processes. The B species are also relevant to structural binding of B into cell walls. Borate is thought to function as the structural ester "bridge" to interlink Rhamnogalacturonan-II monomers within

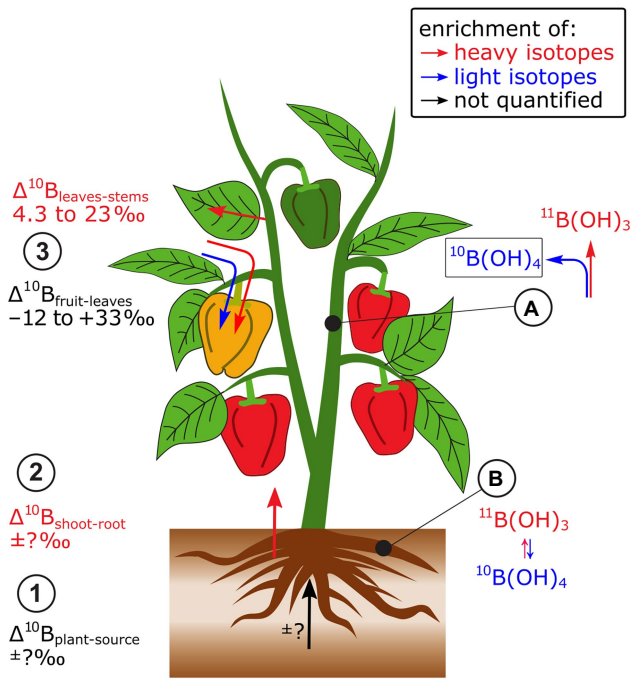

FIGURE 2 | A few studies have investigated B isotope fractionation in plants. Bell pepper has been most systematically investigated. (1) Due to lacking B mass balances, $\Delta^{11}B_{plant\text{-}source}$ is not known, but it can be semi-quantitatively shown that (2) shoots are enriched in heavy isotopes compared to roots. (3) Within plants, leaves are enriched in heavy B isotopes compared to stems while leaves can be heavier and lighter than reproductive organs. **(A)** At equilibrium, boric acid ($B(OH)_3$) is isotopically heavier than borate ($B(OH)_4^-$) which may contribute to the isotope fractionation between root and shoot. **(B)** The integration of borate into cell walls may cause the enrichment of heavy isotopes in leaves compared to stems.

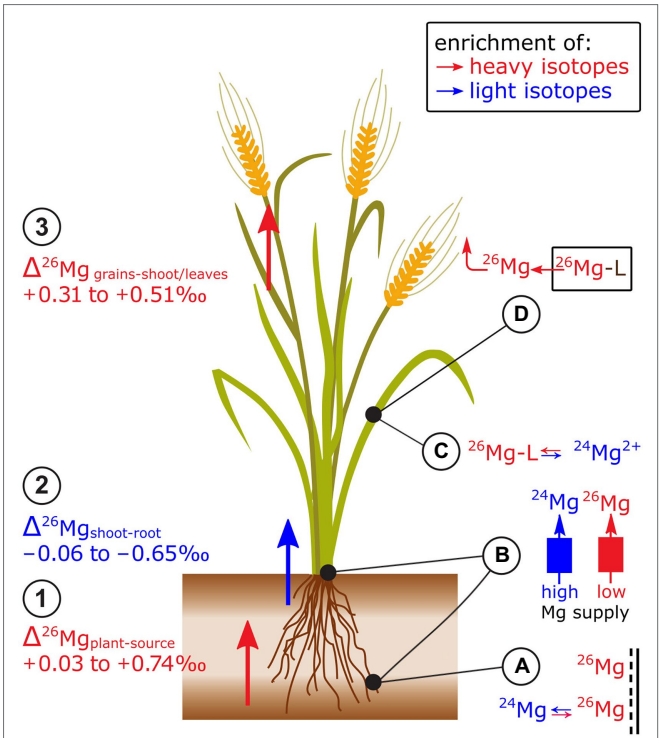

FIGURE 3 | Mg isotope fractionation in plants has been studied in trees and cereals. Exemplified for cereals: (1) Plants are enriched in heavy isotopes compared to the Mg source while (2) shoots tend to be enriched in light isotopes compared to roots. (3) Grains are enriched in heavy isotopes compared to stems and leaves. **(A)** Heavy Mg isotopes preferentially bind onto negatively charged surfaces in the root apoplast. **(B)** Binding of Mg to membrane transporters that are active at low Mg supply may induce a shift towards heavy isotopes during plant uptake and root-to-shoot transport compared to Mg transport at regular (or high) Mg supply. **(C)** It is assumed that the root contains a heavy Mg pool that is bound to organic ligands (Mg-L) while ionic Mg^{2+} is enriched in light isotopes that may be preferentially transported toward the shoots. **(D)** During grain filling, organic ligands that contain Mg degrade (e.g., chlorophyll) and release heavy Mg which may lead to a preferential re-translocation of heavy isotopes from senescent tissues.

the pectin fraction of primary cell walls (Yoshinari and Takano, 2017). Therefore, light B isotopes should be integrated into cell walls, if the integration itself does not fractionate B isotopes, while heavy B isotopes remain soluble and mobile (Geilert et al., 2015, 2019). Hence, the integration of B into cell walls could explain the enrichment of heavy isotopes in leaves compared to stems (Geilert et al., 2019).

Magnesium

Plants preferentially take up heavy isotopes from their Mg sources, such as hydroponic nutrient solutions (Black et al., 2008; Bolou-Bi et al., 2010; Wrobel et al., 2020), phlogopite (Bolou-Bi et al., 2010), soil pore water (Tipper et al., 2010; Kimmig et al., 2018), and phytoavailable soil Mg pools (Bolou-Bi et al., 2012; Opfergelt et al., 2014; Kimmig et al., 2018; Wang et al., 2020; **Figure 3**). In ryegrass and clover, root extracts ($CaCl_2$) of Mg revealed that heavier Mg is preferentially adsorbed to the apoplast (Bolou-Bi et al., 2010). This Mg adsorption likely contributes to the preferential uptake of heavy Mg isotopes into plants (Bolou-Bi et al., 2010; Wang et al., 2020). In wheat, $\Delta^{26}Mg_{plant\text{-}source}$ was more positive under low compared to regular Mg supply (Wang et al., 2020). This difference was ascribed to distinct cross-membrane transport systems. At low supply, active Mg-specific proteins facilitate Mg uptake, while at high supply passive channels facilitate Mg uptake. The former may shift the plant Mg toward a heavier isotope composition through binding to the membrane protein (Bolou-Bi et al., 2010; Wang et al., 2020).

Shoots of grasses and clover tended to be lighter than their roots (Black et al., 2008; Bolou-Bi et al., 2010; Gao et al., 2018; Wang et al., 2020; **Figure 3**). Bolou-Bi et al. (2010) ascribed the negative $\Delta^{26}Mg_{shoot\text{-}root}$ values to two different Mg pools in roots: ionic Mg (favoring light isotopes) and Mg bound to organic ligands (favoring heavy isotopes), such as ATP and proteins. Ionic Mg is thought to be preferentially transported from roots to shoots, leading to an enrichment of light isotopes in shoots compared to the roots. In wheat, the $\Delta^{26}Mg_{shoot\text{-}root}$ was more negative in the initial growth phases ($\Delta^{26}Mg_{shoot\text{-}root}$ −0.85‰) than in the final growth stages ($\Delta^{26}Mg_{shoot\text{-}root}$ −0.25‰) at regular Mg supply (Wang et al., 2020). The inverse was the case for wheat grown with low Mg supply

($\Delta^{26}Mg_{shoot\text{-}root}$ initial −0.25‰, final −0.55‰). Similar as for root uptake, the distinct $\Delta^{26}Mg_{shoot\text{-}root}$ was ascribed to distinct cross-membrane transport modes at low and high Mg supply.

Mg isotope ratios also vary between different organs of plant shoots (**Figure 3**). In wheat and rice, grains were heavier than the remaining shoot (Black et al., 2008; Gao et al., 2018). However, Mg in wheat ears was lighter than the shoots at regular Mg supply, but heavier than shoots at low Mg supply (Wang et al., 2020). In spruce trees, Mg in older needles was lighter than in young needles ($\Delta^{26}M_{old\text{-}young}$ of −0.30‰, Bolou-Bi et al., 2012) while Mg in old leaves of sugar maple tended to be heavier than young leaves (maximum $\Delta^{26}Mg_{old\text{-}young}$ of 0.20‰, Kimmig et al., 2018). These studies indicated that Mg isotope fractionation within shoots may be related to Mg storage during vegetative growth and the subsequent remobilization from these Mg pools during reproductive growth stages. The remobilization of Mg would require a dissociation of Mg from its major organic ligands, such as chlorophyll (Kleczkowski and Igamberdiev, 2021). Theoretical and experimental studies revealed that Mg bound to chlorophyll is isotopically heavier than the bulk leaf or ionic Mg (Black et al., 2007; Moynier and Fujii, 2017; Pokharel et al., 2018; Wrobel et al., 2020). Only one study found that Mg in chlorophyll is lighter than the bulk leaf Mg (Black et al., 2008). Based on these findings, it was suggested that isotopically distinguishable pools of Mg exist in leaves, such as a light ionic Mg pool and a heavy Mg pool stored in chlorophyll (Pokharel et al., 2018). The latter may become a phloem source of Mg during leaf senescence and thereby an export of the heavier chlorophyll-bound Mg pool toward phloem sinks. However, Mg pools other than ionic and chlorophyll-bound exist in leaves and Mg isotopes bound to different organic ligands may be enriched in heavy and light isotopes compared to aqueous ionic Mg (Schott et al., 2016).

Silicon

Most plants take up light Si isotopes from hydroponic nutrient solutions and phytoavailable soil pools (**Figure 4**). Frick et al. (2020) showed that light Si was preferentially taken up by Si-accumulating wheat and non-Si-accumulating tomato and mustard plants. To identify the role of membrane proteins on Si isotope fractionation, Sun et al. (2016a) reduced the biologically mediated Si uptake of rice plants by metabolic inhibitors and by cooling the hydroponic nutrient solution. These treatments reduced the Si uptake 3–4 times and induced a shift toward light isotope uptake compared to the control plants (−0.29‰). In mutant rice plants with non-functional Si membrane channel proteins (Lsi1), the Si concentration in rice shoots was 25 times reduced while $\Delta^{30}Si$ in the shoots did not change (Köster et al., 2009). The enrichment of light isotopes in Si-accumulating and non-Si-accumulating plants was ascribed to diffusion during the membrane passage of Si with or without transport by membrane proteins, respectively (Frick et al., 2020). Note that Si is taken up as uncharged $Si(OH)_4$ and can therefore diffuse through the cell membrane (Ma, 2015).

No consistent pattern for $\Delta^{30}Si_{shoot\text{-}root}$ has been found, for example, for the same plant species (e.g., rice, −0.23 to 1.3‰, Ding et al., 2008; Sun et al., 2016a,b; **Figure 4**) or among non-Si-accumulating plants (−0.37 to +0.72‰, Frick et al., 2020). The processes that may govern the isotope fractionation between root and shoot are the precipitation of Si as phytoliths in roots and xylem loading (Sun et al., 2016b; Frick et al., 2020). The precipitation of Si as phytoliths favors light isotopes (Sun et al., 2016b). For xylem loading, Si needs to cross a membrane either by membrane diffusion (favors light isotopes) or by the membrane transporter Lsi2. Unlike Lsi1, Lsi2 is located at the proximal side of root exodermis and endodermis, effluxes Si out of the cell and, as a carrier protein, requires energy which is provided by the electrochemical proton gradient (Ma, 2015). A knockout of Lsi2 in rice led to a shift toward light isotopes (of ~0.5‰) in the shoots compared to the wild-type plant (Köster et al., 2009) indicating that Lsi2 may favor heavy isotopes.

Shoot organs of rice including stems, leaves, and husks become systematically enriched in heavy isotopes along the transpiration stream (Ding et al., 2005, 2008; Sun et al., 2016a; **Figure 4**). Similar patterns were observed for different shoot organs in banana, bamboo, and cucumber (Opfergelt et al., 2006; Ding et al., 2008; Sun et al., 2016b) and within leaves of banana

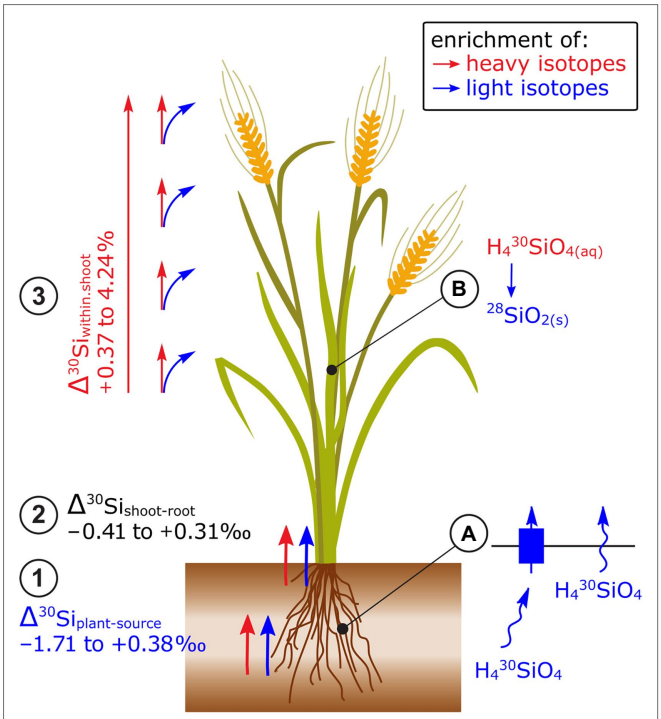

FIGURE 4 | Si isotope fractionation in plants exemplified for cereals. (1) Root uptake of Si leads in most cases to an enrichment of light isotopes while (2) no consistent pattern of Si isotope fractionation has been observed between root and shoot. (3) Within the shoot, plants become significantly enriched in heavy isotopes along the transpiration stream leading to a strong enrichment of heavy isotopes in husks and grains of rice. **(A)** The preferential uptake of light isotopes has been ascribed to a non-membrane protein-mediated transfer of Si (non-Si accumulators) and a membrane protein-mediated transfer of Si (LSi1) in Si-accumulating plants. Both processes may be driven by Si diffusion that favors light Si isotopes. **(B)** Precipitation of light Si isotopes into phytoliths (SiO_2) results in an enrichment of heavy isotopes in the Si pool ($H_4{}^{30}SiO_4$) and thereby in an enrichment of heavy isotopes along the transpiration stream.

and rice (Opfergelt et al., 2006; Ding et al., 2008). There, the lightest $\delta^{30}Si$ were found in petioles, followed by a successive enrichment of heavy Si toward leaf tips. The systematic Si isotope fractionation within shoots was explained by a successive precipitation of light isotopes into phytoliths (Dupuis et al., 2015). The precipitation likely leads to an enrichment of heavy isotopes in the soluble Si fraction that is then further transported along the transpiration stream. In the end points of the transpiration stream, such as rice husk and grains, only a small fraction of the total Si is stored but this fraction is most enriched in heavy isotopes (Sun et al., 2016b). This successive enrichment of heavy isotopes through Si precipitation lead to a Rayleigh-like fractionation (Sun et al., 2008, 2016b). Deviations from the Rayleigh fit could be attributed to membrane protein-facilitated transport (Lsi6) within the shoot (Sun et al., 2016b).

Calcium

In studies that focused on Ca cycling in catchments, Ca in trees (spruce, beech, pines) was lighter compared to its sources (Wiegand et al., 2005; Page et al., 2008; Cenki-Tok et al., 2009; Holmden and Bélanger, 2010; Bullen and Chadwick, 2016; **Figure 5**). These observations were confirmed in hydroponic studies on soybean, wheat, rice, and beans (Cobert et al., 2011; Schmitt et al., 2013; Christensen et al., 2018). In studies that provided full mass balances, Ca in beans and alpine plants was lighter than Ca in nutrient solutions or bulk soils, respectively ($\Delta^{44/40}Ca_{plant\text{-}source}$ −0.23 to −1.03‰, Hindshaw et al., 2013; Schmitt et al., 2013). The enrichment of light Ca isotopes during root uptake was assigned to preferential binding of light Ca to negatively charged surfaces, such as pectines in the root apoplast (Cobert et al., 2011; Schmitt et al., 2017, 2018). The fractionation between nutrient solution and beans could be modeled using a constant equilibrium fractionation factor between free ionic Ca and Ca sorbed to pectin groups ($\Delta^{44/40}Ca_{pectine\text{-}ionic}$ −0.12‰, Schmitt et al., 2013). In addition, Ca channel-mediated membrane transport may fractionate Ca isotopes as the transport rate of Ca ions may be size specific. The effective size of Ca ions depends on the number of water molecules in the first hydration shell and less hydrated Ca ions tend to be isotopically light (Moynier and Fujii, 2017).

There is no systematic fractionation of Ca isotopes between roots and shoots of different species (Hindshaw et al., 2013; Schmitt et al., 2013; Christensen et al., 2018; **Figure 5**). By employing a sequential extraction procedure for roots, Schmitt et al. (2018) showed that 90% of Ca in the roots of beech trees stabilizes cell walls and membranes as Ca-pectate. This structural Ca was lighter than the water soluble Ca fraction, suggesting that light Ca isotopes were retained in the roots while heavy isotopes were transported to the shoot. Hindshaw et al. (2013) explained the retention of light Ca isotopes in roots with Ca precipitation as oxalate in the root cortex of alpine herb. The assumption that Ca oxalate is enriched in light Ca isotopes was confirmed by extraction of Ca oxalate from leaves (Cobert et al., 2011; Schmitt et al., 2018). However, no profound explanation exists yet for the favorable transport of light isotopes from roots to shoots in, for example, soybean (Christensen et al., 2018).

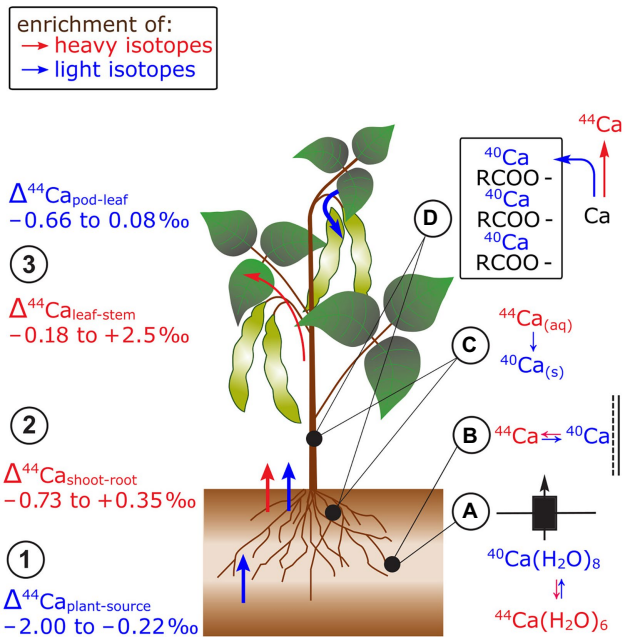

FIGURE 5 | Ca isotope fractionation in plants exemplified for beans. (1) Root uptake of Ca leads to an enrichment of light isotopes. (2) In most cases, shoots are enriched in heavy isotopes compared to roots. (3) Leaves are preferentially enriched in light isotopes compared to stems while reproductive organs are mostly lighter than leaves. The preferential uptake of light isotopes has been ascribed to **(A)** isotope differences in hydrated Ca species with distinct number of water molecules and **(B)** the preferential sorption of light Ca isotopes to negatively charged surfaces in the root apoplast. Within the plant, **(C)** lighter isotopes may precipitate with oxalate (^{40}Ca) and **(D)** are structurally bound in cell walls to pectins ($RCOO^-$ groups). The retention of light Ca isotopes leads to a higher mobility of heavy Ca isotopes within plants.

Leaves tended to be heavier than stems in cereals, beans, and alpine plants (Page et al., 2008; Cobert et al., 2011; Hindshaw et al., 2013; Schmitt et al., 2013, 2017; Christensen et al., 2018; **Figure 5**). This fractionation might be explained by successive removal of light Ca from the xylem sap into cell walls of the xylem tissues (Cobert et al., 2011; Schmitt et al., 2018). Therefore, heavy Ca is further transported along the transpiration stream toward the leaves. Furthermore, pods of beans were lighter than leaves but not distinguishable from stems at regular Ca supply (Cobert et al., 2011; Schmitt et al., 2013). However, the isotope fractionation between leaves and pods was negligible at low Ca supply which strongly suggests that different processes controlled the Ca transfer to the pods at distinct Ca supply. Despite the fact that Ca is usually considered as phloem immobile, Ca mass balances revealed that Ca can be re-translocated from roots and leaves of several plant species at low Ca supply (Maillard et al., 2015). Hence, the degree of Ca re-translocation in plants could determine the Ca isotope composition in phloem sinks and sources.

Iron

Plants preferentially take up heavy Fe from phytoavailable soil pools ($\Delta^{56}Fe_{plant\text{-}phytoavailable}$ −0.11 to +1.36‰, Garnier et al., 2017;

Wu et al., 2019; Liu et al., 2019; Chen et al., 2021; **Figure 6**). Plant Fe acquisition from soils includes the dissolution of Fe(III) minerals and root membrane transport, but the Fe acquisition strategy differs among plant species (Connorton et al., 2017). Strategy I plants (e.g., tomato) are equipped with root surface reductases to reduce insoluble Fe(III) to Fe(II) prior to cross-membrane transport. Strategy II plants (e.g., oat) release phytosiderophores that mobilize Fe(III) from the mineral lattice. The Fe(III)-phytosiderophore complex is then transported across the plasma membrane. The isotope fractionation $\Delta^{56}Fe_{plant\text{-}bulk.soil}$ was 1.8‰ lighter in strategy I (e.g., bean) compared to strategy II (e.g., oat) plants (Guelke and von Blanckenburg, 2007). In strategy I plants, kinetically controlled reduction of Fe(III) to Fe(II) prior to membrane transport could yield large isotope fractionation (Johnson et al., 2020). In strategy II plants, Fe binding to chelating molecules released by the plant may induce comparably small equilibrium Fe isotope fractionation (Dideriksen et al., 2008). These results were confirmed in hydroponics where Fe was supplied as Fe(III)-EDTA (Guelke-Stelling and von Blanckenburg, 2012). The negative isotope fractionation during uptake was more pronounced in strategy I (bean) compared to strategy II (oat) plants. Strategy I plants may have reduced Fe(III)-EDTA to Fe(II) while no reduction was required during the ligand exchange from Fe(III)-EDTA to Fe(III)-phytosiderophores in strategy II plants (Guelke-Stelling and von Blanckenburg, 2012; Liu et al., 2019). Hence, the absence and presence of a Fe reduction step might be the major factor that causes distinct Fe isotope fractionation in strategy I and II plants during Fe acquisition.

Several studies indicated that the distinct $\Delta^{56}Fe_{plant\text{-}source}$ values of strategy I and II plants are not universally applicable (Kiczka et al., 2010; Moynier et al., 2013; Liu et al., 2019; Wu et al., 2021; **Figure 6**). In field studies, the $\Delta^{56}Fe_{plant\text{-}source}$ values of strategy I and II plants differed less. This is probably due to less controlled environmental conditions in the field and/or the use of a variety of non-model plants for which Fe acquisition strategies are less known. In addition, there might be other processes than root surface reduction and chelation by phytosiderophores that cause Fe fractionation during plant acquisition. In paddy soil-rice systems, root plaque is formed in the oxidized rhizosphere where Fe precipitates as Fe(III) oxides in the root apoplast (Garnier et al., 2017; Chen et al., 2021). This precipitation induced a strong isotope fractionation between pore water and root plaque ($\Delta^{56}Fe_{root.plaque\text{-}pore.water}$ +1.41 to +2.24‰). Moreover, Fe isotope composition of roots differed with and without Fe plaque. Similar findings were also reported for plants grown in aerated soils for different Fe pools in the roots of alpine plants (Kiczka et al., 2010). These results highlight that Fe (re-)precipitation processes in the rhizosphere and

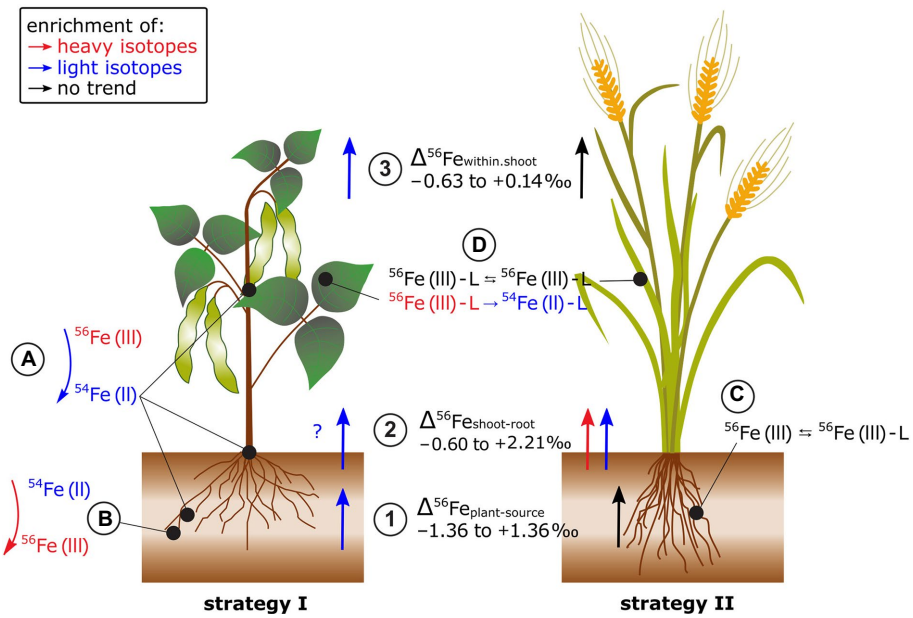

FIGURE 6 | Fe isotope fractionation in plants for Fe acquisition strategy I and II plants. (1) Fe isotope fractionation between the Fe source and the plant strongly depends on the Fe source (i.e., Fe-EDTA in hydroponics, bulk soil, or soil extract). In most cases, Fe acquisition by plants leads to a stronger enrichment of light isotopes in strategy I plants (e.g., tomato and beans) compared to strategy II plants. (2) The Fe isotope fractionation between shoot and root highly depends on the root Fe pools analyzed since significant fractionation can occur between precipitated Fe in the root apoplast compared to Fe that is taken up into the symplast and not deposited in the root apoplast. (3) Reproductive organs tend to be enriched in light isotopes in strategy I plants while no such fractionation step occurs in strategy II plants. **(A)** The Fe reduction from Fe(III) to Fe(II) prior to membrane transport may explain the successive enrichment of light isotopes from soil *via* roots and leaves to reproductive organs in strategy I plants. **(B)** Fe reoxidation from soluble Fe(II) to insoluble Fe(III) in the root apoplast can lead to an enrichment of light Fe isotope in the soluble Fe fraction. **(C)** In strategy II plants, the mobilization of Fe(III) from the mineral lattice of the soil by phytosiderophores (L for ligand, e.g., deoxymugineic acid) does not require a Fe reduction step and leads, if at all, to small Fe isotope fractionation. **(D)** Within the shoot, ligand (L) exchange of Fe (e.g., nicotianamine, citrate, and ferritin) that can include Fe redox changes may further fractionate Fe isotopes.

apoplast need to be considered to approach the "true" $\Delta^{56}Fe_{plant\text{-}source}$ value.

Iron isotope fractionation between root and shoot ($\Delta^{56}Fe_{shoot\text{-}root}$) ranged from −0.60 to +2.02‰ (Kiczka et al., 2010; Guelke-Stelling and von Blanckenburg, 2012; Wu et al., 2019, 2021; Chen et al., 2021; **Figure 6**). There was no clear preference for light or heavy Fe isotope transport from root to shoot while different methodologies to separate Fe root pools limit the comparability of the $\Delta^{56}Fe_{shoot\text{-}root}$ data (see previous paragraph).

Fe isotopes fractionate significantly between different shoot organs (Guelke and Von Blanckenburg, 2007; Guelke-Stelling and von Blanckenburg, 2012; Arnold et al., 2015; Chen et al., 2021; **Figure 6**). $\Delta^{56}Fe_{within.shoot}$ differed between strategy I (e.g., beans) and II plants, similar as for $\Delta^{56}Fe_{plant\text{-}source}$ (e.g., oat, Guelke-Stelling and von Blanckenburg, 2012). Seeds of strategy I plants were lighter than the remaining shoot while no such fractionation occurred in strategy II plants or rice (Guelke and Von Blanckenburg, 2007; Guelke-Stelling and von Blanckenburg, 2012; Arnold et al., 2015; Chen et al., 2021). The preferential transport of light Fe isotopes into seeds in strategy I was ascribed to Fe reduction (Guelke-Stelling and von Blanckenburg, 2012). Within the leaf cells, heavier isotopes are thought to be preferentially stored as Fe(III) in the vacuoles or in proteins, such as ferritin. The remobilization of Fe requires a reduction of Fe(III) to Fe(II) for transport as, for example, Fe(II)-nicotianamine. Likewise, the negligible Fe isotope fractionation within shoots of strategy II plants indicates that Fe(III) is either quantitatively reduced to Fe(II) or such redox changes are absent.

Nickel

Plants that grew on soils with high Ni concentrations were isotopically lighter than phytoavailable soil pools ($\Delta^{60}Ni_{plant\text{-}extract}$ −0.51 to −0.06‰, Estrade et al., 2015; Zelano et al., 2020; **Figure 7**). In hydroponics, light isotopes were also preferentially taken up from the nutrient solution ($\Delta^{60}Ni_{plant\text{-}solution}$, −0.90 to −0.07‰, Deng et al., 2014). Nickel hyperaccumulator plants took up lighter isotopes compared to Ni non-hyperaccumulator plants (Deng et al., 2014). In hyperaccumulators, the Ni uptake may be kinetically controlled due to the high metal transport rate of low-affinity transporters that leads to depletion of Ni in the rhizosphere. The Ni flow from bulk solution toward the roots may be diffusion driven which favors light isotopes (Rodushkin et al., 2004). Besides, Ni speciation in the hydroponic nutrient solution may have induced isotope fractionation between the free ionic Ni^{2+} and the complexed Ni pool. Particularly at low Ni supply, only a small fraction of Ni was present as free ionic Ni, while most of the Ni was complexed to EDTA. The EDTA may have enriched the free ionic Ni fraction in light isotopes and thereby contributed to the uptake of light Ni isotopes in plants. Heavy Ni isotope complexation to organic ligands was corroborated by theoretical and experimental studies on Ni-citrate complexes (Fujii et al., 2014; Zelano et al., 2020).

The $\Delta^{60}Ni_{shoot\text{-}root}$ and $\Delta^{60}Ni_{within.shoot}$ values were positive, negative or zero, depending on the plant and growth conditions (Deng et al., 2014; Estrade et al., 2015; Ratié et al., 2019; Zelano et al., 2020; **Figure 7**). In hydroponically grown plants, a much higher fraction of Ni was transported from roots to shoots in hyperaccumulators, compared to the non-hyperaccumulator. In these experiments, the isotope fractionation followed distinct patterns: hyperaccumulator plants had negative $\Delta^{60}Ni_{shoot\text{-}root}$ values, whereas those of non-hyperaccumulators were positive (Deng et al., 2014). Both $\Delta^{60}Ni_{shoot\text{-}root}$ and $\Delta^{60}Ni_{leaves\text{-}stem}$ varied with plant age and phenological stage of plants (Estrade et al., 2015; Zelano et al., 2020). The biochemical processes that generate the variation in $\Delta^{60}Ni_{shoot\text{-}root}$ and $\Delta^{60}Ni_{leaves\text{-}stem}$ are not well understood except that experimentally derived equilibrium fractionation factors as well as combined speciation and isotopes studies suggest that Ni complexation to organic ligands in plants is not a main driver of Ni isotope fractionation in plants (Zelano et al., 2018, 2020).

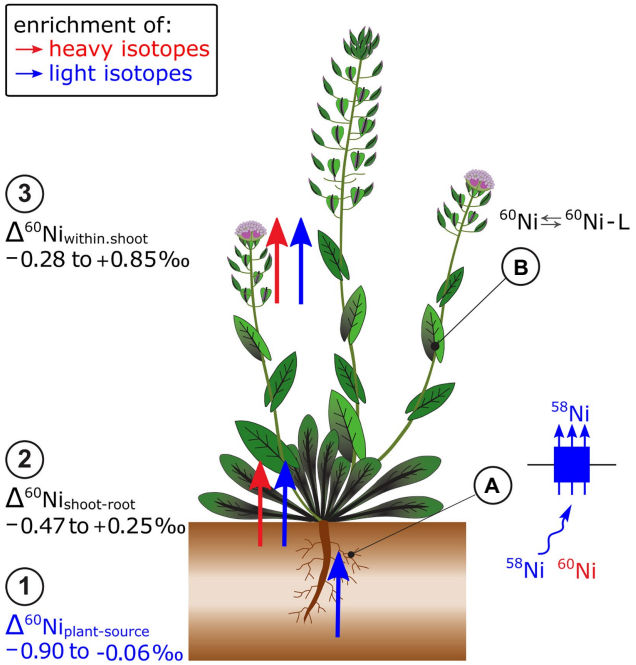

FIGURE 7 | Nickel isotope ratios have been mostly measured in Ni hyperaccumulating plants. (1) Root uptake leads to an enrichment of light Ni isotopes in plants. (2) From roots to shoots as well as (3) within shoots, though no clear pattern of isotope fractionation has been identified so far. **(A)** It is hypothesized that the enrichment of light isotopes during plant uptake of Ni is induced by low-affinity transport. High Ni uptake rates in hyperaccumulator plants may induce a depletion of Ni in the proximity of the membrane transporters and induce a Ni diffusion which leads to additional enrichment of light isotopes during uptake. **(B)** Within the shoot, Ni speciation to organic ligands (L), such as citrate, may be excluded as major factor controlling Ni isotope fractionation.

Copper

Cu isotope fractionation between the Cu source and plants ($\Delta^{65}Cu_{root\text{-}source}$) and the Cu source and the root can be positive, negative, or zero (Jouvin et al., 2012; Ryan et al., 2013; Li et al., 2016; Blotevogel et al., 2022; **Figure 8**). Results on Cu isotope fractionation during plant uptake are difficult to

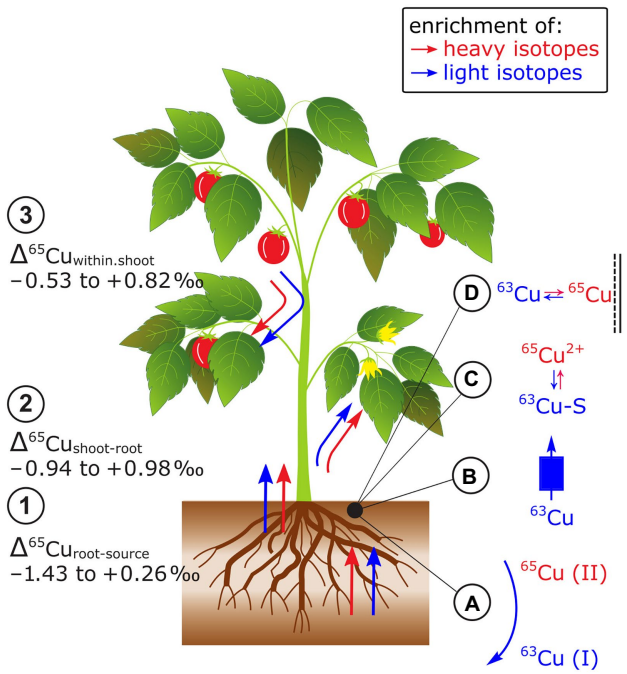

FIGURE 8 | Cu isotope fractionation in plants exemplified for tomato plants. (1) Root uptake can lead to an enrichment of heavy or light Cu isotopes. The isotope fractionation during root uptake is more negative in Fe strategy I plants compared to strategy II plants. At low Cu supply light isotopes were preferentially taken up compared to heavy isotopes at high supply likely due to a shift from active to passive uptake. (2) Shoots can be enriched in light and heavy isotopes compared to roots. The enrichment of light isotopes increases with organ height and Cu availability. (3) Cu isotopes fractionate in shoots of Fe strategy I plants is stronger than in strategy II plants. **(A)** Cu reduction induced by root reductases favors light Cu isotopes, **(B)** Cu membrane transport can favor light Cu isotopes, and **(C)** Cu binding to S to detoxify Cu in the root at high Cu supply may contribute to the retention of light isotopes in roots. **(D)** Cu binding to O ligands in the root apoplast should retain heavy Cu in the roots.

compare as in most cases $\Delta^{65}Cu_{roots\text{-}source}$ values were reported instead of $\Delta^{65}Cu_{plant\text{-}source}$. Furthermore, plants were exposed to distinct Cu sources in hydroponics (e.g., ionic Cu^{2+} vs. chelated Cu) and Cu bound to the root apoplast was desorbed in one study prior to root analyzes (Ryan et al., 2013). Nonetheless, preferential uptake of light isotopes seems to be controlled by the reduction of Cu(II) to Cu(I) prior to root membrane transport into tomato (Jouvin et al., 2012; Ryan et al., 2013). The Cu reduction may explain why strategy I plants (according to their Fe acquisition strategy, see section Iron) take up lighter isotopes than strategy II plants. For the latter, the Cu reduction seems to be not a requirement for Cu uptake (Ryan et al., 2013). However, studies on yeast mutants showed that specific Cu membrane transporters favor light isotopes without a preceding Cu reduction indicating that the preferential uptake of light Cu isotopes is not solely controlled by Cu reduction (Cadiou et al., 2017). Moreover, distinct Fe supply neither affected $\Delta^{65}Cu_{plant\text{-}source}$ nor $\Delta^{65}Cu_{roots\text{-}source}$ (Jouvin et al., 2012; Ryan et al., 2013) while a higher Cu supply shifted $\Delta^{65}Cu_{roots\text{-}source}$ from light to heavy in grapevine plants (Blotevogel et al., 2022). This shift was assigned to a switch from active toward passive uptake pathways due to increased Cu availability. Together, the identified processes that control $\Delta^{65}Cu_{plant\text{-}source}$ are Cu reductase activity at the root surface, membrane transport, and adsorption to root surfaces that may all vary with Cu supply.

Copper isotope fractionation between root and shoot ($\Delta^{65}Cu_{shoot\text{-}root}$) can be positive, negative or zero (Weinstein et al., 2011; Jouvin et al., 2012; Ryan et al., 2013; Li et al., 2016; Blotevogel et al., 2022; **Figure 8**). Similarly, as for the $\Delta^{65}Cu_{plants\text{-}source}$ values, the comparison of $\Delta^{65}Cu_{shoot\text{-}root}$ values may be limited particularly due to different Cu root desorption strategies (Jouvin et al., 2012; Ryan et al., 2013). Enrichment of light isotopes in shoots compared to roots was ascribed to Cu diffusion and membrane transport that were categorized as kinetic fractionation processes (Weinstein et al., 2011; Jouvin et al., 2012). Light isotope enrichment in leaves was accentuated in grapevine at high Cu supply (Blotevogel et al., 2022). Exposed to high Cu concentrations and after root Cu desorption, $\Delta^{65}Cu_{shoot\text{-}root}$ was neutral in oat (strategy II) while tomato (strategy I) shoots were enriched in heavy isotopes compared to their roots (Ryan et al., 2013). The contrasting $\Delta^{65}Cu_{shoot\text{-}root}$ in Fe strategy I and II plants were ascribed to the reoxidation of Cu(I)-S to Cu(II) prior to xylem loading (Ryan et al., 2013). Similar to Fe, this reoxidation step may only occur in strategy I plants which results in a strong enrichment of heavy isotopes in the shoots compared to the roots. However, in strategy II plants, the reoxidation step might be absent or all Cu(I) is reoxidized to Cu(II).

Within plant shoots, an enrichment of light isotopes in leaves appears to increase with plant height in hairy-leaved sedge (Weinstein et al., 2011) and/or with Cu concentration in grapevine leaves (Blotevogel et al., 2019, 2022; **Figure 8**). The enrichment of light Cu isotopes was ascribed to diffusion and membrane transport (Weinstein et al., 2011) as well as Cu immobilization by Cu complexation to S (Cu(I)-S) that favors light isotopes (Cadiou et al., 2017; Blotevogel et al., 2019). However, detailed analyses of the Cu tolerant plant *E. splendens* revealed that redistribution of Cu from senescent to younger leaves and reproductive organs can cancel the correlations between leaf height and Cu concentration with Cu isotope ratios (Li et al., 2016). Ryan et al. (2013) found a more pronounced Cu isotope fractionation between stems and leaves in Fe strategy I than in II plants. Similarly to Fe, the stronger isotope fractionation in strategy I plants is likely driven by Cu redox cycles while these cycles may not control the Cu isotope fractionation in shoots of strategy II plants.

Zinc

A previously published review summarized that adsorption, type of membrane transport (low vs. high-affinity transport), speciation, compartmentalization, and diffusion control the Zn isotope fractionation in plants (Caldelas and Weiss, 2017). This conclusion was based on studies that investigated a diversity of plant species and applied methods, such as (i) Zn uptake studies with unicellular organisms

(Gélabert et al., 2006; John et al., 2007), (ii) root extraction techniques (Tang et al., 2016), (iii) elaborated hydroponic (e.g., Smolders et al., 2013) and pot studies (Houben et al., 2014; Couder et al., 2015), (iv) combined Zn speciation and isotope analyses (Aucour et al., 2015), and (v) a set of theoretically and experimentally determined isotope fractionation factors for Zn binding to organic ligands (Jouvin et al., 2012; Fujii et al., 2014; Marković et al., 2017).

After the review of Caldelas and Weiss (2017); a field study on paddy soil-rice systems showed more positive $\Delta^{66}Zn_{rice\text{-}source}$ values at low Zn than at regular Zn supply (Weiss et al., 2021; **Figure 9**). This shift toward heavy Zn isotopes at low Zn supply can be explained by chelators (e.g., the phytosiderophores 2'deoxymugineic acids) that are secreted by roots to strip Zn from the soil matrix and subsequent uptake of the entire Zn-phytosiderophore complex by a membrane transporter (Smolders et al., 2013; Arnold et al., 2015; Weiss et al., 2021). Since 2'deoxymugineic acids bind heavy Zn isotopes at equilibrium (Marković et al., 2017), the uptake of Zn-phytosiderophore complexes may have induced the shift toward heavy isotopes. Furthermore, a unicellular organism study showed a dependence of $\Delta^{66}Zn_{cell\text{-}source}$ on Zn uptake rates (Köbberich and Vance, 2017). At low uptake rates, heavier Zn isotopes were taken up than at high uptake rates. This study is discussed in detail in section Heavy but More Mobile and the Question of Kinetic vs. Equilibrium Fractionation that focuses on unicell studies.

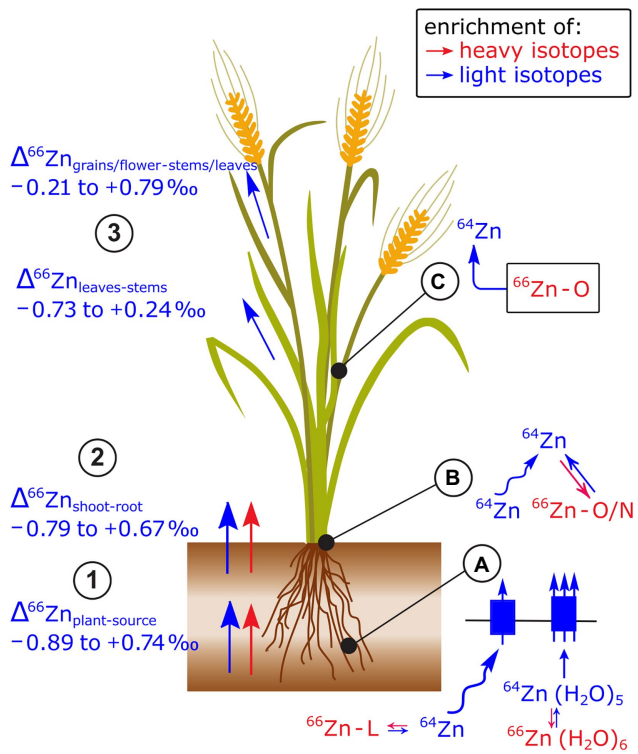

FIGURE 9 | Zn isotope fractionation has been reported in several plant species (see review of Caldelas and Weiss, 2017 and references therein). (1,2) In most cases, light Zn isotopes are preferentially taken up by plants and transported from root to shoot. (3) Within the shoots, leaves are enriched in light isotopes compared to stems and reproductive organs are enriched in light isotopes compared to the remaining shoot or senescent tissues. **(A)** The uptake of light Zn isotopes has been ascribed to diffusion, Zn speciation in solution, and stripping of the hydration shell prior to membrane transport. A set of studies provides robust evidence, that at low Zn supply, Zn complexation to organic ligands (L), such as phytosiderophores followed by the uptake of the Zn-phytosiderophores leads to a shift toward heavy isotopes in cereals. During membrane transport, the enrichment of light isotopes is stronger at regular than at low Zn supply. **(B)** Within the root, binding of Zn to O/N donors of organic ligands in the cytosol and vacuole as well as diffusion of the Zn in the apoplast and symplast toward the xylem may control the preferential transport light isotopes from roots to shoots. **(C)** The enrichment of light Zn isotopes in reproductive plant organs is induced by the strong retention of heavy isotopes in mature leaves or senescing tissues likely induced binding of Zn to O donors of organic ligands in the apoplast, cytosol, or vacuole.

Changes to Zn isotope composition in the shoot of wheat ($\Delta^{66}Zn_{within.shoot}$) were measured during the grain filling period (Wiggenhauser et al., 2018). In this period, leaves and stems showed a net loss of Zn and a depletion of light isotopes, while grains became enriched in light isotopes compared to stems and leaves. These results strongly suggest that light Zn isotopes were transported within the phloem toward the grains while heavy isotopes were retained in senescing shoot organs. The retention of heavy Zn isotopes in senescent shoot organs was ascribed to Zn binding to O containing ligands in the apoplast, such as pectins (Aucour et al., 2017).

Cadmium

Plants were isotopically lighter than their phytoavailable Cd source, in hydroponic and soil studies (Wei et al., 2018; Imseng et al., 2019; Moore et al., 2020; Wiggenhauser et al., 2021a; Zhang et al., 2021; Zhong et al., 2021, 2022; **Figure 10**). An exception was that a hyperaccumulator plant grown on Cd contaminated soil had a heavier isotope composition than the phytoavailable pool (+0.02 to +0.18‰, Zhou et al., 2020). Two rice studies found that the enrichment in light isotopes was slightly enhanced in non-flooded compared to flooded soils (Wiggenhauser et al., 2021a; Zhong et al., 2022) while one found the opposite (Zhang et al., 2021). Possible factors causing this difference may be distinct initial soil properties (e.g., pH and soil Cd concentration) or changes in the phytoavailability of elements, such as Mn and Fe upon flooding. Several studies investigated the role of NRAMP5 on Cd isotope fractionation during uptake. In rice (*Oryza sativa*), both a small upregulation and knockout of *OsNRAMP5* were associated with uptake of lighter Cd isotopes compared to control treatments (Zhang et al., 2021; Zhong et al., 2022). This apparent discrepancy is discussed in section Genetic Approaches for Isotope Fractionation Factors. Yeasts expressing cacao (*Theobroma cacao, Tc*) *TcNRAMP5* preferentially took up lighter Cd isotopes compared to the control yeast (i.e., with empty vector, Moore et al., 2020). In addition to membrane transport, light Cd uptake may be partly due to adsorption of preferentially light Cd onto the root apoplast ($\Delta^{114/110}Cd_{root\ absorbed\text{-}adsorbed}$ of −0.17‰, Zhang et al., 2021).

In most cases, shoots were isotopically heavier than roots in wheat, barley, rice, cacao, and a Cd accumulator plant (Wiggenhauser et al., 2016, 2021a,b; Wei et al., 2018; Imseng et al., 2019; Moore et al., 2020; Wang et al., 2021; Zhong et al., 2021; **Figure 10**). The retention of light Cd

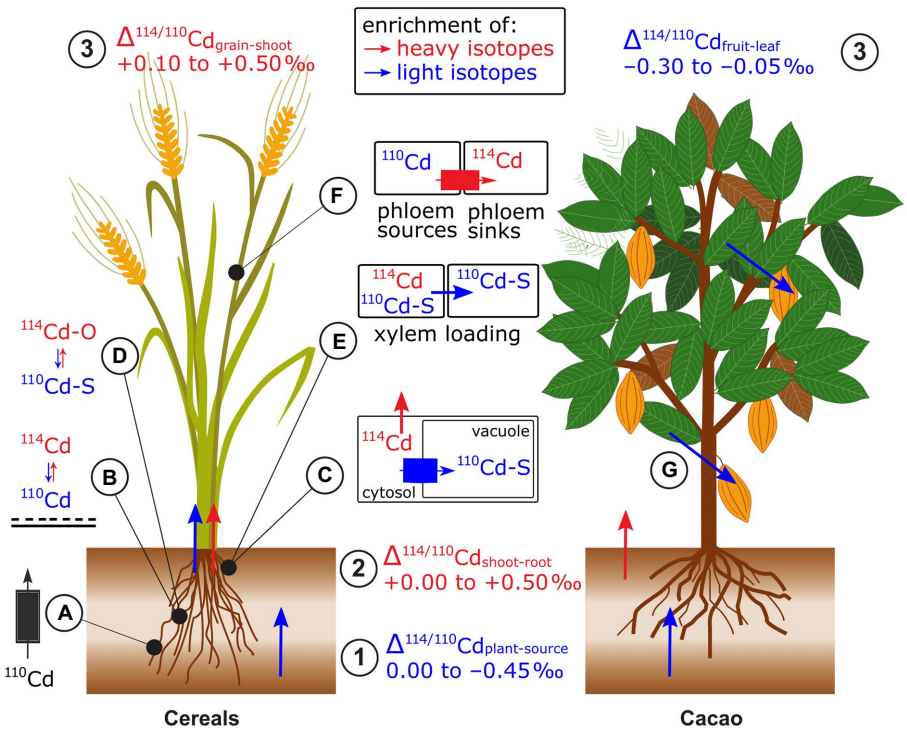

FIGURE 10 | Cadmium isotope fractionation in plants exemplified for cereals and cacao. (1) Root uptake leads to an enrichment of light isotopes in plants. (2) Shoots are mostly enriched in heavy isotopes compared to roots. (3) In cereals, grains are enriched in heavy isotopes compared to the remaining shoot while in cacao, the beans tend to be enriched in light isotopes compared to other shoot parts. **(A)** Root membrane transport of NRAMP5 induces an enrichment or depletion in light Cd isotopes during uptake. **(B)** Light isotopes are preferentially sorbed to the negatively charged surfaces in the root apoplast. **(C)** Light Cd isotopes are sequestrated in root vacuoles *via* tonoplast proteins. **(D)** Chelation of Cd by thiols (Cd-S) contributes to the sequestration of light Cd in roots. **(E)** The non-membrane bound protein CAL1 that preferentially binds light Cd with thiols in the xylem parenchyma cells and transports light Cd into the xylem. **(F)** Xylem to phloem transfer in the nodes favors heavy Cd isotopes through transport by OsHMA2 and LCT. **(G)** In cacao, given that beans are enriched in light isotopes compared to leaves, the processes transporting and loading Cd into beans may differ from cereals.

isotopes in roots of cereals and numerous different cacao genotypes was ascribed to vacuolar sequestration. This explanation is supported by Rayleigh isotope fractionation models (Imseng et al., 2019; Moore et al., 2020). Furthermore, while fitting the same isotope model, substantial differences in translocation of Cd were observed for distinct cacao clones, which was ascribed to differences in the expression of genes that encode dominant Cd transporters, rather than distinct biochemical processes (Moore et al., 2020). The role of vacuolar sequestration on Cd isotope fractionation was further supported by results of wild-type mutant experiments on rice (Zhang et al., 2021). These results suggested that the tonoplast transporter heavy metal ATPase 3 (HMA3) preferentially transports light Cd isotopes into the vacuole. In the vacuole, Cd is then sequestered by strong binding to thiols that may contribute further to the retention of light Cd (Wei et al., 2018). This hypothesis is supported by synchrotron X-ray absorption spectroscopy (XAS) results that showed the majority of Cd in rice roots can be bound to S-containing ligands, such as glutathione or phytochelatins, which are expected to preferentially bind light Cd isotopes (Yan et al., 2016; Wiggenhauser et al., 2021a; Zhao et al., 2021). Alternatively, Zhong et al. (2022) showed that $\Delta^{114/110}Cd_{shoot\text{-}root}$ in rice can be further impacted by the protein CAL1. This protein complexes Cd in xylem parenchyma cells and Cd-CAL1 complexes are then transported into the xylem. Furthermore, the higher expression of *CAL1* coincided with a strong shift toward light isotopes during root to shoot translocation.

Cd isotope composition in reproductive and shoot organs can strongly differ ($\Delta^{114/110}Cd_{reproductive\text{-}shoot.organ}$ −0.30 to +0.50‰, **Figure 10**). While Rayleigh fractionation modeling for different plants suggests dominantly unidirectional xylem flow from roots to shoots (Wiggenhauser et al., 2016; Wei et al., 2018; Moore et al., 2020), it has been shown that cereals likely use phloem redistribution on grain filling (Wiggenhauser et al., 2021b; Zhong et al., 2021). In rice, an important hub for the transfer of Cd from the xylem to the phloem are the nodes (Yamaji and Ma, 2014). First data on Cd isotopes in nodes indicated that the xylem to phloem transfer of Cd contributes to the enrichment of heavy isotopes in grains (Wiggenhauser et al., 2021b; Zhong et al., 2021). Additionally, combined isotope and gene expression analyses strongly suggested that membrane proteins (OsHMA2, OsLCT1) that transfer Cd from the xylem to the phloem in the node contribute to the enrichment of heavy Cd in grains (Zhong et al., 2021). The role of Cd speciation in the nodes (mainly Cd-S) on Cd isotope fractionation

between nodes, leaves, and grains is not understood yet (Wiggenhauser et al., 2021b). In contrast to cereals, Cd loading into cacao beans may use a different mechanism (Barraza et al., 2019) since Cd in cacao beans was found to be isotopically lighter than in the leaves. The identical isotope compositions between cacao leaves and leaf litter support this hypothesis, because isotope fractionation would be expected if there was phloem redistribution on senescence.

Emerging Elements

Potassium

Soybeans and grasses preferentially took up light isotopes from hydroponics ($\Delta^{41/39}K_{plant\text{-}solution}$ of −0.60‰) and also from phytoavailable soil pools (Christensen et al., 2018; Li et al., 2021). $\Delta^{41/39}K_{shoots\text{-}roots}$ were reported to be positive and negative, however, full mass balances were not provided. Within shoots, dead leaves were isotopically lighter than living leaves (Li et al., 2021). During plant uptake and translocation, membrane transport may strongly control K isotope fractionation (Christensen et al., 2018). The selectivity of an ion channel is at least partly controlled by the ionic radius and could explain the preferential uptake of ^{39}K over ^{40}K due to the smaller ionic radius of ^{39}K (Lockless et al., 2007). Additionally, K transport through an ion channel requires dehydration which would favor ^{39}K for membrane transport (MacKinnon, 2003; Hofmann et al., 2012; Christensen et al., 2018). Within the plant, diffusion may only play a minor role for K isotope fractionation in moving saps, such as in the xylem and phloem (Christensen et al., 2018). Binding of heavy isotopes to pectate may be an additional factor that controls the K isotope fractionation in plants, as deduced from combined K isotope and XAS analysis (Li et al., 2021).

Molybdenum

The first Mo isotope analyses in plants revealed that in three out of four plant species (lingonberry, common juniper, and rosebay willowherb), heavy isotopes were preferentially transported from roots to stems ($\Delta^{98}Mo_{stem\text{-}root}$ −0.00 to +0.70‰) and from stems to leaves ($\Delta^{98}Mo_{leaves\text{-}root}$ −0.00 to +0.40‰), while in blueberry, Mo isotopes were not fractionated (Malinovsky and Kashulin, 2018). No processes have been yet ascribed to the systematic Mo isotope fractionation patterns.

Thallium

White mustard grown in hydroponics preferentially took up light isotopes ($\Delta^{205}Tl_{plant\text{-}source}$ −0.20 to −0.09‰) while heavy isotopes were transported from roots to shoots, particularly at high Tl supply ($\Delta^{205}Tl_{shoot\text{-}root}$ −0.07 to +0.72‰, Vaněk et al., 2019). Within shoots, Tl isotope fractionation reached $\Delta^{205}Tl_{shoot\text{-}root}$ of 0.43‰ (Kersten et al., 2014; Rader et al., 2019; Vaněk et al., 2019). Although there is no known biological function for Tl, it has been posited that the isotope fractionation between roots and shoots is due to physiologically controlled translocation which may be related to membrane transport and Tl speciation. Since Tl^+ and K^+ have similar ionic radii (1.76 Å and 1.60 Å), it has also been suggested that Tl uses K channels to translocate (Vaněk et al., 2019). In addition, Tl in plants appears to be mostly present as Tl(I)aq and Tl-acetate (O-ligand) in roots, stems, and leaves.

DISCUSSION

Linkages of biological and physico-chemical processes that are known to fractionate isotopes in plants, and highlights knowledge gaps that could be effectively filled, are summarized in **Supplementary Table S3**. In the next sections, we interlink the information collected for the individual elements in the results section to advance the use of non-traditional isotopes for process tracing in plants.

Similar Elements, Similar Isotope Fractionation?

Chemically similar elements can undergo similar or opposite isotope fractionation in plants. For example, for the redox sensitive transition metals Fe and Cu, reduction can be required prior to membrane transport (Cadiou et al., 2017; Johnson et al., 2020, **Figures 6**; **8**). The reduction enriches the reduced Fe and Cu fractions in light isotopes and may largely control the shift toward light isotopes during acquisition in strategy I plants (Guelke-Stelling and von Blanckenburg, 2012; Ryan et al., 2013).

In contrast, for the non-redox sensitive transition metals Zn and Cd, the within-plant isotope fractionation differs as light Zn but heavy Cd isotopes are more mobile in plants (Arnold et al., 2015; Wiggenhauser et al., 2018; **Figures 9, 10**). Currently, two hypotheses are discussed that explain the opposing isotope fractionation between Zn and Cd. The first is that the distinct isotope fractionation is caused by the higher affinity of Cd to S donors of organic molecules (e.g., cysteine) compared to Zn, which in turn has a higher affinity to O and N donors (e.g., histidine) compared to Cd (Maret and Moulis, 2013). Thiol chelators (e.g., phytochelatin) can strongly bind Cd and contribute to the sequestration of light Cd isotopes in vacuoles (Nocito et al., 2011). Based on *ab initio* calculations, preferentially light Zn and Cd isotopes bind to S chelators at equilibrium (e.g., Fujii et al., 2014; Zhao et al., 2021). Given that Cd has a higher affinity to thiols than Zn, competition for thiol binding could control the opposing isotope fractionation of these trace metals in cereals. The second hypothesis is based on Cd sorption experiments on humic acid and *ab initio* calculations (Ratié et al., 2021; Zhao et al., 2021). Binding of ionic Cd to carboxyl groups (Cd-O) leads to a small shift toward light isotopes (Ratié et al., 2021). The isotope shift was ascribed to the dehydration of Cd from $Cd(H_2O)_6$ to $Cd(H_2O)_5$ prior to binding of Cd to carboxyl groups. The dehydration of Cd favors light isotopes while the opposite is the case for Zn (Fujii et al., 2014; Zhao et al., 2021). Hence, the opposing isotope fractionation of Zn and Cd could be induced by dehydration processes that may take place prior to membrane transport or during ligand exchange and/or by the high affinity of Cd to thiols.

Similarly, the alkaline earth metals Ca and Mg fractionate in an opposite manner during plant uptake (**Figures 3**, **5**).

This is partly due to preferential sorption of light Ca and heavy Mg isotopes onto negatively charged root surfaces (Bolou-Bi et al., 2010; Schmitt et al., 2017). Therefore, plants preferentially take up lighter Ca but heavier Mg isotopes compared to their Ca and Mg source. In a study on goethite, which like pectins provides negatively charged O donors, Mg had a tendency to form inner-sphere complexes, resulting in the loss of its water coordination shell. Calcium, in contrast, formed outer-sphere complexes, keeping its water coordination shell (Rahnemaie et al., 2006). Hence, the opposing isotope fractionation of Ca and Mg can likely be explained by a difference in the stability of their hydration sphere (Essington, 2015), as also hypothesized for Zn and Cd. The within-plant isotope fractionation of Ca and Mg does not clearly differ (**Figures 3**, **5**). Hence, processes, such as structural binding to cell walls or oxalate precipitation for Ca, and cross-membrane transport and partitioning in functional molecules for Mg, may mask isotope effects induced by dehydration and sorption.

These examples illustrate that specific chemical properties can induce marked differences in isotope fractionation in plants, even if elements belong to the same group in the periodic table. Hence, the use of different elements to explain isotope fractionation patterns by analogy is limited.

Heavy but More Mobile and the Question of Kinetic vs. Equilibrium Fractionation

For elements, such as Mg, Si, and Cd, heavy isotopes are more mobile than light isotopes in plants (**Figures 3, 4**, **10**). These findings contradict the established idea that biological processes in plants favor the transport of light isotopes due to enzymatic reactions that are kinetically controlled (Dawson et al., 2002). Preferential uptake of heavy Mg isotopes seems to be controlled by the sorption to root surfaces (**Figure 4**). In this case, equilibrium isotope fractionation seems to outcompete membrane transport, which may be kinetically controlled. Light Si isotopes precipitate in roots as phytoliths and light Cd isotopes are likely sequestered in vacuoles, leading to higher mobility of heavy isotopes within the plant (**Figures 4**, **10**; Ding et al., 2009; Wiggenhauser et al., 2021a). Precipitation of Si in shoots is likely kinetically controlled because it takes place at the end of the transpiration stream, where water evaporation leads to constant supersaturation and new Si influx. In contrast, vacuolar sequestration may be caused by a mix of kinetic and equilibrium fractionation (membrane transport and Cd chelation). These examples illustrate that kinetically controlled processes do not necessarily lead to a higher mobility of light isotopes in plants.

The importance to distinguish between kinetic and equilibrium fractionation was highlighted for Zn uptake of marine diatoms. These unicell organisms preferentially took up heavier Zn isotopes at low supply but light isotopes at high Zn uptake rates (John et al., 2008; Köbberich and Vance, 2017). At high Zn uptake rates, the negative $\Delta^{66}Zn_{organism\text{-}source}$ was ascribed to kinetic effects during membrane transport and to Zn speciation in the nutrient solution. At low Zn uptake rates, a pseudo-equilibrium may have been established between the ionic Zn in solution and the binding site of the membrane transporter, leading to a shift toward heavy isotopes (Jouvin et al., 2009; Fujii et al., 2014). These interpretations suggest that isotope fractionation of one biological process may not in all cases be kinetically or equilibrium controlled. Instead, there might be environmental conditions in which only kinetic, only equilibrium or both, determine the isotope fractionation in biological organisms. Deciphering whether isotope fractionation is kinetic or equilibrium is of high priority to advance process tracing by non-traditional isotope systems in plants.

The general rule that biological processes in plants favor the transport of light isotopes due to enzymatic reactions is based on studies on traditional isotopes, such as C, N, and S. For instance, the enzyme rubisco that catalyzes CO_2 fixation in plants induces a kinetically controlled enrichment of light C isotopes during C assimilation (O'Leary, 1993). Similarly, enzymatic processes involving N assimilation, such as nitrate reductase or glutamine synthetase, favor light N isotopes (Tcherkez, 2011). However, metals and metalloids act as cofactors for enzymes rather than being the target element of complex metabolism pathways as with C, N, and S. Yet, enzyme controlled processes can be crucial for the homeostasis of redox sensitive metals, such as Fe and Cu or the Mg-dechelatase mediated decomposition of chlorophyll (Connorton et al., 2017; Chen et al., 2018; Zandi et al., 2020). Hence, the impact of enzymatically controlled processes on the fractionation for non-traditional isotopes in plants might differ from traditional isotope systems.

Unicellular Organisms: A Suitable Model System for Isotope Studies?

Studies of unicellular organisms (unicell) have proven to be an effective tool to gain a detailed understanding of the biological uptake of nutrients and pollutants. Yeast mutants provided evidence that the reduction of Cu(II) to Cu(I), controlled by the reductase FRE1 and FRE2, leads to light Cu isotope enrichment during uptake (Cadiou et al., 2017). However, the mutants with dysfunctional reductases were still enriched in light isotopes, indicating that the high-affinity Cu transporters CTR1 and CTR3 preferentially transport light Cu isotopes. This illustrates that the negative $\Delta^{65}Cu_{cell\text{-}source}$ is driven by both reduction and membrane transport. The yeast study confirmed previously stated hypotheses that Cu reduction leads to a shift toward light isotopes during root uptake into strategy I plants, such as tomato (Jouvin et al., 2012; Ryan et al., 2013).

Isotope fractionation during uptake and compartmentalization of Cd was investigated using transgenic yeasts and *E. coli* (Horner et al., 2013; Moore et al., 2020). In yeast transformed with cacao (Tc) genes, expression of *TcNRAMP5* was associated with uptake of light Cd isotopes. These findings supported the hypothesis that the preferential binding of light Cd to the membrane transporter contributes to the overall enrichment of light Cd isotopes in cacao plants (**Figure 10**). Although the growth conditions were similar for both organisms, the magnitude of the fractionation was larger for the yeast suggesting that other transporters are contributing significantly to $\Delta_{organism\text{-}source}$ in cacao. Horner et al. (2013) measured Cd isotopes in cell

walls and other compartments of *E. coli*. The cell walls were enriched in light isotopes which was ascribed to Cd binding to cell wall thiols. Similarly to *E. Coli*, Cd isotopes in cereal roots were also enriched in light isotopes possibly due to vacuolar sequestration and detoxification through binding of Cd to chelating thiols in root vacuoles of cereals (Wiggenhauser et al., 2021a).

Cyanobacteria were employed to determine Mg isotope fractionation during uptake and compartmentalization (Pokharel et al., 2018). The positive$\Delta_{organism\text{-}source}$ value for cyanobacteria was related to Mg binding to functional molecules, such as chlorophyll or ATP in the cells. This binding generated intracellular Mg pools that were enriched in heavy (bound Mg) and light Mg isotopes (ionic Mg). Mass balances showed that the light ionic Mg pool was likely transported out of the cell, leading to a net enrichment of heavy Mg isotopes in cyanobacterium and thereby to a positive $\Delta_{organism\text{-}source}$. This intracellular Mg isotope fractionation may explain negative $Mg^{26}\Delta_{shoot\text{-}root}$ found in plants (**Figure 3**) where Mg bound to functional molecules (heavy) is retained in roots while ionic Mg (light) is transported through the xylem into the shoot. Likewise, heavy Mg isotopes stored in functional molecules in leaves could be re-translocated from senescing plant organs *via* phloem toward reproductive plant organs. However, such a relation was not found in wheat sampled at different growth stages (Wang et al., 2020). Hence, Mg binding to functional molecules alone does not explain the changing isotope compositions in leaves, which may be affected by Mg import and export in leaves and/or by long-distance transport pathways *via* xylem and phloem.

Together, unicell studies can provide a powerful method to test specific hypotheses on potential fractionation mechanisms in plants and to identify specific isotope fractionation factors. However, results of unicell studies need to be carefully extrapolated to plants as plants have developed several strategies to acquire elements (e.g., regulation of several membrane transporters, root exudation) and are complex organisms that exchange elements between different cells, tissues, and organs.

Genetic Approaches for Isotope Fractionation Factors

A variety of genetic approaches have been used to determine isotope fractionation factors associated with individual membrane proteins. For example, three different techniques have been used to investigate how NRAMP5 impacts the fractionation of Cd during uptake in cacao and rice (unicell transgenics, gene knockout, and gene expression monitoring). A yeast experiment using a gene from cacao (TcNRAMP5) supported the hypothesis that TcNRAMP5 preferentially transports light Cd isotopes (see section Heavy but More Mobile and the Question of Kinetic vs. Equilibrium Fractionation) and thereby contributes to the enrichment of light isotopes in cacao plants. Conversely, the knockout experiment in rice found that rice without *OsNRAMP5* preferentially took up light Cd compared to its wild type (Zhang et al., 2021). Since plants have a suite of different membrane proteins that can also transport Cd, the result favoring the interpretation that OsNRAMP5 takes up preferentially heavy Cd may reflect the upregulation of genes encoding other membrane proteins that induce an even larger isotopic shift than OsNRAMP5. The two gene expression experiments found that *OsNRAMP5* in rice was moderately upregulated in non-flooded soil (Zhong et al., 2021, 2022). In Zhong et al. (2022), there was no significant difference in $\Delta^{114/110}Cd_{rice\text{-}source}$ between flooded and non-flooded conditions, while Zhong et al. (2021) found an enrichment in light isotopes in rice that grew on the non-flooded conditions where *OsNRAMP5* was upregulated. Although the experimental conditions and the soil-rice systems of these two experiments were identical, the causes of these distinct observations were not discussed. Nevertheless, the studies of Zhong et al. (2021, 2022) are in agreement with the transgenic experiment results, which strongly suggest that NRAMP5 can contribute to preferential uptake of light isotopes in plants. The comparisons show that complementary techniques (e.g., knockout and transgenics), at similar environmental conditions, are necessary to cross-validate results and interpretations. The distinct outcomes of the NRAMP5 studies highlight that carefully obtained isotope fractionation factors with controlled model systems may still be masked by environmental factors in complex soil–plant systems.

FUTURE PERSPECTIVES

Isotope fractionation in plants is usually very systematic and can differ, for example, among plant ages, species, and nutrient supply. Although biotic and abiotic factors induce systematic isotope fractionation in plants, its interpretation is often challenging and relies on basic knowledge in plant sciences. Here we provide recommendations to better exploit the information provided by varying isotope compositions in plants to further advance non-traditional isotope process tracing in plants. Once these recommendations are implemented, isotope process tracing could be applied to detect and quantify changes in uptake and translocation pathways in response to changing nutrient supply as suggested for Mg (Wang et al., 2020), Cu (Blotevogel et al., 2022), and Zn (Weiss et al., 2021).

Basic Requirements for Plant Isotope Experiments

An indispensable requirement for the interpretation of isotope fractionation patterns in plants is the establishment of fractionation factors for specific physico-chemical processes. This requires experiments to quantify isotope fractionation for individual processes, such as precipitation (e.g., Guinoiseau et al., 2018) or binding to organic ligands (e.g., Ratié et al., 2021). In addition, there is a set of minimum requirements that must be taken into account to ensure a meaningful data set and discussion.

Planning phase:

- design experiments to test specific hypotheses and determine (co-)variables. These can range from environmental conditions, such as (i) pH (Cobert et al., 2011), (ii) varying nutrient sources (Rader et al., 2019), or (iii) nutrient limitations (Smolders et al., 2013), to biological changes, such as wild-type–mutant experiments (Zhang et al., 2021),

- include biological replicates to account for experimental variability (Wang et al., 2020),
- conduct plant growth experiments at physiologically relevant conditions to ensure nutrient levels are not additional variables impacting the isotope signatures of the targeted element,
- thoroughly document growth conditions (e.g., nutrient levels, light, temperature, plant protection regime), specific tissue type, and phenological growth stages at harvest (Meier, 2001).

Sample preparation:

- consider root treatments at harvest, such as root desorption by weak salt solutions (Tang et al., 2016). This separates apoplastic and symplastic element pools and enables the determination of isotope fractionation for apoplastic sorption and cross-membrane transport,
- take into account that the phytoavailability of elements and isotope composition in bulk and rhizosphere soil can be very different (e.g., Imseng et al., 2019).

Data analysis and evaluation:

- calculate the average concentration and isotopic mass balance of target elements. This is needed to elucidate fractionation upon root uptake from growth media (the $\Delta_{root\text{-}solution}$ does not inform on the fractionation during root uptake),
- once isotope compositions in different plant organs are measured, geochemical modeling approaches (e.g., Moore et al., 2020) can be used and incorporated with existing plant science knowledge to interpret what biological and physico-chemical processes are responsible for the systematic isotope fractionation patterns,
- analyze concentrations of other elements that may compete with the element of interest for, for example, membrane transporter and organic ligands.

Innovative Research Ideas and Methods

Provided that the requirements that are listed in section Basic Requirements for Plant Isotope Experiments are met, the following ideas can be included to expand the scope of plant stable isotope analyses. The ideas were selected from the individual element reviews and studies beyond those on stable isotope fractionation in plants.

- Isotope analyses in different plant organs and tissues (e.g., cortex, epidermis, rhizodermis) that are sampled at different growth stages (e.g., flowering, plant maturity) can provide useful information on internal transport processes and pathways of elements within plants (e.g., Wang et al., 2020).
- Measuring the isotope composition of different elements in the soil–plant system (e.g., Wiggenhauser et al., 2018).
- Further compartmentalization, for example, analysis of xylem sap, would provide complementary information to $\Delta_{shoot\text{-}root}$ and $\Delta_{shoot\text{-}grain/bean}$ values to understand the processes that control the transfer of elements from the roots to shoot organs including reproductive organs (Álvarez-Fernández et al., 2014).
- To aid such detailed and comprehensive experiments, improvements to sample throughput should be made. The efficiency of sample purification could be improved by (i) automated ion chromatography or sample purification systems (Husson et al., 2015; Morgan et al., 2018; Kidder et al., 2020; Zhou et al., 2021) or (ii) using new generation MC-ICP-MS instruments that are equipped with high-resolution modes, quadrupole pre-mass filters or collision/reaction cells to reduce interferences (e.g., Christensen et al., 2018; Moynier et al., 2021).
- Wild-type mutant comparisons (e.g., Zhang et al., 2021) as well as monitoring the gene expression of plants in response to different environmental conditions (Zhong et al., 2021) can be used to investigate the role of specific proteins in element storage and transport. Determining the isotope fractionation factor for specific proteins using these techniques is challenging as, for example, compensatory mechanisms, such as the abundance alteration of other proteins, may contribute to the signal (Chang et al., 2020).
- Further constraint of isotope fractionation factors associated with individual transporters can be achieved by characterization of their transport features following heterologous expression in simple systems; such as unicellular organisms like yeasts (e.g., *Saccharomyces cerevisiae*, Cadiou et al., 2017; Moore et al., 2020), insect cells or frog eggs (*Xenopus oocytes*, Larsen et al., 2017), model plant species, or the reconstitution of purified transporters in defined lipid bilayers (Xie, 2008).
- Speciation analyses can provide complementary information to isotope analyses (e.g., Li et al., 2021). Synchrotron XAS provides information on the chemical environment of the target element in plant organs (e.g., bound to O, N, or S donors or specific molecules, such as citrate).
- Combining liquid chromatography with MC-ICP-MS. This has been used to measure Mg and Cu isotope ratios in chlorophyll and proteins (Larner et al., 2019; Wrobel et al., 2020). For structural elements, such as B and Ca, extraction techniques can provide crucial insights into isotope fractionation within plants (Schmitt et al., 2018).
- Analysis of organelles, such as vacuoles and cell walls, could improve the understanding of isotope fractionation on a subcellular level in plants (Horner et al., 2013; Song et al., 2014). Such approaches require small volumes of analytes that could be facilitated by bespoke sample introduction systems (Murphy et al., 2020).
- Coupling laser ablation with MC-ICP-MS could provide *in-situ* isotope ratio analyses at tissue level (Lobo et al., 2018). This method has recently been tested to measure Si isotope ratios of phytoliths in leaves (Frick et al., 2019) and can potentially be applied for other elements.
- Finally, it would be interesting to combine isotope analyses for traditional and non-traditional elements. Nitrogen isotopes may be highly complementary to non-traditional isotopes (e.g., Mg due to its role in chlorophyll, Laursen et al., 2013). Another example is C isotope data, which can provide information on water use efficiency (Newton, 2016). Linking, for example, C and K isotope fractionation may also be highly relevant due to the role of K in controlling stomatal conductance.

CONCLUSION

This review illustrates that non-traditional isotopes usually fractionate significantly and systematically in plants. The current knowledge suggests that fractionation is driven by: diffusion for Si uptake, root apoplast adsorption for Ca and Mg, membrane transport and chemical speciation for Zn and Cd, reduction of Fe and Cu, precipitation of elements into insoluble forms, such as phytoliths (Si) or oxalate (Ca), and structural binding to cell walls as shown for Ca and probably also B. These processes can induce similar (Cu, Fe) or distinct (Ca vs. Mg, Zn vs. Cd) isotope fractionation patterns for chemically similar elements. In addition, isotope compositions of the covered elements vary between plant species/varieties and in distinct environmental conditions. Hence, isotope process tracing in plants can potentially provide unique information on dominant biological and physico-chemical processes that control uptake and transport of elements in distinct soil–plant systems. For instance, it can be used to understand changes in uptake and translocation mechanisms that occur in response to changing nutrient supply, as shown for, for example, Mg, Zn, and Cu. Therefore, isotope process tracing could be a valuable tool to identify how plants cope with distinct environmental stresses and soil management strategies. Further exploitation of the scope of isotope process tracing requires the joint expertise of plant scientists and geochemists to develop hypothesis-driven experimental designs for plant growth trials, conduct robust and efficient isotope analyses, employ biological model systems, integrate contrasting environmental conditions, and to ultimately link isotope fractionation in plants to physiological processes. This expertise can only be covered by research collaborations that include (at least) plant and isotope geochemical scientists. Such interdisciplinary research may have great potential to overcome current thinking boundaries and thereby advance isotope and plant physiological knowledge.

AUTHOR CONTRIBUTIONS

The interdisciplinary team of plant and geo scientists including MW, RM, GB, KHL, and SB contributed to conceptualization, methodology, investigation, data curation, writing of original draft, and visualization. PW contributed to writing and editing. MW was responsible for the project administration. All authors contributed to the article and approved the submitted version.

ACKNOWLEDGMENTS

We thank Vaněk Aleš, Christoph Cloquet, Daniel Frick, Xiao-Ming Liu, Dmitriy Malinovskiy, Gildas Ratié, Bei Wu, Nuria Basdediós Prieto, Franziska Stamm, and John Christensen for the technical inputs on isotope analyses. We thank Heinz Wiggenhauser for the grand support for the visualization and Meryl Meyer for editing and literature management.

SUPPLEMENTARY MATERIAL

The Supplementary Material for this article can be found online at: https://www.frontiersin.org/articles/10.3389/fpls.2022.840941/full#supplementary-material

REFERENCES

Álvarez-Fernández, A., Di-az-Benito, P., AbadiA, A., López-Millán, A.-F., and AbadíA, J. (2014). Metal species involved in long distance metal transport in plants. *Front. Plant Sci.* 5:105. doi: 10.3389/fpls.2014.00105

Andresen, E., Peiter, E., and Küpper, H. (2018). Trace metal metabolism in plants. *J. Exp. Bot.* 69, 909–954. doi: 10.1093/jxb/erx465

Arnold, T., Markovic, T., Kirk, G. J. D., Schönbächler, M., Rehkämper, M., Zhao, F. J., et al. (2015). Iron and zinc isotope fractionation during uptake and translocation in rice (*Oryza sativa*) grown in oxic and anoxic soils. *C. R. Geosci.* 347, 397–404. doi: 10.1016/j.crte.2015.05.005

Aucour, A. M., Bedell, J. P., Queyron, M., Magnin, V., Testemale, D., and Sarret, G. (2015). Dynamics of Zn in an urban wetland soil-plant system: coupling isotopic and EXAFS approaches. *Geochim. Cosmochim. Acta* 160, 55–69. doi: 10.1016/j.gca.2015.03.040

Aucour, A. M., Bedell, J. P., Queyron, M., Tholé, R., Lamboux, A., and Sarret, G. (2017). Zn speciation and stable isotope fractionation in a contaminated urban wetland soil-*Typha latifolia* system. *Environ. Sci. Technol.* 51, 8350–8358. doi: 10.1021/acs.est.6b02734

Barraza, F., Moore, R. E. T., Rehkämper, M., Schreck, E., Lefeuvre, G., Kreissig, K., et al. (2019). Cadmium isotope fractionation in the soil-cacao systems of Ecuador: a pilot field study. *RSC Adv.* 9, 34011–34022. doi: 10.1039/C9RA05516A

Bienert, M. D., Werner, L. M., Wimmer, M. A., and Bienert, G. P. (2021). Root hairs: the villi of plants. *Biochem. Soc. Trans.* 49, 1133–1146. doi: 10.1042/BST20200716

Bigeleisen, J. (1965). Chemistry of isotopes: isotope chemistry has opened new areas of chemical physics, geochemistry, and molecular biology. *Science* 147, 463–471. doi: 10.1126/science.147.3657.463

Black, J. R., Epstein, E., Rains, W. D., Yin, Q. Z., and Casey, W. H. (2008). Magnesium-isotope fractionation during plant growth. *Environ. Sci. Technol.* 42, 7831–7836. doi: 10.1021/es8012722

Black, J. R., Yin, Q. Z., Rustad, J. R., and Casey, W. H. (2007). Magnesium isotopic equilibrium in chlorophylls. *J. Am. Chem. Soc.* 129, 8690–8691. doi: 10.1021/ja072573i

Blotevogel, S., Oliva, P., Denaix, L., Audry, S., Viers, J., and Schreck, E. (2022). Stable cu isotope ratios show changes in cu uptake and transport mechanisms in vitis vinifera due to high cu exposure. *Front. Plant Sci.* 12:755944. doi: 10.3389/fpls.2021.755944

Blotevogel, S., Schreck, E., Audry, S., Saldi, G. D., Viers, J., Courjault-Radé, P., et al. (2019). Contribution of soil elemental contents and cu and Sr isotope ratios to the understanding of pedogenetic processes and mechanisms involved in the soil-to-grape transfer (soave vineyard, Italy). *Geoderma* 343, 72–85. doi: 10.1016/j.geoderma.2019.02.015

Bolou-Bi, E. B., Poszwa, A., Leyval, C., and Vigier, N. (2010). Experimental determination of magnesium isotope fractionation during higher plant growth. *Geochim. Cosmochim. Acta* 74, 2523–2537. doi: 10.1016/j.gca.2010.02.010

Bolou-Bi, E. B., Vigier, N., Poszwa, A., Boudot, J. P., and Dambrine, E. (2012). Effects of biogeochemical processes on magnesium isotope variations in a forested catchment in the Vosges Mountains (France). *Geochim. Cosmochim. Acta* 87, 341–355. doi: 10.1016/j.gca.2012.04.005

Brdar-Jokanović, M. (2020). Boron toxicity and deficiency in agricultural plants. *Int. J. Mol. Sci.* 21:1424. doi: 10.3390/ijms21041424

Bullen, T., and Chadwick, O. (2016). Ca, Sr and Ba stable isotopes reveal the fate of soil nutrients along a tropical climosequence in Hawaii. *Chem. Geol.* 422, 25–45. doi: 10.1016/j.chemgeo.2015.12.008

Cadiou, J. L., Pichat, S., Bondanese, V. P., Soulard, A., Fujii, T., Albarède, F., et al. (2017). Copper transporters are responsible for copper isotopic fractionation in eukaryotic cells. *Sci. Rep.* 7, 1–10. doi: 10.1038/srep44533

Caldelas, C., and Weiss, D. J. (2017). Zinc homeostasis and isotopic fractionation in plants: a review. *Plant Soil* 411, 17–46. doi: 10.1007/s11104-016-3146-0

Cenki-Tok, B., Chabaux, F., Lemarchand, D., Schmitt, A. D., Pierret, M. C., Viville, D., et al. (2009). The impact of water-rock interaction and vegetation on calcium isotope fractionation in soil- and stream waters of a small, forested catchment (the Strengbach case). *Geochim. Cosmochim. Acta* 73, 2215–2228. doi: 10.1016/j.gca.2009.01.023

Chan, M. C., and Shukla, D. (2021). Markov state modeling of membrane transport proteins. *J. Struct. Biol.* 213:107800. doi: 10.1016/j.jsb.2021.107800

Chang, J., Huang, S., Yamaji, N., Zhang, W., Ma, J. F., and Zhao, F. (2020). OSNRAMP1 transporter contributes to cadmium and manganese uptake in rice. *Plant Cell Environ.* 12:755944. doi: 10.1111/pce.13843

Chen, G., Liu, T., Li, Y., Gao, T., Huang, F., Li, X., et al. (2021). New insight into iron biogeochemical cycling in soil-rice plant system using iron isotope fractionation. *Fundam. Res.* 1, 277–284. doi: 10.1016/j.fmre.2021.04.006

Chen, Z. C., Peng, W. T., Li, J., and Liao, H. (2018). Functional dissection and transport mechanism of magnesium in plants. *Semin. Cell Dev. Biol.* 74, 142–152. doi: 10.1016/j.semcdb.2017.08.005

Christensen, J. N., Qin, L., Brown, S. T., and Depaolo, D. J. (2018). Potassium and calcium isotopic fractionation by plants (soybean [*Glycine* max], rice [*Oryza sativa*], and wheat [*Triticum aestivum*]). *ACS Earth Space Chem.* 2, 745–752. doi: 10.1021/acsearthspacechem.8b00035

Cobert, F., Schmitt, A.-D., Bourgeade, P., Labolle, F., Badot, P.-M., Chabaux, F., et al. (2011). Experimental identification of Ca isotopic fractionations in higher plants. *Geochim. Cosmochim. Acta* 75, 5467–5482. doi: 10.1016/j.gca.2011.06.032

Coetzee, P. P., Greeff, L., and Vanhaecke, F. (2010). ICP-MS Measurement of 11B/10B Isotope Ratios in Grapevine Leaves and the Investigation of Possible Boron Isotope Fractionation in Grapevine Plants. *South Afr. J. Enol. Vitic.* 32. doi: 10.21548/32-1-1363

Connorton, J. M., Balk, J., and Rodríguez-Celma, J. (2017). Iron homeostasis in plants – a brief overview. *Metallomics* 9, 813–823. doi: 10.1039/C7MT00136C

Couder, E., Mattielli, N., Drouet, T., Smolders, E., Delvaux, B., Iserentant, A., et al. (2015). Transpiration flow controls Zn transport in *Brassica napus* and *Lolium multiflorum* under toxic levels as evidenced from isotopic fractionation. *Compt. Rendus Geosci.* 347, 386–396. doi: 10.1016/j.crte.2015.05.004

Dauphas, N., and Schauble, E. A. (2016). Mass Fractionation Laws, Mass-Independent Effects, and Isotopic Anomalies. *Annu. Rev. Earth Planet. Sci.* 44, 709–783. doi: 10.1146/annurev-earth-060115-012157

Dawson, T. E., Mambelli, S., Plamboeck, A. H., Templer, P. H., and Tu, K. P. (2002). Stable isotopes in plant ecology. *Annu. Rev. Ecol. Syst.* 33, 507–559. doi: 10.1146/annurev.ecolsys.33.020602.095451

de Bang, T. C., Husted, S., Laursen, K. H., Persson, D. P., and Schjoerring, J. K. (2021). The molecular–physiological functions of mineral macronutrients and their consequences for deficiency symptoms in plants. *New Phytol.* 229, 2446–2469. doi: 10.1111/nph.17074

Deng, T. H. B., Cloquet, C., Tang, Y. T., Sterckeman, T., Echevarria, G., Estrade, N., et al. (2014). Nickel and zinc isotope fractionation in hyperaccumulating and nonaccumulating plants. *Environ. Sci. Technol.* 48, 11926–11933. doi: 10.1021/es5020955

Dideriksen, K., Baker, J. A., and Stipp, S. L. S. (2008). Fe isotope fractionation between inorganic aqueous Fe(III) and a Fe siderophore complex. *Mineral. Mag.* 72, 313–316. doi: 10.1180/minmag.2008.072.1.313

Ding, T. P., Ma, G. R., Shui, M. X., Wan, D. F., and Li, R. H. (2005). Silicon isotope study on rice plants from the Zhejiang province, China. *Chem. Geol.* 218, 41–50. doi: 10.1016/j.chemgeo.2005.01.018

Ding, T. P., Zhou, J. X., Wan, D. F., Chen, Z. Y., Wang, C. Y., and Zhang, F. (2008). Silicon isotope fractionation in bamboo and its significance to the biogeochemical cycle of silicon. *Geochim. Cosmochim. Acta* 72, 1381–1395. doi: 10.1016/j.gca.2008.01.008

Dreyer, I., and Michard, E. (2020). High- and Low-Affinity Transport in Plants From a Thermodynamic Point of View. *Front. Plant Sci.* 10:1797. doi: 10.3389/fpls.2019.01797

Dupuis, R., Benoit, M., Nardin, E., and Méheut, M. (2015). Fractionation of silicon isotopes in liquids: The importance of configurational disorder. *Chem. Geol.* 396, 239–254. doi: 10.1016/j.chemgeo.2014.12.027

Essington, M. E. (2015). *Soil and Water Chemistry: An Integrative Approach. Second edition*. Boca Raton, Florida: CRC Press, Taylor & Francis Group.

Estrade, N., Cloquet, C., Echevarria, G., Sterckeman, T., Deng, T., Tang, Y. T., et al. (2015). Weathering and vegetation controls on nickel isotope fractionation in surface ultramafic environments (Albania). *Earth Planet. Sci. Lett.* 423, 24–35. doi: 10.1016/j.epsl.2015.04.018

Falhof, J., Pedersen, J. T., Fuglsang, A. T., and Palmgren, M. (2016). Plasma membrane H+-ATPase regulation in the Center of Plant Physiology. *Mol. Plant* 9, 323–337. doi: 10.1016/j.molp.2015.11.002

Frick, D. A., Remus, R., Sommer, M., Augustin, J., Kaczorek, D., and von Blanckenburg, F. (2020). Silicon uptake and isotope fractionation dynamics by crop species. *Biogeosciences* 17, 6475–6490. doi: 10.5194/bg-17-6475-2020

Frick, D. A., Schuessler, J. A., Sommer, M., and von Blanckenburg, F. (2019). Laser ablation In situ silicon stable isotope analysis of phytoliths. *Geostand. Geoanal. Res.* 43, 77–91. doi: 10.1111/ggr.12243

Fry, B. (2006). *Stable Isotope Ecology*. New York: Springer-Verlag.

Fujii, T., Moynier, F., Blichert-Toft, J., and Albarède, F. (2014). Density functional theory estimation of isotope fractionation of Fe, Ni, Cu, and Zn among species relevant to geochemical and biological environments. *Geochim. Cosmochim. Acta* 140, 553–576. doi: 10.1016/j.gca.2014.05.051

Gao, T., Ke, S., Wang, S.-J., Li, F., Liu, C., Lei, J., et al. (2018). Contrasting mg isotopic compositions between Fe-Mn nodules and surrounding soils: accumulation of light Mg isotopes by Mg-depleted clay minerals and Fe oxides. *Geochim. Cosmochim. Acta* 237, 205–222. doi: 10.1016/j.gca.2018.06.028

Garnier, J., Garnier, J. M., Vieira, C. L., Akerman, A., Chmeleff, J., Ruiz, R. I., et al. (2017). Iron isotope fingerprints of redox and biogeochemical cycling in the soil-water-rice plant system of a paddy field. *Sci. Total Environ.* 574, 1622–1632. doi: 10.1016/j.scitotenv.2016.08.202

Geilert, S., Vogl, J., and Rosner, M. (2015). Boron isotope fractionation in bell pepper. *Mass Spec. Purif. Tech.* 01, 1–6. doi: 10.4172/mso.1000101

Geilert, S., Vogl, J., Rosner, M., and Eichert, T. (2019). Boron isotope variability related to boron speciation (change during uptake and transport) in bell pepper plants and SI traceable n(^{11}B)/n(^{10}B) ratios for plant reference materials. *Rapid Commun. Mass Spectrom.* 33, 1137–1147. doi: 10.1002/rcm.8455

Gélabert, A., Pokrovsky, O. S., Viers, J., Schott, J., Boudou, A., and Feurtet-Mazel, A. (2006). Interaction between zinc and freshwater and marine diatom species: surface complexation and Zn isotope fractionation. *Geochim. Cosmochim. Acta* 70, 839–857. doi: 10.1016/j.gca.2005.10.026

Geldner, N. (2013). Casparian strips. *Curr. Biol.* 23, R1025–R1026. doi: 10.1016/j.cub.2013.08.052

Guelke, M., and Von Blanckenburg, F. (2007). Fractionation of stable iron isotopes in higher plants. *Environ. Sci. Technol.* 41, 1896–1901. doi: 10.1021/es062288j

Guelke-Stelling, M., and von Blanckenburg, F. (2012). Fe isotope fractionation caused by translocation of iron during growth of bean and oat as models of strategy I and II plants. *Plant Soil* 352, 217–231. doi: 10.1007/s11104-011-0990-9

Guinoiseau, D., Galer, S. J. G., and Abouchami, W. (2018). Effect of cadmium sulphide precipitation on the partitioning of Cd isotopes: Implications for the oceanic Cd cycle. *Earth Planet. Sci. Lett.* 498, 300–308. doi: 10.1016/j.epsl.2018.06.039

Hanikenne, M., Esteves, S. M., Fanara, S., and Rouached, H. (2021). Coordinated homeostasis of essential mineral nutrients: a focus on iron. *J. Exp. Bot.* 72, 2136–2153. doi: 10.1093/jxb/eraa483

Hansen, T. H., de Bang, T. C., Laursen, K. H., Pedas, P., Husted, S., and Schjoerring, J. K. (2013). "Multielement plant tissue analysis using ICP spectrometry," in *Plant Mineral Nutrients*. ed. F. J. M. Maathuis (Totowa, NJ: Humana Press), 121–141. doi: 10.1007/978-1-62703-152-3_8

Hindshaw, R. S., Reynolds, B. C., Wiederhold, J. G., Kiczka, M., Kretzschmar, R., and Bourdon, B. (2013). Calcium isotope fractionation in alpine plants. *Biogeochemistry* 112, 373–388. doi: 10.1007/s10533-012-9732-1

Hoefs, J. (2018). *Stable Isotope Geochemistry*. Cham: Springer International Publishing.

Hofmann, A. E., Bourg, I. C., and DePaolo, D. J. (2012). Ion desolvation as a mechanism for kinetic isotope fractionation in aqueous systems. *Proc. Natl. Acad. Sci.* 109, 18689–18694. doi: 10.1073/pnas.1208184109

Holmden, C., and Bélanger, N. (2010). Ca isotope cycling in a forested ecosystem. *Geochim. Cosmochim. Acta* 74, 995–1015. doi: 10.1016/j.gca.2009.10.020

Horner, T. J., Lee, R. B. Y., Henderson, G. M., and Rickaby, R. E. M. (2013). Nonspecific uptake and homeostasis drive the oceanic cadmium cycle. *Proc. Natl. Acad. Sci.* 110, 2500–2505. doi: 10.1073/pnas.1213857110

Houben, D., Sonnet, P., Tricot, G., Mattielli, N., Couder, E., and Opfergelt, S. (2014). Impact of root-induced mobilization of zinc on stable Zn isotope variation in the soil-plant system. *Environ. Sci. Technol.* 48, 7866–7873. doi: 10.1021/es5002874

Husson, J. M., Higgins, J. A., Maloof, A. C., and Schoene, B. (2015). Ca and Mg isotope constraints on the origin of Earth's deepest $\delta^{13}C$ excursion. *Geochim. Cosmochim. Acta* 160, 243–266. doi: 10.1016/j.gca.2015.03.012

Husted, S., Persson, D. P., Laursen, K. H., Hansen, T. H., Pedas, P., Schiller, M., et al. (2011). Review: The role of atomic spectrometry in plant science. *J Anal Spectrom.* 26, 52–79. doi: 10.1039/C0JA00058B

Imseng, M., Wiggenhauser, M., Keller, A., Müller, M., Rehkämper, M., Murphy, K., et al. (2019). Towards an understanding of the cd isotope fractionation during transfer from the soil to the cereal grain. *Environ. Pollut.* 244, 834–844. doi: 10.1016/j.envpol.2018.09.149

John, S. G., Geis, R. W., Saito, M. A., and Boyle, E. A. (2007). Zinc isotope fractionation during high-affinity and low-affinity zinc transport by the marine diatom Thalassiosira oceanica. *Limnol. Oceanogr.* 52, 2710–2714. doi: 10.4319/lo.2007.52.6.2710

John, S. G., Rouxel, O. J., Craddock, P. R., Engwall, A. M., and Boyle, E. A. (2008). Zinc stable isotopes in seafloor hydrothermal vent fluids and chimneys. *Earth Planet. Sci. Lett.* 269, 17–28. doi: 10.1016/j.epsl.2007.12.011

Johnson, C., Beard, B., and Weyer, S. (2020). "Fe isotope fractionation factors," in *Iron Geochemistry: An Isotopic Perspective Advances in Isotope Geochemistry.* ed. J. Hoefs (Cham: Springer International Publishing), 39–84.

Jouvin, D., Louvat, P., Juillot, F., Maréchal, C. N., and Benedetti, M. F. (2009). Zinc isotopic fractionation: why organic matters. *Environ. Sci. Technol.* 43, 5747–5754. doi: 10.1021/es803012e

Jouvin, D., Weiss, D. J., Mason, T. F. M., Bravin, M. N., Louvat, P., Zhao, F., et al. (2012). Stable isotopes of Cu and Zn in higher plants: evidence for Cu reduction at the root surface and two conceptual models for isotopic fractionation processes. *Environ. Sci. Technol.* 46, 2652–2660. doi: 10.1021/es202587m

Kersten, M., Xiao, T., Kreissig, K., Brett, A., Coles, B. J., and Rehkämper, M. (2014). Tracing anthropogenic thallium in soil using stable isotope compositions. *Environ. Sci. Technol.* 48, 9030–9036. doi: 10.1021/es501968d

Kiczka, M., Wiederhold, J. G., Kraemer, S. M., Bourdon, B., and Kretzschmar, R. (2010). Iron isotope fractionation during Fe uptake and translocation in alpine plants. *Environ. Sci. Technol.* 44, 6144–6150. doi: 10.1021/es100863b

Kidder, J. A., Voinot, A., Sullivan, K. V., Chipley, D., Valentino, M., Layton-Matthews, D., et al. (2020). Improved ion-exchange column chromatography for Cu purification from high-Na matrices and isotopic analysis by MC-ICPMS. *J. Anal. At. Spectrom.* 35, 776–783. doi: 10.1039/C9JA00359B

Kimmig, S. R., Holmden, C., and Bélanger, N. (2018). Biogeochemical cycling of Mg and its isotopes in a sugar maple forest in Québec. *Geochim. Cosmochim. Acta* 230, 60–82. doi: 10.1016/j.gca.2018.03.020

Kleczkowski, L. A., and Igamberdiev, A. U. (2021). Magnesium Signaling in Plants. *IJMS* 22:1159. doi: 10.3390/ijms22031159

Köbberich, M., and Vance, D. (2017). Kinetic control on Zn isotope signatures recorded in marine diatoms. *Geochim. Cosmochim. Acta* 210, 97–113. doi: 10.1016/j.gca.2017.04.014

Komárek, M., Ratié, G., Vaňková, Z., Šípková, A., and Chrastný, V. (2021). *Plant Micronutrient Use Efficiency*. Eds. H. Mohammad Anwar, K. Takehiro, J. B. David, T. Lam-Son Phan, and F. Toru. London: Elsevier.

Köster, J. R., Bol, R., Leng, M. J., Parker, A. G., Sloane, H. J., and Ma, J. F. (2009). Effects of active silicon uptake by rice on ^{29}Si fractionation in various plant parts. *Rapid Commun. Mass Spectrom.* 23, 2398–2402. doi: 10.1002/rcm.3971

Łangowski, Ł., Růžička, K., Naramoto, S., Kleine-Vehn, J., and Friml, J. (2010). Trafficking to the outer polar domain defines the root-soil Interface. *Curr. Biol.* 20, 904–908. doi: 10.1016/j.cub.2010.03.059

Larner, F., McLean, C. A., Halliday, A. N., Roberts, B. R., Larner, F., McLean, C. A., et al. (2019). Copper isotope compositions of superoxide dismutase and Metallothionein from post-mortem human frontal cortex. *Inorganics* 7:86. doi: 10.3390/inorganics7070086

Larsen, B., Xu, D., Halkier, B. A., and Nour-Eldin, H. H. (2017). Advances in methods for identification and characterization of plant transporter function. *J. Exp. Bot.* 68, 4045–4056. doi: 10.1093/jxb/erx140

Laursen, K. H., Mihailova, A., Kelly, S. D., Epov, V. N., Bérail, S., Schjoerring, J. K., et al. (2013). Is it really organic? – multi-isotopic analysis as a tool to discriminate between organic and conventional plants. *Food Chem.* 141, 2812–2820. doi: 10.1016/j.foodchem.2013.05.068

Li, W., Liu, X.-M., Hu, Y., Teng, F.-Z., Hu, Y.-F., and Chadwick, O. A. (2021). Potassium isotopic fractionation in a humid and an arid soil–plant system in Hawai'i. *Geoderma* 400:115219. doi: 10.1016/j.geoderma.2021.115219

Li, S. Z., Zhu, X. K., Wu, L. H., and Luo, Y. M. (2016). Cu isotopic compositions in Elsholtzia splendens: influence of soil condition and growth period on Cu isotopic fractionation in plant tissue. *Chem. Geol.* 444, 49–58. doi: 10.1016/j.chemgeo.2016.09.036

Li, S.-Z., Zhu, X.-K., Wu, L.-H., and Luo, Y.-M. (2020). Zinc, iron, and copper isotopic fractionation in Elsholtzia splendens Nakai: a study of elemental uptake and (re)translocation mechanisms. *J. Asian Earth Sci.* 192:104227. doi: 10.1016/j.jseaes.2020.104227

Liu, C., Gao, T., Liu, Y., Liu, J., Li, F., Chen, Z., et al. (2019). Isotopic fingerprints indicate distinct strategies of Fe uptake in rice. *Chem. Geol.* 524, 323–328. doi: 10.1016/j.chemgeo.2019.07.002

Lobo, L., Pereiro, R., and Fernández, B. (2018). Opportunities and challenges of isotopic analysis by laser ablation ICP-MS in biological studies. *Trends Anal. Chem.* 105, 380–390. doi: 10.1016/j.trac.2018.05.020

Lockless, S. W., Zhou, M., and MacKinnon, R. (2007). Structural and thermodynamic properties of selective ion binding in a K^+ channel. *PLoS Biol.* 5:e121. doi: 10.1371/journal.pbio.0050121

Ma, J. F. (2015). A cooperative system of silicon transport in plants. *Trends Plant Sci.* 20:8. doi: 10.1016/j.tplants.2015.04.007

Ma, J. F., and Yamaji, N. (2015). A cooperative system of silicon transport in plants. *Trends Plant Sci.* 20, 435–442. doi: 10.1016/j.tplants.2015.04.007

MacKinnon, R. (2003). Potassium channels. *FEBS Lett.* 555, 62–65. doi: 10.1016/S0014-5793(03)01104-9

Maillard, A., Diquélou, S., Billard, V., Laîné, P., Garnica, M., Prudent, M., et al. (2015). Leaf mineral nutrient remobilization during leaf senescence and modulation by nutrient deficiency. *Front. Plant Sci.* 6:317. doi: 10.3389/fpls.2015.00317

Malinovsky, D., and Kashulin, N. A. (2018). Molybdenum isotope fractionation in plants measured by MC-ICPMS. *Anal. Methods* 10, 131–137. doi: 10.1039/C7AY02316B

Maréchal, C., and Albarède, F. (2002). Ion-exchange fractionation of copper and zinc isotopes. *Geochim. Cosmochim. Acta* 66, 1499–1509. doi: 10.1016/S0016-7037(01)00815-8

Maréchal, C. N., Télouk, P., and Albarède, F. (1999). Precise analysis of copper and zinc isotopic compositions by plasma-source mass spectrometry. *Chem. Geol.* 156, 251–273. doi: 10.1016/S0009-2541(98)00191-0

Maret, W., and Moulis, J.-M. (2013). "The bioinorganic chemistry of cadmium in the context of its toxicity," in *Cadmium: From Toxicity to Essentiality*. eds. A. Sigel, H. Sigel and R. K. Sigel (Dordrecht: Springer Netherlands), 1–29.

Marentes, E., Vanderpool, R. A., and Shelp, B. J. (1997). Boron-isotope fractionation in plants. *Can. J. Plant Sci.* 77, 627–629. doi: 10.4141/P97-010

Marković, T., Manzoor, S., Humphreys-Williams, E., Kirk, G. J. D., Vilar, R., and Weiss, D. J. (2017). Experimental determination of zinc isotope fractionation in complexes with the phytosiderophore 2′-deoxymugeneic acid (DMA) and its structural analogues, and implications for plant uptake mechanisms. *Environ. Sci. Technol.* 51, 98–107. doi: 10.1021/acs.est.6b00566

Marschner, H., and Marschner, P. (2012). *Marschner's Mineral Nutrition of Higher Plants*. London; Waltham, MA: Academic Press.

Meier, U. (2001). *Growth Stages of Mono and Dicotyledonous Plants: BBCH-Monograph*. Berlin, Boston: Blackwell Science.

Mellman, I., and Nelson, W. J. (2008). Coordinated protein sorting, targeting and distribution in polarized cells. *Nat. Rev. Mol. Cell Biol.* 9, 833–845. doi: 10.1038/nrm2525

Meychik, N., Nikolaeva, Y., and Kushunina, M. (2021). The significance of ion-exchange properties of plant root cell walls for nutrient and water uptake by plants. *Plant Physiol. Biochem.* 166, 140–147. doi: 10.1016/j.plaphy.2021.05.048

Mir, A. R., Pichtel, J., and Hayat, S. (2021). Copper: uptake, toxicity and tolerance in plants and management of Cu-contaminated soil. *BioMetals* 34, 737–759. doi: 10.1007/s10534-021-00306-z

Moore, R. E. T., Ullah, I., de Oliveira, V. H., Hammond, S. J., Strekopytov, S., Tibbett, M., et al. (2020). Cadmium isotope fractionation reveals genetic variation in Cd uptake and translocation by Theobroma cacao and role of natural resistance-associated macrophage protein 5 and heavy metal ATPase-family transporters. *Hortic. Res.* 7:71. doi: 10.1038/s41438-020-0292-6

Morgan, L. E., Santiago Ramos, D. P., Davidheiser-Kroll, B., Faithfull, J., Lloyd, N. S., Ellam, R. M., et al. (2018). High-precision $^{41}K/^{39}K$ measurements by MC-ICP-MS indicate terrestrial variability of: $\delta^{41}K$. *J. Anal. At. Spectrom.* 33, 175–186. doi: 10.1039/C7JA00257B

Moynier, F., and Fujii, T. (2017). Theoretical isotopic fractionation of magnesium between chlorophylls. *Sci. Rep.* 7:6973. doi: 10.1038/s41598-017-07305-6

Moynier, F., Fujii, T., Wang, K., and Foriel, J. (2013). Ab initio calculations of the Fe(II) and Fe(III) isotopic effects in citrates, nicotianamine, and phytosiderophore, and new Fe isotopic measurements in higher plants. *C. R. Geosci.* 345, 230–240. doi: 10.1016/j.crte.2013.05.003

Moynier, F., Hu, Y., Wang, K., Zhao, Y., Gérard, Y., Deng, Z., et al. (2021). Potassium isotopic composition of various samples using a dual-path collision cell-capable multiple-collector inductively coupled plasma mass spectrometer, Nu instruments Sapphire. *Chem. Geol.* 571:120144. doi: 10.1016/j.chemgeo.2021.120144

Murphy, D. T., Allen, C. M., Ghidan, O., Dickson, A., Hu, W., Briggs, E., et al. (2020). Analysing Sr isotopes in low-Sr samples such as single insects with inductively coupled plasma tandem mass spectrometry using N_2O as a reaction gas for in-line Rb separation. *Rapid Commun. Mass Spectrom.* 34:e8604. doi: 10.1002/rcm.8604

Newton, J. (2016). "*Stable Isotopes as Tools in Ecological Research*." Chichester, UK: John Wiley & Sons, Ltd, 1–8.

Nocito, F. F., Lancilli, C., Dendena, B., Lucchini, G., and Sacchi, G. A. (2011). Cadmium retention in rice roots is influenced by cadmium availability, chelation and translocation: cadmium retention in rice roots. *Plant Cell Environ.* 34, 994–1008. doi: 10.1111/j.1365-3040.2011.02299.x

Novak, V., Adler, J., Husted, S., Fromberg, A., and Laursen, K. H. (2019). Authenticity testing of organically grown vegetables by stable isotope ratio analysis of oxygen in plant-derived sulphate. *Food Chem.* 291, 59–67. doi: 10.1016/j.foodchem.2019.03.125

Novak, V., Khatri, P. K., and Laursen, K. H. (2021). The oxygen isotopic signature of soil- and plant-derived sulphate is controlled by fertilizer type and water source. *Plant Cell Environ.* 44, 203–215. doi: 10.1111/pce.13877

O'Leary, M. H. (1993). Biochemical basis of carbon isotope fractionation. *Stable Isot. Plant Carbon-Water Relat.*, 19–28. doi: 10.1016/B978-0-08-091801-3.50009-X

O'Leary, M. H., Madhavan, S., and Paneth, P. (1992). Physical and chemical basis of carbon isotope fractionation in plants. *Plant Cell Environ.* 15, 1099–1104. doi: 10.1111/j.1365-3040.1992.tb01660.x

Opfergelt, S., Burton, K. W., Georg, R. B., West, A. J., Guicharnaud, R. A., Sigfusson, B., et al. (2014). Magnesium retention on the soil exchange complex controlling Mg isotope variations in soils, soil solutions and vegetation in volcanic soils, Iceland. *Geochim. Cosmochim. Acta* 125, 110–130. doi: 10.1016/j.gca.2013.09.036

Opfergelt, S., Cardinal, D., Henriet, C., André, L., and Delvaux, B. (2006). Silicon isotope fractionation between plant parts in banana: In situ vs. in vitro. *J. Geochem. Explor.* 88, 224–227. doi: 10.1016/j.gexplo.2005.08.044

Page, B. D., Bullen, T. D., and Mitchell, M. J. (2008). Influences of calcium availability and tree species on Ca isotope fractionation in soil and vegetation. *Biogeochemistry* 88, 1–13. doi: 10.1007/s10533-008-9188-5

Parker, M. D., and Boron, W. F. (2013). The divergence, actions, roles, and relatives of sodium-coupled bicarbonate transporters. *Physiol. Rev.* 93, 803–959. doi: 10.1152/physrev.00023.2012

Pilon-Smits, E. A., Quinn, C. F., Tapken, W., Malagoli, M., and Schiavon, M. (2009). Physiological functions of beneficial elements. *Curr. Opin. Plant Biol.* 12, 267–274. doi: 10.1016/j.pbi.2009.04.009

Pokharel, R., Gerrits, R., Schuessler, J. A., Frings, P. J., Sobotka, R., Gorbushina, A. A., et al. (2018). Magnesium stable isotope fractionation on a cellular level explored by cyanobacteria and black fungi with implications for higher plants. *Environ. Sci. Technol.* 52, 12216–12224. doi: 10.1021/acs.est.8b02238

Rader, S. T., Maier, R. M., Barton, M. D., and Mazdab, F. K. (2019). Uptake and fractionation of thallium by *Brassica juncea* in a geogenic thallium-amended substrate. *Environ. Sci. Technol.* 53, 2441–2449. doi: 10.1021/acs.est.8b06222

Rahnemaie, R., Hiemstra, T., and van Riemsdijk, W. H. (2006). Inner- and outer-sphere complexation of ions at the goethite–solution interface. *J. Colloid Interface Sci.* 297, 379–388. doi: 10.1016/j.jcis.2005.11.003

Ratié, G., Chrastný, V., Guinoiseau, D., Marsac, R., Vaňková, Z., and Komárek, M. (2021). Cadmium isotope fractionation during complexation with humic acid. *Environ. Sci. Technol.* 55, 7430–7444. doi: 10.1021/acs.est.1c00646

Ratié, G., Quantin, C., Maia De Freitas, A., Echevarria, G., Ponzevera, E., and Garnier, J. (2019). The behavior of nickel isotopes at the biogeochemical interface between ultramafic soils and Ni accumulator species. *J. Geochem. Explor.* 196, 182–191. doi: 10.1016/j.gexplo.2018.10.008

Rehkämper, M., Schönbächler, M., and Stirling, C. H. (2001). Multiple collector ICP-MS: introduction to instrumentation, measurement techniques and analytical capabilities. *Geostand. Newslett.* 25, 23–40. doi: 10.1111/j.1751-908X.2001.tb00785.x

Rodushkin, I., Stenberg, A., Andrén, H., Malinovsky, D., and Baxter, D. C. (2004). Isotopic fractionation during diffusion of transition metal ions in solution. *Anal. Chem.* 76, 2148–2151. doi: 10.1021/ac035296g

Rudge, J. F., Reynolds, B. C., and Bourdon, B. (2009). The double spike toolbox. *Chem. Geol.* 265, 420–431. doi: 10.1016/j.chemgeo.2009.05.010

Ryan, B. M., Kirby, J. K., Degryse, F., Harris, H., McLaughlin, M. J., and Scheiderich, K. (2013). Copper speciation and isotopic fractionation in plants: uptake and translocation mechanisms. *New Phytol.* 199, 367–378. doi: 10.1111/nph.12276

Schmitt, A. D., Borrelli, N., Ertlen, D., Gangloff, S., Chabaux, F., and Osterrieth, M. (2018). Stable calcium isotope speciation and calcium oxalate production within beech tree (*Fagus sylvatica* L.) organs. *Biogeochemistry* 137, 197–217. doi: 10.1007/s10533-017-0411-0

Schmitt, A. D., Cobert, F., Bourgeade, P., Ertlen, D., Labolle, F., Gangloff, S., et al. (2013). Calcium isotope fractionation during plant growth under a limited nutrient supply. *Geochim. Cosmochim. Acta* 110, 70–83. doi: 10.1016/j.gca.2013.02.002

Schmitt, A. D., Gangloff, S., Labolle, F., Chabaux, F., and Stille, P. (2017). Calcium biogeochemical cycle at the beech tree-soil solution interface from the Strengbach CZO (NE France): insights from stable Ca and radiogenic Sr isotopes. *Geochim. Cosmochim. Acta* 213, 91–109. doi: 10.1016/j.gca.2017.06.039

Schoenberg, R., and von Blanckenburg, F. (2005). An assessment of the accuracy of stable Fe isotope ratio measurements on samples with organic and inorganic matrices by high-resolution multicollector ICP-MS. *Int. J. Mass Spectrom.* 242, 257–272. doi: 10.1016/j.ijms.2004.11.025

Schott, J., Mavromatis, V., Fujii, T., Pearce, C. R., and Oelkers, E. H. (2016). The control of carbonate mineral Mg isotope composition by aqueous speciation: theoretical and experimental modeling. *Chem. Geol.* 445, 120–134. doi: 10.1016/j.chemgeo.2016.03.011

Smolders, E., Versieren, L., Shuofei, D., Mattielli, N., Weiss, D., Petrov, I., et al. (2013). Isotopic fractionation of Zn in tomato plants suggests the role of root exudates on Zn uptake. *Plant Soil* 370, 605–613. doi: 10.1007/s11104-013-1655-7

Song, W.-Y., Mendoza-Cozatl, D. G., Lee, Y., Schroeder, J. I., Ahn, S.-N., Lee, H.-S., et al. (2014). Phytochelatin-metal(loid) transport into vacuoles shows different substrate preferences in barley and Arabidopsis: Phytochelatin-metal(loid) vacuolar transport in barley. *Plant Cell Environ.* 37, 1192–1201. doi: 10.1111/pce.12227

Stein, W. D., and Litman, T. (eds.) (2015). "Front-matter," in *Channels, Carriers, and Pumps. 2nd Edn,* (London: Elsevier), i–iii.

Sun, L., Wu, L. H., Ding, T. P., and Tian, S. H. (2008). Silicon isotope fractionation in rice plants, an experimental study on rice growth under hydroponic conditions. *Plant Soil* 304, 291–300. doi: 10.1007/s11104-008-9552-1

Sun, Y., Wu, L. H., and Li, X. Y. (2016a). Experimental determination of silicon isotope fractionation in rice. *PLoS One* 11:e0168970. doi: 10.1371/journal.pone.0168970

Sun, Y., Wu, L., Li, X., Sun, L., Gao, J., and Ding, T. (2016b). Silicon isotope fractionation in rice and cucumber plants over a life cycle: laboratory studies at different external silicon concentrations. *J. Geophys. Res. Biogeosci.* 121, 2829–2841. doi: 10.1002/2016JG003443

Taiz, L., Zeiger, E., Møller, I. M., and Murphy, A. (2015). *Plant Physiology and Development*. *6th Edn.* Sunderland, Massachusetts.

Tang, Y.-T., Cloquet, C., Deng, T.-H.-B., Sterckeman, T., Echevarria, G., Yang, W.-J., et al. (2016). Zinc isotope fractionation in the Hyperaccumulator *Noccaea caerulescens* and the nonaccumulating plant *Thlaspi arvense* at low and high Zn supply. *Environ. Sci. Technol.* 50, 8020–8027. doi: 10.1021/acs.est.6b00167

Tang, R.-J., Luan, M., Wang, C., Lhamo, D., Yang, Y., Zhao, F.-G., et al. (2020). Plant membrane transport research in the post-genomic era. *Plant Commun.* 1:100013. doi: 10.1016/j.xplc.2019.100013

Tcherkez, G. (2011). Natural $^{15}N/^{14}N$ isotope composition in C3 leaves: are enzymatic isotope effects informative for predicting the ^{15}N-abundance in key metabolites? *Funct. Plant Biol.* 38: 1. doi: 10.1071/FP10091

Tcherkez, G., and Tea, I. (2013). ^{32} S/^{34} S isotope fractionation in plant sulphur metabolism. *New Phytol.* 200, 44–53. doi: 10.1111/nph.12314

Tejada-Jimenez, M., Alejandro, C.-A., Angel, L., Aurora, G., and Emilio, F. (2018). *Plant Micronutrient Use Efficiency*. eds. M. Anwar Hossain, T. Kamiya, D. J. Burritt, L.-S. Phan Tran and T. Fujiwara (London: Elsevier).

Tipper, E. T., Gaillardet, J., Louvat, P., Capmas, F., and White, A. F. (2010). Mg isotope constraints on soil pore-fluid chemistry: evidence from Santa Cruz, California. *Geochim. Cosmochim. Acta* 74, 3883–3896. doi: 10.1016/j.gca.2010.04.021

Thor, K. (2019). Calcium—Nutrient and Messenger. *Front. Plant Sci.* 10:440. doi: 10.3389/fpls.2019.00440

Vaněk, A., Holubík, O., Oborná, V., Mihaljevič, M., Trubač, J., Ettler, V., et al. (2019). Thallium stable isotope fractionation in white mustard: implications for metal transfers and incorporation in plants. *J. Hazard. Mater.* 369, 521–527. doi: 10.1016/j.jhazmat.2019.02.060

Wang, L., Jin, Y., Weiss, D. J., Schleicher, N. J., Wilcke, W., Wu, L., et al. (2021). Possible application of stable isotope compositions for the identification of metal sources in soil. *J. Hazard. Mater.* 407:124812. doi: 10.1016/j.jhazmat.2020.124812

Wang, Y., and Wu, W.-H. (2017). Regulation of potassium transport and signaling in plants. *Curr. Opin. Plant Biol.* 39, 123–128. doi: 10.1016/j.pbi.2017.06.006

Wang, Y., Wu, B., Berns, A. E., Xing, Y., Kuhn, A. J., and Amelung, W. (2020). Magnesium isotope fractionation reflects plant response to magnesium deficiency in magnesium uptake and allocation: a greenhouse study with wheat. *Plant Soil* 455, 93–105. doi: 10.1007/s11104-020-04604-2

Wei, R., Guo, Q., Yu, G., Kong, J., Li, S., Song, Z., et al. (2018). Stable isotope fractionation during uptake and translocation of cadmium by tolerant Ricinus communis and hyperaccumulator *Solanum nigrum* as influenced by EDTA. *Environ. Pollut.* 236, 634–644. doi: 10.1016/j.envpol.2018.01.103

Weinstein, C., Moynier, F., Wang, K., Paniello, R., Foriel, J., Catalano, J., et al. (2011). Isotopic fractionation of cu in plants. *Chem. Geol.* 286, 266–271. doi: 10.1016/j.chemgeo.2011.05.010

Weiss, D., Northover, G., Hanif, M., García-España, E., Vilar, R., Arnold, T., et al. (2021). Isotope fractionation of zinc in the paddy rice soil-water environment and the role of 2'deoxymugineic acid (DMA) as zincophore under Zn limiting conditions. *Chem. Geol.* 577:120271. doi: 10.1016/j.chemgeo.2021.120271

Wiegand, B. A., Chadwick, O. A., Vitousek, P. M., and Wooden, J. L. (2005). Ca cycling and isotopic fluxes in forested ecosystems in Hawaii. *Geophys. Res. Lett.* 32, 1–4. doi: 10.1029/2005GL022746

Wiggenhauser, M., Aucour, A.-M., Bureau, S., Campillo, S., Telouk, P., Romani, M., et al. (2021a). Cadmium transfer in contaminated soil-rice systems: insights from solid-state speciation analysis and stable isotope fractionation. *Environ. Pollut.* 269:115934. doi: 10.1016/j.envpol.2020.115934

Wiggenhauser, M., Aucour, A.-M., Telouk, P., Blommaert, H., and Sarret, G. (2021b). Changes of cadmium storage forms and isotope ratios in Rice During grain filling. *Front. Plant Sci.* 12:645150. doi: 10.3389/fpls.2021.645150

Wiggenhauser, M., Bigalke, M., Imseng, M., Keller, A., Archer, C., Wilcke, W., et al. (2018). Zinc isotope fractionation during grain filling of wheat and a comparison of zinc and cadmium isotope ratios in identical soil–plant systems. *New Phytol.* 219, 195–205. doi: 10.1111/nph.15146

Wiggenhauser, M., Bigalke, M., Imseng, M., Müller, M., Keller, A., Murphy, K., et al. (2016). Cadmium isotope fractionation in soil–wheat systems. *Environ. Sci. Technol.* 50, 9223–9231. doi: 10.1021/acs.est.6b01568

Wrobel, K., Karasiński, J., Tupys, A., Arroyo Negrete, M. A., Halicz, L., Wrobel, K., et al. (2020). Magnesium–isotope fractionation in chlorophyll-a extracted from two plants with different pathways of carbon fixation (C3, C4). *Molecules* 25:1644. doi: 10.3390/molecules25071644

Wu, B., Amelung, W., Xing, Y., Bol, R., and Berns, A. E. (2019). Iron cycling and isotope fractionation in terrestrial ecosystems. *Earth Sci. Rev.* 190, 323–352. doi: 10.1016/j.earscirev.2018.12.012

Wu, B., Wang, Y., Berns, A. E., Schweitzer, K., Bauke, S. L., Bol, R., et al. (2021). Iron isotope fractionation in soil and graminaceous crops after 100 years of liming in the long-term agricultural experimental site at Berlin-Dahlem, Germany. *Eur. J. Soil Sci.* 72, 289–299. doi: 10.1111/ejss.12944

Xie, H. (2008). Activity assay of membrane transport proteins. *Acta Biochim. Biophys. Sin.* 40, 269–277. doi: 10.1111/j.1745-7270.2008.00400.x

Yamaji, N., and Ma, J. F. (2014). The node, a hub for mineral nutrient distribution in graminaceous plants. *Trends Plant Sci.* 19, 556–563. doi: 10.1016/j.tplants.2014.05.007

Yan, B.-F., Nguyen, C., Pokrovsky, O. S., Candaudap, F., Coriou, C., Bussière, S., et al. (2018). Contribution of remobilization to the loading of cadmium in durum wheat grains: impact of post-anthesis nitrogen supply. *Plant Soil* 424, 591–606. doi: 10.1007/s11104-018-3560-6

Yan, J., Wang, P., Wang, P., Yang, M., Lian, X., Tang, Z., et al. (2016). A loss-of-function allele of OsHMA3 associated with high cadmium accumulation in shoots and grain of japonica rice cultivars. *Plant Cell Environ.* 39, 1941–1954. doi: 10.1111/pce.12747

Yoshinari, A., and Takano, J. (2017). Insights into the mechanisms underlying boron homeostasis in plants. *Front. Plant Sci.* 8:1951. doi: 10.3389/fpls.2017.01951

Zandi, P., Yang, J., Możdżeń, K., and Barabasz-Krasny, B. (2020). A review of copper speciation and transformation in plant and soil/wetland systems. *Adv. Agron.* 160, 249–293. doi: 10.1016/bs.agron.2019.11.001

Zeebe, R. E. (2005). Stable boron isotope fractionation between dissolved $B(OH)_3$ and $B(OH)_4^-$. *Geochim. Cosmochim. Acta* 69, 2753–2766. doi: 10.1016/j.gca.2004.12.011

Zelano, I. O., Cloquet, C., Fraysse, F., Dong, S., Janot, N., Echevarria, G., et al. (2018). The influence of organic complexation on Ni isotopic fractionation and Ni recycling in the upper soil layers. *Chem. Geol.* 483, 47–55. doi: 10.1016/j.chemgeo.2018.02.023

Zelano, I. O., Cloquet, C., van der Ent, A., Echevarria, G., Gley, R., Landrot, G., et al. (2020). Coupling nickel chemical speciation and isotope ratios to decipher nickel dynamics in the Rinorea cf. bengalensis-soil system in Malaysian Borneo. *Plant Soil* 454, 225–243. doi: 10.1007/s11104-020-04541-0

Zhang, S. N., Gu, Y., Zhu, Z. L., Hu, S. H., Kopittke, P. M., Zhao, F. J., et al. (2021). Stable isotope fractionation of cadmium in the soil-rice-human continuum. *Sci. Total Environ.* 761:143262. doi: 10.1016/j.scitotenv.2020.143262

Zhao, Y., Li, Y., Wiggenhauser, M., Yang, J., Sarret, G., Cheng, Q., et al. (2021). Theoretical isotope fractionation of cadmium during complexation with organic ligands. *Chem. Geol.* 571:120178. doi: 10.1016/j.chemgeo.2021.120178

Zhong, S., Li, X., Li, F., Huang, Y., Liu, T., Yin, H., et al. (2022). Cadmium uptake and transport processes in rice revealed by stable isotope fractionation and Cd-related gene expression. *Sci. Total Environ.* 806:150633. doi: 10.1016/j.scitotenv.2021.150633

Zhong, S., Li, X., Li, F., Liu, T., Huang, F., Yin, H., et al. (2021). Water management alters cadmium isotope fractionation between shoots and nodes/leaves in a soil-rice system. *Environ. Sci. Technol.* 55, 12902–12913. doi: 10.1021/acs.est.0c04713

Zhou, F. Y., He, D., Miao, X., Yang, C., Dong, J. H., Zheng, H. T., et al. (2021). Development of an automatic column chromatography separation device for metal isotope analysis based on droplet counting. *Anal. Chem.* 93, 7196–7203. doi: 10.1021/acs.analchem.1c00145

Zhou, J., Li, Z., Liu, M., Yu, H., Wu, L., Huang, F., et al. (2020). Cadmium isotopic fractionation in the soil – plant system during repeated phytoextraction

with a cadmium hyperaccumulating plant species. *Environ. Sci. Technol.* 54, 13598–13609. doi: 10.1021/acs.est.0c03142

Conflict of Interest: The authors declare that the research was conducted in the absence of any commercial or financial relationships that could be construed as a potential conflict of interest.

Publisher's Note: All claims expressed in this article are solely those of the authors and do not necessarily represent those of their affiliated organizations, or those of the publisher, the editors and the reviewers. Any product that may be evaluated in this article, or claim that may be made by its manufacturer, is not guaranteed or endorsed by the publisher.

frontiers | Frontiers in Plant Science

ORIGINAL RESEARCH
published: 06 June 2022
doi: 10.3389/fpls.2022.865578

The Above-Ground Part of Submerged Macrophytes Plays an Important Role in Ammonium Utilization

*Ling Xian[1,2], Wyckliffe Ayoma Ochieng[1,2,3], Samuel Wamburu Muthui[1,2,3], Duncan Ochieng Otieno[1,2,3], Siwei Yu[1], Wei Li[1], Xue Yan[1,3], Quan Yu[1,3] and Fan Liu[1,3]**

[1] Core Botanical Gardens/Wuhan Botanical Garden, Chinese Academy of Sciences, Wuhan, China, [2] University of the Chinese Academy of Sciences, Beijing, China, [3] Sino-Africa Joint Research Centre, Chinese Academy of Sciences, Wuhan, China

As a paradoxical nutrient in water ecosystems, ammonium can promote plants growth under moderate concentration, but excess of it causes phytotoxic effects. Previous research has revealed that glutamate dehydrogenase in the above-ground part of submerged macrophytes plays an important role in ammonium detoxification. However, the strategies of ammonium utilization at the whole plant level of submerged macrophytes are still unclear and the role of the above-ground part in nutrient utilization has not been clearly elucidated in previous studies, hence, directly influencing the application of previous theory to practice. In the present research, we combined the methods of isotopic labeling and enzyme estimation to investigate strategies of ammonium utilization by the submerged macrophytes. The results showed that when [NH_4^+-N] was 50 mg L^{-1}, ^{15}N taken up through the above-ground parts was 13.24 and 17.52 mg g^{-1} DW, while that of the below-ground parts was 4.24 and 8.54 mg g^{-1} DW in *Potamogeton lucens* and *Myriophyllum spicatum*, respectively. The ratios of ^{15}N acropetal translocation to uptake were 25.75 and 35.69%, while those of basipetal translocation to uptake were 1.93 and 4.09% in *P. lucens* and *M. spicatum*, respectively. Our results indicated that the above-ground part was not only the main part for ammonium uptake, but also the major pool of exogenous ammonium. Besides, the dose–response curve of GDH (increased by 20.9 and 50.2% under 15 and 50 mg L^{-1} [NH_4^+-N], respectively) exhibited by the above-ground parts of *M. spicatum* indicates that it is the main site for ammonium assimilation of the tolerant species. This study identifies the ammonium utilization strategy of submerged macrophytes and reveals the important role of the above-ground part in nutrient utilization providing new insight into the researches of nutrient utilization by plants and theoretical supports for water restoration by phytoremediation.

Keywords: ammonium uptake, ammonium translocation, ammonium assimilation, above-ground part, phytoremediation, submerged macrophytes

OPEN ACCESS

Edited by:
Olena Vatamaniuk, Cornell University, United States

Reviewed by:
Maria Amélia Martins-Loução, University of Lisbon, Portugal
Haoping Wu, Guangdong Academy of Agricultural Sciences, China

***Correspondence:**
Fan Liu
fanliu@wbgcas.cn

Specialty section:
This article was submitted to Plant Nutrition, a section of the journal Frontiers in Plant Science

Received: *30 January 2022*
Accepted: *26 April 2022*
Published: *06 June 2022*

Citation:
Xian L, Ochieng WA, Muthui SW, Otieno DO, Yu S, Li W, Yan X, Yu Q and Liu F (2022) The Above-Ground Part of Submerged Macrophytes Plays an Important Role in Ammonium Utilization. Front. Plant Sci. 13:865578. doi: 10.3389/fpls.2022.865578

INTRODUCTION

Nitrogen is an indispensable nutrient in human life and production. As one of the most important determinants for plant growth, nitrogen fertilizer is widely used to increase crop production. However, only half of the applied nitrogen, on average, is taken up by crops (Kanter et al., 2019). Overapplication of nitrogen fertilizer in agriculture together with the nitrogenous discharge from industrial wastewater and livestock causes a number of environmental pollutions such as the destruction of aquatic ecosystems and biodiversity loss (Galloway et al., 2008; Kanter et al., 2019).

Excess nitrogen in the aquatic ecosystem mainly consists of nitrate–nitrogen and ammonium–nitrogen which is the main inorganic nitrogen available for plants (Lopes and Araus, 2006). As the preferred inorganic nitrogen for plants, ammonium can promote growth under the micromolar concentration range (Gazzarrini et al., 1999), but when the concentration reaches millimolar levels, toxicity will occur (Britto and Kronzucker, 2002; Hachiya and Sakakibara, 2017). Previous research has revealed that ammonium metabolism *via* the pathway catalyzed by GDH (glutamate dehydrogenase) plays an important role in the above-ground part of the submerged macrophytes to ammonium detoxification (Xian et al., 2020). However, whether the above-ground part is the main site for ammonium utilization in submerged macrophytes at the whole plant level is puzzling which directly influences the feasibility of the aforementioned research results in water restoration by phytoremediation.

General conceptions imply that the below-ground tissue of plants is the most important part of nature because most essential nutrients for life such as mineral elements enter the biosphere and food chains through the roots of higher plants (Lamont, 1982). Except for carbon, hydrogen, and oxygen, about 14 indispensable nutrient elements required by plants are mainly taken up through their roots from the soil and transported to the shoots for their growth and development (Jukes, 1995; Che et al., 2018). Specific to submerged macrophytes, multitudinous nutrients exist in both the water column and sediments. They uptake nutrients not only from the sediments but also from the overlying water through their leaves (Stapel et al., 1996; Richter and Gross, 2013; Lin et al., 2017). Besides, the below-ground tissues of the most submerged macrophytes are degenerated; typically, the ratio of below-ground to above-ground tissue of submerged macrophytes is no more than 10% (Kautsky, 1987; Huang et al., 2017). Hence, is the ammonium utilization strategy of submerged macrophytes similar to the general conception? Does the above-ground part of submerged macrophytes matter in ammonium utilization?

Submerged macrophytes are important primary producers in freshwater ecosystems (Moss, 1995; Jeppesen et al., 1998; Fritz et al., 2017). They occupy habitats characterized by a phase boundary of water and sediment which contain different nutrient components and are hard to be simulated. This is due to the lack of a suitable method to separate the nutrient of the above- and below-ground parts for the whole plant level of the submerged macrophytes. The existence of this bottleneck makes it difficult for relevant studies to be conducted. Hence, it is still not clear whether it is either the above-ground part or below-ground part that matters the most in nutrient utilization for submerged macrophytes.

In this study, we designed a test to isolate the nutrient solution surrounding the above-ground from that surrounding the below-ground parts of whole plants of submerged macrophytes. To better understand the strategy of ammonium utilization at the whole plant level of submerged macrophytes, a controlled experiment with different ammonium concentrations was set up using $^{15}NH_4^+$ as the sole nitrogen source for the above- and below-ground parts separately. Our research aimed to reveal the strategy of ammonium utilization at the whole plant level of submerged macrophytes and provide new insight on nutrient utilization in plants, therefore, providing theoretical support and reasonable guidance for the phytoremediation technologies.

MATERIALS AND METHODS

Plant Material and Experimental Site

Myriophyllum spicatum L. and *Potamogeton lucens* L. were chosen as experimental materials because of their different sensitivities to ammonium as illustrated in our previous research (Xian et al., 2020). *M. spicatum* is tolerant to high [NH_4^+-N] while *P. lucens* is intolerant. Plants were collected randomly from the same colony in Erhai Lake (25°36′–25°58′N, 100°06′–100°18′E), the second-largest freshwater lake with a subtropical plateau monsoon climate, located on the Yungui Plateau, southwest China (Zhu et al., 2018; Zhong et al., 2019). Approximately 10 cm apices of plants without leaves were used for transplantation. After 4 months of cultivation, healthy plants were collected for the laboratory experiment.

Isolation of Nutrients in Above- and Below-Ground Parts of the Plants

Hermetic bags made with natural emulsion from 15 brands were chosen as the initial material because they are well-sealed and are homogeneous in production. Nutrient leakage from hermetic bags was estimated using high [NH_4^+-N] (1,000 mg L^{-1}) and deionized water to create hyper-osmosis between the inside and outside. The brand of hermetic bags with the least leakage was chosen as the most suitable material to separate the solution between above- and below-ground parts of the two species (results are shown in **Supplementary Figure 1**).

Ammonium-Dosing Experiment in Laboratory

The whole plants of *M. spicatum* and *P. lucens* were collected from cultivation tanks after 4 months of culture and transported in a culture medium at the end of pre-culture using the equipment we designed (**Supplementary Figure 2**). Our experimental design took account of the fact that submerged macrophytes absorb nutrients mainly from the liquid phase, and the liquid medium can not only provide enough nutrition to the plants, but also ensure the uniformity of nutrition within the culture time. Thus, the culture medium was prepared

using 10% Hoagland's solution with either $(^{14}NH_4)_2SO_4$ or $(^{15}NH_4)_2SO_4$ (δ 98%, Sigma, United States) as the sole nitrogen source. We set two groups: (A) ammonium in solutions for the above-ground parts was prepared by $(^{15}NH_4)_2SO_4$ while that of the below-ground parts was prepared by $(^{14}NH_4)_2SO_4$, (B) ammonium in solutions for the above-ground parts were prepared by $(^{14}NH_4)_2SO_4$, while the below-ground part was prepared by $(^{15}NH_4)_2SO_4$ (**Supplementary Figure 3**). Ammonium nitrogen concentrations were set according to our previous study (Apudo et al., 2016; Xian et al., 2020), in brief, 3 concentrations (0.1 mg L^{-1}, 15 mg $L^{-1,}$ and 50 mg L^{-1}) were set for the above-ground part while $[NH_4^+$-N] for the below-ground part was set according to the ratio of $[NH_4^+$-N] in pore water to overlying water from our field investigation of 22 water bodies (**Supplementary Table 1**). Culture conditions were set at 25°C, with a photoperiod of 14/10-h (light/dark) and light intensity of 108 μmol photons/m^2/s. The experiment lasted for 4 days in accordance with our previous study (Xian et al., 2020) after which the samples were collected for further analysis.

Estimation of Parameters

We collected appropriate samples from above- and below-ground parts separately at the end of culture to analyze nitrogen uptake and translocation ability within the two species. After drying by Lyophilizer (Freezone 4.5L, Labconco, United States), samples were sent to Environmental Stable Isotope Laboratory (ESIL), Institute of Environment and Sustainable Development of Agriculture, Chinese Academy of Agricultural Sciences for isotope nitrogen detection. Considering that the water content of submerged macrophyte leaves is much higher than that of terrestrial plants, rapid loss of moisture during the measurement of leaf area would cause significant changes in leaf area. Furthermore, the leaf types of *M. spicatum* and *P. lucens* are quite different which may cause larger errors in the evaluation of the surface area, thus, the content of ^{15}N absorption was expressed as ^{15}N increment per gram of dry weight (Bouma et al., 2002; Guo et al., 2017; Cao et al., 2018; Svennerstam and Jämtgård, 2022). The ^{15}N content in plant tissue was calculated according to the methods of Guo et al. (2017) with minor modifications by the following formulas:

$$\text{Ratio value } (\delta) = \frac{\text{Ratio}_{sample} - \text{Ratio}_{standard}}{\text{Ratio}_{standard}} \times 1000 \quad (1)$$

$$^{15}N\ \left(\text{mg g}^{-1}\right) = \frac{\text{Ratio}_{sample}}{1 + \text{Ratio}_{sample}} \times \frac{\text{N content in sample}}{\text{sample dry weight}} \quad (2)$$

The natural ^{15}N (0.365%) of atmospheric N_2 was used as the $\text{Ratio}_{standard}$.

To determine the plant state, we measured the concentration of dissolved oxygen (DO), chlorophyll fluorescence, and total chlorophyll content under experimental conditions according to the methods used in our previous studies (Apudo et al., 2016; Xian et al., 2020). To better understand the strategy of nitrogen allocation and ammonium assimilation between the above- and below-ground parts, we quantified the contents of soluble proteins, free amino acids (FAAs), and the activities of enzymes associated with ammonium assimilation according to Xian et al. (2020).

Statistical Analysis

Statistical analysis was carried out with SPSS software version 22.0. Student's *t*-test was performed to compare the differences in photosynthetic parameters, ^{15}N uptake and translocation, nitrogen nutrient and activities of enzymes between the two species under the same ammonium concentration. One-way ANOVA was applied to analyze the effects of ammonium concentrations on all the parameters. Tukey test was used for *post hoc* comparisons for all the analyses. Significance level for all tests was set at p-value < 0.05. Data shown in figures are presented as mean ± SD from five independent replicates for each concentration.

RESULTS

Differences in Ammonium-Nitrogen Uptake and Translocation

We found that both the above- and below-ground parts of *M. spicatum* and *P. lucens* have the ability to take up external ammonium (**Figures 1A,B**). Under normal $[NH_4^+$-N] (0.1 mg L^{-1}), both species exhibited the highest uptake ability of below-ground part (**Figures 1A,B**). However, with the increase in $[NH_4^+$-N], nitrogen uptake ability of above-ground part was always higher than that of the below-ground part in both the species (**Figures 1A,B**). The content of ^{15}N uptake through the above-ground part was 1.4- and 2.1-folds higher than the below-ground parts for *P. lucens* under 15 and 50 mg L^{-1} $[NH_4^+$-N], respectively, while that of *M. spicatum* was 1.6- and 1.1-folds higher for the same concentrations.

We further analyzed the translocation of nitrogen from exogenous ammonium–nitrogen between above- and below-ground parts by comparing the proportion of ^{15}N translocation to uptake content. During the 4-day culture, both species exhibited two directions of nitrogen translocation (from above to below and *vice versa*) (**Figures 1C,D**). Under normal $[NH_4^+$-N] condition (0.1 mg L^{-1}), the acropetal and basipetal translocation of ^{15}N in *P. lucens* did not show any significant differences (**Figure 1D**). However, the acropetal translocation was significantly higher than basipetal in *M. spicatum* (**Figure 1C**). Under high $[NH_4^+$-N] (≥15 mg L^{-1}), acropetal translocation dominated in both species (**Figures 1C,D**). At 15 mg L^{-1} $[NH_4^+$-N], ^{15}N acropetal translocation/uptake was about 23.0 and 35.5% while basipetal was about 3.5 and 3.1% in *P. lucens* and *M. spicatum*, respectively. When ammonium was excess (50 mg L^{-1}), ^{15}N acropetal translocation/uptake was about 25.8 and 35.7% while

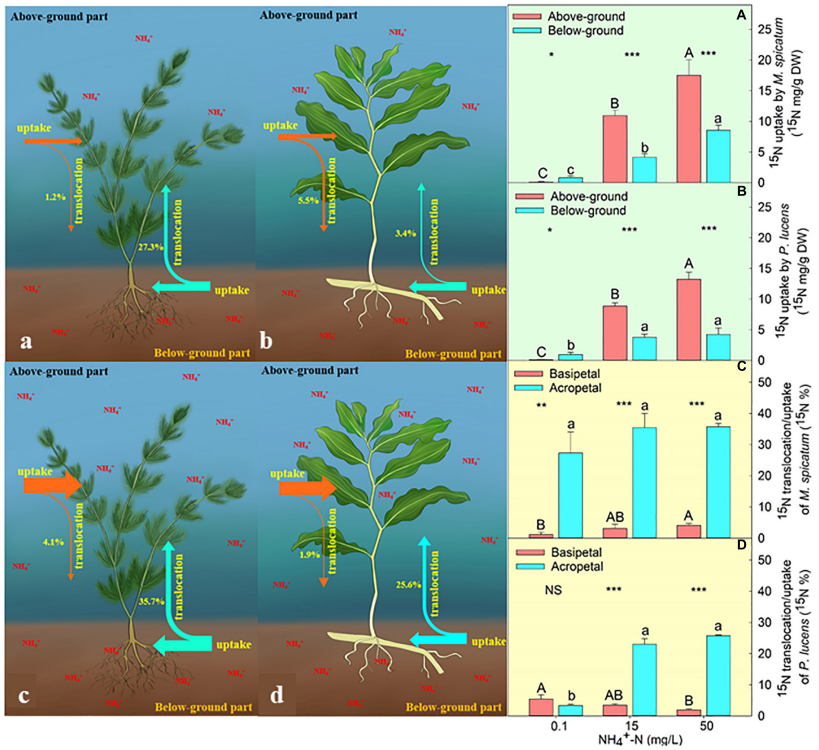

FIGURE 1 | Characteristics of ^{15}N uptake and translocation in plants. Schematic diagram of ^{15}N uptake and translocation of *M. spicatum* and *P. lucens* under normal **(a,b)** and high **(c,d)** [NH_4^+–N]. The effects of different [NH_4^+–N] on the ^{15}N uptake of *M. spicatum* **(A)** and *P. lucens* **(B)** through the above-ground part (red bar) and the below-ground part (blue bar) and ^{15}N translocation of basipetal (red bar) and acropetal (blue bar) of *M. spicatum* **(C)** and *P. lucens* **(D)**. Different letters represent significant differences ($p < 0.05$). Statistical Student's *t*-tests are shown, $^*p < 0.05$, $^{**}p < 0.01$, $^{***}p < 0.001$, NS: no significance.

basipetal movement was about 1.9 and 4.1% in *P. lucens* and *M. spicatum*, respectively.

Estimation of Physiological Parameters

With an increase in [NH_4^+-N], no significant differences were witnessed in the photosynthesis of *M. spicatum*, however, a considerable decrease was exhibited by *P. lucens* (**Supplementary Figure 4**). A significant increase in FAA could be observed in both above- and below-ground parts of the two species with an increase in [NH_4^+-N] (**Figures 2A,B**). Soluble proteins in the two species displayed different tendencies. For *M. spicatum*, it increased with the increase in [NH_4^+-N] concentration in the above-ground part but no significant changes were noted in its below-ground part. However, a significant decrease was observed in both the above- and below-ground parts of *P. lucens* (**Figures 2C,D**). Through enzymatic estimation, we found that with an increase in ammonium concentration, a decline in GS activities was detected in the above-ground parts of the two species (**Figure 2E**). However, different changes were observed in GDH activities of the above-ground parts of the two species: a sharp rise in *M. spicatum* and stable activities in *P. lucens* (**Figure 2G**). Compared with 0.1 mg L^{-1} [NH_4^+-N], the activity of GDH in the above-ground of *M. spicatum* was increased by 20.9 and 50.2% under 15 and 50 mg L^{-1} [NH_4^+-N] treatments, respectively. For below-ground parts, a significant decline was exhibited in both GS and GDH of *M. spicatum*, however, no significant changes were witnessed in *P. lucens* (**Figures 2F,H**).

DISCUSSION

Nutrient utilization by plants has always been a major hotspot in ecological researches, furthermore, the importance of the below-ground part has been emphasized for a long time. However, whether submerged macrophytes in freshwater ecosystems still follow the general strategy (in which the below-ground part dominates in nutrient utilization) is still unknown. In this research, new findings were revealed where the above-ground parts of submerged macrophytes have been found to play a much bigger role in nutrient utilization than was previously thought.

Uptake and Translocation of Nitrogen From Exogenous Ammonium

The use of isotopic labeling in this study demonstrated that both species uptake ammonium mainly through their below-ground parts under normal [NH_4^+-N] (0.1 mg L^{-1}). This strategy is similar to the one found in terrestrial plants where nutrient uptake is mainly through the below-ground part. Due to the limitation of nutrients in the overlying water column for above-ground parts, submerged macrophytes may solely take up

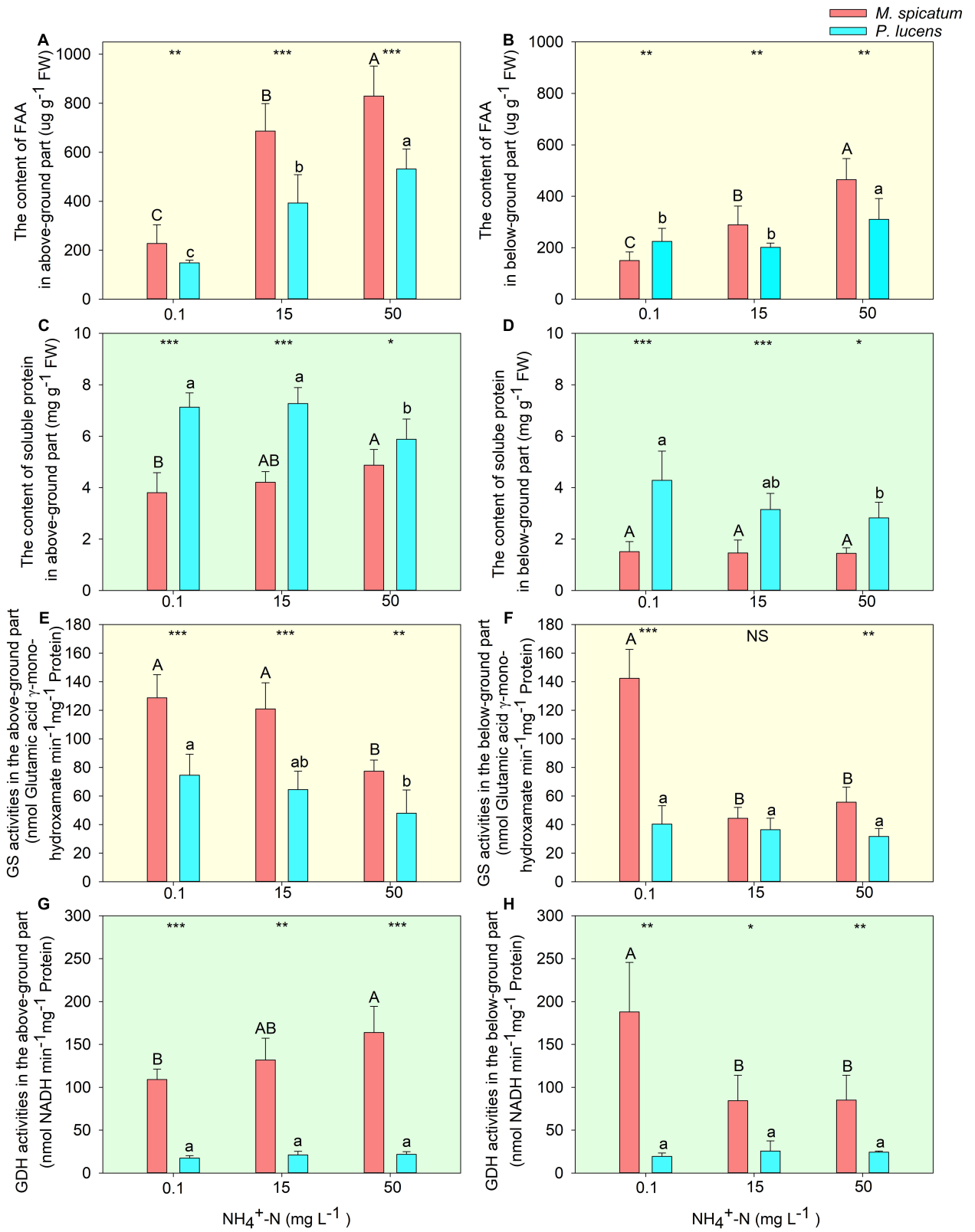

FIGURE 2 | Estimation of nitrogen allocation and ammonium assimilation in plants. The effect of $[NH_4^+$-N] on the content of FAA **(A,B)**, soluble protein **(C,D)**, enzymes activities of GS **(E,F)**, and GDH **(G,H)** in the above- and below-ground parts of *M. spicatum* (red bar) and *P. lucens* (blue bar). Different letters represent significant differences ($p < 0.05$), capital letters: *M. spicatum*, lowercase letters: *P. lucens*. Statistical differences between the two species are designed as follows: $^*p < 0.05$, $^{**}p < 0.01$, $^{***}p < 0.001$, NS stands for no significance, based on the Student's *t*-tests.

nutrients from sediments where the concentrations are sufficient to meet plant's requirements. However, based on our study, the above-ground parts of submerged macrophytes occupy a great position in ammonium uptake, especially under conditions of high [NH_4^+-N] (15 mg L^{-1}). Although abundant pieces of evidence have shown that the above-ground parts (e.g., leaves, stems, fruits) have the ability to take up nutrients (Bouma et al., 2002; Fernandez and Brown, 2013), studies comparing uptake capacities between the below-ground and above-ground parts are rare, especially in freshwater ecosystems. The above-ground part has always been the key center of research for submerged macrophytes; it is not only the main site of photosynthesis but also the part in contact with the water environment. In this study, the same strategy of ammonium uptake was exhibited by both *M. spicatum* and *P. lucens*, which reveals the importance of above-ground parts in nutrient uptake (because uptake through the below-ground part only dominates when the nutrient of above-ground part is limited). This may be due to the fact that the contact surface between the above-ground part and water is much larger than the below-ground part and the flowing water also increases the collision between nutrients and plant tissues, which makes it easier for the above-ground part to obtain nutrients from the environment. Furthermore, nutrients taken up through the above-ground part are directly added into the plant's metabolism, which could potentially and readily influence plant's growth than nutrients from sediments (Sparks, 2009). This process cannot only supply nutrients to the below-ground part when nutrients in sediment are limited but also improves plants' tolerance when suffering from the excess nutrient supply (Yang et al., 2009; Guha et al., 2010; Khan et al., 2010). The below-ground part of submerged macrophytes is capable of taking up nutrients although its main function is plant's anchorage and energy storage to guarantee plant growth. Since the below-ground parts of most submerged macrophytes are degenerated, they are often characterized by relatively smaller root systems compared to their terrestrial counterparts (Kautsky, 1987; Huang et al., 2017). For this reason, many species of submerged macrophyte have been found to survive very well even without the below-ground parts, for instance, *Ceratophyllum demersum*.

Plants transfer nutrients to different organs through a series of processes to meet their growth requirements. In this study, when [NH_4^+-N] is 0.1 mg L^{-1}, different strategies of nitrogen translocation are observed in *P. lucens* and *M. spicatum*, thereby revealing different nitrogen requirements for the above- and below-ground parts of the two species. Under normal conditions, plants that uptake and store nutrients for their growth and reproduce asexually are considered to be more advantageous in mild habitats (Williams, 1975; Grant, 1981; Li, 2014). For *P. lucens*, its rhizome (the below-ground part) is the most common vegetative propagule, thus, the storage of nutrients in the below-ground part provides enough energy to support its reproduction. However, the shoot fragment is the main vegetative propagule for *M. spicatum*. Therefore, more nutrients are required for the above-ground part which makes the acropetal translocation dominant in *M. spicatum*. Nevertheless, under high [NH_4^+-N] ($\geq$ 15 mg L^{-1}), the acropetal translocation dominates in the allocation of nitrogen, which makes the above-ground part to be the main nitrogen pool. For terrestrial plants, transpiration in the leaves is the main driving force for mineral element translocation (Campbell et al., 1999; Tanner and Beevers, 2001), thus, the main translocate direction of most mineral nutrients is acropetal. It is interesting that the translocation pattern for the submerged macrophytes under high-ammonium concentrations is similar to that in the terrestrial plants. However, the main driving force for the submerged macrophytes may result from water pressure, nutrient concentrations, and also other reasons which are beyond the scope of this study. Except for the driving force, there are two main reasons that could be used to explain this result. First, sexual reproduction is considered to be more advantageous in heterogeneous or challengeable environments (Williams, 1975; Grant, 1981). Plants have to maintain their population through sexual reproduction under harsh environments (Li, 2014), which forces the above-ground part to store more nutrients and energy required for blossom formation, pollination, seed and fruit development, etc. Second, the above-ground part of plants is not only the main site for photosynthesis but also the main area for energy synthesis. In addition, it provides the most suitable place for plants to perform and maintain their physiological functions efficiently (Piao et al., 2020). When sufficient nutrients are present in water, submerged macrophytes uptake considerably enough amounts through their above-ground parts and assimilate them directly. This could reduce energy consumption in nutrient translocation from the below-ground to the above-ground parts and improve efficiency of energy utilization.

Ammonium Assimilation and Nitrogen Allocation

Although the strategies of ammonium uptake and translocation in *M. spicatum* and *P. lucens* are much similar under conditions of high-ammonium concentrations, different adaptations to the changeable environment can be found between the two species: high tolerance in *M. spicatum* and sensitivity in *P. lucens*. This could be explained by the strategy of ammonium assimilation and nitrogen allocation in plant tissue.

Ammonium absorbed by plants is assimilated through glutamine synthetase (GS) and glutamate dehydrogenase (GDH) (Glevarec et al., 2004; Skopelitis et al., 2006; Fontaine et al., 2012; Xian et al., 2020), afterward, transamination and synthesis produce new amino acids and protein. In this research, the significant increases in FAA and soluble protein in the above-ground tissue of *M. spicatum* reveal its strong ability to assimilate ammonium, which is supported by an increase in GDH activity in the above-ground part. GDH is a stress-responsive enzyme (Zhou et al., 2015) and catalyzes the reversible reaction that converts ammonium to glutamate; the biosynthesis direction of GDH plays an important role when ammonium is in excess (Abiko et al., 2010; Xian et al., 2020). The other enzyme, GS, displayed a sharp decline in both above- and below-ground parts of *M. spicatum* under excess [NH_4^+-N] (50 mg L^{-1}). This may be the strategy of submerged plants to save energy because GS catalyzes a more energy-consuming pathway for

ammonium assimilation; it costs about 18% more energy than the pathway catalyzed by GDH (Helling, 1994, 1998; Geisseler et al., 2009). Furthermore, GS is an enzyme with a high affinity to ammonium, the enzyme plays a dominant role in ammonium assimilation when ammonium is in limited supply, however, the activity is inhibited when ammonium is in excess (Zhou et al., 2017). The same tendency of GS activity can be observed in the above-ground part of *P. lucens*, whereas, the activity of GDH in both the above- and below-ground part did not show many differences under various ammonium concentrations. This may be due to the limitation of energy [e.g., Fv/Fm, total chlorophyll content and DO in solutions decreased under high [NH_4^+-N] ($\geq$ 15mg L^{-1})] and nitrogen accumulation which makes the ability of ammonium assimilation to decrease, causing toxicity of ammonium in *P. lucens* especially under excess [NH_4^+-N] (50 mg L^{-1}), followed by the degradation of protein and the increase of FAA exhibited in both the above- and below-ground tissues (Skopelitis et al., 2006; Xian et al., 2020).

The Investigation of Ammonium Detoxification Mechanism in *Myriophyllum spicatum*

In our research, *M. spicatum* exhibited higher plasticity in its physiology under various ammonium concentrations in comparison with *P. lucens*. The higher capacity of photosynthesis efficiently transforms light energy into chemical energy which improves plants' ability to balance C:N ratios in their tissue, thus improving the tolerance of plants subjected to excessive ammonium environments (Xiao et al., 2007; Apudo et al., 2016). Furthermore, the major site (above-ground part) of ammonium uptake and assimilation helps plants to avoid energy wastage in nutrient translocation. Moreover, the energy-efficient pathway catalyzed by GDH, not only plays an important role in ammonium detoxification (Xian et al., 2020), but also improves the conversion efficiency of ammonium to organics in *M. spicatum*. Hence, *M. spicatum* possesses a stronger ability than *P. lucens* to adapt to changeable environments which supports it survival in conditions characterized with excess ammonium.

CONCLUSION

As one of the most suitable candidates for water restoration in phytoremediation, submerged macrophytes are still enigmatic in many aspects such as nutrient uptake, translocation, and assimilation. In this research, we found that both the above- and below-ground parts of the two species could uptake ammonium from the environment, meanwhile, the acropetal and basipetal translocation of nitrogen were exhibited in both the species. However, ammonium uptake through the above-ground part and the acropetal translocation were dominant in both species when ammonium is in excess. The ammonium-tolerant species, *M. spicatum*, has higher plasticity in photosynthesis and ammonium utilization under various [NH_4^+-N] than *P. lucens*, moreover, the pathway catalyzed by GDH in the above-ground part of *M. spicatum* contributes more in ammonium detoxification.

This study explored the characteristics of ammonium utilization in two representative species of submerged macrophytes and firstly found the importance of the above-ground part in ammonium utilization under high-ammonium concentrations. Hence, we propose that more attention should be paid to the above-ground part of submerged macrophytes in phytoremediation for water restoration, and we suggest the use of *M. spicatum* with luxuriant above-ground part as a candidate for phytoremediation in the restoration of water bodies polluted by ammonium. The results not only provide theoretical support for the research on ammonium utilization of submerged macrophytes but also offer technical support for water restoration by the submerged macrophytes.

DATA AVAILABILITY STATEMENT

The raw data supporting the conclusions of this article will be made available by the authors, without undue reservation.

AUTHOR CONTRIBUTIONS

LX performed the experiments and wrote the manuscript. WL designed the research and reviewed the manuscript. LX and FL analyzed the data. LX and SY drew the figures. WO and SM participated in the collection of samples. WO, SM, DO, and XY reviewed the manuscript. FL conceptualized the study and obtained financial support for the work. All authors revised and approved the manuscript.

FUNDING

This work was supported by the National Natural Science Foundation of China (Grant Nos. 32070383 and 31670369), the Ministry of Science & Technology of China (Grant Nos. KY202001019 and 2016YFA0601001), and the Scientific Research Program of Sino-Africa Joint Research Center (Grant No. SAJC201601).

ACKNOWLEDGMENTS

We thank Yizhi Zhang, Hongsheng Jiang, and Yu Cao for their helpful advice and polish the language.

SUPPLEMENTARY MATERIAL

The Supplementary Material for this article can be found online at: https://www.frontiersin.org/articles/10.3389/fpls.2022.865578/full#supplementary-material

REFERENCES

Abiko, T., Wakayama, M., Kawakami, A., Obara, M., Kisaka, H., Miwa, T., et al. (2010). Changes in nitrogen assimilation, metabolism, and growth in transgenic rice plants expressing a fungal NADP(H)-dependent glutamate dehydrogenase (gdhA). *Planta* 232, 299–311. doi: 10.1007/s00425-010-1172-3

Apudo, A. A., Cao, Y., Wakibia, J., Li, W., and Liu, F. (2016). Physiological plastic responses to acute NH_4^+–N toxicity in *Myriophyllum spicatum* L. cultured in high and low nutrient conditions. *Environ. Exp. Bot.* 130, 79–85.

Bouma, T. J., Stapel, J., van der Heiden, J., Koutstaal, B., van Soelen, J., and van Ijzerloo, L. (2002). Relative importance of macrophyte leaves for nitrogen uptake from flood water in tidal salt marshes. *Mar. Ecol. Prog. Ser.* 240, 93–104.

Britto, D. T., and Kronzucker, H. J. (2002). NH_4^+ toxicity in higher plants: a critical review. *J. Plant Physiol.* 159, 567–584.

Campbell, N. A., Reece, J. B., and Mitchell, L. G. (1999). *Biology*, 5th Edn. Reading, MA: Addison Wesley Longman.

Cao, X., Zhong, C., Zhu, C., Zhu, L., Zhang, J., Wu, L., et al. (2018). Ammonium uptake and metabolism alleviate PEG-induced water stress in rice seedlings. *Plant Physiol. Biochem.* 132, 128–137. doi: 10.1016/j.plaphy.2018.08.041

Che, J., Yamaji, N., and Ma, J. F. (2018). Efficient and flexible uptake system for mineral elements in plants. *New Phytol.* 219, 513–517. doi: 10.1111/nph.15140

Fernandez, V., and Brown, P. H. (2013). From plant surface to plant metabolism: the uncertain fate of foliar-applied nutrients. *Front. Plant Sci.* 4:289. doi: 10.3389/fpls.2013.00289

Fontaine, J. X., Terce-Laforgue, T., Armengaud, P., Clement, G., Renou, J. P., Pelletier, S., et al. (2012). Characterization of a NADH-dependent glutamate dehydrogenase mutant of Arabidopsis demonstrates the key role of this enzyme in root carbon and nitrogen metabolism. *Plant Cell* 24, 4044–4065. doi: 10.1105/tpc.112.103689

Fritz, C., Schneider, T., and Geist, J. (2017). Seasonal variation in spectral response of submerged aquatic macrophytes: a case study at lake starnberg (Germany). *Water* 9:527.

Galloway, J. N., Townsend, A. R., Erisman, J. W., Bekunda, M., Cai, Z., Freney, J. R., et al. (2008). Transformation of the nitrogen cycle: recent trends, questions, and potential solutions. *Science* 320, 889–892. doi: 10.1126/science.1136674

Gazzarrini, S., Lejay, L., Gojon, A., Ninnemann, O., Frommer, W. B., and von Wiren, N. (1999). Three functional transporters for constitutive, diurnally regulated, and starvation-induced uptake of ammonium into Arabidopsis roots. *Plant Cell* 11, 937–948. doi: 10.1105/tpc.11.5.937

Geisseler, D., Doane, T. A., and Horwath, W. R. (2009). Determining potential glutamine synthetase and glutamate dehydrogenase activity in soil. *Soil Biol. Biochem.* 41, 1741–1749. doi: 10.3389/fmicb.2021.774707

Glevarec, G., Bouton, S., Jaspard, E., Riou, M. T., Cliquet, J. B., Suzuki, A., et al. (2004). Respective roles of the glutamine synthetase/glutamate synthase cycle and glutamate dehydrogenase in ammonium and amino acid metabolism during germination and post-germinative growth in the model legume *Medicago truncatula*. *Planta* 219, 286–297. doi: 10.1007/s00425-004-1214-9

Grant, V. (1981). *Plant Speciation*, 2nd Edn. New York, NY: Columbia University Press.

Guha, A., Sengupta, D., Rasineni, G. K., and Reddy, A. R. (2010). An integrated diagnostic approach to understand drought tolerance in mulberry (*Morus indica* L.). *Flora* 205, 144–151.

Guo, H., Wang, H., Liu, Q., An, H., Liu, C., Xia, X., et al. (2017). ^{15}N-labeled ammonium nitrogen uptake and physiological responses of poplar exposed to $PM_{2.5}$ particles. *Environ. Sci. Pollut. Res. Int.* 24, 500–508. doi: 10.1007/s11356-016-7620-2

Hachiya, T., and Sakakibara, H. (2017). Interactions between nitrate and ammonium in their uptake, allocation, assimilation, and signaling in plants. *J. Exp. Bot.* 68, 2501–2512. doi: 10.1093/jxb/erw449

Helling, R. B. (1994). Why does *Escherichia coli* have two primary pathways for synthesis of glutamate? *J. Bacteriol.* 176, 4664–4668. doi: 10.1128/jb.176.15.4664-4668.1994

Helling, R. B. (1998). Pathway choice in glutamate synthesis in *Escherichia coli*. *J. Bacteriol.* 180, 4571–4575. doi: 10.1128/JB.180.17.4571-4575.1998

Huang, X. L., Shen, N., Guan, X., Xu, X., Kong, F. J., Liu, C. H., et al. (2017). Root morphological and structural comparisons of introduced and native aquatic plant species in multiple substrates. *Aquat. Ecol.* 52, 65–76.

Jeppesen, E., Sondergaard, M., Sondergaard, M., and Christoffersen, K. E. (1998). *The Structuring Role of Submerged Macrophytes in Lakes*. New York, NY: Springer-Verlag.

Jukes, T. H. (1995). Mineral nutrition of plants. *Photosynth. Res.* 46, 13–15.

Kanter, D. R., Bartolini, F., Kugelberg, S., Leip, A., Oenema, O., and Uwizeye, A. (2019). Nitrogen pollution policy beyond the farm. *Nat. Food* 1, 27–32.

Kautsky, L. (1987). Life-cycles of three populations of *Potamogeton pectinatus* L. at different degrees of wave exposure in the Askö area, Northern Baltic proper. *Aquat. Bot.* 27, 177–186.

Khan, H. R., Paull, J. G., Siddique, K. H. M., and Stoddard, F. L. (2010). Faba bean breeding for drought-affected environments: a physiological and agronomic perspective. *Field Crops Res.* 115, 279–286.

Lamont, B. (1982). Mechanisms for enhancing nutrient uptake in plants, with particular reference to mediterranean South Africa and Western Australia. *Bot. Rev.* 48, 597–689.

Li, W. (2014). Environmental opportunities and constraints in the reproduction and dispersal of aquatic plants. *Aquat. Bot.* 118, 62–70. doi: 10.1111/1365-2656.12709

Lin, Q., Gu, B., and Hong, J. (2017). Tracking uptake of submerged macrophytes (*Ceratophyllum demersum*)—Derived nitrogen by cattail (*Typha angustifolia*) using nitrogen stable isotope enrichments. *Ecol. Eng.* 99, 114–118.

Lopes, M. S., and Araus, J. L. (2006). Nitrogen source and water regime effects on durum wheat photosymntesis and stable carbon and nitrogen isotope composition. *Physiol. Plant.* 126, 435–445.

Moss, B. (1995). The microwaterscape - A four-dimensional view of interactions among water chemistry, phytoplankton, periphyton, macrophytes, animals and ourselves. *Water Sci. Technol.* 32, 105–116.

Piao, H. C., Li, S. L., Yan, Z. F., and Li, C. (2020). Understanding nutrient allocation based on leaf nitrogen isotopes and elemental ratios in the karst region of Southwest China. *Agric. Ecosyst. Environ.* 294:106864.

Richter, D., and Gross, E. M. (2013). Chara can outcompete *Myriophyllum* under low phosphorus supply. *Aquat. Sci.* 75, 457–467.

Skopelitis, D. S., Paranychianakis, N. V., Paschalidis, K. A., Pliakonis, E. D., Delis, I. D., Yakoumakis, D. I., et al. (2006). Abiotic stress generates ROS that signal expression of anionic glutamate dehydrogenases to form glutamate for proline synthesis in tobacco and grapevine. *Plant Cell* 18, 2767–2781. doi: 10.1105/tpc.105.038323

Sparks, J. P. (2009). Ecological ramifications of the direct foliar uptake of nitrogen. *Oecologia* 159, 1–13. doi: 10.1007/s00442-008-1188-6

Stapel, J., Aarts, T. L., van Duynhoven, B. H. M., de Groot, J. D., van den Hoogen, P. H. W., and Hemminga, M. A. (1996). Nutrient uptake by leaves and roots of the seagrass *Thalassia hemprichii* in the Spermonde Archipelago, Indonesia. *Mar. Ecol. Prog. Ser.* 134, 195–206.

Svennerstam, H., and Jämtgård, S. (2022). Timing is everything-obtaining accurate measures of plant uptake of amino acids. *New Phytol.* 234, 311–318. doi: 10.1111/nph.17964

Tanner, W., and Beevers, H. (2001). Transpiration, a prerequisite for long-distance transport of minerals in plants? *Proc. Natl. Acad. Sci. U. S. A.* 98, 9443–9447. doi: 10.1073/pnas.161279898

Williams, G. C. (1975). *Sex and Evolution*. Princeton, NJ: Princeton University Press.

Xian, L., Zhang, Y., Cao, Y., Wan, T., Gong, Y., Dai, C., et al. (2020). Glutamate dehydrogenase plays an important role in ammonium detoxification by submerged macrophytes. *Sci. Total Environ.* 722:137859.

Xiao, K. Y., Yu, D., and Wu, Z. H. (2007). Differential effects of water depth and sediment type on clonal growth of the submersed macrophyte *Vallisneria natans*. *Hydrobiologia* 589, 265–272.

Yang, F., Hu, J. J., Li, J. L., Wu, X. L., and Qian, Y. R. (2009). Chitosan enhances leaf membrane stability and antioxidant enzyme activities in apple seedlings under drought stress. *Plant Growth Regul.* 58, 131–136.

Zhong, S., Geng, Y., Qian, Y., Chen, W., and Pan, H. (2019). Analyzing ecosystem services of freshwater lakes and their driving forces: the case of Erhai Lake, China. *Environ. Sci. Pollut. Res.* 26, 10219–10229. doi: 10.1007/s11356-019-04476-9

Zhou, Q., Gao, J., Zhang, R., and Zhang, R. (2017). Ammonia stress on nitrogen metabolism in tolerant aquatic plant-*Myriophyllum aquaticum*. *Ecotoxicol. Environ. Saf.* 143, 102–110. doi: 10.1016/j.ecoenv.2017.04.016

Zhou, Y., Zhang, C., Lin, J., Yang, Y., Peng, Y., Tang, D., et al. (2015). Over-expression of a glutamate dehydrogenase gene, MgGDH, from *Magnaporthe grisea* confers tolerance to dehydration stress in transgenic rice. *Planta* 241, 727–740. doi: 10.1007/s00425-014-2214-z

Zhu, G., Yuan, C., Di, G., Zhang, M., Ni, L., Cao, T., et al. (2018). Morphological and biomechanical response to eutrophication and hydrodynamic stresses. *Sci. Total Environ.* 62, 421–435. doi: 10.1016/j.scitotenv.2017.11.322

Conflict of Interest: The authors declare that the research was conducted in the absence of any commercial or financial relationships that could be construed as a potential conflict of interest.

Publisher's Note: All claims expressed in this article are solely those of the authors and do not necessarily represent those of their affiliated organizations, or those of the publisher, the editors and the reviewers. Any product that may be evaluated in this article, or claim that may be made by its manufacturer, is not guaranteed or endorsed by the publisher.

frontiers | Frontiers in Plant Science

ORIGINAL RESEARCH
published: 22 June 2022
doi: 10.3389/fpls.2022.868661

OsVIT2 Mutation Increases Fe and Zn of Grain Without Compromising the Growth in Paddy Field

*Prashant Kandwal, Toru Fujiwara and Takehiro Kamiya**

Laboratory of Plant Nutrition and Fertilizers, Department of Applied Biological Chemistry, Graduate School of Agriculture and Life Sciences, The University of Tokyo, Tokyo, Japan

Nearly 2 billion people who reside in developing countries are suffering from nutrient deficiency, also known as hidden hunger. A hidden hunger includes iron (Fe) and zinc (Zn) deficiency. One of the most efficient solutions to hidden hunger is the biofortification of crops through breeding. In this study, we characterized the mutant 1095_k, which has high grain Fe (∼1.4-fold) and Zn (∼1.2-fold) concentration compared with wild-type plants for a 5-year field trial. The yield components of 1095_k are similar to wild-type plants in a paddy field. In addition, 1095_k has a non-sense mutation in *OsVIT2,* a vacuolar localized Fe transporter. F2 crosses between 1095_k and wild type having the mutation showing higher grain Fe and Zn concentration. In contrast, plants without the mutation showed similar element concentrations as the wild type. These results suggest that *OsVIT2* would be responsible for high Fe and Zn of grain and the 1095_k would be a useful breeding material for the biofortification of Fe and Zn.

Keywords: hidden hunger, biofortification, Fe, Zn, OsVIT2

OPEN ACCESS

Edited by:
Anja Schneider, Ludwig Maximilian University of Munich, Germany

Reviewed by:
Kurniawan Rudi Trijatmiko, International Rice Research Institute (IRRI), Philippines
Jeeyon Jeong, Department of Biology, Amherst College, United States

****Correspondence:***
Takehiro Kamiya
akamiyat@g.ecc.u-tokyo.ac.jp

Specialty section:
This article was submitted to Plant Nutrition, a section of the journal Frontiers in Plant Science

Received: *03 February 2022*
Accepted: *24 May 2022*
Published: *22 June 2022*

Citation:
Kandwal P, Fujiwara T and Kamiya T (2022) OsVIT2 Mutation Increases Fe and Zn of Grain Without Compromising the Growth in Paddy Field. Front. Plant Sci. 13:868661. doi: 10.3389/fpls.2022.868661

INTRODUCTION

Micronutrients are the inorganic nutrients that are required by a living organism in a small amount to sustain its life. The deficiency of micronutrients is also known as hidden hunger which is becoming a global burden by affecting more than two billion people, nearly one-third of the world population (Bailey et al., 2015; Harding et al., 2018). Among the micronutrients, the deficiency of iron (Fe) and zinc (Zn) is one of the leading public health concerns (Harding et al., 2018). Anemia is the well-known symptom of Fe deficiency in which hemoglobin count gets reduced, and the body has difficulty meeting the oxygen demand (Owais et al., 2021). The prevalence of anemia is higher in South Asia, Southeast Asia, and sub-Saharan Africa, where women of the reproductive age group suffer more because of the menstrual cycle and pregnancy (Sunuwar et al., 2020). In addition to Fe deficiency, the deficiency of Zn results in varying adverse effects, such as stunting, impaired reproduction, immune disorders, and mortality rate of diseases (e.g., diarrhea, malaria, and pneumonia) (Berhe et al., 2019; Palanog et al., 2019). Within Africa, Zn deficiency results in 14.4% of deaths due to diarrhea, 10.4% due to malaria, and 6.7% of deaths due to pneumonia (Berhe et al., 2019).

The deficiency of micronutrients, Fe and Zn, can be accounted for various reasons, such as poor dietary intake, malabsorption, food insecurity, and non-affordability of the nutrient-rich diet (Khush et al., 2012; Gupta et al., 2020). Rice is a staple food and rich in energy but not in micronutrients. In a developing country, where rice is a staple food, people consume rice and intake energy from it but consume fewer animal products and vegetables enriched in nutrients

(Van Der Straeten et al., 2020). To overcome the deficiency, biofortification of rice has been carried out using conventional breeding, an agronomic approach, and genetic modifications. The practice of crossing beneficial trait lines over several generations and selection of beneficial lines by their phenotype is the basics of conventional breeding (Kumar et al., 2019). In the agronomic approach, direct application of micronutrients either into the soil or foliar application on the plants is performed (Cakmak and Kutman, 2018). However, both conventional breeding and agronomic approaches are slow to process the release of a new crop variety (Shi et al., 2013; Ahmar et al., 2020). To overcome the limitations, the development of genetically modified organisms (GMOs) has been adopted. The transgenic approach allows the increase of micronutrients and can further introduce novel traits into plants (Christou and Twyman, 2004). Many efforts have been made to biofortify the Fe and Zn in rice, for instance, an increase in Fe content in rice by expressing the Nicotianamine aminotransferase (*NAAT*) gene (Takahashi et al., 2001), overexpression of *Oryza sativa* Nicotianamine synthase (*OsNAS2*) and *OsNAS3* (Lee et al., 2009, 2011), the introduction of soybean ferritin gene (*SoyferH1*) into rice (Goto et al., 1999), an increase of Fe and Zn in rice by expressing barley genes involved in phytosiderophore synthesis (Masuda et al., 2008). Using T-DNA insertion lines or CRISPR/Cas9 lines of rice tonoplast-localized transporters named Vacuolar Iron Transporter, OsVIT1, and OsVIT2, results in the increase of rice grain Fe and Zn content (Zhang et al., 2012; Bashir et al., 2013; Che et al., 2021). All these lines are GMOs, which are facing mass rejection, therefore limiting their availability in the market (Dipti et al., 2012). In addition, in most of the reports, yield in an actual paddy field remains to be tested (Goto et al., 1999; Lee et al., 2009, 2011; Zhang et al., 2012; Bashir et al., 2013; Che et al., 2021).

In recent years, different approaches, such as chemical-induced mutations, gamma radiation, and fast neutron-mediated mutagenesis have been adopted to improve the rice character, such as early flowering, tolerance to salinity, and drought (Sevanthi et al., 2018; Kumawat et al., 2019; Abdelnour-Esquivel et al., 2020). Once we identify the gene responsible for a phenotype, mutants are applicable for marker-assisted breeding (Karunarathna et al., 2021). Furthermore, mutants are not GMOs and are easily accepted by the market (Grover et al., 2020).

In the current study, we characterized a rice ethyl methanesulfonate (EMS)-mutagenized rice, named 1095_k, which showed a high grain Fe and Zn phenotype in paddy fields. It was found that mutant 1095_k has a nonsense mutation in *OsVIT2*. Furthermore, the mutation of *OsVIT2* did not affect yield in the fields. These results indicate 1095_k is a candidate for breeding high Fe and Zn content rice and *OsVIT2* mutation is used for marker-assisted breeding.

MATERIALS AND METHODS

Plant Material and Growth Conditions

Field experiments were performed in the paddy field of the Institute of Sustainable Agroecosystem Services, the University of Tokyo (hereafter referred to as Tokyo field) (35°44′19.5″N 139°32′31.6″E) and Experimental Farm Station of Graduate School of Life Sciences, Tohoku University (hereafter referred to as Miyagi field) (38°15′24.4″N 140°51′29.6″E) during rice cultivation season. For the F2 population (225 lines) between WT and 1095_k grown in the Yayoi campus of The University of Tokyo (hereafter referred to as Yayoi field) (35°43′01.2″N 139°45′45.4″E).

Determination of Fe and Zn Concentration

Five seeds for each genotype were selected to determine the Fe and Zn concentrations after removing the husk. After the measurement of dry weight, grains were applied to HNO_3 digestion in PYREX® tubes (Iwaki) as described. Two milliliters of HNO_3 (Wako) were applied to the tubes and heated for an initial 1 h at 70°C and then 120°C. After complete evaporation of HNO_3, 1 ml of HNO_3 was added, and the same temperature setting was applied. After complete evaporation of HNO_3, 1 ml of hydrogen peroxide (H_2O_2) was applied to the samples until they evaporated. Finally, the samples were dissolved in a 0.08 N HNO_3 solution and used for element concentration determination using the Inductive Coupled Plasma Mass Spectrometry (ICP-MS, Agilent 7800; Agilent Technologies).

For the polishing of rice, 15 seeds from WT and 1095_k were polished using a Pearlest grain polisher (Kett) for 1 cycle of 40 s.

Agronomic Trait Measurement

For agronomic trait measurements, WT and 1095_k were grown in the Tokyo field. The harvesting of the WT and 1095_k plant was performed 3 cm above the ground level. The plant height was measured from the tip of the panicle to the harvested end of the plant using a regular scale. The panicle from each tiller has been removed right from the panicle base and the length was measured. The number of ripe panicles was counted.

DNA Isolation, Sequencing, Real-Time PCR (RT-PCR), and Quantitative Real-Time PCR (qRT-PCR)

For DNA isolation, plant leaves of 15-days seedlings were used. The leaves were crushed using Zirconia beads using 300 μl of TPS buffer (100 mM Tris-HCl pH 6.8, 1 mM EDTA pH 8.0, 1.2 M KCl) followed by centrifugation at 10,000 × *g* for 13 min at 4°C. A 200 μl of the sample was transferred into the fresh tubes, and an equal volume of isopropylalchol was added. The solution was mixed and centrifuged at 10,000 × *g* for 30 min at 4°C. The supernatant was removed, and 70% ethanol was added, followed by centrifugation at 10,000 × *g* for 15 min. Again, the supernatant was removed, and the tubes were dried for not more than 10 min. The pellet was dissolved with 100 μl of TE buffer (10 mM Tris-HCl pH 8.0, 0.1 mM EDTA pH 8.0).

To determine the genomic sequence of *OsVIT1* (LOC_Os04g38940), the region containing the promoter (2,078 bp) and downstream sequence (1,002 bp), was amplified by using a forward primer 5′-CGTGCCGGAGAGAAGAACTA-3′ and a reverse primer 5′-GAATGGTTTCTGCAAGCTGGG-3′. The sequence of the *OsVIT1* genome was determined by the primers in **Table S1** (Primer ID 3–12) using Sanger sequencing. For the determination of the *OsVIT2* (LOC_Os09g23300) genomic

sequence, the region containing the promoter (2,035 bp) and downstream sequence (2,047 bp) was amplified by using a forward primer 5′-GACCGGTTAATTTCCCAACCG-3′ and a reverse primer 5′-AACCGACGGCACCGATCTAC-3′. The genome sequence is determined by the primers in **Table S1** (Primer ID 15–23) using Sanger sequencing.

The genotype of the F2 generation was determined by derived cleaved amplified polymorphic sequences (dCAPS) marker. The DNA was isolated from the F3 bulk (6 seeds). The *OsVIT2* genomic fragment was amplified with 5′-CCGCGGAGATCGCGGACATACTGTCGCACTA-3′ and 5′-AATTAGTTTTTTCCCCTTACTTCATC-3′ (Primer ID 30 and 31 in **Table S1**), which introduce a DdeI site. The DdeI digested PCR product was applied to 3% agarose gel.

For real-time quantification, plants were germinated for 1 week in tap water followed by another 1 week in Kimura B solution (Uraguchi et al., 2009). RNA extraction was performed by the NucloSpin RNA plant (TaKaRa Bio). The relative quantification of *OsVIT2* was performed using a forward primer 5′-GGTATCTGGCGGCGAAGAG-3′ and a reverse primer 5′-CGACAGTATGTCCGCGATCT-3′ using the Thermal Cycler Dice Real-Time System III (TaKaRa Bio). Relative expression levels were calculated against the reference gene, *Ubiquitin* (*OsUBQ10*), amplified with a forward primer 5′-AACCAGCTGAGGCCCAAGA-3′ and a reverse primer 5′-ACGATTGATTTAACCAGTCCATGA-3′.

RESULTS

Mutant 1095_k Showed High Grain Fe and Zn in Different Field Conditions

The EMS mutant 1095_k was isolated from the EMS mutant of *Oryza sativa* cv. Hitomebore population through ionome screening (Tanaka et al., 2016). The consistency of the mutant (1095_k) phenotype was assessed by growing both Hitomebore [wild type (WT)] and 1095_k in the paddy field condition. Both WT and 1095_k lines were grown in four independent years in the Tokyo field. After harvesting, ionome analysis was done using ICP-MS. It was found that the mutant 1095_k has a 1.4-fold higher grain Fe concentration compared with the WT (**Figure 1A**: Tokyo). To observe the consistency in the phenotype in a different field, WT and 1095_k were grown in the Miyagi field (**Figure 1A**: Miyagi). In addition, 1095_k showed a 1.5-fold higher grain Fe concentration compared with WT. Besides Fe, 1095_k has a 1.2-fold higher grain Zn concentration than WT (**Figure 1B**: Tokyo). In the Miyagi field, 1095_k showed a 1.5-fold higher grain Zn concentration compared with WT (**Figure 1B**: Miyagi). High Zn phenotype was observed in 2013, 2016, 2019, and 2021 in the Tokyo field. These results indicate that 1095_k has high Fe and Zn concentration in brown rice independent of field condition.

Hence, as commercial rice is available in the polished form, we determine the elemental concentrations of polished rice harvested in the year 2021. Polishing of brown rice resulted in ∼11.37% decline in the weight of WT grains and ∼12.01% decline in 1095_k grains. The polished 1095_k grains showed a 1.4-fold increase in Fe and a 1.2-fold increase in Zn concentration compared with WT (**Figures 1B,D**).

Apart from Fe and Zn concentration, little difference in toxic elements, such as Cd and As, was observed between WT and 1095_k in both brown rice and polished rice (**Figure S1**).

Yield Components Are Similar Between WT and 1095_k in the Paddy Field

Agronomic characters are an essential factor when considering breeding. Both WT and mutant 1095_k were cultivated in the Tokyo field. In each line, 41 plants were cultivated. The following yield components were measured: number of panicles/plant, number of tillers/plant, panicle weight/plant, panicle length, plant height, and 100 grain weight. No significant difference was observed in yield components between WT and 1095_k (**Figures 2A–D,F**, **Figure S2B**). The plant height was significantly smaller in 1095_k than that of the WT (**Figure 2E**, **Figure S2A**). These results suggest that 1095_k is a potential mutant that can retain high Fe and Zn without compromising yield components.

OsVIT2 Is a Possible Candidate for the Causal Gene of 1095_k

Several genes have been identified to be involved in the transport of Fe and Zn to the grain of rice. Fe transporters, *OsVIT1* and *OsVIT2*, have been characterized, whose T-DNA insertion lines show the increase in Fe and Zn concentration of grain (Zhang et al., 2012; Bashir et al., 2013). In 1095_k, there is an increase in Fe and Zn concentration in grains similarly to the mutant of *OsVIT*s (**Figure 1**). Therefore, we hypothesized that the alteration in *OsVIT* genes might be a cause of the phenotype. To test this, the genomic sequence of *OsVIT1* and *OsVIT2* was determined: the promoter (2,078 bp for *OsVIT1* and 2,035 bp for *OsVIT2*), gene body, and downstream sequence (1,002 bp of *OsVIT1* and 2,047 bp for *OsVIT2*). There is no nucleotide change in the *OsVIT1*. In *OsVIT2*, there is a nonsense mutation in the third exon, where thymine (T) at the 360th position in CDS was replaced by adenine (A), resulting in the formation of the stop codon (TAA) (**Figure 3A**). The relative mRNA accumulation of *OsVIT2* is reduced in 1095_k both in shoot and roots (**Figure 3B**), which might be due to nonsense-mediated mRNA decay. These data suggest that nonsense mutation in *OsVIT2* of 1095_k is a possible candidate gene behind the high Fe and Zn phenotype.

To confirm if *OsVIT2* is a causal gene of 1095_k, we observed the correlation between genotype and element concentrations in the F2 crosses between WT and 1095_k. The plants were grown in the Yayoi field, and the concentrations of the elements were determined by ICP-MS. The Fe and Zn concentration increase was observed in 1095_k compared with WT in this field, which confirms that the Yayoi field condition can be used for the F2 population phenotyping (**Figure 3C**). Fe and Zn concentrations were determined in F2 populations and there is a positive correlation (Pearson's $r = 0.418$) between Fe and Zn concentration (**Figure 3D**), suggesting that high Fe and Zn phenotype is caused by the same gene. Next,

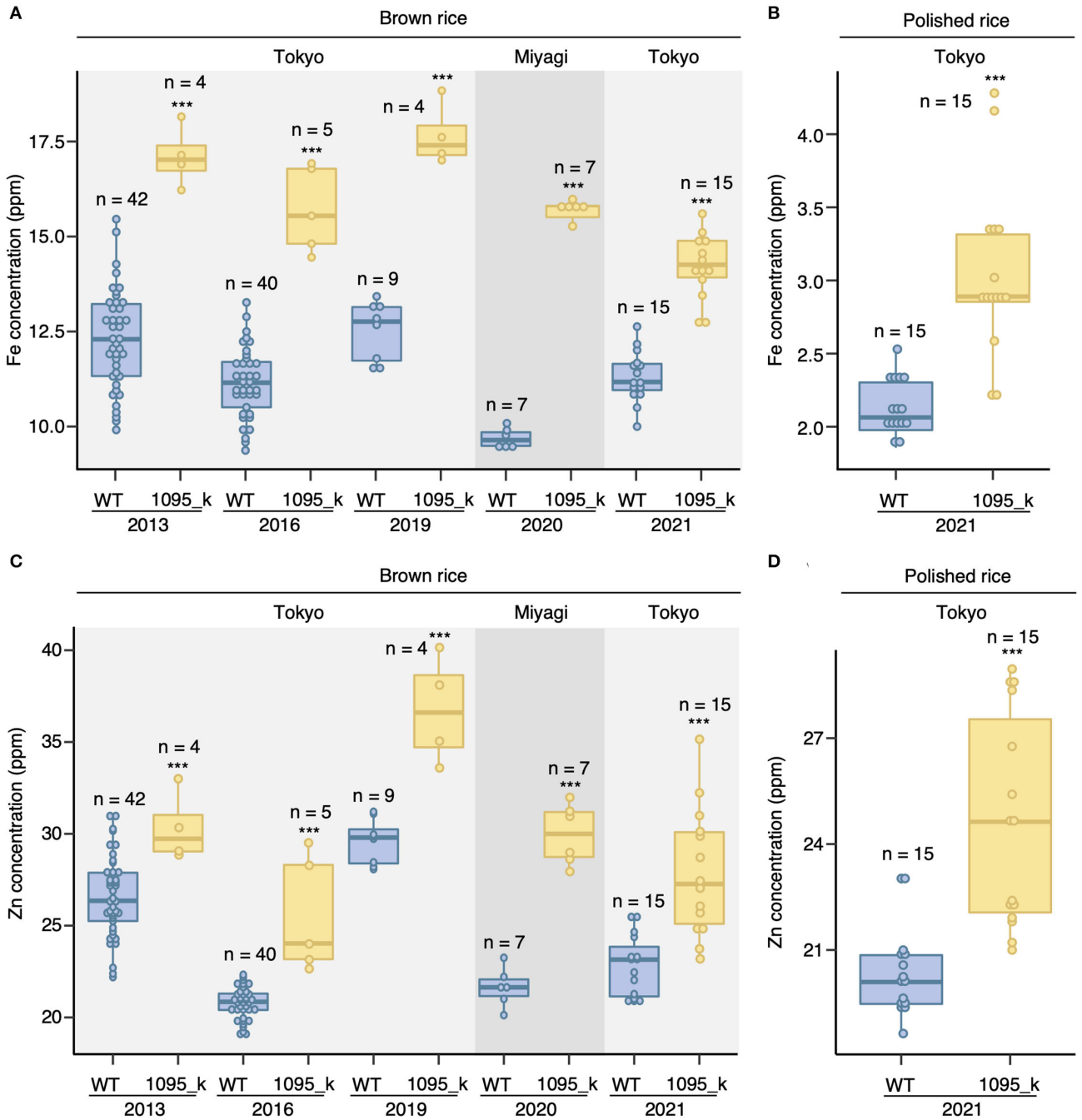

FIGURE 1 | Brown rice Fe and Zn concentration. **(A)** Fe concentration in brown rice, **(B)** Fe concentration in polished rice, **(C)** Zn concentration in brown rice, and **(D)** Zn concentration in polished rice of wild type (WT) Hitomebore and mutant (1095_k). Plants were cultivated in 5 independent years on the paddy field of the Institute of Sustainable Agro-ecosystem Services, The University of Tokyo, in Tokyo, and on the field of Tohoku University in Miyagi. The number of replicates is shown in figure. Significant differences were calculated using Student's *t*-test. *** $p < 0.001$.

we observed the relationship between the *OsVIT2* genotype and Fe or Zn concentration in the F2 population. The genotype of all the F2 (225 lines) was determined by the dCAPS marker (**Figure 3E**). To see the association between genotype and phenotype, a statistical analysis was performed for Fe and Zn concentration (**Figure 3D**). For both Fe and Zn concentrations, there is a statistical significance between the wild-type homozygous and mutant-type homozygous lines (WT Homo and 1095_k Homo in **Figures 3D,E**). These results strongly suggest that nonsense mutation of *OsVIT2* is responsible for the high Fe and Zn phenotypes in 1095_k.

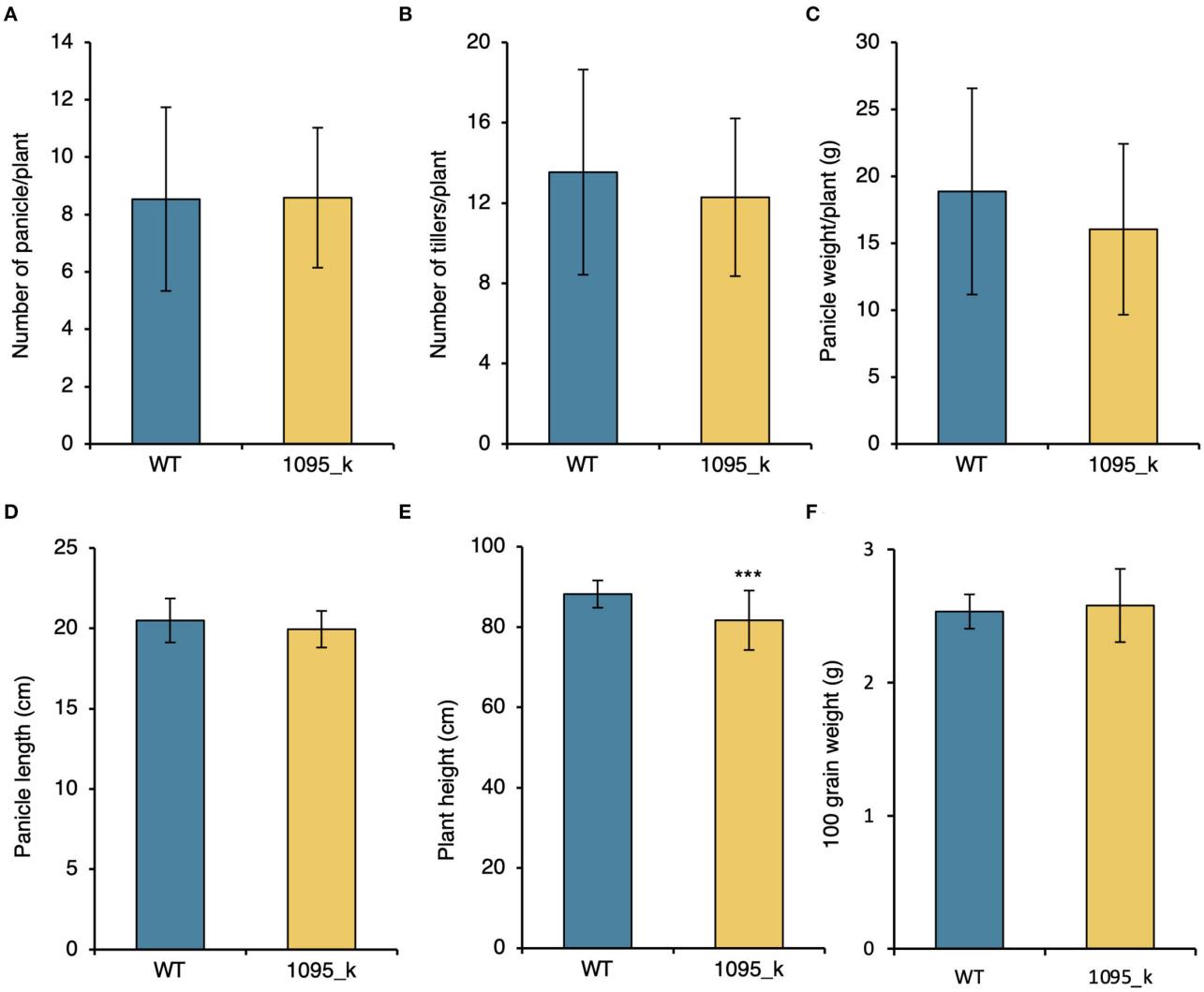

FIGURE 2 | Characteristics of the high Fe mutant. **(A)** Number of panicle/plant, **(B)** number of tillers/plant, **(C)** panicle weight/plant, **(D)** Panicle length, **(E)** Plant height, and **(F)** 100 grain weight of WT and 1095_k. Plants were harvested from the paddy field after maturation. Significant difference using Student's *t*-test. *** $p < 0.001$. Error bar = SD. $n = 41$.

DISCUSSION

OsVIT2 Could Be a Possible Causal Gene for 1095_k

An EMS mutant, 1095_k, has an increase in Fe and Zn concentration in brown rice as well as in polished rice (**Figures 1**, **3C**). Furthermore, there is an association between Fe and Zn concentration and *OsVIT2* mutation in F2 crosses between WT and 1095_k. The OsVIT2 is a vacuolar localized transporter, which plays an important role in the vacuolar sequestration of Fe to regulate Fe homeostasis (Zhang et al., 2012; Bashir et al., 2013). It has been demonstrated that the disruption of *OsVIT2* results in an increase in Fe and Zn concentration in rice grains. In addition to these elements, Cu and Mn change, although it varies from experiment to experiment: Cu increases in *OsVIT2* mutant but no change in Mn (Bashir et al., 2013); no change both in Cu and Mn (Zhang et al., 2012). In terms of plant growth, the *OsVIT2* mutant shows a decrease in shoot length at the seedling stage (Zhang et al., 2012). Although we did not perform the growth test in the seedling stage, in the field test, the plant height of 1095_k was lower than WT (**Figure 2E**). Taken together, these results suggest that *OsVIT2* could be a causal gene for the high grain Fe and Zn phenotype of 1095_k.

1095_k Can Be a Material for Breeding High Fe and Zn Cultivars

In 1095_k, *OsVIT2* mutation increased Fe and Zn content of grain in fields without increasing toxic elements, such as Cd and As, for humans (**Figure 1** and **Figure S1**). In addition, we showed that the mutation does not affect the growth of rice, and furthermore, no reduction in the yield components was

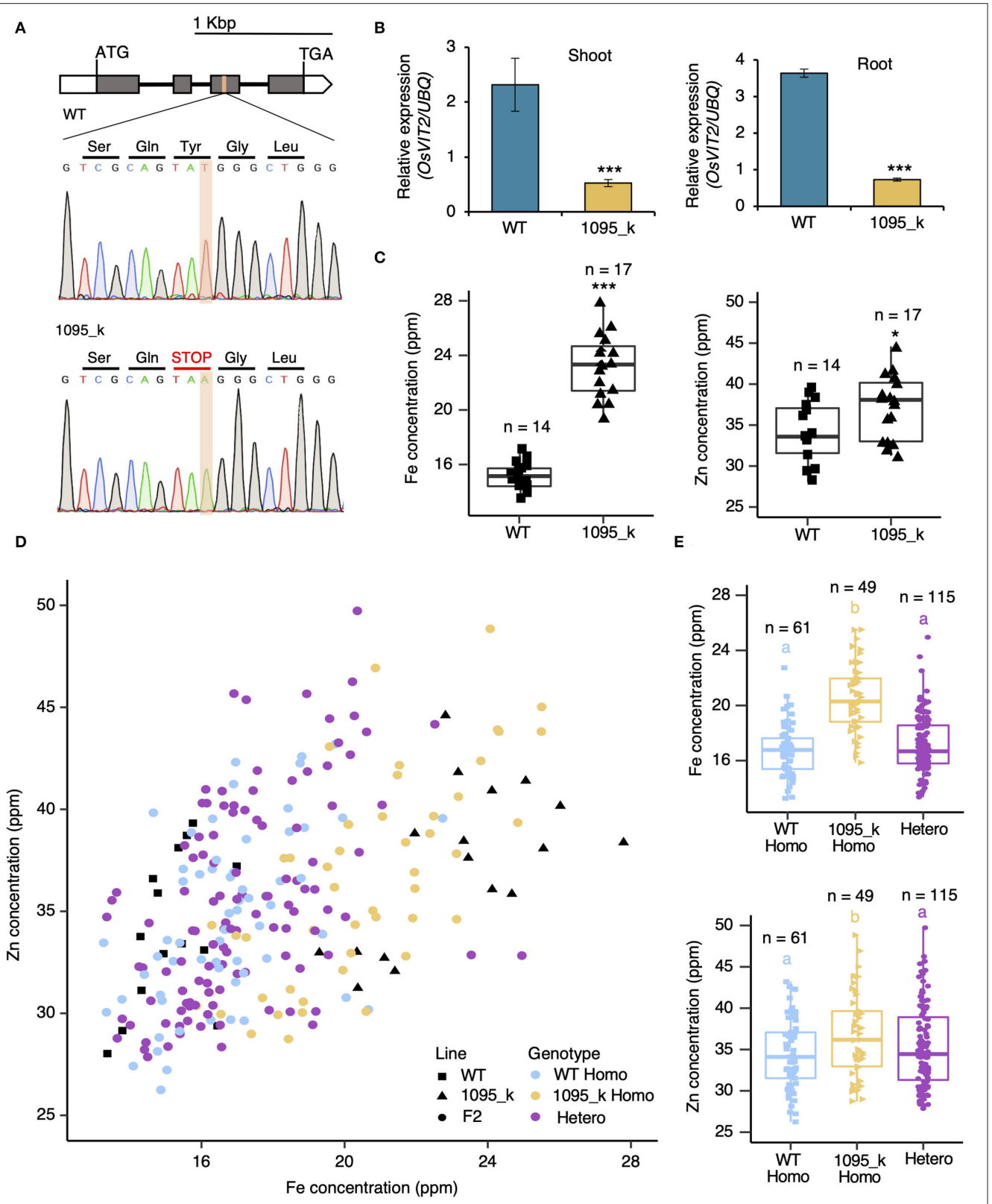

FIGURE 3 | The correlation between mutated OsVIT2 and high Fe phenotype. **(A)** Intron-exon structure of *OsVIT2* with sequence alignment of WT and 1095_k (box and line are exon and intron, whereas white box and gray box represent UTR and CDS, respectively). Nucleotide changes are indicated by the red box in the

(Continued)

FIGURE 3 | sequence spectrum. Thymine in WT is changed to Adenine in 1095_k at the third exon of *OsVIT2*. **(B)** The mRNA expression of *OsVIT2* relative to the *UBQ* gene in shoot and root samples from WT and 1095_k. Plants were grown for 1 week in normal Kimura's B solution. Significant differences were calculated using Student's *t*-test. *** $p < 0.001$. Error bar = SD. $n = 3$. **(C)** Fe and Zn concentration of WT and 1095_k in brown rice. Plants were cultivated in the rice field of the Yayoi campus, The University of Tokyo. Significant differences were calculated using Student's *t*-test. * $p < 0.05$, *** $p < 0.001$. Error bar = SD. **(D)** A correlation plot between Fe and Zn concentration in brown rice for each genotype in the F2 population. F2 plants were grown together with parental line **(C)** and Inductive Coupled Plasma Mass Spectrometry (ICP-MS) analysis was performed. WT and 1095_k are the same data as in **(C, E)** Boxplot of different F2 genotypes in **(C)**. Significant differences were calculated using Tukey's HSD ($p < 0.05$). Letters indicate significant differences. The number of replicates is shown in figure.

observed (**Figure 2** and **Figure S2**). These results indicate that the mutation in *OsVIT2* could be a candidate for DNA marker to breed high Fe and Zn. All of these characters are beneficial for breeding new cultivars.

OsVIT2 is localized to vacuole and sequester Fe into vacuole (Zhang et al., 2012). *OsVIT2* mRNA is expressed throughout whole growth stages (Bashir et al., 2013) and upregulated by high Fe in the seedling stage (Zhang et al., 2012). These results suggest the function of OsVIT2 in excess Fe tolerance. Bashir et al. (2013) grew the T-DNA knockdown line under excess Fe conditions and found that under 100 and 500 μM Fe-EDTA conditions, the plant height is shorter than that of control plants, while root length and soil plant analysis development (SPAD) values are similar between them. Therefore, OsVIT2 may have some function in excess Fe tolerance but may not affect the growth severely. In our experiments, although the plant height is short at 1095_k, the yield of 1095_k is similar to WT. Therefore, the yield of the *OsVIT2* mutant would not be affected so much. The other possible disadvantage is the high accumulation of toxic elements in humans, such as Cd and As. In our field condition and also in Cd-contaminated soil (Che et al., 2021), there is no significant difference between WT and mutants. Taken together with yield results, *OsVIT2* is suitable as a breeding material.

There have been many efforts made in the past to increase the Fe and Zn concentration in the rice grains, but are generated by the transgenic means due to which they are restricted to use around the world (Takahashi et al., 2001; Lee and An, 2009; Zheng et al., 2010). In the case of 1095_k, an EMS mutant, the freedom of usage increases compared with genetically modified rice. Furthermore, if transgenic lines are accepted, breeders can use 1095_k as a material for transformation by overexpression of genes enhancing Fe and/or Zn concentration in grain as the mutant does not have any selection marker (e.g., hygromycin) gene. Hence, mutant 1095_k is a strong candidate to address the hidden hunger problem in the coming future.

DATA AVAILABILITY STATEMENT

The original contributions presented in the study are included in the article/**Supplementary Material**, further inquiries can be directed to the corresponding author/s.

AUTHOR CONTRIBUTIONS

PK, TF, and TK conceived and designed the experiment. PK and TK performed the experiments, and data analysis and, wrote the manuscript. All authors contributed to the article and approved the submitted version.

FUNDING

This work was supported by JST, PRESTO grant number JPMJPR16Q3, Science and Technology Research Partnership for Sustainable Development (SATREPS), Japan Science and Technology Agency (JST)/Japan International Cooperation Agency (JICA) grant number JPMJSA2107, and Steel Foundation for Environmental Protection Technology to TK. It is also supported in part by the JSPS KAKENHI 18H05490 and 19H05637, Cabinet Office, Government of Japan, Moonshot R&D Program for Agriculture, Forestry, and Fisheries (founding agency: 252 Bio-oriented Technology Research Advancement Institution) to TF.

ACKNOWLEDGMENTS

We thank Maki Saiki and Emiko Yokota for technical assistance.

SUPPLEMENTARY MATERIAL

The Supplementary Material for this article can be found online at: https://www.frontiersin.org/articles/10.3389/fpls.2022.868661/full#supplementary-material

REFERENCES

Abdelnour-Esquivel, A., Perez, J., Rojas, M., Vargas, W., and Gatica-Arias, A. (2020). Use of gamma radiation to induce mutations in rice (*Oryza sativa* L.) and the selection of lines with tolerance to salinity and drought. *Vitr. Cell. Dev. Biol. - Plant* 56, 88–97. doi: 10.1007/s11627-019-10015-5

Ahmar, S., Gill, R. A., Jung, K. H., Faheem, A., Qasim, M. U., Mubeen, M., et al. (2020). Conventional and molecular techniques from simple breeding to speed breeding in crop plants: recent advances and future outlook. *Int. J. Mol. Sci.* 21, 2590. doi: 10.3390/ijms21072590

Bailey, R. L., West, K. P., and Black, R. E. (2015). The epidemiology of global micronutrient deficiencies. *Ann. Nutr. Metab.* 66, 22–33. doi: 10.1159/000371618

Bashir, K., Takahashi, R., Akhtar, S., Ishimaru, Y., Nakanishi, H., and Nishizawa, N. K. (2013). The knockdown of OsVIT2 and MIT affects iron localization in rice seed. *Rice* 6, 31. doi: 10.1186/1939-8433-6-31

Berhe, K., Gebrearegay, F., and Gebremariam, H. (2019). Prevalence and associated factors of zinc deficiency among pregnant women and children in Ethiopia: a systematic review and meta-analysis. *BMC Public Health* 19, 1663. doi: 10.1186/s12889-019-7979-3

Cakmak, I., and Kutman, U. B. (2018). Agronomic biofortification of cereals with zinc: a review. *Eur. J. Soil Sci.* 69, 172–180. doi: 10.1111/ejss.12437

Che, J., Yamaji, N., and Ma, J. F. (2021). Role of a vacuolar iron transporter OsVIT2 in the distribution of iron to rice grains. *New Phytol.* 230, 1049–1062. doi: 10.1111/NPH.17219

Christou, P., and Twyman, R. M. (2004). The potential of genetically enhanced plants to address food insecurity. *Nutr. Res. Rev.* 17, 23–42. doi: 10.1079/nrr200373

Dipti, S. S., Bergman, C., Indrasari, S. D., Herath, T., Hall, R., Lee, H., et al. (2012). The potential of rice to offer solutions for malnutrition and chronic diseases. *Rice* 5, 1–18. doi: 10.1186/1939-8433-5-16

Goto, F., Yoshihara, T., Shigemoto, N., Toki, S., and Takaiwa, F. (1999). *Iron fortification of rice seed by the soybean ferritin gene*. Available online at: http://biotech.nature.com (accessed March 30, 2021).

Grover, N., Kumar, A., Yadav, A. K., Gopala Krishnan, S., Ellur, R. K., Bhowmick, P. K., et al. (2020). Marker assisted development and characterization of herbicide tolerant near isogenic lines of a mega basmati rice variety, "Pusa Basmati 1121." *Rice* 13, 68. doi: 10.1186/s12284-020-00423-2

Gupta, S., Brazier, A. K. M., and Lowe, N. M. (2020). Zinc deficiency in low- and middle-income countries: prevalence and approaches for mitigation. *J. Hum. Nutr. Diet.* 33, 624–643. doi: 10.1111/jhn.12791

Harding, K. L., Aguayo, V. M., and Webb, P. (2018). Hidden hunger in South Asia: a review of recent trends and persistent challenges. *Public Health Nutr.* 21, 785–795. doi: 10.1017/S1368980017003202

Karunarathna, N. L., Patiranage, D. S. R., Harloff, H. J., Sashidhar, N., and Jung, C. (2021). Genomic background selection to reduce the mutation load after random mutagenesis. *Sci. Rep.* 11, 19404. doi: 10.1038/s41598-021-98934-5

Khush, G. S., Lee, S., Cho, J., Il, and Jeon, J. S. (2012). Biofortification of crops for reducing malnutrition. *Plant Biotechnol. Rep.* 6, 195–202. doi: 10.1007/s11816-012-0216-5

Kumar, S., Palve, A., Joshi, C., Srivastava, R. K., and Rukhsar (2019). Crop biofortification for iron (Fe), zinc (Zn) and vitamin A with transgenic approaches. *Heliyon* 5, e01914. doi: 10.1016/j.heliyon.2019.e01914

Kumawat, S., Rana, N., Bansal, R., Vishwakarma, G., Mehetre, S. T., Das, B. K., et al. (2019). Expanding avenue of fast neutron mediated mutagenesis for crop *Improvement*. 8, 164. doi: 10.3390/plants8060164

Lee, S., and An, G. (2009). Over-expression of OsIRT1 leads to increased iron and zinc accumulations in rice. *Plant Cell Environ.* 32, 408–416. doi: 10.1111/J.1365-3040.2009.01935.X

Lee, S., Jeon, U. S., Lee, S. J., Kim, Y. K., Persson, D. P., Husted, S., et al. (2009). Iron fortification of rice seeds through activation of the nicotianamine synthase gene. *Proc. Natl. Acad. Sci. U. S. A.* 106, 22014–22019. doi: 10.1073/pnas.0910950106

Lee, S., Persson, D. P., Hansen, T. H., Husted, S., Schjoerring, J. K., Kim, Y. S., et al. (2011). Bio-available zinc in rice seeds is increased by activation tagging of nicotianamine synthase. *Plant Biotechnol. J.* 9, 865–873. doi: 10.1111/J.1467-7652.2011.00606.X

Masuda, H., Suzuki, M., Morikawa, K. C., Kobayashi, T., Nakanishi, H., Takahashi, M., et al. (2008). Increase in iron and zinc concentrations in rice grains via the introduction of barley genes involved in phytosiderophore synthesis. *Rice* 1, 100–108. doi: 10.1007/s12284-008-9007-6

Owais, A., Merritt, C., Lee, C., and Bhutta, Z. A. (2021). Anemia among women of reproductive age: an overview of global burden, trends, determinants, and drivers of progress in low- and middle-income countries. *Nutrients* 13, 2745. doi: 10.3390/NU13082745

Palanog, A. D., Calayugan, M. I. C., Descalsota-Empleo, G. I., Amparado, A., Inabangan-Asilo, M. A., Arocena, E. C., et al. (2019). Zinc and iron nutrition status in the philippines population and local soils. *Front. Nutr.* 6, 81. doi: 10.3389/FNUT.2019.00081

Sevanthi, A. M. V., Kandwal, P., Kale, P. B., Prakash, C., Ramkumar, M. K., Yadav, N., et al. (2018). Whole genome characterization of a few EMS-induced mutants of upland rice variety nagina 22 reveals a staggeringly high frequency of SNPs which show high phenotypic plasticity towards the wild-type. *Front. Plant Sci.* 9, 1179. doi: 10.3389/fpls.2018.01179

Shi, R., Tong, Y., Jing, R., Zhang, F., Zou, C. (2013). Characterization of quantitative trait loci for grain minerals in hexaploid wheat (*Triticum aestivum* L.). *J. Integr. Agric.* 12, 1512–1521. doi: 10.1016/S2095-3119(13)60559-6

Sunuwar, D. R., Singh, D. R., Chaudhary, N. K., Pradhan, P. M. S., Rai, P., and Tiwari, K. (2020). Prevalence and factors associated with anemia among women of reproductive age in seven South and Southeast Asian countries: evidence from nationally representative surveys. *PLoS One* 15, e0236449. doi: 10.1371/journal.pone.0236449

Takahashi, M., Nakanishi, H., Kawasaki, S., Nishizawa, N. K., and Mori, S. (2001). Enhanced tolerance of rice to low iron availability in alkaline soils using barley nicotianamine aminotransferase genes. Available online at: http://biotech.nature.com (accessed March 30, 2021).

Tanaka, N., Nishida, S., Kamiya, T., and Fujiwara, T. (2016). Large-scale profiling of brown rice ionome in an ethyl methanesulphonate-mutagenized hitomebore population and identification of high- and low-cadmium lines. *Plant Soil.* 407, 109–117. doi: 10.1007/s11104-016-2812-6

Uraguchi, S., Mori, S., Kuramata, M., Kawasaki, A., Arao, T., and Ishikawa, S. (2009). Root-to-shoot Cd translocation via the xylem is the major process determining shoot and grain cadmium accumulation in rice. *J. Exp. Bot.* 60, 2677–2688. doi: 10.1093/jxb/erp119

Van Der Straeten, D., Bhullar, N. K., De Steur, H., Gruissem, W., MacKenzie, D., Pfeiffer, W., et al. (2020). Multiplying the efficiency and impact of biofortification through metabolic engineering. *Nat. Commun.* 11, 5203. doi: 10.1038/s41467-020-19020-4

Zhang, Y., Xu, Y. H., Yi, H. Y., and Gong, J. M. (2012). Vacuolar membrane transporters OsVIT1 and OsVIT2 modulate iron translocation between flag leaves and seeds in rice. *Plant J.* 72, 400–410. doi: 10.1111/j.1365-313X.2012.05088.x

Zheng, L., Cheng, Z., Ai, C., Jiang, X., Bei, X., Zheng, Y., et al. (2010). Nicotianamine, a novel enhancer of rice iron bioavailability to humans. *PLoS One* 5, e10190. doi: 10.1371/journal.pone.0010190

Conflict of Interest: The authors declare that the research was conducted in the absence of any commercial or financial relationships that could be construed as a potential conflict of interest.

Publisher's Note: All claims expressed in this article are solely those of the authors and do not necessarily represent those of their affiliated organizations, or those of the publisher, the editors and the reviewers. Any product that may be evaluated in this article, or claim that may be made by its manufacturer, is not guaranteed or endorsed by the publisher.

frontiers | Frontiers in Plant Science

ORIGINAL RESEARCH
published: 30 June 2022
doi: 10.3389/fpls.2022.916168

Regulation of the Zinc Deficiency Response in the Legume Model *Medicago truncatula*

*Feixue Liao[1], Grmay Hailu Lilay[1], Pedro Humberto Castro[2,3], Herlander Azevedo[2,3,4] and Ana G. L. Assunção[1,2]**

[1] Department of Plant and Environmental Sciences, University of Copenhagen, Frederiksberg, Denmark, [2] CIBIO-InBIO Research Centre in Biodiversity and Genetic Resources, University of Porto, Vairão, Portugal, [3] BIOPOLIS Biodiversity and Land Planning, Vairão, Portugal, [4] Departamento de Biologia, Faculdade de Ciências, Universidade do Porto, Porto, Portugal

The zinc deficiency response in *Arabidopsis thaliana* is regulated by F-group basic region leucine-zipper (F-bZIP) transcription factors, and there is evidence of evolutionary conservation of this regulatory network in land plants. Fundamental knowledge on the zinc homeostasis regulation in crop species will contribute to improving their zinc nutritional value. Legumes are protein-rich crops, used worldwide as part of traditional diets and as animal forage, being therefore a good target for micronutrient biofortification. Here, we identified F-bZIP transcription factors in representative legume species and functionally characterized the two F-bZIPs from *Medicago truncatula*. Results indicate that MtFbZIP1 is the functional homolog of *A. thaliana* bZIP19 and bZIP23, while MtFbZIP2 does not play a role in the zinc deficiency response. Additionally, analysis of *M. truncatula* genes from the Zrt/Irt-like protein (ZIP) family of zinc transporters or encoding nicotianamine synthase enzymes that produce the zinc ligand nicotianamine, support the conservation of the F-bZIP-regulated zinc deficiency response in *M. truncatula*. Phylogenetic analysis of F-bZIP homologs enriched in legume species reinforces the branching into two groups, with MtFbZIP1 and MtFbZIP2 mapping in Groups 1 and 2, respectively. This phylogeny combined with the functional characterization of MtFbZIPs supports the suggested conservation of the zinc deficiency response associated with Group 1 F-bZIPs, and the more variable evolutionary paths associated with Group 2. Overall, we provide novel insight on the mechanisms of response to zinc deficiency in *M. truncatula*, which contributes to developing strategies for improving zinc content in legume crops.

Keywords: ***Medicago truncatula*** **(Medicago), Zn deficiency response, F-bZIP transcription factors, ZIP transporters, nicotianamine (NA), legume**

OPEN ACCESS

Edited by:
Anja Schneider, Ludwig Maximilian University of Munich, Germany

Reviewed by:
Roberto Espinoza Corral, Michigan State University, United States
Dorina Podar, Babeş-Bolyai University, Romania

***Correspondence:**
Ana G. L. Assunção
agla@plen.ku.dk

Specialty section:
This article was submitted to Plant Nutrition, a section of the journal Frontiers in Plant Science

Received: *08 April 2022*
Accepted: *30 May 2022*
Published: *30 June 2022*

Citation:
Liao F, Lilay GH, Castro PH, Azevedo H and Assunção AGL (2022) Regulation of the Zinc Deficiency Response in the Legume Model Medicago truncatula. Front. Plant Sci. 13:916168. doi: 10.3389/fpls.2022.916168

INTRODUCTION

In biological systems, the importance of zinc (Zn) as an essential micronutrient relates with its requirement as a key structural and catalytic component for a large number of proteins (Maret and Li, 2009). It is estimated that Zn-binding proteins represent nearly 10% of the proteome in eukaryotes, and it is the second most abundant transition metal in living organisms, after iron

(Fe) (Andreini et al., 2006). A large number of proteins have structural Zn sites, such as the Zn-finger transcription factors, but catalytic Zn sites are also frequent, being present in all six enzyme classes including key metabolic enzymes such as carbonic anhydrase, alkaline phosphatase and Cu/Zn superoxide dismutase (Vallee and Auld, 1990; Colvin et al., 2010). Micronutrient Zn acquisition, distribution and intracellular availability rely on membrane transporters and low-molecular-weight ligands, which are part of the Zn homeostasis network. This network is tightly regulated to avoid Zn deficiency or toxicity (Clemens, 2001; Sinclair and Krämer, 2012). In *Arabidopsis thaliana* (Arabidopsis), the Zn homeostasis regulators bZIP19 and bZIP23 are basic region leucine-zipper transcription factors from the F group (F-bZIP), which play a central role in the transcriptional regulation of the Zn deficiency response. They bind to Zinc Deficiency Response Elements (ZDRE) in the promoters of target genes, which are activated under Zn deficiency (Assunção et al., 2010). The target genes comprise a small set of genes involved in Zn transport and distribution. These include genes encoding Zn transporters from the Zrt/Irt-like protein (ZIP) family, which mediate Zn uptake into the cell, and nicotianamine synthase (NAS) enzymes that produce the low-molecular-weight Zn ligand nicotianamine (NA), which is involved in Zn intercellular and long-distance movement (Guerinot, 2000; Clemens et al., 2013). The *bzip19 bzip23* double mutant (*bzip19/23*) is hypersensitive to Zn deficiency and shows no visible phenotype at Zn sufficiency (Assunção et al., 2010). The bZIP19 and bZIP23 transcription factors not only function as key regulators of the Zn deficiency response, but also as direct sensors of the intracellular Zn concentration, through direct binding of Zn^{2+} ions to the transcription factor's Zn-Sensor Motif (ZSM) (Lilay et al., 2021).

There is evidence for the evolutionary conservation of F-bZIP transcription factors and the Zn deficiency response across land plants (Castro et al., 2017). This is supported by functional analysis of F-bZIP homologs from cereals, i.e., barley, wheat and rice (Evens et al., 2017; Nazri et al., 2017; Lilay et al., 2020). These studies support a conserved mechanism of Zn deficiency response anchored at functional homologs of the Arabidopsis bZIP19 and bZIP23 transcription factors. Furthermore, there is evidence from Arabidopsis that the activity of F-bZIP transcription factors can be modulated through modifications in their ZSM to increase plant and seed Zn content (Lilay et al., 2021). Therefore, exploring such conservation can help unravel the Zn homeostasis network and its regulation in other plant species, and contribute to the development of strategies that target increased Zn nutritional value in crops (biofortification).

Zn deficiency in agricultural soils is widespread and about one-third of the world's human population is at high risk of Zn malnutrition, mainly populations depending on cereal-rich diets (Wessells and Brown, 2012). Legume crops are characterized by their high nutritional value as an important source of protein, but also fiber, oil, phytochemicals and micronutrients Fe and Zn (Beebe et al., 2000; Castro-Guerrero et al., 2016; Robinson et al., 2019). Legume pulse crops are present in traditional diets throughout the world, and are considered an affordable and important component of healthy diets. Also legume forages are used worldwide for animal feed (Castro-Guerrero et al., 2016). The high protein content of legume plants is related with their ability to establish symbiotic associations with nitrogen-fixing bacteria (rhizobia), which is also the basis for legume use in crop rotation strategies, as an alternative to synthetic nitrogen fertilizers (Escudero et al., 2020). Moreover, these are broadly resilient crops, able to colonize marginal land and nutrient-poor soils (Ibrahim and Ramadan, 2015). Therefore, legume species are considered important targets for micronutrient Fe and Zn biofortification efforts, to help tackle these micronutrient deficiencies in human diets (Kumar and Pandey, 2020).[1]

In recent years, the mechanisms of Zn homeostasis in the model legume *Medicago truncatula* are being unraveled, with the identification of members from different metal micronutrient transporter families, including the ZIP transporters, and the metal ligand producing enzymes NAS. Studies have particularly targeted the transport and delivery of Zn and other metal micronutrients to the nodule-rhizobia infected cells (López-Millán et al., 2004; Avenhaus et al., 2016; Abreu et al., 2017; Escudero et al., 2020). In legume species, this is an important component of the plant metal micronutrient homeostasis, with a significant allocation to the symbiosome, where an adequate metal delivery and availability is essential for metalloprotein requirements and a proper symbiotic nitrogen fixation (Abreu et al., 2020). Here, considering the evolutionary conservation of the F-bZIP transcription factors (Castro et al., 2017), we investigated the Zn deficiency response in the legume model *M. truncatula*. The F-bZIP homologs from *M. truncatula* and other legume species were identified and the *M. truncatula* F-bZIP regulatory network was investigated. This knowledge contributes to a deeper understanding of the mechanisms of Zn homeostasis regulation in *M. truncatula* and legume species in general.

MATERIALS AND METHODS

Phylogenetic Analysis

Phylogeny of F-bZIP genes was determined as previously reported (Castro et al., 2017). The amino acid sequences of F-bZIPs were retrieved from multiple databases (Plaza Dicots 4.5[2]; Phytozome v13[3]; Legume Information System[4]), and included the following species: *Arachis ipaensis, Glycine max, Lotus japonicus*, *Lupinus angustifolius, Phaseolus vulgaris, Pisum sativum*, and *Trifolium pratense*. Due to incomplete F-bZIP assignment in the above mentioned databases, F-bZIPs from *Cajanus cajan, Cicer arietinum, Medicago truncatula* and *Vigna radiata var. radiate* were derived *via* NCBI blastp,[5] with default settings. For an evolutionary contextualization, the analysis also included other species as representatives of major plant taxa, namely a bryophyte (*Physcomitrella*

[1]https://bpi.harvestplus.org

[2]https://bioinformatics.psb.ugent.be/plaza/versions/plaza_v4_5_dicots/

[3]https://phytozome-next.jgi.doe.gov/

[4]https://legumeinfo.org/

[5]https://blast.ncbi.nlm.nih.gov/Blast.cgi?PAGE=Proteins

patens), a pteridophyte (*Selaginella moellendorffii)*, the basal angiosperm (*Amborella trichopoda*), a model monocot (*Oryza sativa*), the model angiosperm eudicot (*A. thaliana*), and four species from the clade Fabids, which are not from the Fabaceae family (*Prunus persica*, *Cucumis melo*, *Cucumis sativus*, and *Citrullus lanatus*). Sequence information is summarized in **Supplementary Table 1**. The phylogenetic analysis was performed on CIPRES Science Gateway V3.3[6] (Miller et al., 2011). The sequence alignment was performed with MAFFT v.7471 and tree computation was performed with RAxML-HPC v.8, inputting 1000 bootstrap iterations, as described by Castro et al. (2017). The phylogenetic tree was visualized *via* SeaView Version 4 software (Gouy et al., 2010). For the gene enrichment analysis, the phylogenetic relationship between species was established based on the information available in the Dicots Plaza database and published by Champagne et al. (2007).

The ZIP phylogenetic analysis was performed with *M. truncatula*, *A. thaliana*, and *A. trichopoda ZIP* family members to infer on their relationship. The sequences used in the analysis were retrieved from the Plaza Dicots 4.5 database and TAIR, The Arabidopsis Information Resource.[7] The *M. truncatula* genes Medtr3g081630 and Medtr4g006710 were annotated as *MtZIP17* and *MtZIP18*, respectivly. The sequences used in the analysis are summarized in **Supplementary Table 2**. The amino acid sequences were aligned and an unrooted phylogenetic analysis was performed with the neighbor-joining method (Jukes-Cantor model with 1,000 bootstrap replicates), using the CLC Main Workbench 8.0.1 software.

A motif search was performed on the gene promoter sequences of the *M. truncatula*, *A. thaliana*, and *A. trichopoda ZIP* genes previously incorporated in the unrooted tree. This analysis was extended to the four annotated *M. truncatula NAS* genes (Escudero et al., 2020), which were retrieved from the Plaza Dicots 4.5 database (**Supplementary Table 2**). Promoter regions were downloaded in FASTA format from the Sequence retrieval feature of the Plaza database, and consisted of the –2 kb span, or the intergenic region when in the presence of a gene within the –2 kb span. To search for the presence of 10-bp ZDRE motifs, the consensus sequence (RTGWCGACAY; A/GTGT/ACGACAC/T) (Castro et al., 2017) was used and the MEME Suite 5.3.3[8] and Motif Alignment & Search Tool (MAST v4.11.2) software were employed. Only motifs with a position p-value inferior to 0.0001 were selected. One mismatch from the consensus sequence was allowed.

Plasmid Construction and Plant Transformation

The *pCaMV35S:MtFbZIP1-CFP-HA* and *pCaMV35S:MtFbZIP2-CFP-HA* constructs for stable transformation of the Arabidopsis *bzip19/23* double mutant and *bzip19/23-pZIP4:GUS* reporter line, respectively, were generated as follows: the full-length coding sequence (CDS) of *MtFbZIP1* (MtrunA17_Chr4g0036971) and *MtFbZIP2* (MtrunA17_Chr3g0090531) were amplified from the cDNA of *M. truncatula* using, for MtFbZIP1, forward and reverse primers containing *Not*I and *Asc*I restriction sites, respectively, and for MtFbZIP2, forward and reverse primers designed for TOPO® reaction (**Supplementary Table 3**). The *MtFbZIP1* and *MtFbZIP2* were then cloned into pENTR™-D-TOPO® vector by restriction-ligation and TOPO reaction, respectively. The cloning into pEarleyGate-102 Gateway vector (Earley et al., 2006), carrying a *Cauliflower mosaic virus* (CaMV) 35S promoter, a C-terminal cyan fluorescent protein (CFP), and a HA-tag, the transformation into *Agrobacterium tumefaciens*, and generation of Arabidopsis mutant lines were performed as described by Lilay et al. (2019). Transgenic plants were selected for Basta (phosphinothricin) resistance. For *MtFbZIP1*, homozygous transgenic seeds (T3 generation) of three independently transformed lines were selected. The expression of *MtFbZIP1* in each line was confirmed by real-time quantitative reverse transcription–PCR (RT–qPCR). The lines were referred to as *bzip19/23-OEMtFbZIP1*. For *MtFbZIP2*, transgenic seeds of three independently transformed lines (T2 generation exhibiting a 3:1 segregation ratio) were selected. The lines were referred to as *bzip19/23-pZIP4:GUS-OEMtFbZIP2.*

Plant Material and Growth Conditions

The Arabidopsis genotypes used in this study were the wild-type accession Columbia (Col-0), the double T-DNA insertion mutant *bzip19 bzip23* (*bzip19/23*) obtained from a cross between homozygous *bzip19-1* (SALK_144252) and *bzip23-1* (SALK_045200) lines in the Col-0 background, as described previously (Assunção et al., 2010); the *bzip19/23*-OE19 line, an overexpression of *AtbZIP19* in the *bzip19/23* mutant, as described previously (Lilay et al., 2019); the *pZIP4:GUS* reporter line containing the promoter of Arabidopsis *ZIP4* transporter gene fused to GUS and the *bzip19/23-pZIP4:GUS* reporter line obtained from a cross between *bzip19/23* and *pZIP4:GUS* lines, as described previously (Castro et al., 2017). The *bzip19/23-OEMtFbZIP1* and *bzip19/23-pZIP4:GUS-OEMtFbZIP2* lines were described above. The *M. truncatula* R108 ecotype was used as wild-type.

For the analysis of *M. truncatula* plants, seeds were scarified with 96% H_2SO_4 for 5 min, rinsing five times with cold sterile ddH_2O, superficial sterilization with 30% (v/v) commercial bleach for 7 min, and rinsing five times with sterile ddH_2O. The seeds were germinated on filter paper soaked with sterile ddH_2O in a Petri dish, placed at 4°C for 1–2 h, then maintained in the dark at 4°C for 3 days, followed by room temperature for 1 day, and then placed in the climate chamber to allow cotyledons to emerge. The germinated seedlings were transferred to pots filled with sand, in a total of four pots per Zn treatment, with 1 seedling per pot. They were watered with 1 L per week for 6 weeks with a modified half-strength Hoagland nutrient solution containing:1 mM $Ca(NO_3)_2$, 1 mM $MgSO_4$, 2 mM KNO_3, 1 mM NH_4NO_3, 1 mM KH_2PO_4, 50 μM Fe-Na-EDTA, 25 μM H_3BO_3, 3 μM $MnSO_4$, 0.1 μM $CuSO_4$, 0.5 μM $(NH_4)_6Mo_7O_{24}$, 50 μM KCl, buffered with 1 mM MES at pH 5.8, containing 2 μM $ZnSO_4$ (Zn sufficiency; control) or 0.002 μM $ZnSO_4$ (Zn deficiency; -Zn). For agar-grown Arabidopsis seedlings, sterilized seeds were sown on half-strength Murashige and Skoog (1/2 MS) medium

[6]http://www.phylo.org

[7]https://www.arabidopsis.org/

[8]https://meme-suite.org/meme

containing 15 μM $ZnSO_4$ (Zn sufficiency; control), or no added Zn (Zn deficiency; –Zn) as previously described (Lilay et al., 2019). Five seedlings for each genotype were sown on each plate, with control or –Zn 1/2 MS media, and grown for 14 days. Three plates (replicates) per Zn treatment were grown simultaneously. For hydroponically grown Arabidopsis plants, sterilized seeds were germinated and grown for 6 weeks with a modified half-strength Hoagland nutrient solution with 2 μM $ZnSO_4$ (Zn sufficiency; control) or with 0.002 μM $ZnSO_4$ (Zn deficiency; -Zn), with six plants per genotype as previously described (Lilay et al., 2019). The pot experiment, the MS plate assay and the hydroponic set-up, were performed in a growth chamber with 125 mmol photons m^{-2} s^{-1} white light, 22/20°C light/dark temperature, 70% relative humidity, and 8/16 h (hydroponics) or 16/8 h (pot experiment and plate assay) light/dark cycle.

Real-Time Quantitative RT–PCR Analysis

Shoots and roots of four-week-old *M. truncatula* plants, sand-grown in control or –Zn nutrient solution, were harvested separately. Three plants per Zn treatment were harvested and immediately frozen in liquid nitrogen. Shoot and root tissue were ground using a mortar and pestle in liquid nitrogen, and total RNA was extracted using the Direct-zol RNA Kit (Zymo Research). Fourteen-day-old Arabidopsis seedlings of the wild-type, *bzip19/23* mutant, *bzip19/23-OE19* and *bzip19/23-OEMtFbZIP1* lines, grown in control and –Zn MS medium, were harvested and immediately frozen in liquid nitrogen in pools of five seedlings per genotype, per plate and Zn treatment (control or –Zn). Three different plates per Zn treatment were grown simultaneously and considered as biological replicates. Three independently transformed T3 homozygous lines of *bzip19/23-OEMtFbZIP1* were analyzed. Seedlings were grinded with liquid nitrogen in a microtube, with the help of polypropylene pestles, and total RNA was extracted using the RNeasy Plant Mini Kit (Qiagen). *M. truncatula* and Arabidopsis RNA samples quantity and integrity were assessed, and cDNA synthesis was performed as previously described (Lilay et al., 2019). Primers for RT–qPCR (**Supplementary Table 3**) were designed using NCBI Primer-BLAST,[9] and the primer amplification efficiency for each primer pair was between 1.9 and 2.1. RT–qPCR was performed with a LightCycler 96 Real-Time PCR System (Roche Diagnostics), using HOT FIREPol EvaGreen qPCR Mix (Solis BioDyne) in a 20 μL PCR mixture, as described previously (Lilay et al., 2019). The *M. truncatula* ubiquitin gene (*MtUBQ*, Medtr3g091400.1) and Arabidopsis *Actin-2* (*ACT2*, At3g18780) were used to normalize the gene expression analysis in *M. truncatula* and Arabidopsis, respectively. The calculated cycle threshold (Ct) value for each gene was normalized to the reference gene's calculated Ct value. The relative transcript levels were expressed against the wild-type grown under control conditions, and calculated according to the $2^{-\Delta\Delta\ CT}$ method (Livak and Schmittgen, 2001).

The *in silico* analysis of expression of *MtFbZIP1* and *MtFbZIP2* genes was performed using MtExpress V2, the *M. truncatula* expression atlas[10] (Carrere et al., 2021). Normalized expression values (Log2TMM) for each gene were retrieved from three datasets (reference_dataset; abiotic_factor; biotic_stress). Expression was visualized as an XY scatter plot of the RNA-seq normalized expression value for each gene, i.e., MtFbZIP1 (MtrunA17_Chr4g0036971) versus MtFbZIP2 (MtrunA17_Chr3g0090531).

Histochemical Staining for GUS Assay and Imaging

Histochemical GUS (ß-glucuronidase) staining was performed with 12-day-old seedlings of *pZIP4:GUS, bzip19/23-pZIP4:GUS, bzip19/23-pZIP4:GUS-OEAtbZIP19* and *bzip19/23-pZIP4:GUS-OEMtFbZIP2*, grown with control or –Zn MS medium, as described by Lilay et al. (2021). Three independently transformed T2 generation seedlings were tested. Seedlings were immersed in GUS staining solution containing 50 mM phosphate buffer, 10 mM Na_2-EDTA, 20% (v/v) methanol, 0.1% (v/v) Triton X-100, 1.4 mM $K_3[Fe(CN)_6]$, 1.4 mM $K_4[Fe(CN)_6]\cdot 3H_2O$ with 1.9 mM X-Gluc and were incubated overnight at 37°C in the dark (Jefferson et al., 1987). After incubation, the pigments were removed by successive incubations in 50%, 70% and 96% (v/v) ethanol, and the seedlings were stored in 50% (v/v) glycerol. Bright-field images of GUS-stained seedlings, were recorded using a Leica M205FA stereo fluorescence microscope equipped with a digital Leica DFC450 C camera.

Subcellular Localization Analysis

Fourteen-day-old seedlings of the *bzip19/23-OEMtFbZIP1* and *bzip19/23-pZIP4:GUS-OEMtFbZIP2* lines grown in control or –Zn MS medium were analyzed with confocal laser scanning microscopy (CLSM). Roots were incubated in 50 μM propidium iodide (PI) solution for 30 s to stain cell walls. Roots were visualized using a Leica TCS SP5 II laser scanning confocal microscope (Leica Microsystems) with a HC PL APO CS × 63/1.30 Glycerine objective. Argon 458 and 514 nm laser lines were used for CFP and PI excitation, respectively. The emission settings were between 470 and 533 nm for CFP and between 602 and 684 nm for PI. Three independently transformed lines were analyzed, with observations of 2–3 seedlings per line and Zn treatment.

Tissue Element Analysis

Shoots and roots from 6-week-old *M. truncatula* plants, sand-grown with control or –Zn nutrient solution (3–4 plants per Zn treatment), were harvested. Shoots and roots from 6-week-old hydroponically grown Arabidopsis plants from the wild-type, *bzip19/23*, *bzip19/23-OE19* and *bzip19/23-OEMtFbZIP1* lines (3–6 plants per line per Zn treatment), grown with control and –Zn nutrient solution, were harvested. For the *bzip19/23* plants grown at –Zn, six plants were harvested, following the same procedure, and were analyzed in pools of two. Shoot and root harvest, tissue digestion, multielemental analysis performed with Inductively Coupled Plasma Optical Emission Spectroscopy (ICP-OES), and

[9] www.ncbi.nlm.nih.gov/tools/primer-blast

[10] https://medicago.toulouse.inrae.fr/MtExpress

data analysis performed with Agilent ICP Expert Software v.7.3, were previously described (Lilay et al., 2021).

Statistical Analysis

To compare different lines and treatments, one-way ANOVA followed by Tukey's *post hoc* test was performed with IBM SPSS Statistics V22.0, and the Student's t-test was carried out in Microsoft Excel.

RESULTS

Phylogenetic Analysis of F-bZIP Homologs From Legume Species

A phylogenetic characterization of F-bZIP homologs across land plants had previously identified the presence of one F-bZIP member from *M. truncatula* (Castro et al., 2017). In order to obtain a more detailed evolutionary perspective of F-bZIP homologs from legume species, we performed a phylogenetic analysis with a set of 11 species from the Fabaceae family, i.e., *Arachis ipaensis, Cajanus cajan, Cicer arietinum, Glycine max, Lotus japonica, Lupinus angustifolius, M. truncatula*, *Phaseolus vulgaris, Pisum sativum, Trifolium pratense* and *Vigna radiata*. For evolutionary contextualization, the analysis included other species that served as representatives of major plant taxa (*P. patens*, *S. moellendorffii*, *A. trichopoda, O.sativa*, and *A. thaliana*) and species from the clade Fabids but not from the Fabaceae family (*P. persica*, *C. melo*, *C. sativus*, and *C. lanatus*), as described in the Methods section. In total, 24 F-bZIP sequences from 11 species of the Fabaceae family were identified and the full protein sequences were subsequently used for phylogenetic inference (**Figure 1A**). The sequences used in the phylogenetic analysis contain the conserved bZIP domain (basic region leucine-zipper) (Vinson et al., 2006) and the cysteine/histidine (Cys/His)-rich motif that is characteristic of F-bZIP proteins (Castro et al., 2017; **Supplementary Table 1**). The divergence of F-bZIP proteins into two groups, well established in previous phylogenetic analysis of F-bZIP homologs across land plants (Castro et al., 2017), and phylogenetic analysis of F-bZIP homologs enriched with Monocot species (Lilay et al., 2020), was also observed in this analysis. More specifically, the Bryophyte and Pteridophyte sequences' positioning supports a single monophyletic origin for F-bZIP proteins, with differentiated branches forming Group 1 and Group 2 F-bZIPs (**Figure 1A**). In line with the previously reported phylogenetic analysis by Castro et al. (2017), we identified one Group 1 F-bZIP member for *M. truncatula*. Its gene ID is Medtr4g073100 based on Plaza Dicots 4.5 and Phytozome, which uses the *M. truncatula* genome assembly MedtrA17_4.0. Considering the recent release of a newer *M. truncatula* genome assembly (MedtrA17_5.0[11]), we carried out a protein blast in NCBI against the *M. truncatula* A17 r5.0 genome, and were able to detect a second F-bZIP gene (MtrunA17_Chr3g0090531). In this newer genome assembly, MedtrA17_5.0, the gene ID of Medtr4g073100 is MtrunA17_Chr4g0036971. To disambiguate the identification of the second *M. truncatula* F-bZIP, we analyzed the locus' positioning in the genome and confirmed that it belongs to a small genomic region that was not present in the previous *M. truncatula* MedtrA17_4.0 assembly. Importantly, this second F-bZIP mapped as a Group 2 F-bZIP in our phylogenetic analysis (**Figure 1A**). The *M. truncatula* F-bZIPs MtrunA17_Chr4g0036971 and MtrunA17_Chr3g0090531 were annotated as MtFbZIP1 and MtFbZIP2, respectively. The gene enrichment plot deduced from the phylogenetic analysis (**Figure 1B**) shows that all analyzed species have at least one F-bZIP member in Group 1. All Fabaceae family members possess one F-bZIP member from Group 2, with the exception of *Arachis ipaensis*, while in the sister clade Cucurbitaceae, the loss of Group 2 members is observed. The *Arachis ipaensis* exception may derive from poor genome assembly/gene curation, and it would seem that the consensus is the presence of one Group 1 and one Group 2 F-bZIP members across the Fabaceae family.

M. truncatula F-bZIPs Are Not Transcriptionally Responsive to Zn Deficiency

To investigate the role of the identified *M. truncatula* F-bZIP proteins (**Figure 1**) in the Zn deficiency response, we performed gene expression analysis in *M. truncatula* plants grown under Zn sufficient or Zn deficient conditions. Four-week-old plants, grown in sand and supplied with nutrient solution, showed mild phenotypic differences between the two Zn supply conditions (**Figure 2A**), whereas in the six-week-old plants the Zn deficiency treatment showed symptoms of leaf chlorosis (**Figure 2B**). Although there were no significant differences between Zn treatments regarding plant shoot or root dry weight (**Figure 2C**), the element analysis showed a significant reduction in the concentration of Zn in shoots and roots of plants grown at Zn deficiency, in comparison to Zn sufficiency (**Figure 2D**). The analysis of other nutrient elements (Fe, Cu, Mn and P) did not show significant differences between Zn supply conditions, except for Fe concentration in the shoot, which was significantly lower at Zn sufficiency than Zn deficiency (**Supplementary Figure 1**).

Next, we analyzed the expression of *MtFbZIP1* and *MtFbZIP2* genes. The transcript levels of *MtFbZIP1* and *MtFbZIP2* were not significantly different between plants grown with Zn sufficiency and Zn deficiency, both in shoots and roots (**Figures 2E,F**). Results also indicate that *MtFbZIP1* has a similar expression level in shoots and roots. In order to obtain information on the comparative expression between the two genes, we looked at available RNA-seq datasets from the *M. truncatula* RNA-seq Gene Expression Atlas Project (see text footnote 11). Expression data, comprising development, abiotic and biotic stress datasets, were retrieved for each gene and plotted in XY scatter for comparison of the gene pair's expression values in the same experimental samples (**Figure 2G** and **Supplementary Figure 2**). The results suggest that the *MtFbZIP1* gene is consistently expressed across all tissues and stress conditions,

[11] https://medicago.toulouse.inra.fr/MtrunA17r5.0-ANR/

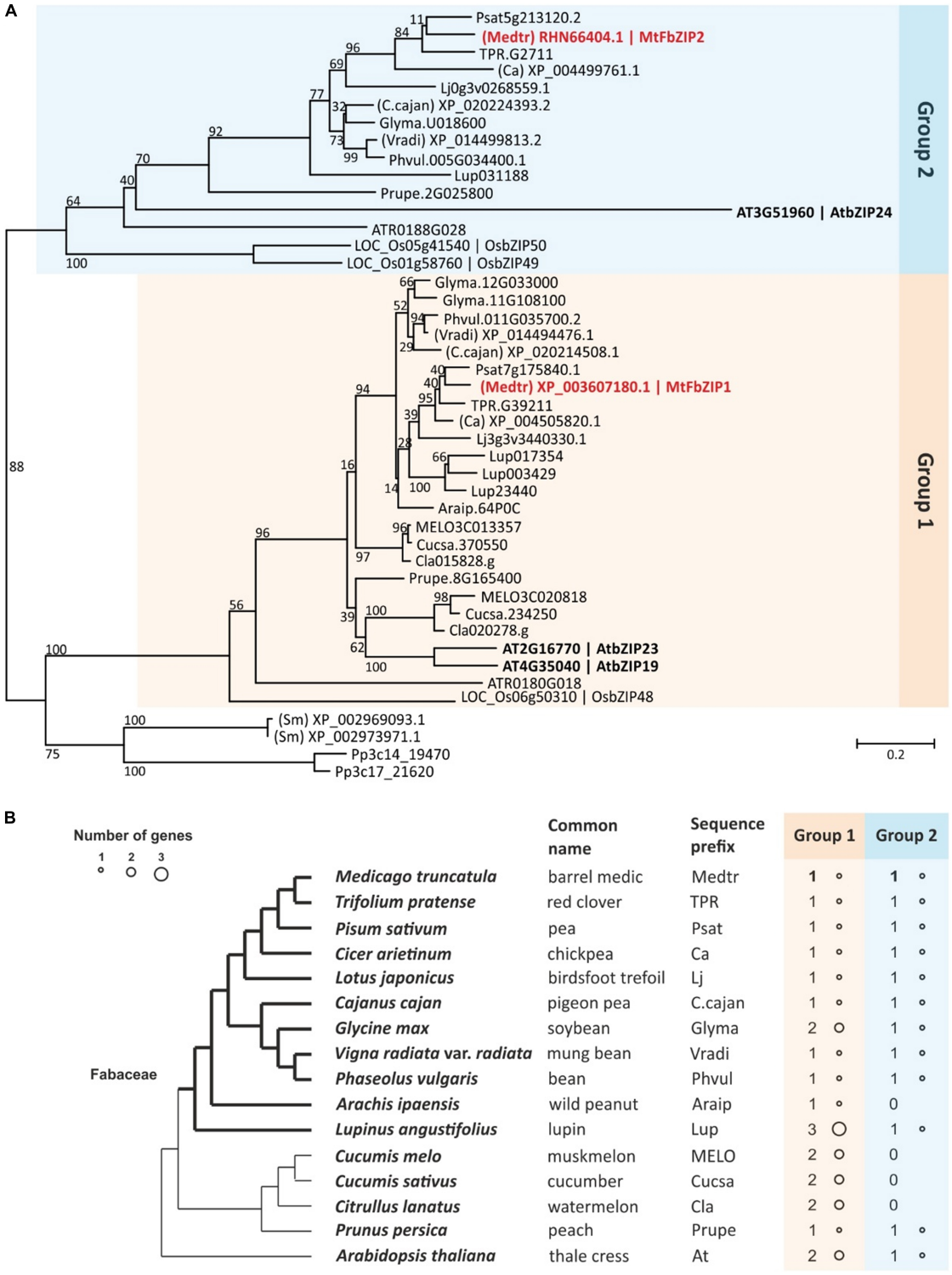

FIGURE 1 | Phylogenetic analysis of the F-bZIP proteins in Fabaceae species. **(A)** Phylogenetic tree representing 11 species from the Fabaceae family, four species from the clade Fabids but not from the Fabaceae family (*Cucumis melo*, *Cucumis sativus*, *Citrullus lanatus*, and *Prunus persica*), and five representative species from major plant taxa (*Physcomitrella patens* (Pp), *Selaginella moellendorffii* (Sm), *Amborella trichopoda* (ATR), *Oryza sativa* (LOC_OS), and *Arabidopsis thaliana*). The species prefix of the 11 Fabaceae species, the four non-Fabaceae Fabid species and the five species representing major taxa are indicated here (above) and in panel **(B)**. The phylogenetic tree was constructed using maximum-likehood and shows bootstrap support from 1,000 replicates (numbers on each branch represent the percentages of bootstrap). **(B)** F-bZIP gene enrichment for the species from the Fabaceae family, non-Fabaceae Fabids and *A. thaliana* analyzed in the phylogeny. Circle size represents the number of genes for each species in Group 1 and Group 2.

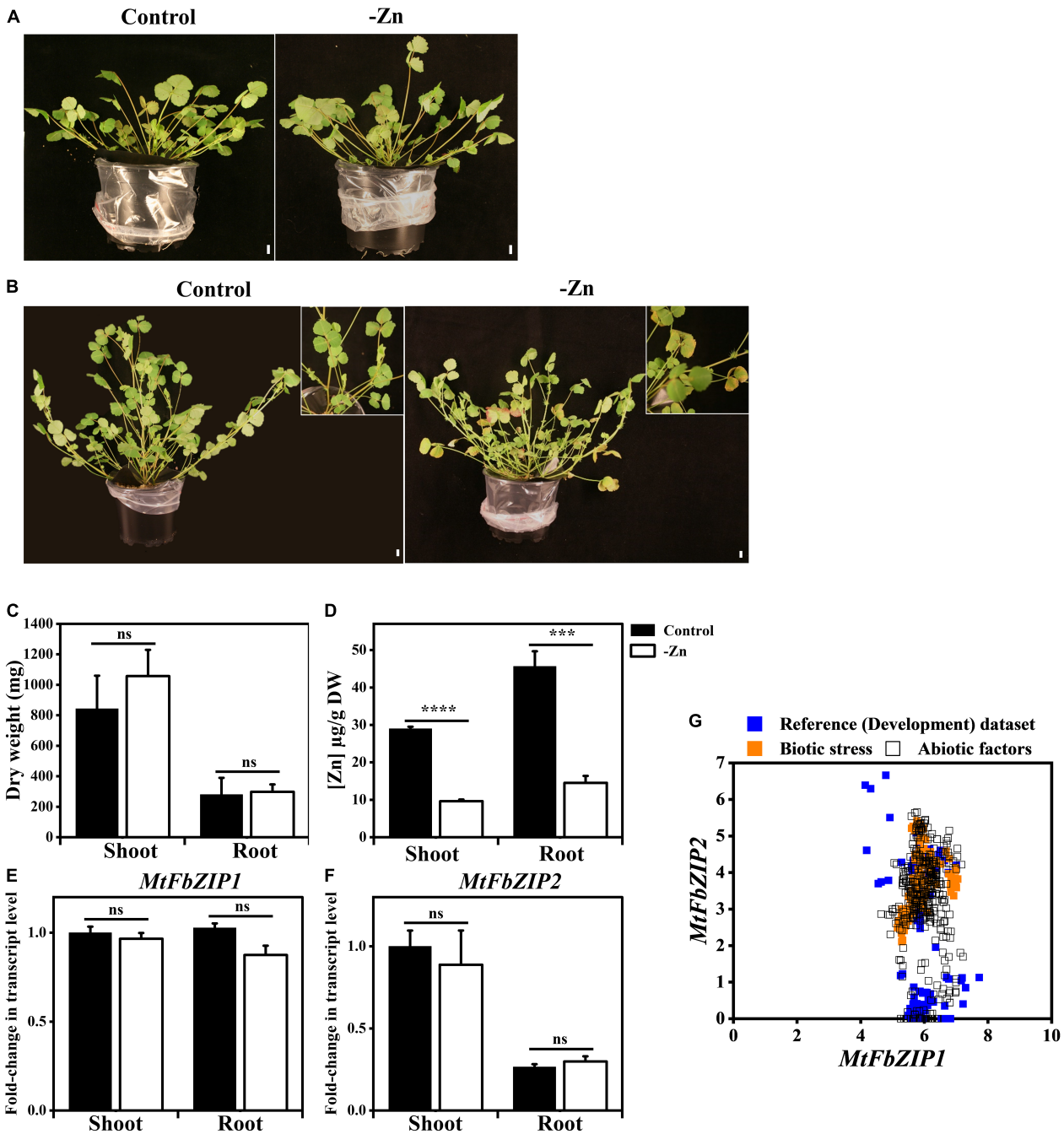

FIGURE 2 | Analysis of *M. truncatula* plants exposed to Zn deficiency. Phenotypes of **(A)** 4-week-old and **(B)** 6-week-old *M. truncatula* plants grown on sand with nutrient solution at Zn sufficiency (Control) or Zn deficiency (–Zn). Top-right inset in panel **(B)** shows a detail of plant leaves. Scale bar = 1 cm. Quantification of **(C)** shoot and root dry weight and **(D)** shoot and root Zn concentration in 6-week-old plants. **(E–G)** Expression analysis of *M. truncatula F-bZIP* genes. Shoot and root transcript levels of **(E)** *MtFbZIP1* and **(F)** *MtFbZIP2* in 4-week-old plants grown at Zn sufficiency (Control) or Zn deficiency (–Zn). Data are represented as means ± SE ($n \geq 3$). Significant differences between Control and –Zn treatments were determined by Student's *t*-test (***$p < 0.001$, ****$p < 0.0001$, ns means not significant). **(G)** Comparative gene expression atlas analysis between *MtFbZIP1* (x-axis) and *MtFbZIP2* (y-axis) expression values using RNA-seq datasets from *M. truncatula* MtExpress (https://medicago.toulouse.inrae.fr/MtExpress). Log2/TMM (scale) is used for absolute normalized gene expression values. The different RNA-seq experimental conditions are grouped into three categories: reference (development), abiotic stress and biotic stress dataset (**Supplementary Figure 2**).

within the expression value range of 4 to 8. This strongly points toward *MtFbZIP1* having a constitutive expression. On the other hand, the expression of the *MtFbZIP2* gene varies extensively with tissue type and abiotic stress imposition, showing relatively consistent expression levels within the biotic stress dataset (**Figure 2G**).

Functional Analysis of MtFbZIP1 Indicates a Role in the Zn Deficiency Response

Expression analysis of the *MtFbZIP* genes indicated that *MtFbZIP1* is generally more expressed than *MtFbZIP2* (**Figure 2G**), and considering that MtFbZIP1 maps to Group 1 F-bZIPs (**Figure 1A**) as the Arabidopsis bZIP19 and bZIP23 (Castro et al., 2017), we started with the functional analysis of MtFbZIP1. To that effect, we performed a heterologous complementation analysis by expressing *MtFbZIP1* in the Arabidopsis *bzip19/23* background, which is characterized by a Zn deficiency hypersensitive phenotype (Assunção et al., 2010). To generate the complementation lines, the CDS of *MtFbZIP1* under control of the constitutive CaMV 35S promoter and containing a C-terminal CFP-HA fusion was stably transformed into the *bzip19/23* double mutant (i.e., *bzip19/23-OEMtbFZIP1*). The transcript levels of *MtFbZIP1* in three independently transformed lines were verified (**Supplementary Figure 3**). To test the complementation of the *bzip19*/23 Zn deficiency phenotype, the *bzip19/23-OEMtFbZIP1* lines were grown on a plate assay. The analysis of 14-day-old seedlings at Zn deficiency showed that the lines overexpressing *MtFbZIP1* were able to complement the *bzip19/23* mutant phenotype (**Figure 3A**). At Zn deficiency, the growth of the seedlings was comparable between the *bzip19/23-OEMtFbZIP1* lines and the wild-type, whereas the *bzip19/23* line exhibited reduced growth and chlorosis. The *bzip19/23* mutant is fully complemented with the Arabidopsis bZIP19 transcription factor (*bzip19/23-OE19*) (Lilay et al., 2019), and here it was used as an additional control. At Zn sufficiency, there was no visible difference between the seedlings from all analyzed lines (**Figure 3A**). Seedlings from the plate assay were further analyzed for the expression of two Arabidopsis *ZIP* genes (*AtZIP4* and At*ZIP5*), which are targets of AtbZIP19 and AtbZIP23 transcription factors (Assunção et al., 2010). The transcript levels of *AtZIP4* and *AtZIP5* were higher at Zn deficiency than Zn sufficiency in the wild-type, *bzip19/23-OE19* and *bzip19/23-OEMtFbZIP1* lines, but not in the *bzip19/23* mutant, which had low transcript level at both Zn conditions (**Figures 3B,C**). Although the transcript level of *AtZIP4 and AtZIP5* in the *bzip19/23-OEMtFbZIP1* was generally higher than in the wild-type and *bzip19/23-OE19*, they all showed a comparable pattern of response to Zn supply (**Figures 3B,C**). We also looked at the *bzip19/23-OEMtFbZIP1* lines grown in hydroponics, in a longer-term experiment. The 5-week-old plants grown at Zn deficiency showed a partial complementation of the Zn deficiency phenotype in comparison with the wild-type, whereas under control conditions there were no visible differences between plants, in line with the shoot dry weight and tissue Zn concentration data (**Supplementary Figure 4**). This partial complementation in plants could relate to the fact that it is a heterologous complementation with a *M. truncatula* gene in Arabidopsis background. Overall, the functional complementation analysis, including the expression of AtbZIP19/23 target genes, clearly indicate that MtFbZIP1 protein is a functional homolog of Arabidopsis bZIP19 and bZIP23 transcription factors.

MtFbZIP2 Does Not Activate the *pZIP4:GUS* Reporter

We proceeded to obtain functional information on the MtFbZIP2. To that effect we used the reporter line *pZIP4:GUS*, in Col-0 wild-type background, which uses the target gene *AtZIP4* as a Zn deficiency marker. While the *bzip19/23-pZIP4:GUS* line does not show GUS reporter activity (**Figure 3D**) (Castro et al., 2017), the Zn-dependent activity of *pZIP4:GUS* reporter is restored upon complementation with the *AtbZIP19* (*bzip19/23-pZIP4:GUS-OEAtbZIP19*) (**Figure 3D**) (Lilay et al., 2021). Here, we tested this reporter system with the *MtFbZIP2*. To generate the complementation lines, the CDS of *MtFbZIP2* under control of the constitutive CaMV 35S promoter and containing a C-terminal CFP-HA fusion was stably transformed into the *bzip19/23-pZIP4:GUS* line (i.e., *bzip19/23-pZIP4:GUS-OEMtbFZIP2*). The analysis of 12-day-old seedlings in a plate assay showed that the lines overexpressing *MtFbZIP2* did not show GUS expression, likewise the *bzip19/23-pZIP4:GUS* line (**Figure 3D**). The *pZIP4:GUS* expression patterns in the wild-type background (*pZIP4:GUS)*, in the *bzip19/23* mutant (*bzip19/23-pZIP4:GUS)* and in the complementation line with *AtbZIP19* (*bzip19/23-pZIP4:GUS-OEAtFbZIP19*) (**Figure 3D**) are in agreement with the transcript levels of the *AtZIP4* gene in the wild-type, *bzip19/23* and *bzip19/23*-OE19 lines, respectively (**Figure 3B**). The *bzip19/23* lines complemented with *MtFbZIP1* show Zn deficiency induced *AtZIP4* gene expression, whereas the *bzip19/23-pZIP4:GUS* lines complemented with *MtFbZIP2* show no Zn deficiency induced *pZIP4:GUS* expression (**Figures 3B,D**). These results reveal that the MtFbZIP2 does not activate AtbZIP19/23 target gene expression, indicating that MtFbZIP2 is not a functional homolog of AtbZIP19/23 transcription factors and does not play a role in the Zn deficiency response.

MtFbZIP1 and MtFbZIP2 Localize in the Nucleus

To investigate the subcellular localization of the MtFbZIP1 and MtFbZIP2 proteins, we analyzed seedling roots of the *bzip19/23-OEMtFbZIP1* and *bzip19/23-pZIP4:GUS-OEMtFbZIP2* lines, grown at Zn sufficiency and Zn deficiency. The fluorescence signal of the C-terminal Cyan Fluorescent Protein (CFP) fluorophore of the MtFbZIP1 and MtFbZIP2 fusions (MtFbZIP1-CFP and MtFbZIP2-CFP, respectively) were visualized with confocal laser scanning microscopy (CLSM). The analyses showed that the MtFbZIP1 and MtFbZIP2 fusion proteins localized in the nucleus of the cell. The analysis of seedlings grown at Zn deficiency also revealed that the subcellular localization was identical between seedlings grown at Zn sufficient or Zn deficient conditions. This indicates that the cellular Zn status is not involved in the subcellular targeting of *M. truncatula* F-bZIP proteins (**Figure 4**).

Analysis of *M. truncatula ZIP* and *NAS* Genes as Candidate Targets of MtFbZIP1

To examine the conservation of the Zn deficiency response in *M. truncatula*, and in order to identify candidate target genes of MtFbZIP1, we analyzed the *M. truncatula* genes encoding

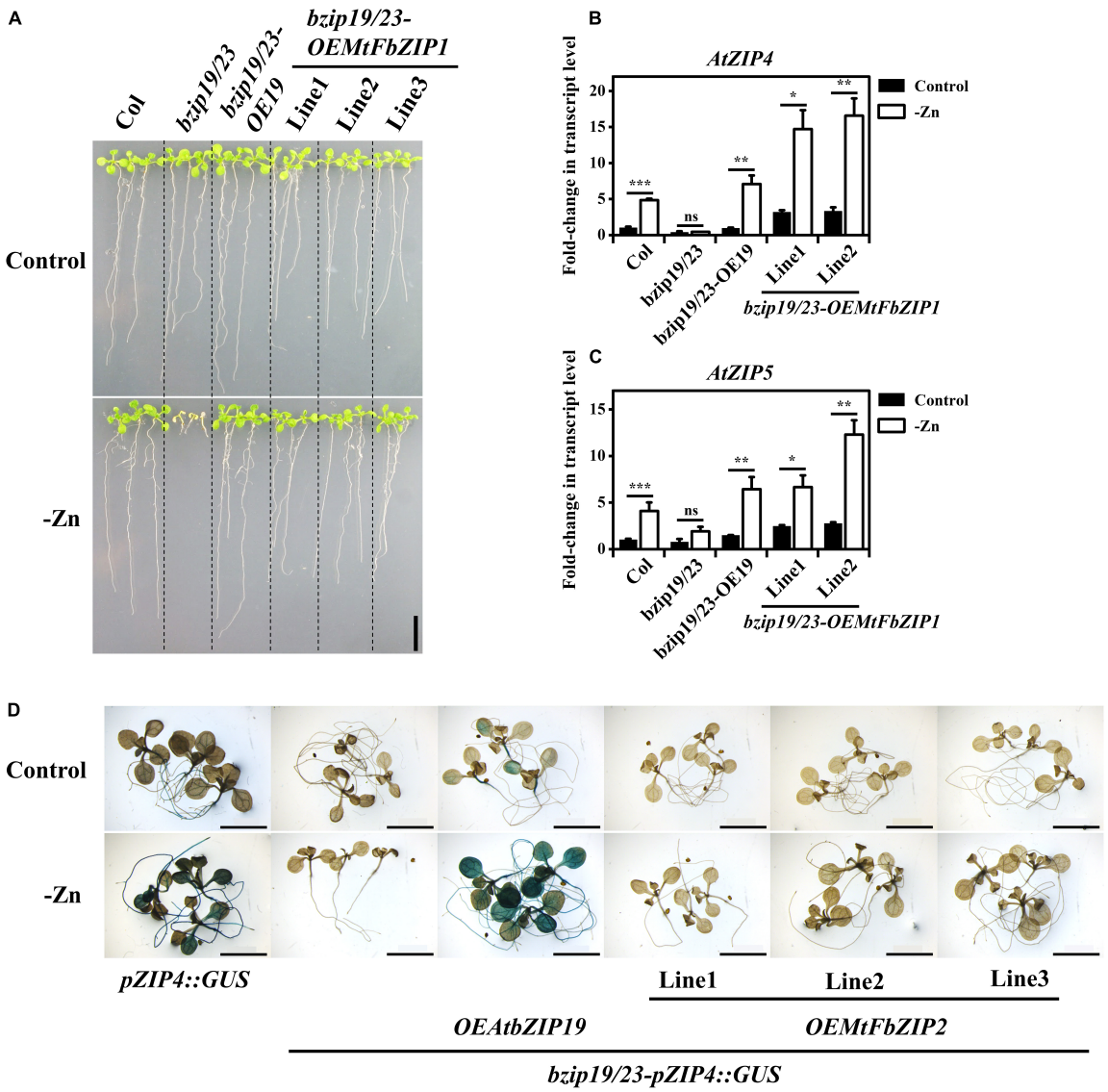

FIGURE 3 | Functional analysis of *MtFbZIPs* in Arabidopsis *bzip19/23* double mutant. **(A–C)** Complementation analysis with *bzip19/23-OEMtFbZIP1* lines, wild-type (Col), *bzip19/23* double mutant and *bzip19/23-OEAtbZIP19* (*bzip19/23-OE19*; Lilay et al., 2019) grown at Zn sufficiency (Control) or Zn deficiency (–Zn). Homozygous T3 progeny of three independently transformed lines of *bzip19/23-OEMtFbZIP1* are designated Line 1–3. **(A)** Phenotype of 2-week-old seedlings grown on MS medium. Scale bar = 1 cm. **(B,C)** Gene expression analysis of **(B)** Arabidopsis *ZIP4* (*AtZIP4*) and **(C)** Arabidopsis *ZIP5* (*AtZIP5*) in 2-week-old seedlings. Data represent mean-fold change in transcript level ± SE (n = 2–3 biological replicates). Significant differences between Control and –Zn treatments were determined by Student's t-test (*$p < 0.05$, **$p < 0.01$, ***$p < 0.001$, ns means not significant). **(D)** Histochemical GUS staining analysis of *pZIP4:GUS*, *bzip19/23-pZIP4:GUS*, *bzip19/23-pZIP4:GUS-OEAtbZIP19 (bzip19/23-pZIP4:GUS-bZIP19;* Lilay et al., 2021*)* and *bzip19/23-pZIP4:GUS-OEMtFbZIP2* lines. The images represent 10–15 12-day-old seedlings grown with Zn sufficient (Control) or Zn deficient (–Zn) MS medium. The *bzip19/23-pZIP4:GUS-OEMtFbZIP2* lines are T2 progeny of three independently transformed lines designated Line 1–3. Scale bars = 5 mm.

ZIP family transporters and NAS enzymes. First, to visualize the relationship between *M. truncatula* and Arabidopsis ZIP transporters, we produced a phylogenetic tree, including 15 *M. truncatula* and 14 Arabidopsis ZIP members. In addition, 14 ZIP members from *Amborella trichopoda* were included, representing a basal lineage in the clade of Angiospersms, and in order to provide evolutionary context (**Figure 5A**). The tree showed the presence of ZIP proteins from the three species in most of the clades produced in the phylogeny, thus resolving distinct functional ortholog groups within the different ZIP homologs. As an example, the clade with the Arabidopsis ZIP4/9 and IRT3 transporters suggests that MtZIP5 and MtZIP11 are their functional equivalents in *M. truncatula*. Overall results are in line with previous phylogenetic analysis of Arabidopsis and *M. truncatula* ZIP proteins (Mäser et al., 2001; Abreu et al., 2017). Next, we analyzed the promoter region of all *ZIP* genes used in the phylogenetic analysis, to search the presence of ZDRE cis-regulatory elements to which the Arabidopsis

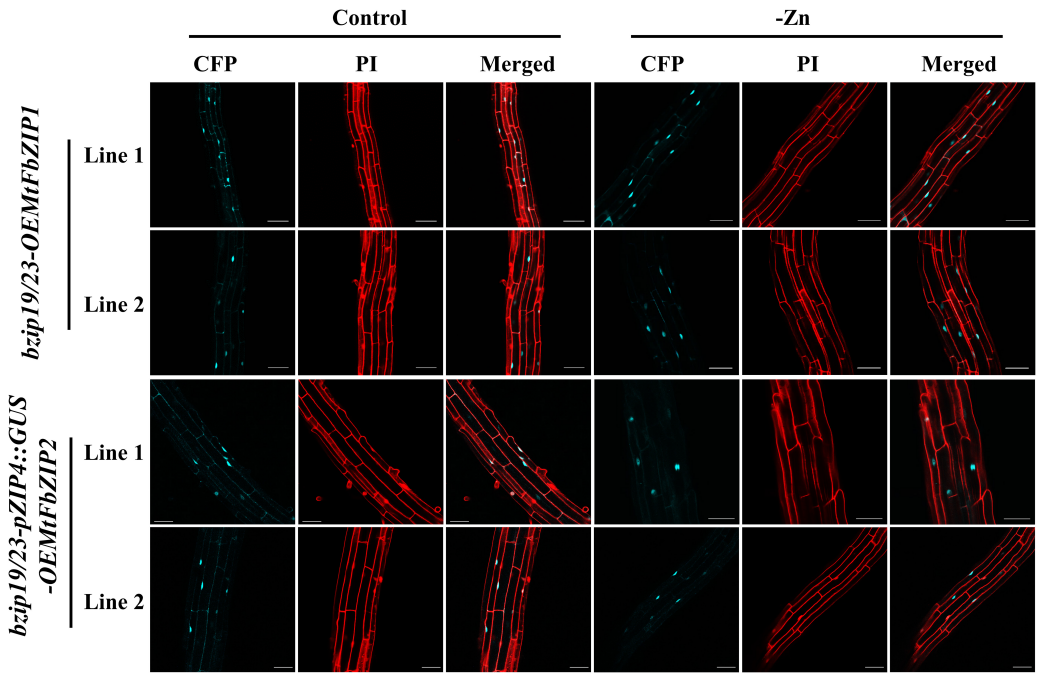

FIGURE 4 | Subcellular localization analysis of MtFbZIP1-CFP and MtFbZIP2-CFP fusion proteins in Arabidopsis roots. Two-week-old seedlings of *bzip19/23-OEMtFbZIP1* and *bzip19/23-pZIP4:GUS-OEMtFbZIP2* lines, grown on MS media at Zn sufficiency (Control) or Zn deficiency (–Zn) were analyzed. Emissions of CFP and propidium iodide (PI) were determined by CLSM. Two to three seedlings for each independent line were used. Scale bars = 50 μm.

bZIP19 and bZIP23 transcription factors bind to (Assunção et al., 2010). The consensus sequence RTGWCGACAY was used, and an overview of the detected ZDRE motifs, including their numbers and positions, is shown in **Supplementary Table 2**. In general, ZDREs were identified in the promoters of *M. truncatula* and *A. trichopoda ZIP* genes which are in clades together with Arabidopsis *ZIP* genes that are targets of AtbZIP19/23. Accordingly, no ZDRE motifs were detected in the promoters of *M. truncatula* and *A. trichopoda ZIP* genes positioned in the clade containing the Arabidopsis *ZIP2*, which is not a target gene of AtbZIP19/23 (**Figure 5A**). In order to extend the information on the presence of ZDRE promoter elements to the *M. truncatula NAS* genes, a similar *in silico* search was performed in the four annotated *MtNAS* genes (**Supplementary Table 2**).

Based on the phylogeny of ZIP transporters, we focused on four *MtZIPs* (*MtZIP1/2/5/11*) to investigate their gene expression in *M. truncatula* plants in response to Zn supply. As mentioned, MtZIP5 and MtZIP11 are close homologs of AtZIP4/9 and IRT3 (**Figure 5A**, orange shadow). In a different clade, MtZIP1 is a close homolog of AtZIP1 (**Figure 5A**, blue shadow). All the Arabidopsis ZIP members from these two clades are target genes of AtbZIP19/23. In a more distantly related clade, MtZIP2 is a close homolog of AtZIP2, (**Figure 5A**, gray shadow) a non-target gene. The expression analysis showed that the transcript levels of *MtZIP1*, *MtZIP5* and *MtZIP11* were significantly higher in Zn-deficient than in Zn-sufficient plants. The three genes had higher Zn-deficiency induced expression in shoots than in roots (**Figures 5B,D,E**). The transcript level of *MtZIP2* was not significantly different between the Zn treatments, and *MtZIP2* was more expressed in roots, with a comparatively very low detection in shoots (**Figure 5C**). The gene expression analysis was extended to the four *MtNAS* genes (*MtNAS1-4*). The transcript levels of *MtNAS1* and *MtNAS4* were induced in Zn-deficiency in roots but not in shoots (**Figures 5F,H**). The transcript level of *MtNAS2* was not significantly affected by Zn treatments, with *MtNAS2* more expressed in roots than in shoots (**Figure 5G**). For *MtNAS3,* we could not detect transcript level signal. Concerning the presence of promoter ZDRE motifs in these genes, we identified the presence of two motifs in both *MtZIP5* and *MtZIP11* promoters, with one mismatch in one ZDRE from *MtZIP5*. In addition, we identified one ZDRE in both, the *MtNAS1* and in *MtNAS4* promoters, with one mismatch in *MtNAS1* (**Supplementary Table 2**). Together these results suggest an association between the presence of ZDREs in the promoter of *M. truncatula ZIP* and *NAS* genes and their transcriptional response to Zn deficiency.

DISCUSSION

Phylogenetic Analysis Identifies Two *M. truncatula* F-bZIP Homologs

In order to obtain a more detailed evolutionary characterization of F-bZIP homologs from legume species, we performed a phylogenetic analysis enriched in species from the Fabaceae family. The analysis supported the emergence of F-bZIP Groups 1 and 2 associated with seed plant differentiation (**Figure 1**). This is in line with our previous phylogenetic

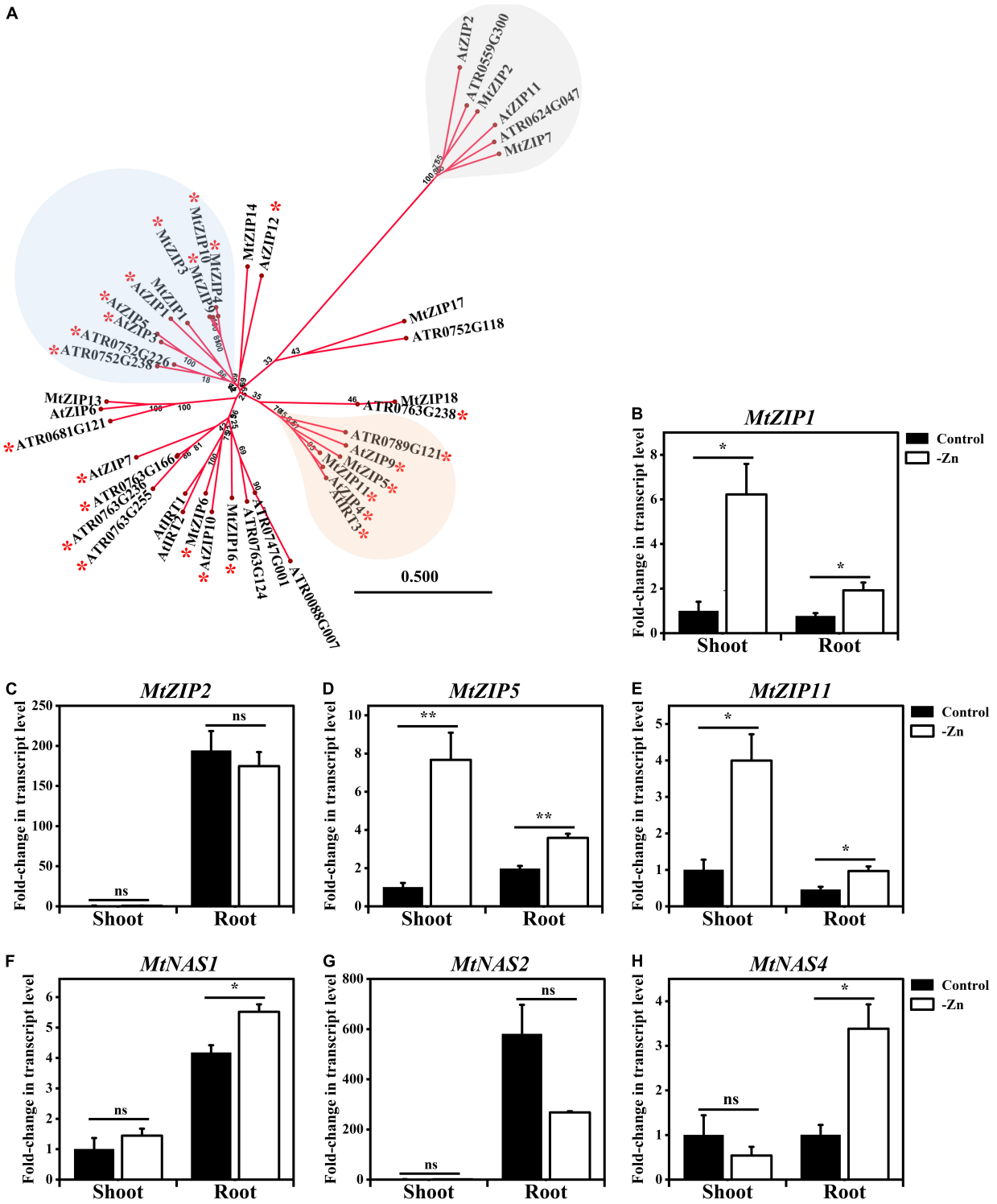

FIGURE 5 | Analysis of *M. truncatula* ZIP and NAS family members. **(A)** Phylogenetic tree of *M. truncatula* (Mt), Arabidopsis (At) and *A. trichopoda* (ATR) ZIP transporters. Branch lengths are proportional to phylogenetic distance. Numbers on each branch represent the percentages of bootstrap. An asterisk (*) next to a ZIP transporter gene ID means that one or more ZDRE motifs were detected in the gene promoter (**Supplementary Table 2**). The orange, blue and gray shadows highlight different clades of the phylogenetic tree. **(B–H)** Gene expression analysis of 4-week-old *M. truncatula* plants grown on sand watered with Zn sufficient (Control) or Zn deficient (–Zn) nutrient solution. Shoot and root transcript level of **(B)** *MtZIP1*, **(C)** *MtZIP2*, **(D)** *MtZIP5*, **(E)** *MtZIP11*, **(F)** *MtNAS1*, **(G)** *MtNAS2*, and **(H)** *MtNAS4*. Data represent mean fold-change in transcript level ± SE (n = 3 biological replicates). Significant differences between control and –Zn treatments were determined by Student's *t*-test (*$p < 0.05$, **$p < 0.01$, ns means not significant).

analysis of F-bZIP homologs across land plants (Castro et al., 2017), which was further supported in a phylogenetic and synteny analysis enriched in Monocot species (Lilay et al., 2020). Here, we identified two *M. truncatula* F-bZIP homologs: MtFbZIP1 (MtrunA17_Chr4g0036971) in Group 1 and MtFbZIP2 (MtrunA17_Chr3g0090531) in Group 2. In the previous phylogenies, all species had at least one Group 1 F-bZIP, whereas Group 2 appeared more prone to gene loss or expansion events (Castro et al., 2017). For example, indication of gene expansion in Group 2 was observed in the Monocot enriched analysis (Lilay et al., 2020). In this phylogeny, a Group 1 F-bZIP is also present in all species, whereas Group 2, rather than expansion or loss, displays conservation of a single member per Fabaceae genome, while in the sister clade Cucurbitaceae the loss of Group 2 members is observed. Thus, this phylogenetic analysis reinforces the branching of F-bZIPs into two groups, with F-bZIP homologs from Group 1 consistently present in all species, with at least one member, whereas homologs from Group 2 display more variable evolutionary paths. The central regulators of the Zn deficiency response in Arabidopsis, AtbZIP19 and AtbZIP23, and its functional homolog in rice, OsbZIP48, belong to Group 1 (Assunção et al., 2010; Lilay et al., 2020). The Arabidopsis F-bZIP Group 2 single member, AtbZIP24, has no major role in the Zn deficiency response (Lilay et al., 2019), and is involved in salt stress regulation (Yang et al., 2009). In rice, bZIP49 from Group 2 seems to be a truncated protein not involved in the Zn deficiency response. Whereas OsbZIP50, also from Group 2, plays a role in the Zn deficiency response, however its ectopic expression in Arabidopsis suggests an altered regulatory response at Zn sufficiency (Lilay et al., 2020). These observations support the suggested conservation of the Zn deficiency response associated with Group 1 members, while the Group 2 F-bZIPs, on the other hand, are more prone to gene loss or expansion events that might lead to non-, sub- or neo-functionalization (Castro et al., 2017). To obtain information about the *M. truncatula* F-bZIPs, we proceeded with their functional characterization.

MtFbZIP1 Is the Functional Homolog of Arabidopsis bZIP19/23 Transcription Factors

To investigate the role of *M. truncatula* F-bZIPs in the Zn deficiency response, we analyzed *M. truncatula* plants grown with different Zn supply (**Figure 2**). At Zn deficiency, plants showed a mild visible phenotype, but the element analysis in shoot and root showed a reduced Zn concentration in comparison to the control condition. The expression of *MtFbZIP1* and *MtFbZIP2* genes in these plants was not Zn-responsive, indicating that they are not transcriptionally regulated by Zn status. Similar results were obtained for Arabidopsis *F-bZIP* genes *AtbZIP19/23/24* (Lilay et al., 2019) and for rice *F-bZIP* genes *OsbZIP48/49/50* (Lilay et al., 2020). Current knowledge in Arabidopsis indicates that the Zn-dependent activity of the AtbZIP19/23 is not controlled at the transcriptional level, but at the protein level where activity is repressed at Zn sufficiency (Lilay et al., 2019). This is the result of a direct binding of Zn^{2+} ions to the characteristic Cys/His-rich motif, the Zn-sensor motif (ZSM), of AtbZIP19/23 transcription factors, which also act as direct sensors of the intracellular Zn concentration (Lilay et al., 2021). In order to obtain information on the comparative expression between the *MtFbZIP1* and *MtFbZIP2* genes, we analyzed available RNA-seq datasets from *M. truncatula* (**Figure 3**). Expression data, comprising development, abiotic and biotic stress datasets, indicated that *MtFbZIP1* is broadly expressed with a more constitutive pattern across different tissue types and stress factors than *MtFbZIP2*, with the latter showing a high degree of variation.

Next, we performed a functional characterization of MtFbZIP1 by heterologous complementation analysis in the Arabidopsis *bzip19/23* double mutant. The *bzip19/23* mutant is hypersensitive to Zn deficiency, and overexpression of *AtbZIP19* or *AtbZIP23* functionally complements the mutant. In these complementation lines, the transcriptional activation of the Arabidopsis bZIP19/23 target genes at Zn deficiency is restored (Lilay et al., 2019). Here, the analysis of *bzip19/23-OEMtFbZIP1* seedlings showed complementation of the *bzip19/23* Zn deficiency phenotype, and the expression of Arabidopsis *ZIP* transporter target genes, *AtZIP4* and *AtZIP5*, was induced at Zn deficiency (**Figure 4**). Comparable results were observed in heterologous complementation analysis of wheat, barley and rice F-bZIPs in the Arabidopsis *bzip19/23* mutant (Evens et al., 2017; Nazri et al., 2017; Lilay et al., 2020). We also performed a functional analysis of MtFbZIP2 in the Arabidopsis *bzip19/23-pZIP4:GUS* line, which uses the *AtZIP4* promoter fused to GUS as a reporter for transcriptional activation by AtbZIP19/23 in response to Zn deficiency, as described in Lilay et al. (2021). However, GUS expression was not observed in the *bzip19/23-pZIP4:GUS-OEMtFbZIP2* seedlings. These results indicate that MtFbZIP1, but not MtFbZIP2, functionally complement the *bzip19/23* mutant. Localization analysis showed that both, MtFbZIP1 and MtFbZIP2, are in the nucleus and their nuclear localization seems to be independent of cellular Zn status. Comparable results were reported in localization analysis of Arabidopsis (AtbZIP19/23/24) and rice (OsbZIP48/49/50) F-bZIP proteins, from Group 1 and Group 2 (Lilay et al., 2019, 2020). Overall, results indicate that Group 1 MtFbZIP1 is a functional homolog of the Arabidopsis bZIP19 and bZIP23 transcription factors, and, as such, it is likely a regulator of the Zn deficiency response in *M. truncatula*. On the other hand, Group 2 MtFbZIP2 does not seem to play a role in the Zn deficiency response. The RNA-seq analysis showed *MtFbZIP2* gene expression varying extensively with tissue type and abiotic stress imposition, but more consistent within the biotic stress dataset (**Figure 3**), suggesting that MtFbZIP2 may be sub-functionalizing into specific roles. This is in line with the suggested conservation of the Zn deficiency response associated with Group 1 members, whereas Group 2 displays more variable evolutionary paths (Castro et al., 2017).

Exploring the F-bZIP Regulated Zn Deficiency Response in *M. truncatula*

To further unravel the Zn deficiency response in *M. truncatula*, we investigated the putative MtFbZIP1 regulatory network, and

analyzed the expression of *M. truncatula ZIP* and *NAS* genes in response to Zn supply. In Arabidopsis, bZIP19/23 target genes include members of the ZIP transporter family and NAS enzymes, which contain ZDRE motifs in the promoter and are transcriptionally activated at Zn deficiency (Assunção et al., 2010). The ZIP family members are divalent cation transporters involved in uptake of Zn, Fe and manganese (Mn) into the cell cytoplasm (Guerinot, 2000; Sinclair and Krämer, 2012). The *ZIP* target genes of AtbZIP19 and AtbZIP23 are *AtZIP1/3/4/5/9/10/12 and AtIRT3*, and *AtIRT3*, and except for *AtZIP5*, the encoded proteins have been shown to mediate Zn transport (Grotz et al., 1998; Lin et al., 2009; Assunção et al., 2010; Milner et al., 2013; Lee et al., 2021). In *M. truncatula,* there are 15 annotated members from the ZIP family, where MtZIP1-7 were characterized and shown to mediate Zn, Fe and Mn transport (Burleigh et al., 2003; López-Millán et al., 2004; Abreu et al., 2017). MtZIP6 is involved in Zn uptake by rhizobia-infected nodule cells, playing a role in the symbiosome Zn homeostasis (Abreu et al., 2017). To obtain information on the relationship between Arabidopsis and *M. truncatula* ZIP transporters, we produced a phylogenetic tree to which we included the detected ZDRE motifs in the *ZIP* gene promoters (**Figure 5**). Previously, the analysis of gene promoters of *AtZIP4/9* and *AtIRT3* homologs across land plants identified an enrichment in ZDREs in the promoter regions (Castro et al., 2017). Here, the phylogenetic analysis supports such enrichment, and additionally, it highlights an enrichment of ZDREs in other clades containing other *AtZIP* target genes of AtbZIP19/23. The *MtZIP1*, *MtZIP5* and *MtZIP11*, close homologs of *AtZIP* target genes, and on the other hand, *MtZIP2*, a close homolog of *AtZIP2*, a non-target gene, were analyzed in *M. truncatula* plants (**Figure 5**; Abreu et al., 2017). The expression of *MtZIP1*, *MtZIP5* and *MtZIP11* genes is induced by Zn deficiency, both in shoots and roots, but with higher transcript level in shoots than in roots. This is consistent with earlier observations on *MtZIP1* and *MtZIP5* expression, except that *MtZIP5* expression in roots was previously reported as non Zn-responsive (López-Millán et al., 2004). MtZIP5 and MtZIP11 were functionally characterized as Zn transporters (López-Millán et al., 2004), and, considering their Zn-responsive gene expression patterns and presence of ZDRE promoter elements (**Figure 5**), they constitute target gene candidates of the MtFbZIP1 transcription factor, to play a role in the Zn deficiency response. MtZIP1 also mediates Zn transport (López-Millán et al., 2004), but no ZDRE was detected in the promoter of *MtZIP1* gene. This may suggest regulation by transcription factors other than the F-bZIPs, or other F-bZIP-DNA binding *cis*-elements. The expression of *MtZIP2* gene is not Zn-deficiency responsive and it does not contain ZDREs in the promoter, which is in line with reports for *AtZIP2*, and for rice *OsZIP2*, another *AtZIP2* homolog (Assunção et al., 2010; Lilay et al., 2020). Previously, MtZIP2 was shown to mediates Zn transport, with *MtZIP2* mainly expressed in roots (Burleigh et al., 2003), in line with our observations. This supports a role for MtZIP2 in *M. truncatula* Zn homeostasis, but not in the F-bZIP mediated Zn deficiency response.

In addition, to *MtZIP* we also analyzed *MtNAS* genes. The NAS enzymes produce NA ligand that forms complexes with Zn, Fe and other metal micronutrients. NA is involved in Zn and Fe homeostasis and contributes to their intercellular and long-distance distribution (Clemens, 2019). In *M. truncatula*, MtNAS1 is suggested to play a role in the efficient Fe supply to the nodule with impact in nitrogen fixation acclimation efficiency (Avenhaus et al., 2016), while MtNAS2 is required for symbiotic nitrogen fixation (Escudero et al., 2020), supporting an important role for NA in Fe delivery and Fe homeostasis in the symbiosome. In Arabidopsis, *AtNAS2* and *AtNAS4* are among the target genes of AtbZIP19 and AtbZIP23, and are transcriptionally activated at Zn deficiency (Assunção et al., 2010). Here, the expression of *MtNAS2* gene was not induced by Zn deficiency and it is mainly expressed in roots, in agreement with Escudero et al. (2020), whereas the expression of *MtNAS1* and *MtNAS4* was induced by Zn deficiency in roots, but not in shoots. In the promoter of *MtNAS1* we found one ZDRE with one mismatch (**Supplementary Table 2**). However, its relevance is questionable since a mutation in the same position (i.e., RTGTAGACAY) was previously shown to fail binding to Arabidopsis AtbZIP19 and AtbZIP23, and to rice OsbZIP48, in pull-down *in vitro* assays (Assunção et al., 2010; Lilay et al., 2020) suggesting that it is an essential nucleotide for the F-bZIP-DNA binding. *MtNAS4* showed stronger Zn-deficiency induced expression than *MtNAS1* and it contains one ZDRE in the promoter, therefore *MtNAS4* could be a candidate target gene of MtFbZIP1. Nevertheless, the regulation of *NAS* genes seems to be complex and controlled by multiple mechanisms. In Arabidopsis, bHLH and MYB transcription factors, which regulate the Fe deficiency response, control the expression of *NAS* genes, with indication of cross-talk between Fe and Zn homeostasis (Palmer et al., 2013; Chen et al., 2018). Overall, the analysis of *M. truncatula ZIP* and *NAS* genes suggests that *MtZIP5*, *MtZIP11* and *MtNAS4* are candidate target genes of the MtFbZIP1 transcription factor, and integrate the Zn deficiency response regulatory network in *M. truncatula*.

CONCLUDING REMARKS

Our results suggest that the Zn deficiency response regulated by F-bZIP transcription factors is conserved in the legume model *M. truncatula*. In legumes species, an important component of the plant Zn homeostasis is the transport of Zn to the nodule-rhizobia infected cells where an adequate delivery to metalloproteins is required for proper nitrogen fixation (Abreu et al., 2020). It is conceivable that the Zn deficiency response includes the regulation of Zn homeostasis in symbiosomes in *M. truncatula.* The functional analysis of the two identified *M. truncatula* F-bZIPs indicates that Group 1 MtFbZIP1 is the functional homolog of Arabidopsis bZIP19 and bZIP23 transcription factors. The analyses of *M. truncatula ZIP* and *NAS* genes, namely the Zn-deficiency responsive expression associated with the presence of ZDREs in the promoter region, support the conservation of the F-bZIP-regulated Zn deficiency response in *M. truncatula*. This conservation paves the way to follow-up investigations on the modulation of F-bZIP transcription factor's activity to impact plant Zn content (Lilay et al., 2021). The analysis of Group 2 MtFbZIP2 suggests that it does not play a role in the Zn deficiency response and may be

subfunctionalizing into other roles. A phylogenetic analysis of F-bZIP homologs enriched in legume species provides support for the translation of functional insight on the F-bZIP regulatory network from the model *M. truncatula* to legume crops as a strategy to obtain improved Zn nutritional value.

DATA AVAILABILITY STATEMENT

The original contributions presented in this study are included in the article/**Supplementary Material**, further inquiries can be directed to the corresponding author.

AUTHOR CONTRIBUTIONS

FL, GHL, and AGLA designed and performed the experimental work. FL and AGLA analyzed the data and wrote the manuscript. FL, PHC, and HA performed the phylogenetic analysis. All authors revised the manuscript.

FUNDING

This work was supported by the Independent Research Fund Denmark (DFF-FTP, Grant No. 9041-00182B), the Novo Nordisk Foundation, Biotechnology-based Synthesis and Production Research program (NNF18OC0034598), the Chinese Scholarship Council (Grant No. 201907940009), the Portuguese Foundation for Science and Technology, FCT (PTDC/BAA-AGR/31122/2017; POCI-01-0145- FEDER-031122) to FL, GHL, PHC, and AGLA, and the FCT Stimulus to Scientific Employment – Individual Support (CEECIND/00399/2017/CP1423/CT0004) to HA. Element analysis was performed at CHEMI Center, and imaging data were collected at the CAB Center at PLEN, University of Copenhagen.

SUPPLEMENTARY MATERIAL

The Supplementary Material for this article can be found online at: https://www.frontiersin.org/articles/10.3389/fpls.2022.916168/full#supplementary-material

REFERENCES

Abreu, I., Escudero, V., Montiel, J., Castro-Rodríguez, R., and González-Guerrero, M. (2020). "Metal transport in *Medicago truncatula* nodule rhizobia-infected cells," in *The Model Legume Medicago Truncatula*, ed. F de Bruijn (Hoboken: Wiley), 652–664. doi: 10.1002/9781119409144.ch81

Abreu, I., Saéz, Á, Castro-Rodríguez, R., Escudero, V., Rodríguez-Haas, B., Senovilla, M., et al. (2017). Medicago truncatula Zinc-Iron Permease6 provides zinc to rhizobia-infected nodule cells. *Plant Cell Environ.* 40, 2706–2719. doi: 10.1111/pce.13035

Andreini, C., Banci, L., Bertini, I., and Rosato, A. (2006). Zinc through the three domains of life. *J. Proteome Res.* 5, 3173–3178. doi: 10.1021/pr0603699

Assunção, A. G. L., Herrero, E., Lin, Y.-F., Huettel, B., Talukdar, S., Smaczniak, C., et al. (2010). Arabidopsis thaliana transcription factors bZIP19 and bZIP23 regulate the adaptation to zinc deficiency. *Proc. Natl. Acad. Sci. U. S. A.* 107, 10296–10301. doi: 10.1073/pnas.1004788107

Avenhaus, U., Cabeza, R. A., Liese, R., Lingner, A., Dittert, K., Salinas-Riester, G., et al. (2016). Short-Term Molecular Acclimation Processes of Legume Nodules to Increased External Oxygen Concentration. *Front. Plant Sci.* 6:1133. doi: 10.3389/fpls.2015.01133

Beebe, S., Gonzalez, A. V., and Rengifo, J. (2000). Research on Trace Minerals in the Common Bean. *Food Nutr. Bull.* 21, 387–391. doi: 10.1177/156482650002100408

Burleigh, S. H., Kristensen, B. K., and Bechmann, I. E. (2003). A plasma membrane zinc transporter from Medicago truncatula is up-regulated in roots by Zn fertilization, yet down-regulated by arbuscular mycorrhizal colonization. *Plant Mol. Biol.* 52, 1077–1088. doi: 10.1023/a:1025479701246

Carrere, S., Verdier, J., and Gamas, P. (2021). MtExpress, a Comprehensive and Curated RNAseq-based Gene Expression Atlas for the Model Legume Medicago truncatula. *Plant Cell Physiol.* 62, 1494–1500. doi: 10.1093/pcp/pcab110

Castro, P. H., Lilay, G. H., Munoz-Merida, A., Schjoerring, J. K., Azevedo, H., and Assuncao, A. G. L. (2017). Phylogenetic analysis of F-bZIP transcription factors indicates conservation of the zinc deficiency response across land plants. *Sci. Rep.* 7:3806. doi: 10.1038/s41598-017-03903-6

Castro-Guerrero, N. A., Isidra-Arellano, M. C., Mendoza-Cozatl, D. G., and Valdés-López, O. (2016). Common Bean: A Legume Model on the Rise for Unraveling Responses and Adaptations to Iron, Zinc, and Phosphate Deficiencies. *Front. Plant Sci.* 7:600. doi: 10.3389/fpls.2016.00600

Champagne, C. E. M., Goliber, T. E., Wojciechowski, M. F., Mei, R. W., Townsley, B. T., Wang, K., et al. (2007). Compound Leaf Development and Evolution in the Legumes. *Plant Cell* 19, 3369–3378. doi: 10.1105/tpc.107.052886

Chen, C.-L., Cui, Y., Cui, M., Zhou, W.-J., Wu, H.-L., and Ling, H.-Q. (2018). A FIT-binding protein is involved in modulating iron and zinc homeostasis in Arabidopsis. *Plant Cell Environ.* 41, 1698–1714. doi: 10.1111/pce.13321

Clemens, S. (2001). Molecular mechanisms of plant metal tolerance and homeostasis. *Planta* 212, 475–486. doi: 10.1007/s004250000458

Clemens, S. (2019). Metal ligands in micronutrient acquisition and homeostasis. *Plant Cell Environ.* 42, 2902–2912. doi: 10.1111/pce.13627

Clemens, S., Deinlein, U., Ahmadi, H., Höreth, S., and Uraguchi, S. (2013). Nicotianamine is a major player in plant Zn homeostasis. *BioMetals* 26, 623–632. doi: 10.1007/s10534-013-9643-1

Colvin, R. A., Holmes, W. R., Fontaine, C. P., and Maret, W. (2010). Cytosolic zinc buffering and muffling: their role in intracellular zinc homeostasis. *Metallomics* 2, 297–356. doi: 10.1039/b926662c

Earley, K. W., Haag, J. R., Pontes, O., Opper, K., Juehne, T., Song, K., et al. (2006). Gateway-compatible vectors for plant functional genomics and proteomics. *Plant J.* 45, 616–629. doi: 10.1111/j.1365-313X.2005.02617.x

Escudero, V., Abreu, I., del Sastre, E., Tejada-Jiménez, M., Larue, C., Novoa-Aponte, L., et al. (2020). Nicotianamine Synthase 2 Is Required for Symbiotic Nitrogen Fixation in Medicago truncatula Nodules. *Front. Plant Sci.* 10:1780. doi: 10.3389/fpls.2019.01780

Evens, N. P., Buchner, P., Williams, L. E., and Hawkesford, M. J. (2017). The role of ZIP transporters and group F bZIP transcription factors in the Zn-deficiency response of wheat (Triticum aestivum). *Plant J.* 92, 291–304. doi: 10.1111/tpj.13655

Gouy, M., Guindon, S., and Gascuel, O. (2010). SeaView Version 4: A Multiplatform Graphical User Interface for Sequence Alignment and Phylogenetic Tree Building. *Mol. Biol. Evol.* 27, 221–224. doi: 10.1093/molbev/msp259

Grotz, N., Fox, T., Connolly, E., Park, W., Guerinot, M. L., and Eide, D. (1998). Identification of a family of zinc transporter genes from Arabidopsis that respond to zinc deficiency. *Proc. Natl. Acad. Sci. U. S. A.* 95, 7220–7224. doi: 10.1073/pnas.95.12.7220

Guerinot, M. L. (2000). The ZIP family of metal transporters. *Biochim. Biophys. Acta Biomembr.* 1465, 190–198. doi: 10.1016/S0005-2736(00)00138-3

Ibrahim, E. A., and Ramadan, W. A. (2015). Effect of zinc foliar spray alone and combined with humic acid or/and chitosan on growth, nutrient elements content and yield of dry bean (Phaseolus vulgaris L.) plants sown at different dates. *Sci. Hortic.* 184, 101–105. doi: 10.1016/j.scienta.2014.11.010

Jefferson, R. A., Kavanagh, T. A., and Bevan, M. W. (1987). GUS fusions: beta-glucuronidase as a sensitive and versatile gene fusion marker in higher plants. *EMBO J.* 6, 3901–3907. doi: 10.1002/j.1460-2075.1987.tb02730.x

Kumar, S., and Pandey, G. (2020). Biofortification of pulses and legumes to enhance nutrition. *Heliyon* 6:e03682. doi: 10.1016/j.heliyon.2020.e03682

Lee, S., Lee, J., Ricachenevsky, F. K., Punshon, T., Tappero, R., Salt, D. E., et al. (2021). Redundant roles of four ZIP family members in zinc homeostasis and seed development in Arabidopsis thaliana. *Plant J.* 108, 1162–1173. doi: 10.1111/tpj.15506

Lilay, G. H, Castro, P. H., Campilho, A., and Assunção, A. G. L. (2019). The Arabidopsis bZIP19 and bZIP23 Activity Requires Zinc Deficiency – Insight on Regulation From Complementation Lines. *Front. Plant Sci.* 9:1955. doi: 10.3389/fpls.2018.01955

Lilay, G. H, Persson, D. P., Castro, P. H., Liao, F., Alexander, R. D., Aarts, M. G. M., et al. (2021). Arabidopsis bZIP19 and bZIP23 act as zinc sensors to control plant zinc status. *Nat. Plants* 7, 137–143. doi: 10.1038/s41477-021-00856-7

Lilay, G. H., Castro, P. H., Guedes, J. G., Almeida, D. M., Campilho, A., Azevedo, H., et al. (2020). Rice F-bZIP transcription factors regulate the zinc deficiency response. *J. Exp. Bot.* 71, 3664–3677. doi: 10.1093/jxb/eraa115

Lin, Y.-F., Liang, H.-M., Yang, S.-Y., Boch, A., Clemens, S., Chen, C.-C., et al. (2009). Arabidopsis IRT3 is a zinc-regulated and plasma membrane localized zinc/iron transporter. *New Phytol.* 182, 392–404. doi: 10.1111/j.1469-8137.2009.02766.x

Livak, K. J., and Schmittgen, T. D. (2001). Analysis of Relative Gene Expression Data Using Real-Time Quantitative PCR and the 2−ΔΔCT Method. *Methods* 25, 402–408. doi: 10.1006/meth.2001.1262

López-Millán, A.-F., Ellis, D. R., and Grusak, M. A. (2004). Identification and Characterization of Several New Members of the ZIP Family of Metal Ion Transporters in Medicago Truncatula. *Plant Mol. Biol.* 54, 583–596. doi: 10.1023/B:PLAN.0000038271.96019.aa

Maret, W., and Li, Y. (2009). Coordination Dynamics of Zinc in Proteins. *Chem. Rev.* 109, 4682–4707. doi: 10.1021/cr800556u

Mäser, P., Thomine, S., Schroeder, J. I., Ward, J. M., Hirschi, K., Sze, H., et al. (2001). Phylogenetic relationships within cation transporter families of Arabidopsis. *Plant Physiol.* 126, 1646–1667. doi: 10.1104/pp.126.4.1646

Miller, M. A., Pfeiffer, W., and Schwartz, T. (2011). "The CIPRES science gateway," in *Proceedings of the 2011 TeraGrid Conference on Extreme Digital Discovery - TG '11*, (New York, NY: ACM Press), 1. doi: 10.1145/2016741.2016785

Milner, M. J., Seamon, J., Craft, E., and Kochian, L. V. (2013). Transport properties of members of the ZIP family in plants and their role in Zn and Mn homeostasis. *J. Exp. Bot.* 64, 369–381. doi: 10.1093/jxb/ers315

Nazri, A. Z., Griffin, J. H. C., Peaston, K. A., Alexander-Webber, D. G. A., and Williams, L. E. (2017). F-group bZIPs in barley-a role in Zn deficiency. *Plant Cell Environ.* 40, 2754–2770. doi: 10.1111/pce.13045

Palmer, C. M., Hindt, M. N., Schmidt, H., Clemens, S., Guerinot, M., and Lou. (2013). MYB10 and MYB72 Are Required for Growth under Iron-Limiting Conditions. *PLoS Genet.* 9:e1003953. doi: 10.1371/journal.pgen.1003953

Robinson, G. H. J., Balk, J., and Domoney, C. (2019). Improving pulse crops as a source of protein, starch and micronutrients. *Nutr. Bull.* 44, 202–215. doi: 10.1111/nbu.12399

Sinclair, S. A., and Krämer, U. (2012). The zinc homeostasis network of land plants. *Biochim. Biophys. Acta* 1823, 1553–1567. doi: 10.1016/j.bbamcr.2012.05.016

Vallee, B. L., and Auld, D. S. (1990). Active-site zinc ligands and activated H2O of zinc enzymes. *Proc. Natl. Acad. Sci. U. S. A.* 87, 220–224. doi: 10.1073/pnas.87.1.220

Vinson, C., Acharya, A., and Taparowsky, E. J. (2006). Deciphering B-ZIP transcription factor interactions *in vitro* and *in vivo*. *Biochim. Biophys. Acta* 1759, 4–12. doi: 10.1016/j.bbaexp.2005.12.005

Wessells, K. R., and Brown, K. H. (2012). Estimating the Global Prevalence of Zinc Deficiency: Results Based on Zinc Availability in National Food Supplies and the Prevalence of Stunting. *PLoS One* 7:e50568. doi: 10.1371/journal.pone.0050568

Yang, O., Popova, O. V., Süthoff, U., Lüking, I., Dietz, K.-J., and Golldack, D. (2009). The Arabidopsis basic leucine zipper transcription factor AtbZIP24 regulates complex transcriptional networks involved in abiotic stress resistance. *Gene* 436, 45–55. doi: 10.1016/j.gene.2009.02.010

Conflict of Interest: The authors declare that the research was conducted in the absence of any commercial or financial relationships that could be construed as a potential conflict of interest.

Publisher's Note: All claims expressed in this article are solely those of the authors and do not necessarily represent those of their affiliated organizations, or those of the publisher, the editors and the reviewers. Any product that may be evaluated in this article, or claim that may be made by its manufacturer, is not guaranteed or endorsed by the publisher.

frontiers | Frontiers in Plant Science

TYPE Mini Review
PUBLISHED 16 September 2022
DOI 10.3389/fpls.2022.959840

OPEN ACCESS

EDITED BY
Anja Schneider,
Ludwig Maximilian University of Munich, Germany

REVIEWED BY
Ajay Kumar Pandey,
National Agri-Food Biotechnology Institute, India
Anamika Pandey,
Selçuk University, Turkey
Jon Lucas Boatwright,
Clemson University, United States
Behrooz Darbani,
Aarhus University, Denmark

*CORRESPONDENCE
Joohyun Lee
joohyun.lee@duke.edu
Jeeyon Jeong
jjeong@amherst.edu

†These authors share senior authorship

SPECIALTY SECTION
This article was submitted to Plant Nutrition, a section of the journal Frontiers in Plant Science

RECEIVED 02 June 2022
ACCEPTED 31 August 2022
PUBLISHED 16 September 2022

CITATION
Su J, Yao Z, Wu Y, Lee J and Jeong J (2022) Minireview: Chromatin-based regulation of iron homeostasis in plants.
Front. Plant Sci. 13:959840.
doi: 10.3389/fpls.2022.959840

Minireview: Chromatin-based regulation of iron homeostasis in plants

Justin Su[1], Zhujun Yao[2], Yixuan Wu[2], Joohyun Lee[2*†] and Jeeyon Jeong[1*†]

[1]Department of Biology, Amherst College, Amherst, MA, United States, [2]Division of Natural and Applied Sciences, Duke Kunshan University, Kunshan, China

Plants utilize delicate mechanisms to effectively respond to changes in the availability of nutrients such as iron. The responses to iron status involve controlling gene expression at multiple levels. The regulation of iron deficiency response by a network of transcriptional regulators has been extensively studied and recent research has shed light on post-translational control of iron homeostasis. Although not as considerably investigated, an increasing number of studies suggest that histone modification and DNA methylation play critical roles during iron deficiency and contribute to fine-tuning iron homeostasis in plants. This review will focus on the current understanding of chromatin-based regulation on iron homeostasis in plants highlighting recent studies in Arabidopsis and rice. Understanding iron homeostasis in plants is vital, as it is not only relevant to fundamental biological questions, but also to agriculture, biofortification, and human health. A comprehensive overview of the effect and mechanism of chromatin-based regulation in response to iron status will ultimately provide critical insights in elucidating the complexities of iron homeostasis and contribute to improving iron nutrition in plants.

KEYWORDS

iron, chromatin, histone modification, DNA methylation, nutrition, epigenetics

Introduction

Plants evolved complex regulatory mechanisms to cope with changes in the environment, including nutrient availability (Secco et al., 2017). At the molecular level, plants respond to nutritional status by modulating gene expression at multiple levels through a network of transcription factors and *via* post-translational regulation. Multiple studies have also revealed that changes in chromatin state by histone modification or DNA methylation play important roles in nutrient homeostasis in plants (Secco et al., 2017; Séré and Martin, 2020).

Post-translational modification of histone and DNA methylation lead to transcriptional regulation by altering chromatin packaging and chemical properties

of the nucleosome surface, both of which influence association of DNA-binding transcriptional regulators (Berger, 2007). Emerging evidence reveals the importance of chromatin regulation in nutritional homeostasis in plants. For example, phosphate starvation-induced genes are regulated by the histone acetyltransferase GCN5 (Wang T. et al., 2019) and histone deacetylases HDA19 and HDC1 (Chen et al., 2015; Xu et al., 2020). Histone 3 lysine 4 trimethylation (H3K4me3) was also shown to regulate gene expression under phosphate deficiency (Chandrika et al., 2013a,b). In high nitrogen, increased H3K27me3 deposition, and decreased H3K4me3 and H3K36me3 contribute to the repression of the high affinity nitrate transporter gene, *AtNRT2.1* (Widiez et al., 2011). H3K27me3 also modulates *AtNRT2.1* by limiting its induction under low nitrogen (Bellegarde et al., 2018). Multiple genes involved in sulfate uptake and assimilation are direct targets of histone methylation and acetylation (Huang et al., 2019). In addition, global changes in DNA methylation were observed under phosphate starvation (Yong-Villalobos et al., 2015; Secco et al., 2017), sulfur deficiency (Huang et al., 2016), and zinc deficiency (Chen et al., 2018). Chromatin remodeling genes were differentially expressed upon zinc or iron treatment, implying chromatin-level responses to maintain mineral homeostasis (Darbani et al., 2015). Although chromatin remodeling has not been extensively studied in the context of metal homeostasis, reports increasingly suggest the involvement of histone modification and DNA methylation in regulating iron. This minireview will focus on the current knowledge of chromatin-based regulation of iron homeostasis in plants.

Iron is an essential micronutrient for plant growth and development. Iron is an indispensable cofactor in vital metabolic processes, but improperly regulated iron causes cytotoxicity by facilitating the generation of reactive oxygen species (ROS) (Halliwell and Gutteridge, 1992). Despite being abundant in the soil, iron is not readily accessible for plants, as it is highly insoluble in aerobic conditions at neutral or alkaline pH (Colombo et al., 2014). Iron's importance as an essential micronutrient with low bioavailability and its potential for toxicity necessitates a tightly regulated system of iron acquisition and regulation in plants. Understanding iron homeostasis is important to answer fundamental biological questions, but also to improve agriculture and human health.

Iron deficiency response and iron uptake

In response to iron deficiency, plants induce iron uptake mechanisms that involve reducing or chelating iron (Connorton et al., 2017; Riaz and Guerinot, 2021). Dicots acquire iron *via* a reduction-based process known as Strategy I, which involves proton efflux to the rhizosphere by proton ATPases such as AHA2 to solubilize ferric chelates (Santi et al., 2005), coumarin secretion to facilitate iron mobilization (Clemens and Weber, 2016), reduction of ferric chelates to ferrous iron by FERRIC REDUCTASE OXIDASE 2 (FRO2) (Robinson et al., 1999), and ferrous iron import into root epidermal cells by IRON-REGULATED TRANSPORTER 1 (IRT1) (Eide et al., 1996). IRT1, FRO2, and AHA2 co-localize in interactomes, which likely optimize iron uptake (Martín-Barranco et al., 2020). Grasses use a chelation-based process or Strategy II for iron uptake. When iron is limited, phytosiderophores, mugineic acid (MA) and its derivatives, are synthesized (Mori and Nishizawa, 1987; Shojima et al., 1990) and secreted into the rhizosphere by Transporter of Mugineic acid family phytosiderophores 1 (TOM1) to chelate iron (Nozoye et al., 2011). Fe^{3+}-phytosiderophore complexes are then transported into the root epidermal cells by the Yellow Stripe (YS) family transporters (Curie et al., 2001). Even though grasses are considered as Strategy II plants, Strategy I is used or its components exist in graminaceous plants (Bughio et al., 2002; Ishimaru et al., 2006; Cheng et al., 2007; Bashir et al., 2011; Li et al., 2016; Kaur et al., 2019; Wairich et al., 2019; Wang M. et al., 2019).

Regulation of iron deficiency response

Responses to iron availability are controlled from transcriptional to post-translational levels (Vélez-Bermúdez and Schmidt, 2022). In particular, the complex network of basic helix-loop-helix (bHLH) family transcription factors involved in iron deficiency response has been extensively studied (Gao et al., 2020; Schwarz and Bauer, 2020). In Arabidopsis, FER-LIKE IRON DEFICIENCY-INDUCED TRANSCRIPTION FACTOR (FIT)/bHLH29 directly regulates *IRT1*, *FRO2*, *FIT*, and other genes involved in iron uptake under iron deficiency (Colangelo and Guerinot, 2004; Jakoby et al., 2004; Yuan et al., 2005). FIT forms heterodimers with subgroup Ib bHLH transcription factors, bHLH038/39/100/101, to activate FIT-dependent gene expression (Yuan et al., 2008; Wang et al., 2013). FIT also interacts with subgroup IVa bHLHs, triggering the degradation of FIT *via* the 26S proteasome pathway (Cui et al., 2018). Alongside FIT, POPEYE (PYE)/bHLH47 is another major transcriptional regulator of iron deficiency response in Arabidopsis (Long et al., 2010). *PYE* is expressed under iron deficiency and negatively regulates its target genes, which include those involved in iron translocation, storage, and assimilation. ILR3/bHLH105 plays a dual role in iron homeostasis; depending on the heterodimer it forms, ILR3 activates *PYE* expression (Zhang J. et al., 2015) or represses PYE-target genes (Tissot et al., 2019). UPSTREAM REGULATOR OF IRT1 (URI)/bHLH121 directly or indirectly positively regulates multiple iron homeostasis genes of the bHLH network (Kim et al., 2019; Gao et al., 2020; Lei et al., 2020). URI controls nearly half of iron-regulated genes, including

both FIT-dependent and independent genes (Kim et al., 2019; Gao et al., 2020). Although *URI* expression is not iron-regulated, phosphorylation of its protein stabilizes it to form heterodimers with subgroup IVc bHLH transcription factors and activate subgroup Ib bHLH genes under iron deficiency (Kim et al., 2019). Upon iron re-supply, phosphorylated URI is targeted by the E3 ligase BRUTUS (BTS) and subjected to proteasome-mediated degradation. The IRONMAN/FE-UPTAKE-INDUCING PEPTIDE (IMA/FEP) peptides also positively regulate iron deficiency response in Arabidopsis (Grillet et al., 2018; Hirayama et al., 2018) by sequestering BTS to prevent degradation of bHLH105/bHLH115 and activate iron uptake (Li et al., 2021).

Responses to iron deficiency in grasses also utilize several bHLH transcription factors (Gao and Dubos, 2021). OsFIT/OsbHLH156 positively regulates Strategy II-related genes such as those involved in MA biosynthesis and also regulates *OsIRT1,* a Strategy I-related gene (Liang et al., 2020; Wang et al., 2020). OsIRO2 interacts with OsFIT to promote its nuclear localization and positively regulate iron uptake by OsIRT1 (Ogo et al., 2006, 2007; Liang et al., 2020; Wang et al., 2020). OsIRO3/OsbHLH63 represses iron deficiency response possibly *via* antagonizing OsIRO2 to avoid iron overload by limiting iron uptake (Zheng et al., 2010; Gao and Dubos, 2021).

Iron homeostasis and histone modification

Each nucleosome consists of an octameric complex of histones subjected to a wide range of post-translational modifications. These modifications are reversible but are controlled by many histone modifying enzymes and play key roles in regulating chromatin structure and transcription (Bannister and Kouzarides, 2011; Zhang T. et al., 2015). Multiple iron homeostasis genes in Arabidopsis have been found to be controlled by histone modifications as discussed in this section.

H3K4me3

H3K4me3, the trimethylation of histone 3 lysine 4, generally leads to gene activation (Liu et al., 2010; Xiao et al., 2016). Using a forward genetics screen in Arabidopsis, Singh et al. (2021) identified a regulator of iron deficiency response, NON-RESPONSE TO Fe-DEFICIENCY2 (NRF2). In Arabidopsis, NRF2 is known as EARLY FLOWERING8 (ELF8), which regulates *FLOWERING LOCUS C (FLC)* expression *via* H3K4me3 (He, 2009). NRF2/ELF8 belongs to the trithorax group (TrxG) methyltransferases that modify histones to activate genes *via* relaxing chromatin structure and serve as antagonistic regulators of polycomb group proteins (Schuettengruber et al., 2011).

Under iron deficiency, AtNRF2/ELF8 is required for *AtGRF11* expression as it modulates H3K4me3 levels at its transcription start site (Singh et al., 2021). While AtGRF11 does not directly interact with *AtFIT*, it acts downstream of NO to induce *AtFIT* expression in iron deficient roots (Singh et al., 2021). In the *nrf2* mutant, AtGRF11-regulated iron uptake was repressed and iron transport and storage genes were downregulated. The mutant normally induced NO under iron deficiency, suggesting that the repression of *AtGRF11* was solely responsible for the regulation of iron uptake genes (Singh et al., 2021).

H3K4me3 also likely regulates the expression of iron storage genes *AtFERRITIN1 (FER1)*, *AtFER3*, and *AtFER4* in iron sufficient seedlings (Tissot et al., 2019). At the promoter regions of these ferritin genes, activation marks such as H3K4me3 and histone 3 lysine 9 acetylation (H3K9ac) were detected in seedlings grown under iron sufficient conditions, whereas H3K27me3 was not present based on analysis of publicly available epigenome profiles (Tissot et al., 2019; Park et al., 2020).

H3K27me3

The trimethylation of histone 3 lysine 27 (H3K27me3) is typically associated with gene repression; it spreads along the chromatin, resulting in compaction and the silencing of targeted genes (Liu et al., 2010; Xiao et al., 2016). H3K27me3 is catalyzed by Polycomb Repressive Complex 2 (PRC2) (Margueron and Reinberg, 2011). CURLY LEAF (CLF) is a predominant methyltransferase of the core PRC2 complex (Chanvivattana et al., 2004; Schubert et al., 2006; Zhang et al., 2007). In Arabidopsis, H3K27me3 was found to modulate the expression of FIT-dependent genes by directly targeting their loci (Park et al., 2019). Under iron deficiency, the expression of FIT-dependent genes, such as *AtFIT, AtIRT1*, *AtFRO2*, and *AtF6'H1,* was significantly higher in *clf* than in wild type roots, and their transcript levels inversely correlated with H3K27me3 deposition on their loci (Park et al., 2019). However, expression of PYE-dependent genes was not significantly affected (Park et al., 2019). Transcriptomic analysis revealed that transcript levels of FIT-dependent genes were consistently higher in *clf* even under iron-sufficient conditions where FIT-dependent gene expression is extremely low, but the lack of the H3K27me3 mark in iron sufficient *clf* mutants was not sufficient to fully induce FIT-dependent genes when upstream iron-deficiency signals were not present. In iron-deficient conditions, the residual H3K27me3 on FIT-dependent genes may be attenuating the induction of iron acquisition genes to limit their maximum induction to prevent plants from iron-induced cytotoxicity.

H3K27me3 was also implicated to play a role in iron translocation from roots to shoots in Arabidopsis (Park et al., 2020). Iron-deficient *clf* mutants accumulated less iron in the

roots than the shoots, but *clf* seedlings still had higher levels of iron compared to wild type. This phenotype and the higher expression of iron acquisition genes in *clf* roots (Park et al., 2019) suggest that *clf* mutants may still be acquiring more iron without retention in the roots due to greater translocation (Park et al., 2020). Indeed, the expression of *AtYSL1*, which encodes an iron-NA transporter involved in supplying iron to sink tissues (Waters et al., 2006), was significantly increased in *clf* compared to wild type and *AtYSL1* was verified to be a direct target of H3K27me3 (Park et al., 2020). *AtIMA1* was also revealed to be a direct target of H3K27me3, but under iron deficiency, H3K27me3 appears to play a limited role in regulating *AtIMA1* expression (Park et al., 2020).

H4R3sme2

Shk1 binding protein 1 (SKB1) catalyzes the symmetric dimethylation of histone4 arginine3 (H4R3sme2) and regulates diverse biological processes including response to salt stress (Niu et al., 2007; Pei et al., 2007; Wang et al., 2007; Schmitz et al., 2008; Zhang et al., 2011). SKB1-mediated H4R3sme2 also affects iron homeostasis by negatively modulating the expression of Ib subgroup bHLH genes that encode FIT-interacting partners, such as *AtbHLH38/39/100/101*, in response to iron (Fan et al., 2014). While *AtSKB1* expression is not regulated by iron, the level of SKB1 association and H4R3sme2 deposition on the Ib subgroup bHLH loci positively correlated with the iron status of plants. As a result, transcript levels of the Ib subgroup *AtbHLH* genes and its downstream genes including *AtFRO2* and *AtIRT1* that are not direct targets of SKB1 were higher in *skb1* mutants than in wild type roots. Although SKB1 did not affect *AtFIT* expression, transcript levels of *AtFRO2* and *AtIRT1* were not significantly increased in the *skb1 fit1* double mutant, indicating that the negative regulation of iron acquisition genes by SKB1 was dependent on FIT (Fan et al., 2014). The mechanism by which SKB1 perceives iron levels and other environmental signals to determine the degree of H4R3sme2 in specific genes remains to be understood.

Histone acetylation

Histone acetylation is generally associated with transcriptional activation, in contrast to the more complex effects of histone methylation on gene expression (Berger, 2007). The combined action of histone acetylation and deacetylation is crucial for regulating gene expression (Grunstein, 1997). GENERAL CONTROL NON-REPRESSED PROTEIN5 (GCN5) is responsible for the acetylation of H3K14 and facilitates the acetylation of H3K9 and H3K27, which are required for the expression of a large number of genes (Vlachonasios et al., 2003; Earley et al., 2007; Benhamed et al., 2008).

Xing et al. (2015) reported that AtGCN5 contributes to iron homeostasis by modulating the expression of Arabidopsis *FERRIC REDUCTASE DETECTIVE3 (AtFRD3)*, which encodes a transporter that loads citrate into the xylem to aid translocation of iron-citrate complexes to the shoots (Durrett et al., 2007). AtGCN5 directly binds to the promoters of *AtFRD3* and other iron responsive genes to control H3K9ac and/or H3K14ac levels. In the *gcn5* mutant, iron-related phenotypes similar to those of *frd3* were observed due to significantly decreased H3K9ac and/or H3K14ac deposition at the *AtFRD3* locus and reduced expression of *AtFRD3* (Xing et al., 2015). In the mutants of two histone deacetylases, *hda7* and *hda14*, *AtFRD3* transcript level was increased, providing an example of the coordination between histone acetylation and deacetylation to precisely regulate gene expression (Xing et al., 2015).

Iron homeostasis and DNA methylation

DNA methylation controls gene expression and contributes to silencing of transposons to maintain genome stability (Law and Jacobsen, 2010; Zhang et al., 2018). In plants, methylation of cytosine occurs in symmetric methylation at CG and CHG, where H represents A, T, or C, and asymmetric methylation at CHH (Matzke and Mosher, 2014; Matzke et al., 2015). While CG and CHG methylations are maintained during DNA replication, CHH methylations are established *de novo* after DNA replication *via* RNA-dependent mechanisms and are frequently found between condensed and relaxed chromatin near highly expressed genes (Gent et al., 2013; Martin et al., 2021).

A recent report suggested that CHH DNA methylation modulates iron deficiency response in rice *via* changing methylation status of genes encoding two major positive regulators of iron deficiency response, *OsIRO2* and *OsbHLH156* (Sun et al., 2021). In this study, widespread hypermethylation, mainly CHH methylation, was detected in rice roots and shoots grown in iron deficient conditions by mapping the DNA methylome at a single-base resolution. Although little correlation was found between CHH hypermethylation and expression of iron deficiency response genes, *OsIRO2* and *OsbHLH156* exhibited CHH hypermethylation and their expression increased under iron deficiency. Furthermore, treatment of 5-aza-2-deoxycytidine (Aza), a DNA methylation inhibitor, and the loss of *OsDRM2*, a key methyltransferase responsible for CHH methylation, resulted in lower expression of *OsIRO2* and *OsbHLH156*, accumulation of less iron, and growth retardment under iron deficiency (Sun et al., 2021). It was speculated that small RNAs might play a critical role

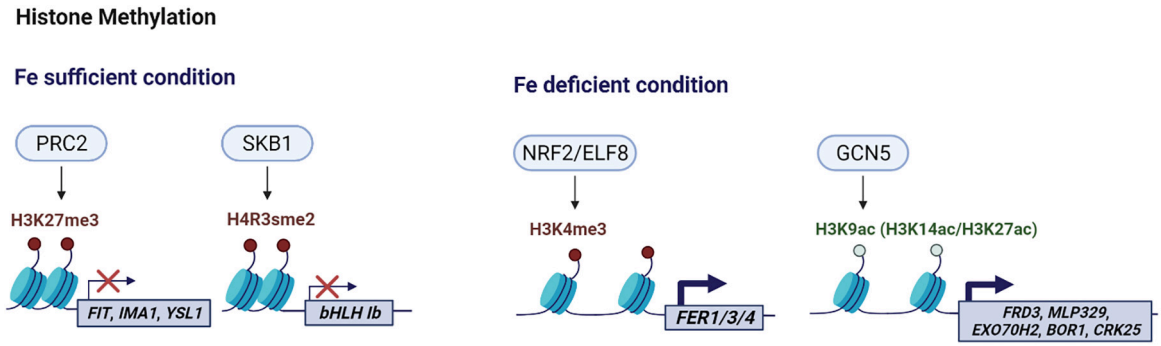

FIGURE 1
Schematic overview of histone modifications involved in iron homeostasis in Arabidopsis. Under iron sufficiency, PRC2-mediated H3K27me3 induces chromatin condensation in Arabidopsis, resulting in gene silencing of the target genes such as *AtFIT*, *AtIMA1* and *AtYSL1*. AtSKB1-induced H4R3sme2 also suppresses *AtbHLH1b* transcripts when iron is sufficient. Under iron deficiency, AtNRF2/ELF8 catalyzes the trimethylation of H3K4 generating H3K4me3, and AtGCN5 acetylates H3K9 producing H3K9ac and facilitates the generation of H3K14ac and H3K27ac to activate corresponding target genes. The color scheme denotes methylation (red), acetylation (light green), histone (light blue). This figure was created with BioRender.com.

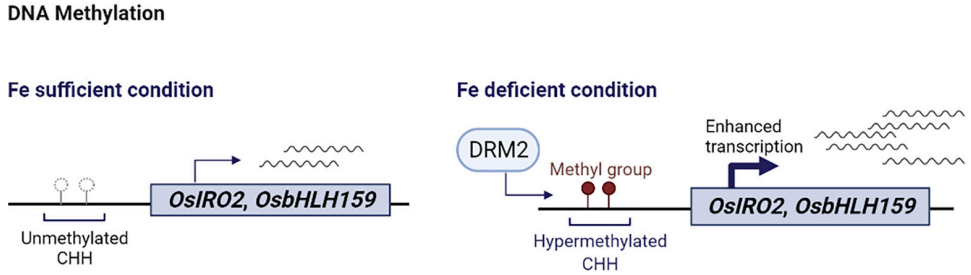

FIGURE 2
Schematic summary of DNA hypermethylation and iron deficiency response in rice. Under iron sufficient conditions, the CHH sequences of *OsIRO2* and *OsbHLH159* promoters remain unmethylated and basal levels of *OsIRO2* and *OsbHLH159* are expressed. Upon iron deficiency, hypermethylation of CHH nucleotides on the promoters of *OsIRO2* and *OsbHLH159* by DRM2 leads to activation of the expression of the corresponding downstream genes in response to iron deficiency. This figure was created with BioRender.com.

as rice acclimates to iron deficiency, as the levels of 24-nt siRNAs increased, whereas transcript levels of canonical RNA-dependent DNA methyltransferases involved in CHH methylation did not change under iron deficient conditions (Sun et al., 2021).

In barley, iron deficiency led to a general reduction of CG methylation, but the overall methylation and demethylation status was not recovered after iron resupply (Bocchini et al., 2015). Further studies are necessary to understand the extent to which DNA methylation or demethylation is maintained upon changes in iron conditions and mechanisms therein.

DNA methylation status was also proposed to be involved in feedback mechanisms between iron status and tolerance to cadmium stress (Fan et al., 2020). Arabidopsis plants exposed to cadmium stress expressed lower levels of the three DNA demethylase genes *AtROS1/DML2/DML3 (RDD)* and exhibited increased global DNA methylation that resembled the methylation profile of *rdd* triple mutants (Fan et al., 2020). The *rdd* mutants were more tolerant against cadmium stress and accumulated more iron in the shoots by expressing higher levels of iron deficiency response genes than wild type. However, inadequate iron supply abolished cadmium tolerance in *rdd* mutants (Fan et al., 2020).

Conclusion and perspectives

Increasing evidence has shown that iron homeostasis gene expression is affected by histone modification (**Figure 1**) and DNA methylation (**Figure 2**). Such chromatin-based regulation is critical during iron deficiency and allows to fine-tune iron homeostasis in plants. Given that chromatin-based regulation is a dynamic process, it will be important to understand the mechanistic details regarding changes in histone modification or DNA methylation in response to changes in iron status. Research to date has mainly focused on iron deficiency and little is known about the effect of iron overload on chromatin remodeling *via* histone modification or

DNA methylation. Global changes in H3K9me2 and H3K4me3 levels under high iron stress conditions were detected in the proximal root meristem in rice (Polosoro et al., 2019), but further studies are needed to understand the underlying mechanisms and the biological implications. Furthermore, it will be necessary to integrate large scale datasets of various histone modifications, DNA methylation, and the combinatorial effect of different modifications, as well as comparative analyses of transcriptomics and epigenetics of specific cell-types or at a single cell level. Although chromatin-based regulation is an integral part of epigenetics, some chromatin modifications are not heritable or considered epigenetic (Eichten et al., 2014). Thus, transgenerational studies to determine the heritability of chromatin modifications in response to iron will lead to insightful information. Considering the growing evidence that reveal the significance of dynamic adjustment in chromatin structure and subsequent transcriptional changes in response to nutritional status, a clear understanding of chromatin-based iron homeostasis is necessary for a comprehensive understanding of iron homeostasis. Such efforts will contribute insights toward developing crops with improved nutritional profiles and enhanced tolerance to undesirable conditions in the long run.

Author contributions

JS primarily wrote the initial draft of the manuscript. ZY and YW contributed to the manuscript writing and generated the figures. JL and JJ conceived the idea and made final edits. All authors contributed to the article and approved the submitted version.

Funding

This work was supported by the Gregory Call Student Research Fund to JS, the Interdisciplinary Seed Grant, Synear and Wang-Cai Seed Grant, and Wang-Cai Biochemistry Lab Grant to JL, and the National Science Foundation grant (IOS#1754969) and the Alex Schupf '57 Fund for Intellectual Life to JJ.

Acknowledgments

We regret that we were unable to cite all relevant literature due to restrictions in the length of this manuscript.

Conflict of interest

The authors declare that the research was conducted in the absence of any commercial or financial relationships that could be construed as a potential conflict of interest.

Publisher's note

References

Bannister, A. J., and Kouzarides, T. (2011). Regulation of chromatin by histone modifications. *Cell Res.* 21, 381–395. doi: 10.1038/cr.2011.22

Bashir, K., Ishimaru, Y., Shimo, H., Kakei, Y., Senoura, T., Takahashi, R., et al. (2011). Rice phenolics efflux transporter 2 (PEZ2) plays an important role in solubilizing apoplasmic iron. *Soil Sci. Plant Nutr.* 57, 803–812. doi: 10.1080/00380768.2011.637305

Bellegarde, F., Herbert, L., Séré, D., Caillieux, E., Boucherez, J., Fizames, C., et al. (2018). Polycomb repressive complex 2 attenuates the very high expression of the Arabidopsis gene NRT2.1. *Sci. Rep.* 8:7905. doi: 10.1038/s41598-018-26349-w

Benhamed, M., Martin-Magniette, M.-L., Taconnat, L., Bitton, F., Servet, C., De Clercq, R., et al. (2008). Genome-scale Arabidopsis promoter array identifies targets of the histone acetyltransferase GCN5. *Plant J.* 56, 493–504. doi: 10.1111/j.1365-313X.2008.03606.x

Berger, S. L. (2007). The complex language of chromatin regulation during transcription. *Nature* 447, 407–412. doi: 10.1038/nature05915

Bocchini, M., Bartucca, M. L., Ciancaleoni, S., Mimmo, T., Cesco, S., Pii, Y., et al. (2015). Iron deficiency in barley plants: Phytosiderophore release, iron translocation, and DNA methylation. *Front. Plant Sci.* 6:514. doi: 10.3389/fpls.2015.00514

Bughio, N., Yamaguchi, H., Nishizawa, N. K., Nakanishi, H., and Mori, S. (2002). Cloning an iron-regulated metal transporter from rice. *J. Exp. Bot.* 53, 1677–1682. doi: 10.1093/jxb/erf004

Chandrika, N. N. P., Sundaravelpandian, K., and Schmidt, W. (2013a). A PHD in histone language: On the role of histone methylation in plant responses to phosphate deficiency. *Plant Signal. Behav.* 8:e24381. doi: 10.4161/psb.24381

Chandrika, N. N. P., Sundaravelpandian, K., Yu, S.-M., and Schmidt, W. (2013b). ALFIN-LIKE 6 is involved in root hair elongation during phosphate deficiency in Arabidopsis. *N. Phytol.* 198, 709–720. doi: 10.1111/nph.12194

Chanvivattana, Y., Bishopp, A., Schubert, D., Stock, C., Moon, Y.-H., Sung, Z. R., et al. (2004). Interaction of Polycomb-group proteins controlling flowering in Arabidopsis. *Development* 131, 5263–5276. doi: 10.1242/dev.01400

Chen, C.-Y., Wu, K., and Schmidt, W. (2015). The histone deacetylase HDA19 controls root cell elongation and modulates a subset of phosphate starvation responses in Arabidopsis. *Sci. Rep.* 5:15708. doi: 10.1038/srep15708

Chen, X., Schï Nberger, B., Menz, J., and Ludewig, U. (2018). Plasticity of DNA methylation and gene expression under zinc deficiency in Arabidopsis roots. *Plant Cell Physiol.* 59, 1790–1802. doi: 10.1093/pcp/pcy100

Cheng, L., Wang, F., Shou, H., Huang, F., Zheng, L., He, F., et al. (2007). Mutation in nicotianamine aminotransferase stimulated the Fe(II) acquisition system and led to iron accumulation in rice. *Plant Physiol.* 145, 1647–1657. doi: 10.1104/pp.107.107912

Clemens, S., and Weber, M. (2016). The essential role of coumarin secretion for Fe acquisition from alkaline soil. *Plant Signal. Behav.* 11:e1114197. doi: 10.1080/15592324.2015.1114197

Colangelo, E. P., and Guerinot, M. L. (2004). The essential basic helix-loop-helix protein FIT1 is required for the iron deficiency response. *Plant Cell* 16, 3400–3412. doi: 10.1105/tpc.104.024315

Colombo, C., Palumbo, G., He, J.-Z., Pinton, R., and Cesco, S. (2014). Review on iron availability in soil: Interaction of Fe minerals, plants, and microbes. *J. Soils Sediments* 14, 538–548. doi: 10.1007/s11368-013-0814-z

Connorton, J. M., Balk, J., and Rodríguez-Celma, J. (2017). Iron homeostasis in plants - a brief overview. *Metallomics* 9, 813–823. doi: 10.1039/c7mt00136c

Cui, Y., Chen, C.-L., Cui, M., Zhou, W.-J., Wu, H.-L., and Ling, H.-Q. (2018). Four IVa bHLH transcription factors are novel interactors of FIT and mediate JA inhibition of iron uptake in Arabidopsis. *Mol. Plant* 11, 1166–1183. doi: 10.1016/j.molp.2018.06.005

Curie, C., Panaviene, Z., Loulergue, C., Dellaporta, S. L., Briat, J. F., and Walker, E. L. (2001). Maize yellow stripe1 encodes a membrane protein directly involved in Fe(III) uptake. *Nature* 409, 346–349. doi: 10.1038/35053080

Darbani, B., Noeparvar, S., and Borg, S. (2015). Deciphering mineral homeostasis in barley seed transfer cells at transcriptional level. *PLoS One* 10:e0141398. doi: 10.1371/journal.pone.0141398

Durrett, T. P., Gassmann, W., and Rogers, E. E. (2007). The FRD3-mediated efflux of citrate into the root vasculature is necessary for efficient iron translocation. *Plant Physiol.* 144, 197–205. doi: 10.1104/pp.107.097162

Earley, K. W., Shook, M. S., Brower-Toland, B., Hicks, L., and Pikaard, C. S. (2007). In vitro specificities of Arabidopsis co-activator histone acetyltransferases: Implications for histone hyperacetylation in gene activation. *Plant J.* 52, 615–626. doi: 10.1111/j.1365-313X.2007.03264.x

Eichten, S. R., Schmitz, R. J., and Springer, N. M. (2014). Epigenetics: Beyond chromatin modifications and complex genetic regulation. *Plant Physiol.* 165, 933–947. doi: 10.1104/pp.113.234211

Eide, D., Broderius, M., Fett, J., and Guerinot, M. L. (1996). A novel iron-regulated metal transporter from plants identified by functional expression in yeast. *Proc. Natl. Acad. Sci. U.S.A.* 93, 5624–5628. doi: 10.1073/pnas.93.11.5624

Fan, H., Zhang, Z., Wang, N., Cui, Y., Sun, H., Liu, Y., et al. (2014). SKB1/PRMT5-mediated histone H4R3 dimethylation of Ib subgroup bHLH genes negatively regulates iron homeostasis in *Arabidopsis thaliana*. *Plant J.* 77, 209–221. doi: 10.1111/tpj.12380

Fan, S. K., Ye, J. Y., Zhang, L. L., Chen, H. S., Zhang, H. H., Zhu, Y. X., et al. (2020). Inhibition of DNA demethylation enhances plant tolerance to cadmium toxicity by improving iron nutrition. *Plant Cell Environ.* 43, 275–291. doi: 10.1111/pce.13670

Gao, F., and Dubos, C. (2021). Transcriptional integration of plant responses to iron availability. *J. Exp. Bot.* 72, 2056–2070. doi: 10.1093/jxb/eraa556

Gao, F., Robe, K., Bettembourg, M., Navarro, N., Rofidal, V., Santoni, V., et al. (2020). The transcription factor bHLH121 interacts with bHLH105 (ILR3) and its closest homologs to regulate iron homeostasis in Arabidopsis. *Plant Cell* 32, 508–524. doi: 10.1105/tpc.19.00541

Gent, J. I., Ellis, N. A., Guo, L., Harkess, A. E., Yao, Y., Zhang, X., et al. (2013). CHH islands: De novo DNA methylation in near-gene chromatin regulation in maize. *Genome Res.* 23, 628–637. doi: 10.1101/gr.146985.112

Grillet, L., Lan, P., Li, W., Mokkapati, G., and Schmidt, W. (2018). IRON MAN is a ubiquitous family of peptides that control iron transport in plants. *Nat. Plants* 4, 953–963. doi: 10.1038/s41477-018-0266-y

Grunstein, M. (1997). Histone acetylation in chromatin structure and transcription. *Nature* 389, 349–352. doi: 10.1038/38664

Halliwell, B., and Gutteridge, J. M. C. (1992). Biologically relevant metal ion-dependent hydroxyl radical generation. *FEBS Lett.* 307, 108-12. doi: 10.1016/0014-5793(92)80911-y

He, Y. (2009). Control of the transition to flowering by chromatin modifications. *Mol. Plant* 2, 554–564. doi: 10.1093/mp/ssp005

Hirayama, T., Lei, G. J., Yamaji, N., Nakagawa, N., and Ma, J. F. (2018). The putative peptide gene FEP1 regulates iron deficiency response in arabidopsis. *Plant Cell Physiol.* 59, 1739–1752. doi: 10.1093/pcp/pcy145

Huang, X.-Y., Chao, D.-Y., Koprivova, A., Danku, J., Wirtz, M., Müller, S., et al. (2016). Nuclear Localised MORE SULPHUR ACCUMULATION1 epigenetically regulates sulphur homeostasis in *Arabidopsis thaliana*. *PLoS Genet.* 12:e1006298. doi: 10.1371/journal.pgen.1006298

Huang, X.-Y., Li, M., Luo, R., Zhao, F.-J., and Salt, D. E. (2019). Epigenetic regulation of sulfur homeostasis in plants. *J. Exp. Bot.* 70, 4171–4182. doi: 10.1093/jxb/erz218

Ishimaru, Y., Suzuki, M., Tsukamoto, T., Suzuki, K., Nakazono, M., Kobayashi, T., et al. (2006). Rice plants take up iron as an Fe3+-phytosiderophore and as Fe2+. *Plant J.* 45, 335–346. doi: 10.1111/j.1365-313X.2005.02624.x

Jakoby, M., Wang, H.-Y., Reidt, W., Weisshaar, B., and Bauer, P. (2004). FRU (BHLH029) is required for induction of iron mobilization genes in *Arabidopsis thaliana*. *FEBS Lett.* 577, 528–534. doi: 10.1016/j.febslet.2004.10.062

Kaur, G., Shukla, V., Kumar, A., Kaur, M., Goel, P., Singh, P., et al. (2019). Integrative analysis of hexaploid wheat roots identifies signature components during iron starvation. *J. Exp. Bot.* 70, 6141–6161. doi: 10.1093/jxb/erz358

Kim, S. A., LaCroix, I. S., Gerber, S. A., and Guerinot, M. L. (2019). The iron deficiency response in Arabidopsis thaliana requires the phosphorylated transcription factor URI. *Proc. Natl. Acad. Sci. U.S.A.* 116, 24933–24942. doi: 10.1073/pnas.1916892116

Law, J. A., and Jacobsen, S. E. (2010). Establishing, maintaining and modifying DNA methylation patterns in plants and animals. *Nat. Rev. Genet.* 11, 204–220. doi: 10.1038/nrg2719

Lei, R., Li, Y., Cai, Y., Li, C., Pu, M., Lu, C., et al. (2020). bHLH121 functions as a direct link that facilitates the activation of FIT by bHLH IVc transcription factors for maintaining fe homeostasis in Arabidopsis. *Mol. Plant* 13, 634–649. doi: 10.1016/j.molp.2020.01.006

Li, S., Zhou, X., Chen, J., and Chen, R. (2016). Is there a strategy I iron uptake mechanism in maize? *Plant Signal. Behav.* 13:e1161877. doi: 10.1080/15592324.2016.1161877

Li, Y., Lu, C. K., Li, C. Y., Lei, R. H., Pu, M. N., Zhao, J. H., et al. (2021). IRON MAN interacts with BRUTUS to maintain iron homeostasis in Arabidopsis. *Proc. Natl. Acad. Sci. U.S.A.* 118:e2109063118. doi: 10.1073/pnas.2109063118

Liang, G., Zhang, H., Li, Y., Pu, M., Yang, Y., Li, C., et al. (2020). Oryza sativa fer-like fe deficiency-induced transcription factor (OsFIT/OsbHLH156) interacts with OsIRO2 to regulate iron homeostasis. *J. Integr. Plant Biol.* 62, 668–689. doi: 10.1111/jipb.12933

Liu, C., Lu, F., Cui, X., and Cao, X. (2010). Histone methylation in higher plants. *Annu. Rev. Plant Biol.* 61, 395–420. doi: 10.1146/annurev.arplant.043008.091939

Long, T. A., Tsukagoshi, H., Busch, W., Lahner, B., Salt, D. E., and Benfey, P. N. (2010). The bHLH transcription factor POPEYE regulates response to iron deficiency in Arabidopsis roots. *Plant Cell* 22, 2219–2236. doi: 10.1105/tpc.110.074096

Margueron, R., and Reinberg, D. (2011). The Polycomb complex PRC2 and its mark in life. *Nature* 469, 343–349. doi: 10.1038/nature09784

Martin, G. T., Seymour, D. K., and Gaut, B. S. (2021). CHH Methylation Islands: A nonconserved feature of grass genomes that is positively associated with transposable elements but negatively associated with gene-body methylation. *Genome Biol. Evol.* 13:evab144. doi: 10.1093/gbe/evab144

Martín-Barranco, A., Spielmann, J., Dubeaux, G., Vert, G., and Zelazny, E. (2020). Dynamic control of the high-affinity iron uptake complex in root epidermal cells. *Plant Physiol.* 184, 1236–1250. doi: 10.1104/pp.20.00234

Matzke, M. A., and Mosher, R. A. (2014). RNA-directed DNA methylation: An epigenetic pathway of increasing complexity. *Nat. Rev. Genet.* 15, 394–408. doi: 10.1038/nrg3683

Matzke, M. A., Kanno, T., and Matzke, A. J. M. (2015). RNA-directed DNA Methylation: The evolution of a complex epigenetic pathway in flowering plants. *Annu. Rev. Plant Biol.* 66, 243–267. doi: 10.1146/annurev-arplant-043014-114633

Mori, S., and Nishizawa, N. (1987). Methionine as a dominant precursor of phytosiderophores in graminaceae plants. *Plant Cell Physiol.* 28, 1081–1092. doi: 10.1093/oxfordjournals.pcp.a077388

Niu, L., Lu, F., Pei, Y., Liu, C., and Cao, X. (2007). Regulation of flowering time by the protein arginine methyltransferase AtPRMT10. *EMBO Rep.* 8, 1190–1195. doi: 10.1038/sj.embor.7401111

Nozoye, T., Nagasaka, S., Kobayashi, T., Takahashi, M., Sato, Y., Sato, Y., et al. (2011). Phytosiderophore efflux transporters are crucial for iron acquisition in graminaceous plants. *J. Biol. Chem.* 286, 5446–5454. doi: 10.1074/jbc.M110.180026

Ogo, Y., Itai, R. N., Nakanishi, H., Inoue, H., Kobayashi, T., Suzuki, M., et al. (2006). Isolation and characterization of IRO2, a novel iron-regulated bHLH transcription factor in graminaceous plants. *J. Exp. Bot.* 57, 2867–2878. doi: 10.1093/jxb/erl054

Ogo, Y., Itai, R. N., Nakanishi, H., Kobayashi, T., Takahashi, M., Mori, S., et al. (2007). The rice bHLH protein OsIRO2 is an essential regulator of the genes involved in Fe uptake under Fe-deficient conditions. *Plant J.* 51, 366–377. doi: 10.1111/j.1365-313X.2007.03149.x

Park, E. Y., Tsuyuki, K. M., Hu, F., Lee, J., and Jeong, J. (2019). PRC2-Mediated H3K27me3 contributes to transcriptional regulation of FIT-dependent iron deficiency response. *Front. Plant Sci.* 10:627. doi: 10.3389/fpls.2019.00627

Park, E. Y., Tsuyuki, K. M., Parsons, E. M., and Jeong, J. (2020). PRC2-mediated H3K27me3 modulates shoot iron homeostasis in *Arabidopsis thaliana*. *Plant Signal. Behav.* 15:1784549. doi: 10.1080/15592324.2020.1784549.

Pei, Y., Niu, L., Lu, F., Liu, C., Zhai, J., Kong, X., et al. (2007). Mutations in the type II protein arginine methyltransferase AtPRMT5 result in pleiotropic developmental defects in Arabidopsis. *Plant Physiol.* 144, 1913–1923. doi: 10.1104/pp.107.099531

Polosoro, A., Enggarini, W., and Ohmido, N. (2019). Global epigenetic changes of histone modification under environmental stresses in rice root. *Chromosome Res.* 27, 287–298. doi: 10.1007/s10577-019-09611-3

Riaz, N., and Guerinot, M. L. (2021). All together now: Regulation of the iron deficiency response. *J. Exp. Bot.* 72, 2045–2055. doi: 10.1093/jxb/erab003

Robinson, N. J., Procter, C. M., Connolly, E. L., and Guerinot, M. L. (1999). A ferric-chelate reductase for iron uptake from soils. *Nature* 397, 694–697. doi: 10.1038/17800

Santi, S., Cesco, S., Varanini, Z., and Pinton, R. (2005). Two plasma membrane H(+)-ATPase genes are differentially expressed in iron-deficient cucumber plants. *Plant Physiol. Biochem.* 43, 287–292. doi: 10.1016/j.plaphy.2005.02.007

Schmitz, R. J., Sung, S., and Amasino, R. M. (2008). Histone arginine methylation is required for vernalization-induced epigenetic silencing of FLC in winter-annual *Arabidopsis thaliana*. *Proc. Natl. Acad. Sci. U.S.A.* 105, 411–416. doi: 10.1073/pnas.0710423104

Schubert, D., Primavesi, L., Bishopp, A., Roberts, G., Doonan, J., Jenuwein, T., et al. (2006). Silencing by plant Polycomb-group genes requires dispersed trimethylation of histone H3 at lysine 27. *EMBO J.* 25, 4638–4649. doi: 10.1038/sj.emboj.7601311

Schuettengruber, B., Martinez, A.-M., Iovino, N., and Cavalli, G. (2011). Trithorax group proteins: Switching genes on and keeping them active. *Nat. Rev. Mol. Cell Biol.* 12, 799–814. doi: 10.1038/nrm3230

Schwarz, B., and Bauer, P. (2020). FIT, a regulatory hub for iron deficiency and stress signaling in roots, and FIT-dependent and -independent gene signatures. *J. Exp. Bot.* 71, 1694–1705. doi: 10.1093/jxb/eraa012

Secco, D., Whelan, J., Rouached, H., and Lister, R. (2017). Nutrient stress-induced chromatin changes in plants. *Curr. Opin. Plant Biol.* 39, 1–7. doi: 10.1016/j.pbi.2017.04.001

Séré, D., and Martin, A. (2020). Epigenetic regulation: Another layer in plant nutrition. *Plant Signal. Behav.* 15:1686236. doi: 10.1080/15592324.2019.1686236

Shojima, S., Nishizawa, N. K., Fushiya, S., Nozoe, S., Irifune, T., and Mori, S. (1990). Biosynthesis of phytosiderophores : In vitro biosynthesis of 2'-deoxymugineic acid from l-methionine and nicotianamine. *Plant Physiol.* 93, 1497–1503. doi: 10.1104/pp.93.4.1497

Singh, S., Kailasam, S., Lo, J.-C., and Yeh, K.-C. (2021). Histone H3 lysine4 trimethylation-regulated *GRF11* expression is essential for the iron-deficiency response in *Arabidopsis thaliana*. *N. Phytol.* 230, 244–258. doi: 10.1111/nph.17130

Sun, S., Zhu, J., Guo, R., Whelan, J., and Shou, H. (2021). DNA methylation is involved in acclimation to iron-deficiency in rice (Oryza sativa). *Plant J.* 107, 727–739. doi: 10.1111/tpj.15318

Tissot, N., Robe, K., Gao, F., Grant-Grant, S., Boucherez, J., Bellegarde, F., et al. (2019). Transcriptional integration of the responses to iron availability in Arabidopsis by the bHLH factor ILR3. *N. Phytol.* 223, 1433–1446. doi: 10.1111/nph.15753

Vélez-Bermúdez, I. C., and Schmidt, W. (2022). How plants recalibrate cellular iron homeostasis. *Plant Cell Physiol.* 63, 154–162. doi: 10.1093/pcp/pcab166

Vlachonasios, K. E., Thomashow, M. F., and Triezenberg, S. J. (2003). Disruption mutations of ADA2b and GCN5 transcriptional adaptor genes dramatically affect Arabidopsis growth, development, and gene expression. *Plant Cell* 15, 626–638. doi: 10.1105/tpc.007922

Wairich, A., de Oliveira, B. H. N., Arend, E. B., Duarte, G. L., Ponte, L. R., Sperotto, R. A., et al. (2019). The combined strategy for iron uptake is not exclusive to domesticated rice (Oryza sativa). *Sci. Rep.* 9:16144. doi: 10.1038/s41598-019-52502-0

Wang, M., Kawakami, Y., and Bhullar, N. K. (2019). Molecular analysis of iron deficiency response in hexaploid wheat. *Front. Sustain. Food Syst.* 3:67. doi: 10.3389/fsufs.2019.00067

Wang, N., Cui, Y., Liu, Y., Fan, H., Du, J., Huang, Z., et al. (2013). Requirement and functional redundancy of Ib subgroup bHLH proteins for iron deficiency responses and uptake in *Arabidopsis thaliana*. *Mol. Plant* 6, 503–513. doi: 10.1093/mp/sss089

Wang, S., Li, L., Ying, Y., Wang, J., Shao, J. F., Yamaji, N., et al. (2020). A transcription factor OsbHLH156 regulates strategy II iron acquisition through localising IRO2 to the nucleus in rice. *N. Phytol.* 225, 1247–1260. doi: 10.1111/nph.16232

Wang, T., Xing, J., Liu, Z., Zheng, M., Yao, Y., Hu, Z., et al. (2019). Histone acetyltransferase GCN5-mediated regulation of long non-coding RNA At4 contributes to phosphate starvation response in Arabidopsis. *J. Exp. Bot.* 70, 6337–6348. doi: 10.1093/jxb/erz359

Wang, X., Zhang, Y., Ma, Q., Zhang, Z., Xue, Y., Bao, S., et al. (2007). SKB1-mediated symmetric dimethylation of histone H4R3 controls flowering time in Arabidopsis. *EMBO J.* 26, 1934–1941. doi: 10.1038/sj.emboj.7601647

Waters, B. M., Chu, H.-H., Didonato, R. J., Roberts, L. A., Eisley, R. B., Lahner, B., et al. (2006). Mutations in Arabidopsis yellow stripe-like1 and yellow stripe-like3 reveal their roles in metal ion homeostasis and loading of metal ions in seeds. *Plant Physiol.* 141, 1446–1458. doi: 10.1104/pp.106.082586

Widiez, T., El Kafafi, E. S., Girin, T., Berr, A., Ruffel, S., Krouk, G., et al. (2011). High nitrogen insensitive 9 (HNI9)-mediated systemic repression of root NO3- uptake is associated with changes in histone methylation. *Proc. Natl. Acad. Sci. U.S.A.* 108, 13329–13334. doi: 10.1073/pnas.1017863108

Xiao, J., Lee, U.-S., and Wagner, D. (2016). Tug of war: Adding and removing histone lysine methylation in Arabidopsis. *Curr. Opin. Plant Biol.* 34, 41–53. doi: 10.1016/j.pbi.2016.08.002

Xing, J., Wang, T., Liu, Z., Xu, J., Yao, Y., Hu, Z., et al. (2015). General control nonrepressed protein5-mediated histone acetylation of ferric reductase defective3 contributes to iron homeostasis in Arabidopsis. *Plant Physiol.* 168, 1309–1320. doi: 10.1104/pp.15.00397

Xu, J. M., Wang, Z. Q., Wang, J. Y., Li, P. F., Jin, J. F., Chen, W. W., et al. (2020). Low phosphate represses histone deacetylase complex1 to regulate root system architecture remodeling in Arabidopsis. *N. Phytol.* 225, 1732–1745. doi: 10.1111/nph.16264

Yong-Villalobos, L., González-Morales, S. I., Wrobel, K., Gutiérrez-Alanis, D., Cervantes-Peréz, S. A., Hayano-Kanashiro, C., et al. (2015). Methylome analysis reveals an important role for epigenetic changes in the regulation of the Arabidopsis response to phosphate starvation. *Proc. Natl. Acad. Sci. U.S.A.* 112, E7293–E7302. doi: 10.1073/pnas.1522301112

Yuan, Y. X., Zhang, J., Wang, D. W., and Ling, H. Q. (2005). AtbHLH29 of *Arabidopsis thaliana* is a functional ortholog of tomato FER involved in controlling iron acquisition in strategy I plants. *Cell Res.* 15, 613–621. doi: 10.1038/sj.cr.7290331

Yuan, Y., Wu, H., Wang, N., Li, J., Zhao, W., Du, J., et al. (2008). FIT interacts with AtbHLH38 and AtbHLH39 in regulating iron uptake gene expression for iron homeostasis in Arabidopsis. *Cell Res.* 18, 385–397. doi: 10.1038/cr.2008.26

Zhang, H., Lang, Z., and Zhu, J.-K. (2018). Dynamics and function of DNA methylation in plants. *Nat. Rev. Mol. Cell Biol.* 19, 489–506. doi: 10.1038/s41580-018-0016-z

Zhang, J., Liu, B., Li, M., Feng, D., Jin, H., Wang, P., et al. (2015). The bHLH transcription factor bHLH104 interacts with IAA-LEUCINE RESISTANT3 and modulates iron homeostasis in Arabidopsis. *Plant Cell* 27, 787–805. doi: 10.1105/tpc.114.132704

Zhang, T., Cooper, S., and Brockdorff, N. (2015). The interplay of histone modifications - writers that read. *EMBO Rep.* 16, 1467–1481. doi: 10.15252/embr.201540945

Zhang, X., Clarenz, O., Cokus, S., Bernatavichute, Y. V., Pellegrini, M., Goodrich, J., et al. (2007). Whole-genome analysis of histone H3 lysine 27 trimethylation in Arabidopsis. *PLoS Biol.* 5:e129. doi: 10.1371/journal.pbio.0050129

Zhang, Z., Zhang, S., Zhang, Y., Wang, X., Li, D., Li, Q., et al. (2011). Arabidopsis floral initiator SKB1 confers high salt tolerance by regulating transcription and pre-mRNA splicing through altering histone H4R3 and small nuclear ribonucleoprotein LSM4 methylation. *Plant Cell* 23, 396–411. doi: 10.1105/tpc.110.081356

Zheng, L., Ying, Y., Wang, L., Wang, F., Whelan, J., and Shou, H. (2010). Identification of a novel iron regulated basic helix-loop-helix protein involved in Fe homeostasis in *Oryza sativa*. *BMC Plant Biol.* 10:166. doi: 10.1186/1471-2229-10-166

frontiers | Frontiers in Plant Science

TYPE Original Research
PUBLISHED 19 December 2022
DOI 10.3389/fpls.2022.1007300

OPEN ACCESS

EDITED BY
Anja Schneider,
Ludwig Maximilian University of Munich, Germany

REVIEWED BY
Miguel A Pineros,
Robert W. Holley Center for Agriculture and Health, (USDA), United States
Jeeyon Jeong,
Amherst College, United States

*CORRESPONDENCE
Xinli Sun
xinlisun@hotmail.com

SPECIALTY SECTION
This article was submitted to Plant Nutrition, a section of the journal Frontiers in Plant Science

RECEIVED 30 July 2022
ACCEPTED 01 December 2022
PUBLISHED 19 December 2022

CITATION
Yang X, Xie H, Weng Q, Liang K, Zheng X, Guo Y and Sun X (2022) Rice OsCASP1 orchestrates Casparian strip formation and suberin deposition in small lateral roots to maintain nutrient homeostasis.
Front. Plant Sci. 13:1007300.
doi: 10.3389/fpls.2022.1007300

Rice OsCASP1 orchestrates Casparian strip formation and suberin deposition in small lateral roots to maintain nutrient homeostasis

Xianfeng Yang, Huifang Xie, Qunqing Weng, Kangjing Liang, Xiujuan Zheng, Yuchun Guo and Xinli Sun*

Key Laboratory of Ministry of Education for Genetics, Breeding and Multiple Utilization of Crops, College of Agriculture, Fujian Agriculture and Forestry University, Fuzhou, China

Arabidopsis Casparian strip membrane domain proteins (CASPs) form a transmembrane scaffold to recruit lignin biosynthetic enzymes for Casparian strip (CS) formation. Rice is a semi-aquatic plant with a more complex root structure than *Arabidopsis* to adapt its growing conditions, where the different deposition of lignin and suberin is crucial for adaptive responses. Here, we observed the structure of rice primary and small lateral roots (SLRs), particularly the deposition patterns of lignin and suberin in wild type and *Oscasp1 mutants*. We found that the appearance time and structure of CS in the roots of rice are different from those of *Arabidopsis* and observed suberin deposition in the sclerenchyma in wild type roots. Rice CASP1 is highly similar to AtCASPs, but its expression is concentrated in SLR tips and can be induced by salt stress especially in the steles. The loss of OsCASP1 function alters the expression of the genes involved in suberin biosynthesis and the deposition of suberin in the endodermis and sclerenchyma and leads to delayed CS formation and uneven lignin deposition in SLRs. These different depositions may alter nutrient uptake, resulting in ion imbalance in plant, withered leaves, fewer tillers, and reduced tolerance to salt stress. Our findings suggest that OsCASP1 could play an important role in nutrient homeostasis and adaptation to the growth environment.

KEYWORDS

CASP, exodermis, endodermis, sclerenchyma, leaf senescence, ion, salt stress

Introduction

Plant roots acquire nutrients from soil and transport them across all external cell layers into the central vasculature and then upward to the aerial parts. Water and nutrients move radially into the stele through a combination of three pathways. The first is the apoplastic pathway, where solutes diffuse in free spaces and cell walls of the

epidermis and cortex, which can be completely blocked by Casparian strips (CS) (Barberon and Geldner, 2014; Doblas et al., 2017a; Barberon, 2017). The second is the symplastic pathway involving cell-to-cell transport *via* plasmodesmata, and the third is the coupled transcellular pathway, where polarized influx and efflux carriers transport solutes in a vectorial fashion (Barberon and Geldner, 2014; Doblas et al., 2017a; Barberon, 2017). The solutes obstructed by CS are transported into endodermal cells by relevant influx carriers and then move into the stele *via* efflux carriers and/or plasmodesmata. Suberin lamellae do not block apoplastic transport but rather limit transcellular transport of nutrients (Doblas et al., 2017a), which coat the entire endodermal cell surface between the plasma membrane and secondary cell wall and isolate the solute from carriers (Robbins II et al., 2014).

CS formation is initiated at Casparian strip domain proteins (CASPs) at the Casparian strip membrane domain (CSD) in *Arabidopsis*. LORD OF THE RINGS 1 (LOTR1), a putative extracellular protease, is a crucial regulator in CSD positioning (Kolbeck et al., 2022). AtCASPs form a scaffold or a stable matrix at CSD for the subsequent lignification machinery (Roppolo et al., 2011; Lee et al., 2013). The transcription factor MYB36 controls the expression of the main genes involved in CS establishment, and AtCASPs recruit secreted proteins to the CSD, such as ENHANCED SUBERIN 1 (ESB1), Peroxidase 64 (PER64), and RESPIRATORY BURST OXIDASE HOMOLOG F (RbohF), to form localized lignin depositions (Doblas, Geldner and Barberon, 2017). SCHENGEN3/GASSHO1 (SGN3/GSO1) and SGN1 modulate the fusion of the CS into a continuous ring, which is constantly checked by two small peptides (Casparian strip integrity factor 1/2, CIF1/2) produced in the vasculature that diffuse into the apoplastic space in order to test endodermal barrier integrity (Nakayama et al., 2017; Wang P. et al., 2019). A similar mechanism of CS formation was uncovered in tomato (Li et al., 2018). Three OsMYB36 members redundantly regulate multiple genes implicated in CS formation at the root endodermis (Wang Z. et al., 2022). Maize Salt-Tolerant Locus 1 (*ZmSTL1*) encodes a dirigent protein localized at the CSD, and its mutation impairs lignin deposition at endodermal CS domain which leads to a defective CS barrier (Wang Y. et al., 2022).

Endodermal suberin plays crucial roles in plant nutrition by forming barriers for the free diffusion of water and nutrients. Deposition of suberin requires biosynthesis of aliphatic, phenolic and glycerol monomers, and transportation to the cell wall to form an insoluble macromolecular assembly (Woolfson et al., 2022). Those *Arabidopsis* genes involved in and regulating suberin biosynthesis were summarized in Table S1. Arabidopsis 3-ketoacyl-CoA synthase 2 (AtKCS2) and AtKCS20 is responsible for the production of long-chain fatty acids (Lee et al., 2009), CYTOCHROME P450, FAMILY 86, SUBFAMILY A1 (CYP86A1) and CYP86B1 are required for ω-hydroxy acid biosynthesis (Hofer et al., 2008; Compagnon et al., 2009), Fatty acyl-coenzyme A reductase 1 (FAR1), FAR4, and FAR5 are involved in the production of different chain-length primary fatty alcohols (Domergue et al., 2010), GLYCEROL-3-PHOSPHATE ACYLTRANSFERASE 5 (GPAT5) is involved in the synthesis of monoacylglycerol esters (Beisson et al., 2007), and ALIPHATIC SUBERIN FERULOYL TRANSFERASE (ASFT), ATP binding cassette transporter subfamily G2 (ABCG2), AtABCG6, and AtABCG20 transfer from feruloyl-CoA to ω-hydroxy acids and fatty alcohols (Molina et al., 2009; Yadav et al., 2014). Several Myb transcription factors, including *Myb41, Myb53, Myb92*, *Myb93*, and *Myb39*, have been identified to regulate suberin deposition by modulating the expression of suberin biosynthetic genes (Kosma et al., 2014; Wang C. et al., 2020; Shukla et al., 2021). Several homologous genes in potato (*Solanum tuberosum*) show similar functions to that in *Arabidopsis* (Woolfson et al., 2022). The rice transporter REDUCED CULM NUMBER1 (RCN1/OsABCG5) is involved in the suberization of the hypodermis/exodermis of rice roots (Shiono et al., 2014). In addition, suberization of endodermal cells responds to a wide range of nutrient stresses, is induced by ABA, and is depressed by ethylene (Barberon et al., 2016).

CS formation and suberin deposition are interrelated. The CS defective mutants, excluding *sgn3*, show ectopic suberin deposition in *Arabidopsis* and usually alter the ion permeability and sensitivity to salt and drought stress (Doblas et al, 2017a; Barberon, 2017). These ectopic endodermal lignification and suberization could act as compensation and are triggered through the endodermal integrity control system consisting of SGN3 and CIF1/2 (Doblas et al., 2017b; Fujita et al., 2020; Okuda et al., 2020). CIF1/2 and ABA treatment enhances the expression of *Myb41, Myb53, Myb92*, and *Myb93*, and ABA and SGN3/CIFs pathways can induce ectopic endodermal suberization by regulating the expression of these *Myb* genes (Wang C. et al., 2020).

There are 5 CASPs and 34 CASP-likes (CASPLs) in *Arabidopsis*, and CASPLs should have a conserved module for membrane subdomain formation and are expressed in a tissue-specific manner. At least twelve AtCASPLs are able to reach the plasma membrane under the control of the AtCASP1 promoter, and nine of these are clearly located at the CSD just like AtCASPs. These results address different cell wall-modifying machineries in different tissues (Roppolo et al., 2014). However, the positions in the cell of the other CASPLs are less known. *AtCASPL4C1* knock-out plants shows earlier flowering compared to wild type and overexpressing *CICASPL* (The ortholog of *AtCASPL4C1* in *Citrullus lanatus*) results in increased sensitivity to cold stress in *Arabidopsis* (Yang et al., 2015). There are 6 OsCASPs and 28 OsCASPLs in rice (Figure S1), and the function of OsCASP1 has recently been studied, which indicates that OsCASP1 is required for CS formation in endodermal cells (Wang Z. et al., 2019). OsCASP1 can form complexes with itself and OsCASP2, which leads to ectopic protein accumulation in rice cell under control of the 35S promoter (Wang Z. et al., 2020). The rice root system is more

complex than that of *Arabidopsis*, and its radial structure includes the epidermis, exodermis, sclerenchyma, midcortex, endodermis, and stele from the outside inward (Rebouillat et al., 2009). There is no CS of the exodermis, sclerenchyma, and aerenchyma in *Arabidopsis* root (Rebouillat et al., 2009; Robbins II at al., 2014). These specified tissues could allow rice to adapt to its growth condition.

Here we report the discovery of a novel mutant, which exhibits withered leaf phenotype and fewer tillers comparing to the wild type. We discovered that the loss of OsCASP1 function results in the mutant phenotype using map-based cloning. OsCASP1 shows high sequence similarity to AtCASPs (Figure S1), is highly upregulated at small lateral root tips (SLRs), and is strongly expressed in roots, especially in the stele and sclerenchyma, after salt treatment. The loss of OsCASP1 function leads to delayed CS formation and ectopic suberin deposition in SLRs and alters ion balance in plants.

Materials and methods

Constructions for the complementation test and tissue-specific expression

Recombinant plasmids were constructed using the In-Fusion cloning kit (Takara). To generate *OsCASP1pro:OsCASP1*, the *OsCASP1* promoter (1128 bp upstream of the *OsCASP1* gene including the whole intergenic sequence between *Os04g0684200* and *OsCASP1*) and gene was amplified, and the PCR product was recombined into pCAMBIA-1300 digested with Hind III with the In-Fusion cloning kit. To generate *OsCASP1pro:OsCASP1-GUS*, the *OsCASP1* promoter and gene was amplified and recombined into pCXGUS-P digested with Xcm I, respectively. The details of these constructs are shown in Figure S2, and the primers used in this study were shown in Table S2.

To perform the complementation experiment, some seeds were first collected from a few F2 individuals, which exhibited a mutant phenotype and a Nipponbare-like morphology, from a cross between the *Oscasp1-3* mutant and Nipponbare; the construct of *OsCASP1pro:OsCASP1* was transformed into the calli from these seeds; and the transgenic plants with the construct were observed and examined using PCR. The construct of *OsCASP1pro:OsCASP1-GUS* was transformed into Zhonghua 11 (ZH11).

Plant materials and growth conditions

In the study, three *Oscasp1* mutants were used. The first is *Oscasp1-3*, a natural mutant in a paddy field, which is derived from a high generation progeny of Jinhui2629 and TR-2 with an *indica* genetic background. The second is *Oscasp1-4*, a CRISPR/Cas9 mutant, which was generated by the Biogle Company. The CRISPR target sequence was localized to exon 1 of the *OsCASP1* gene. Sixteen mutant lines were obtained, but only one line (*Oscasp1-4*) survived. The third is *Oscasp1-1* with a Nipponbare background (Wang Z. et al., 2019), which was kindly provided by Dr. Jixing Xia (Guangxi University, Nanning, China).

Rice plants were grown under two different conditions: soil and hydroponics. For soil experiments, the F_2 and F_3 populations of the cross of the *Oscasp1-3* mutant and Nipponbare were grown in the experimental paddy field in Putian, Fujian province. For hydroponic experiments, rice seeds were soaked in a dark incubator (28°C) for 48h. After germination, seeds were grown in 1×Kimura B nutrient (Table S2) under a photoperiod of 28°C/14 h of light and 28°C/10 h of darkness. The seedlings were grown in a growth cabinet in the nutrient solution to test the sensitivity of the plants to nutrient deficiency.

DNA and protein sequence analysis

The new molecular markers were designed according to the Nipponbare sequence, and the CASP and CASP-like proteins in rice were obtained by searching the RAP-DB database with the BlastP programmes. The Molecular Evolutionary Genetic Analysis programme (MEGA X) was used to generate phylogenetic trees using the maximum likelihood method and JTT matrix-based model (Kumar et al., 2018).

Histochemical staining

Roots of 5~12-d-old seedling were used for the study, and freehand cross-sections were cut at different regions. To observe the Casparian strip, root cross-sections were stained with 0.1% (w/v) berberine chloride (Sangon) and 0.5% (w/v) aniline blue (Sangon) as described by Brundrett et al. (Brundrett et al., 1988). Casparian strips were visualized as bright white/yellow fluorescence (UV filter set) under Nikon (MODEL ECLIPSE Ni-U) microscope. To visualize lignin with cinnamyl aldehyde groups in the roots, cross-sections were stained for 30 min with 1% phloroglucinol (Sangon) in 20% (w/v) hydrochloric acid at room temperature and observed using a Nikon microscope (MODEL ECLIPSE Ni-U). Lignin appears orange/red under white light (Pradhan Mitra and Loque, 2014; Shiono et al., 2014). Suberin deposition in the root was visualized with Fluorol Yellow 088 (ACMEC) as described by Barberon et al. (Barberon et al., 2016). Lignin in SLR was visualized with Basic Fuchsin (Sangon) or Auramine O (Sangon) in ClearSee solution as described by Urache et al. (Ursache et al., 2018). The excitation wavelength of FY088 and Auramine O is 488 nm, and the emission fluorescence was detected at 516-593 nm. The excitation wavelength of Basic Fuchsin is 561 nm, and the emission fluorescence was detected at 600-650 nm. Suberin or

lignin deposition in roots was observed with the Leica TCS SP8 laser scanning confocal microscope.

Electron microscopy

The endodermis was visualized using root sections collected 10 mm and 20 mm from the root tips in 17-d-old seedlings. Transmission electron microscopy (TEM) was conducted using a previously described protocol (Hulskamp et al., 2010). Samples were observed using the Hitachi HT-7800 transmission electron microscope operating at 20-120 kV.

Permeability test

For the propidium iodide (488 nm excitation, 500-550 nm emission) (Sangon) penetration assay, the roots of 5~7-d-old seedlings were incubated in a fresh solution of 10 μg/ml, 50μg/ml, or 100μg/ml propidium iodide for the indicated time in the dark, and then rinsed twice in water. Ater staining, freehand sections or small lateral roots were then observed with the Leica TCS SP8 confocal laser-scanning microscope (Naseer et al., 2012). To quantify PI penetration, SLRs with similar diameter were selected in the middle region of the primary roots of 12-d-old seedling for observation.

Elemental analysis

The leaves in the tillering period were collected and used for elemental analysis, among which the *Oscasp1-3* mutant showed a few cell death dots. The tissues were completely dried in an oven, and the samples were treated as described by Hosmani et al. (2013) (Hosmani et al., 2013; Wang Z. et al., 2019). Elemental analysis was performed on a CIC-260 ion chromatograph (K, Na, Mg, and Ca) and ICP-MS (Cd, As, Mo, Fe, and Mn), and nine elements were monitored.

Results

Identification of the mutant with withered leaves and few tillers

The mutant was discovered in a paddy field, came from a high generation progeny of Jinhui2629 and TR-2, and showed withered leaf phenotype and few tillers. The mutant and wild type (WT) used in the study showed stable inheritance. The mutant phenotype appears at the beginning of the tillering stage. Cell death usually begins at the blade tip or upper part of the leaf and then extends to the entire leaf as it grows. The mutant exhibits fewer tillers and shorter internodes at the adult stage relative to the WT (Figures 1A–C and Figures S3A–D).

To reveal the genetic basis of the mutant, we performed a cross between the mutant and Nipponbare and investigated 426 individual plants from the F_2 population. Genetic analysis showed that a single recessive gene controls the mutant phenotype. We mapped the locus of interest on chromosome 4 and delimited it to a region of approximately 265-kb between the insertion-deletion (Indel) molecular markers ID4-3 and ID4-10. To further fine-map the mutant gene, we selected several F_2 individual plants with a heterozygous genotype in the candidate region to establish the F_3 population. The locus of interest was narrowed down to an 11.3-kb region between ID4-371 and ID4-3-8 using Indel markers, which contained two genes - *Os04g0684200* and *Os04g0684300* (Figure S3E). We sequenced the two genes and found a 15-bp deletion in the coding region of the *Os04g0684300* gene and no mutation in the *Os04g0684200* gene in the mutant (Figure 1D). *Os04g0684300* encodes a Casparian strip membrane domain protein1 (CASP1), and the mutation of *Os04g0684300* could cause withered leaves and few tillers.

To further validate CASP1 function, we performed genetic complementation by introducing the *OsCASP1* gene with its promoter into the calli from F_3 seeds, which arose from a few individuals that exhibited mutant and Nipponbare-like phenotypes from the F_2 population. We found that all transgenic lines carrying the *OsCASP1* gene have a restored WT phenotype (Figures 1E, F), which confirmed that OsCASP1 regulates the leaf senescence and tiller development. We therefore named the mutant *Oscasp1-3*.

We also generated transgenic plants with knockout *OsCASP1* gene using CRISPR/Cas9 technology. Most transgenic plants with the homozygous genotype exhibited obvious withered leaf phenotype, sterility, or eventual death (Figure S4), with only one line (*Oscasp1-4*) surviving at the end (Figure S4C). Some of transgenic lines with the heterozygous genotype also exhibited mutant phenotype, while further analysis showed that both alleles at the *OsCASP1* locus contain mutant sites (Figure S4A). These results suggest that the mutation of *OsCASP1* gene leads to the mutant phenotype.

Pattern and induction of *OsCASP1* gene expression

Arabidopsis CASPs were thought to control the formation of CS, and they are specially expressed at CS domain in roots. To further reveal the function of OsCASP1, we examined GUS activation in transgenic lines carrying *OsCASP1pro:OsCASP1-GUS* to reveal tissue-specific expression of *OsCASP1* and observed an intense blue color at the tips of SLRs, but not all tips of SLRs (Figure 2A). Salt stress strongly induced *OsCASP1* expression in roots and leaves (Figures 2B, C, and S5). We examined the cross and longitudinal sections of primary root

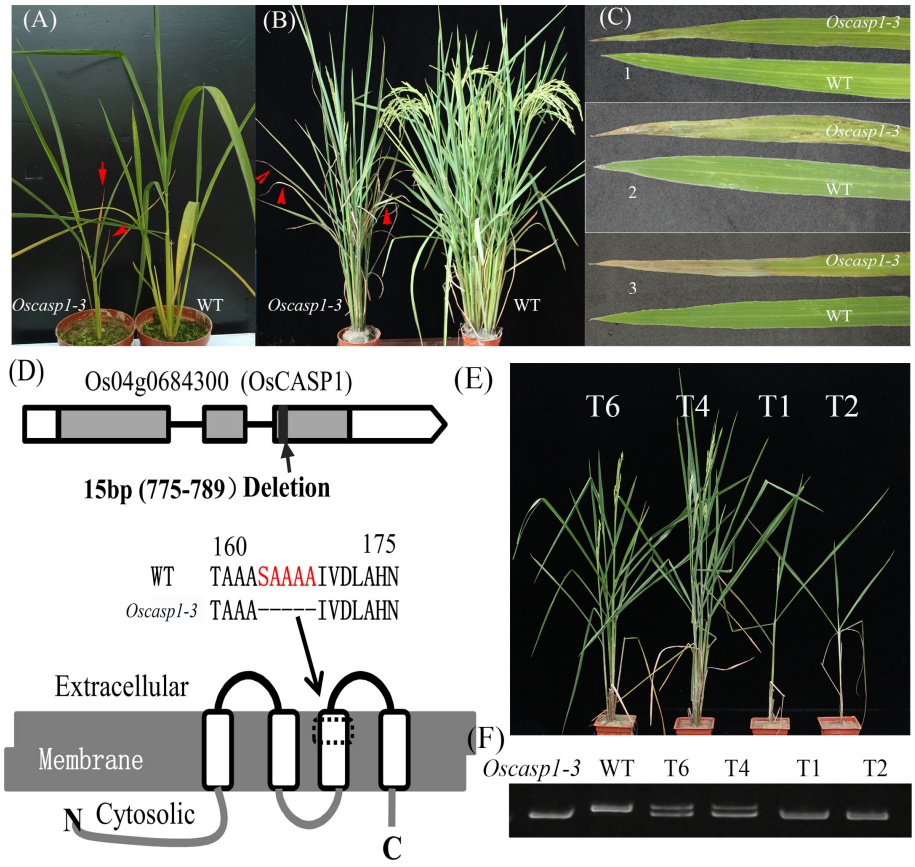

FIGURE 1
The phenotypes of the wild type and *Oscasp1-3* mutant and characterization of *Oscasp1-3*. **(A)** Seedlings of wild type and *Oscasp1-3* mutant plants. **(B)** The phenotypes of wild type and *Oscasp1-3* mutant plants at the heading stage. Red arrows indicate leaves with necrosis. **(C)** Phenotype of the leaves. 1, 2, and 3 indicate the relative positions from top to bottom. **(D)** The structure of OsCASP1 and deletion region in the *Oscasp1-3* mutant. **(E)** Phenotypic comparison of transgenic plants with the *OsCASP1* gene (T6 and T4) and segregant individuals without the *OsCASP1* gene (T1 and T2). **(F)** The PCR result indicated transgenic plants with or without the *OsCASP1* gene.

after staining and found that GUS activity was mainly concentrated in the stele of roots (Figures 2D and S5D–E). We also uncovered *OsCASP1* gene expression in other root tissues treated with NaCl, especially sclerenchyma cells (Figures 2 and Figure S5). The *OsCASP1* gene was highly upregulated in SLR tips and steles after NaCl treatment (Figures 2E and S5A). We also accessed the expression levels using RT-qPCR in different tissues and uncovered that *OsCASP1* is highly expressed in SLRs and younger roots, moderately expressed in primary root tip, and weakly expressed in leaves (Figure 2F).

Characterization and CS structure of the WT and *Oscasp1* mutant in primary roots

In *Arabidopsis*, the *casp1-1/casp3-1* mutant shows abnormal CS structure and delayed establishment of a functional apoplastic barrier (Hosmani et al., 2013). OsCASP1 exhibits high sequence similarity with AtCASP1~4 (Figure S1), therefore it seems reasonable that OsCASP1 can regulate the formation of CS in rice. We first observed the structures of the primary roots (embryonic crown roots and postembryonic crown roots) and large lateral roots of the *Oscasp1-3* mutant after staining with phloroglucinol and berberine-aniline blue, respectively. We did not find obvious differences in root structure between the *Oscasp1-3* mutant and WT, including CS structure by observing the cross-sections (Figure S6).

Basic Fuchsin was used to visualize CSs and the lignin-based cell wall impregnations of the endodermis in *Arabidopsis* (Vermeer et al., 2014, Doblas et al., 2017b, Kalmbach et al., 2017). However, we also used this method to visualize CS in cross-sections in the primary roots and discovered that it is difficult to locate CS in the endodermis based on the result of Basic Fuchsin staining, which displayed a different lignin deposition patterns compared with phloroglucinol and

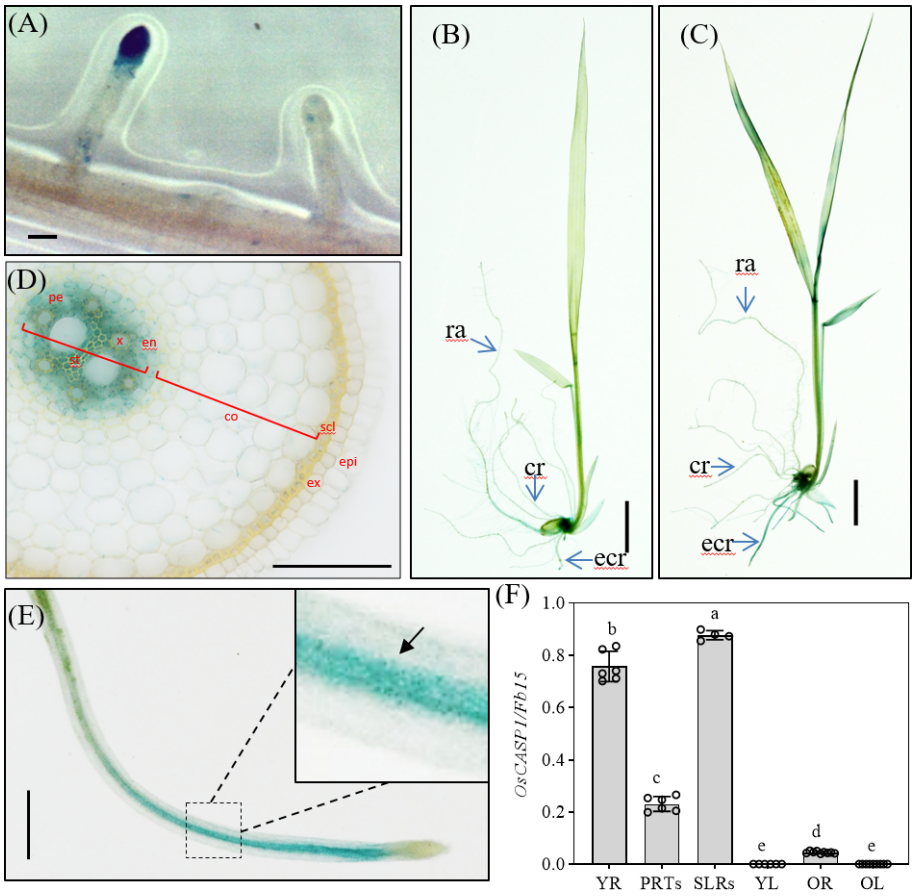

FIGURE 2
Localization of *OsCASP1pro:OsCASP1-GUS* expression. **(A)** GUS activity in SLR tip. **(B)** GUS staining of whole seedling plant grown in 1×Kimura B solution. **(C)** GUS staining of the plant treated with 100 mM NaCl for 3 hours. **(D)** Cross-section of a crown root (10 mm distal from the root tip) derived from a 10-d-old seedling treated with NaCl. **(E)** GUS activity in SLR treated with NaCl. **(F)** Expression levels of *OsCASP1* in different tissues. YR, young root. PRTs, primary root tips. SLRs, small lateral roots. YL, young leaves. OR, old roots. OL, old leaves. Different letters denote significant differences in one-way ANOVA test (Tukey test $p < 0.05$) among different lines. *Fb15* (Fiber protein 15) (Os02g0175800) was used as reference gene in the RT-qPCR analysis. Scale bars: **(A, D, E)** 100μm; **(B, C)** 1cm.

berberine-aniline blue staining (Figures S6, S7). The CS is at the radial walls of endodermal cells, but we discovered that lignin deposition was disrupted in many radial walls of endodermal cells and that there was an area of the radial walls that could not be stained with Basic Fuchsin (Figure S7). We suspected that some unknown components in rice cell walls could influence the staining. In addition, Basic Fuchsin strongly stained many outer peripheral wall and stele-facing wall of endodermal cells and cell wall of cortical cells (Figure S7). We observed cross-sections at 10mm, 20mm, and 30mm from root tip and found that the farther endodermal cells from root tip, the more cells with increased lignin deposition. Lignin deposition in the *Oscasp1-3* mutant was higher in endodermal cells than that in the WT at the same slice position (Figure S7A). The *Oscasp1-1* mutant (Nipponbare background) was used to study the function of *OsCASP1* gene in the previous report (Wang Z. et al., 2019). Thus, we also examined lignin deposition patterns in the roots of the *Oscasp1-1* and *Oscasp1-4* mutants after staining with Basic Fuchsin. However, we did not observe the difference between Nipponbare and *Oscasp1-1*, and ZH11 and *Oscasp1-4* (Figures S7B, C).

To reveal the fine structures of CSs, we used a transmission electron microscope (TEM) to observe the sections of primary roots and found no difference between the *Oscasp1-3* mutant and WT (Figure 3A). We also checked the CSs after treatment with salt stress and still found no CS difference between the *Oscasp1-3* mutant and WT (Figure 3A). These results differ from the previous report (Wang Z. et al., 2019). Therefore, we

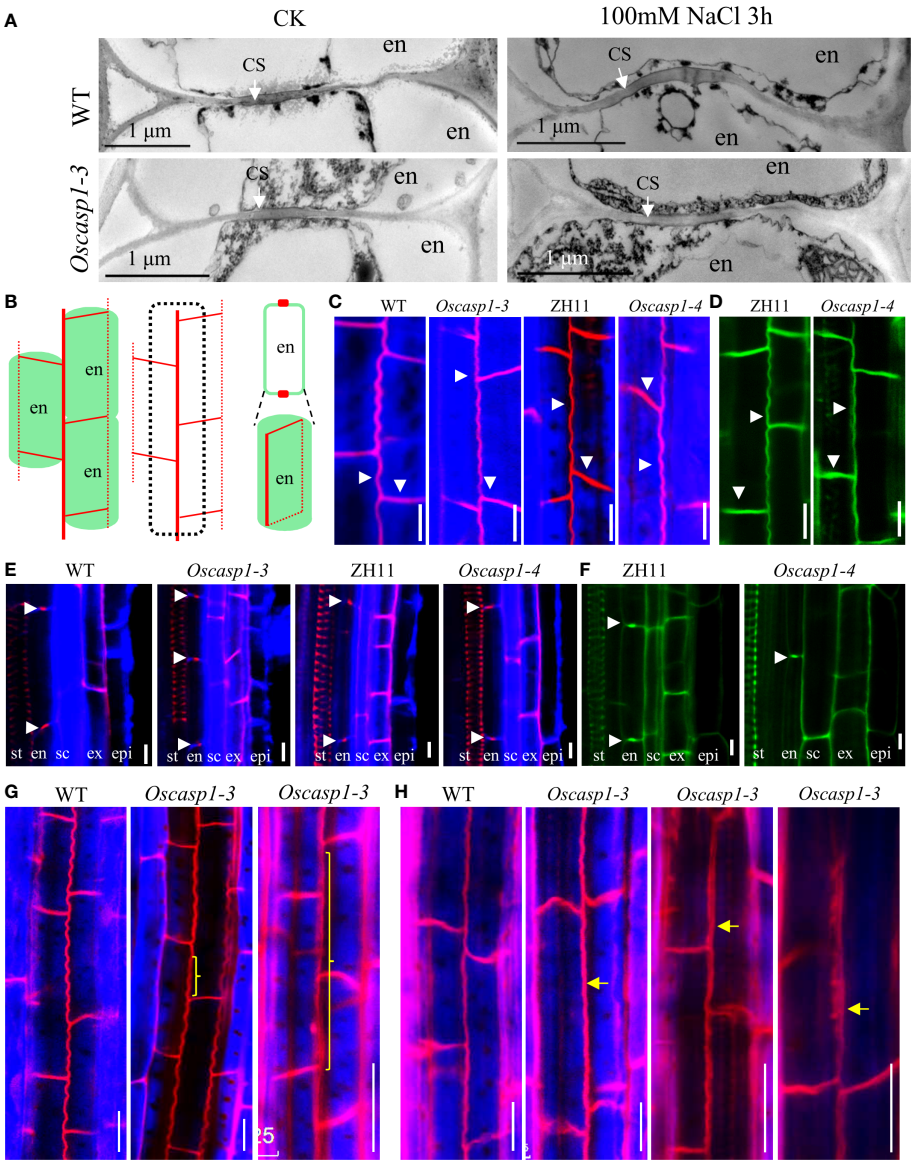

FIGURE 3
The Casparian strip structures of the roots. **(A)** The representative transmission electron micrographs of CS in primary roots of WT and *Oscasp1-3*, WT and *Oscasp1-3* treated with salt stress. These transverse sections were at 10 mm from primary root tip. **(B)** Cartoons of the observed lines and dots in an optical section, which represent a longitudinal and horizontal band in three dimensions, respectively. **(C, E, G, H)** SLRs stained with Basic Fuchsin and Calcofluor White in ClearSee solution. **(D, F)** SLRs stained with Auramine O in ClearSee solution. **(C, D)** The representative longitudinal and horizontal normal CS bands. **(E, F)** The representative CS dots. epi: epidermis; ex: exodermis; sc: sclerenchyma; en: endodermis. **(G, H)** The abnormal longitudinal CS bands in *Oscasp1-3*. Yellow curly brackets and arrows indicate abnormal CSs. **(G)** SLRs of 5-d-old seedling. **(C–F, H)** SLRs of 10-d-old seedling. Scale bar = 10μm.

observed CSs of the *Oscasp1-1* mutant using TEM too. Regrettably we did not uncover structural differences in CS between the *Oscasp1-1* mutant and Nipponbare (Figure S8A).

We assessed the expression levels of the genes involved in the formation of CS in the *Oscasp1-3* mutant and WT primary roots using RT-qPCR (Table S1). The result showed that the expression levels of *OsPER64* and *OsLOTR1* were significantly lower and the expression levels of *OsCASP3* and *OsCASP5* were significantly higher in WT than in *Oscasp1-3* (Figure S8B). These results suggest that the mutation of *OsCASP1* might enhance or accelerate lignin deposition due to high expression of *OsPER64* and *OsLOTR1* in primary roots (Figure S8B).

Structural characteristics of small lateral roots in the wild type and *Oscasp1* mutant

In *Arabidopsis*, researchers determined CS structure and quantitatively described CS formation in very small roots by surface view of its autofluorescence (Naseer et al., 2012). Thus, we observed the structure of small lateral root (SLR) using these methods and found that there was no autofluorescence in SLR tips and no or very weak autofluorescence in SLR elongation zone of 6-d-old plants (Figures S9A, B), and stronger autofluorescence in most SLRs of 9-d-old and 15-d-old plants (Figures S9C–I). We could not determine where CS was in SLRs based on autofluorescence intensity, which was not stronger in CS than in other cells (Figure S9J). Moreover, almost all cells of primary roots displayed different intensities of autofluorescence, among which the sclerenchyma exhibited strongest fluorescence (Figure S9J). Older plants contain more lignin in the roots.

Basic Fuchsin was used for lignin staining and Auramine O was used for lignin and suberin staining (Ursache et al., 2018). Basic Fuchsin staining and Auramine O staining can clearly visualize the lignin deposition and CSs in endodermal cells in SLRs (Figures 3B–F). In the region close to SLR tips, we observed normal CS bands (Figures 3C, D) and normal CS dots (Figures 3E, F) in both the mutant and WT. In the region far from SLR tips, we discovered that approximately one-fifth of SLRs of 5-d-old seedlings and approximately one-half of SLRs of 10-d-old seedling contain abnormal CS in the *Oscasp1-3* mutant. These abnormal CSs either displayed wider bands with uneven lignin deposition (Figures 3G, H) or stronger bands with enhanced deposition (Figure 3H). The loss of OsCASP1 function may have reduced the control of lignin deposition.

We also examined lignin deposition in SLRs stained with phloroglucinol, which specifically reacts with cinnamaldehyde end-groups of lignin to give a pink or fuchsia color. This method is less sensitive and more specific and quantitative than Basic Fuchsin staining (Pradhan Mitra and Loque, 2014; Hubbe et al., 2019). The result showed that the lignin deposition in the endodermis of the *Oscasp1-3* mutant was stronger than that of WT (Figure 4A). However, the lignin in the endodermis in the *Oscasp1-3* mutant SLRs was deposited not only in the radial walls but also in the outer peripheral walls of endodermal cells. Summarizing above results, the loss of OsCASP1 function leads to abnormal CS and enhanced lignin deposition in the endodermis.

Loss of OsCASP1 function delays CS formation in SLRs

Mutations of most *Arabidopsis* genes regulating or participating in CS formation delay the CS formation (Doblas et al., 2017a). We wondered whether loss of OsCASP1 function would lead to delayed CS formation in SLRs. Thus, we selected some SLRs with similar diameter in the middle region of the primary root and observed the CS formation of the Basic Fuchsin-stained SLRs. The result showed that the appearance of the first CS in the *Oscasp1-3* and *Oscasp1-4* mutants was significantly delayed compared with their relevant WT (Figures 5A–C), and the difference between the *Oscasp1-3* and WT appeared to be greater than the difference between the *Oscasp1-4* and ZH11 (Figure 5C).

In order to explore the difference between the *Oscasp1-3* mutant and the WT, the *Oscasp1-4* mutant and ZH11, we assessed the expression levels of the genes involved in CS formation in SLRs using RT-qPCR (Table S1). With the exception of OsCASP4, the expression levels of these genes were significantly lower in the *Oscasp1-3* mutant than in its corresponding WT, while the expression levels of *OsCASP2*, *3*, *4*, and *5* were significantly higher in the *Oscasp1-4* mutant than in ZH11, and the expression level of *PER64* was significantly lower in the *Oscasp1-4* mutant than in ZH11 (Figure 5D). The genetic background may influence the expression of the genes involved in CS formation. Therefore, it is difficult to conclude that the delayed CS formation and abnormal CS in the *Oscasp1* mutant is due to altered expression of these genes. OsCASP1 may indirectly regulate CS formation.

Characterization of SLRs revealed by berberine-aniline blue staining

An improved method for clearing with lactic acid saturated with chloral hydrate and staining with berberine-aniline blue was applied to visualize CS (Lux et al., 2005). We used this method to determine SLR structure and did not find CSs in SLR by surface observation (Figure 4B). We observed the cross-sections of the SLRs and discovered that the fluorescence of the sclerenchyma was much stronger than that of the endodermis in the WT. In contrast, the sclerenchyma in SLRs displayed much lower white-blue fluorescence in the *Oscasp1-3* mutant (Figure 4C). We observed that many SLRs of the *Oscasp1-3* mutant contained patchy white-blue zones from endodermal cells, whereas only a few SLRs of WT did. Some endodermal cells in patchy regions of the *Oscasp1-3* mutant displayed strong white-blue fluorescence, while the SLRs of the WT displayed continuous white-blue fluorescence, which was strong or weak (Figure 4B). Younger SLRs, which were closer to the primary root tip, exhibited lower white-blue fluorescence, and older SLRs, which were closer to seeds, showed continuous white-blue fluorescence in WT and more patchy white-blue fluorescence in the *Oscasp1-3* mutant (Figure 4C). Fluorescence intensity depended on the positions of the SLRs in the primary root. However, since berberine-aniline blue can stain both lignin and suberin, it is difficult to distinguish whether the white-blue fluorescence arises from lignin or suberin (Brundrett et al., 1988). We have not observed patchy deposition of lignin in SLRs of the *Oscasp1-3* mutant and WT (Figure S10),

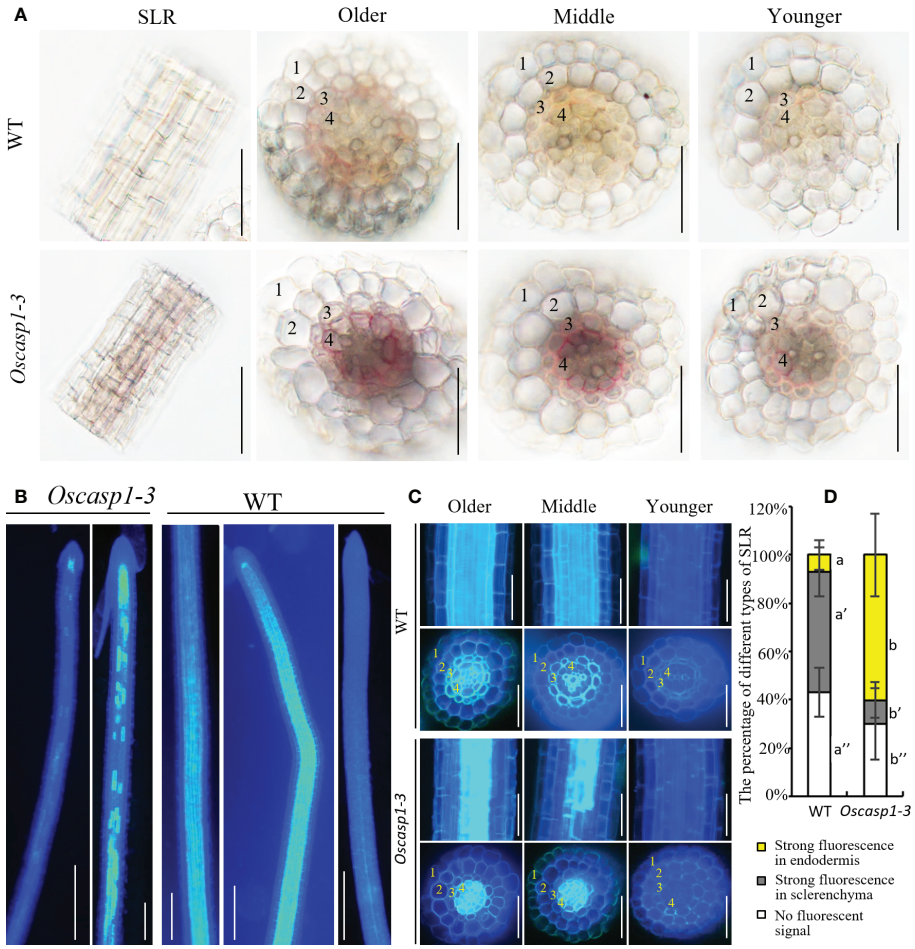

FIGURE 4
Characterization of the *Oscasp1-3* mutant and WT SLRs stained with berberine-aniline blue and phloroglucinol. **(A)** The representative SLR regions and cross-sections stained with phloroglucinol. Scale bar = 50 μm. **(B)** The representative images of whole SLRs stained with berberine-aniline blue. Scale bar = 100μm. **(C)** The representative SLR regions and cross-sections stained with berberine-aniline blue. Scale bar = 25 μm. **(D)** The percentage of different type of SLRs. Autofluorescence of cell walls is detected as blue. 1, epidermis; 2, exodermis; 3, sclerenchyma; 4, endodermis. Different letters denote significant differences in one-way ANOVA test (Tukey test $p < 0.05$) among different lines.

therefore, we speculated that the patchy fluorescence in *Oscasp1-3* and strong fluorescence of the sclerenchyma in WT could come from the suberin deposition.

The small lateral roots of the *Oscasp1* mutant display ectopic suberin deposition

The previous report indicated that the *Oscasp1-1* mutant showed priority accumulation of suberin in primary roots by checking root cross-sections at different root positions (Wang Z. et al., 2019). We repeated the experiment in the same way, but it is very difficult to obtain a consistent result with the method due to considerable variation among roots. This may be because suberin deposition is very sensitive to ionic change and other environment factors (Barberon et al., 2016).

The above result hinted that the patchy fluorescence in the mutant SLRs stained with berberine-aniline blue arose from suberin accumulation. We then evaluated suberin deposition in SLRs with Fluorol Yellow 088. The results showed that the patterns of suberin deposition depended on the position of SLRs in the primary root. The newborn lateral roots near the primary root tip (2~3 cm behind the root apex) usually had no suberin deposition, and the SLRs without suberin deposition occurred more frequently in the WT than in the mutant (Figure 6B). The SLRs farther from the primary root tip in WT usually exhibited uniform staining and some SLRs contained a few strongly staining cells (Figure 6A). This result indicated that suberin deposition was evenly distributed along

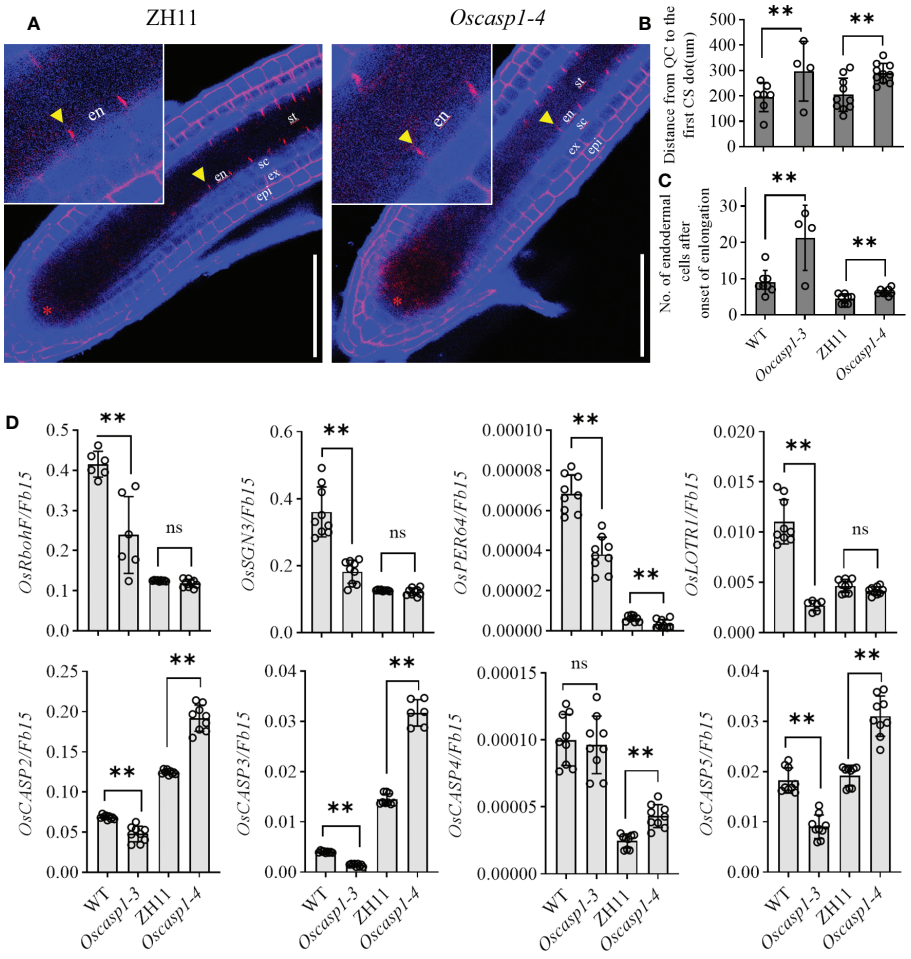

FIGURE 5
Significant delay of dot-like appearance of CS in *Oscasp1* mutants comparing with wild type plants. **(A)** The representative CS dots of the *Oscasp1-4* mutant and ZH11 SLRs stained with Basic Fuchsin and Calcofluor White in ClearSee solution. Yellow arrow heads indicate the first appearance of CS in endodermal cells. The red asterisks indicate the quiescent center (QC). st: stele; en: endodermis; sc: sclerenchyma; ex: exodermis; epi: epidermis. Scale bars = 75 μm. **(B)** The distance between QC and the first appearance of CS in endodermis were measured. **(C)** No. of endodermal cells between the first appearance of CS and "onset of elongation" were counted. "Onset of elongation" was defined as the zone where an endodermal cell was clearly more than twice its width. **(D)** Expression levels of the genes encoding the proteins that could participate in CS formation. Black circles represent independent replicates of specific values. Student's T-test was used for statistical analysis, and ** represents statistically significant difference (p value < 0.01); ns: no significance. *Fb15* (Fiber protein 15) (*Os02g0175800*) was used as reference gene in the RT-qPCR analysis.

the SLRs in the WT. However, most SLRs in *Oscasp1-3* showed abnormal suberin deposition and an uneven distribution along the SLRs, and suberization increased along with root growth (Figure 6A). To further determine in which cell layer the suberin is deposited, we observed the cross-sections of the SLRs after FY088 staining. The result showed that strong fluorescence signal was mainly concentrated in the sclerenchyma cell wall and weak fluorescence signal was in the radial wall of endodermal cells in WT (Figures 6C, D). Nevertheless, we detected strong fluorescence signal in the endodermal cell wall and weak in the sclerenchyma cells of the *Oscasp1-3* mutant (Figures 6C, D). This is in good agreement with the result of berberine-aniline blue staining. These results suggest that the loss of OsCASP1 function changes the pattern and location of suberin deposition in rice SLRs.

In *Arabidopsis*, many genes regulating or participating in suberin synthesis were revealed (Table S1). Since many of the characterized suberin biosynthetic enzymes and their encoding genes exhibit conserved functionality across species, we assessed the expression levels of these genes that are orthologs of *Arabidopsis* genes involved in suberin synthesis (Woolfson et al., 2022)(Table S1). The expression levels of these genes were significantly higher in the two *Oscasp1* mutants than in their corresponding WTs, and the

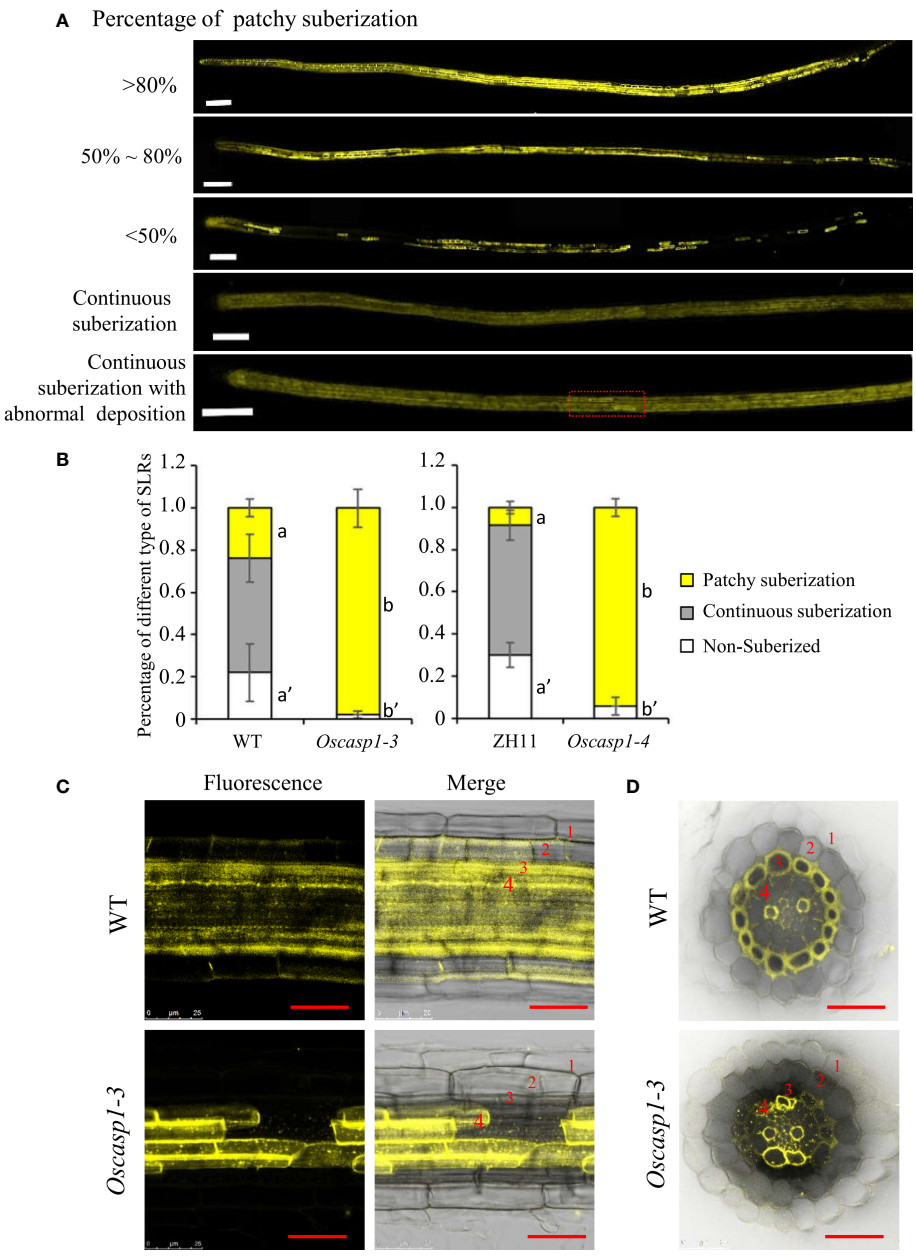

FIGURE 6
The patterns of suberin deposition of the small lateral roots. **(A)** The patterns of suberin deposition in small lateral roots of the WT and *Oscasp1-3* mutant, which were obtained with laser confocal microscopy. Scale bar = 100μm. **(B)** The percentage of small lateral roots of each deposition pattern. Different letters denote significant differences in one-way ANOVA test (Tukey test $p < 0.05$) among different lines. **(C)** The representative pattern of suberin deposition in the WT and *Oscasp1-3*. Scale bar = 25μm. **(D)** Representative transverse sections from small lateral roots. Scale bar = 25μm. 1, epidermis; 2, exodermis; 3, sclerenchyma; 4, endodermis.

expression level of *Os08g0298700* was significantly higher in *Oscasp1-3* than the WT (Figure 7). We also determined the expression levels of four Myb transcription factors that could regulate the expression of suberin biosynthetic genes (Table S1) and found that the expression levels of two Myb TF genes (*Os06g0221000* and *OsMyb4-like*) were significantly higher in the two mutants and that expression level of *OsMyb7* was significantly lower in *Oscasp1-3* (Figure 7). These results further confirmed that the loss of OsCASP1 function enhanced the expression of most related genes and resulted in ectopic suberin deposition. Finally, we summarized the above results and presented a schematic diagram to reveal the

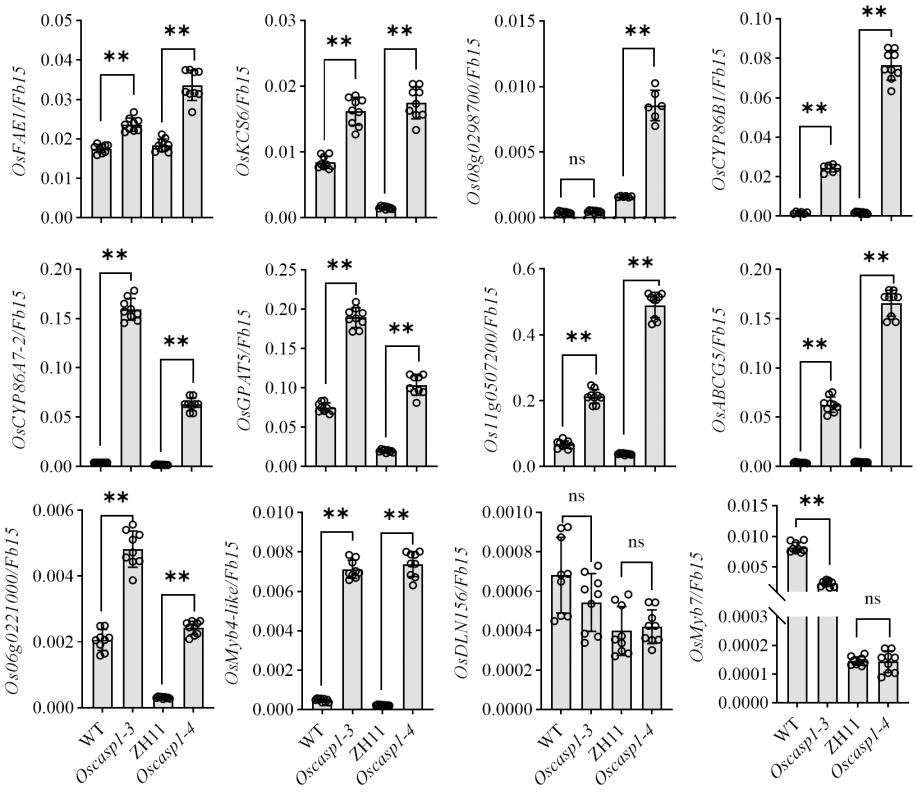

FIGURE 7
Expression levels of the genes involved in suberin synthesis. Student's T-test was used for statistical analysis, and ** represents statistically significant difference (p value < 0.01); ns: no significance.

characteristics of SLRs and the differences between WT and *Oscasp1-3* in rice (Figure 8).

The apoplastic barrier function to PI

Propidium iodide (PI) was widely used as an apoplastic tracer to reveal the functional apoplastic barrier in roots of *Arabidopsis* (Alassimone et al., 2012) and rice (Wang Z. et al., 2019; Wang Z.et al., 2022), thus we applied this substance in our study. However, we occasionally found that high concentration of PI easily penetrated CSs into the steles of rice roots and that CSs could not completely block the PI penetration. Therefore, we investigated whether PI could be used as an apoplastic tracer in rice root research. We first examined the permeability of primary roots to PI and uncovered that lower PI concentration took more time and higher concentration required less time to enter into the stele of rice roots. Younger root might show higher permeability than older root (Figure S11). WT roots could not block, but could hinder PI penetration into stele (Figure S11). Since PI was firstly used in *Arabidopsis*, we wondered whether higher concentration or longer staining time was able to overcome obstruction of CS into root stele. We stained the roots of 5-d-old seedling and discovered that *Arabidopsis* roots could completely block the entry of PI into stele regardless of concentration and staining time (Figure S12). These results suggest that the permeability and CS structure of rice roots are different from those of *Arabidopsis*.

We also examined the permeability of SLRs and found that different locations of primary roots and different zones of SLR showed different permeability to PI. SLRs farther from the primary root tip usually exhibited more retardation to PI, and the nascent SLR completely lost PI block (Figure S13A). We examined SLRs of eight 6-d-old and 7-d-old seedlings. The number of SLRs that could not prevent PI from entering varied greatly from plant to plant (Figure S13). Furthermore, we found that environmental condition appeared to affect the permeability of SLRs to PI, which resulted in the difficulties in quantitative analysis.

We examined PI permeability of mutant roots. The primary roots of WT appeared to exhibit lower permeability than that of the *Oscasp1-3* mutant (Figure S11), and SLRs of the *Oscasp1-3* mutant were more sensitive to staining time (Figures S13C, D). We selected some SLRs that were in the middle of the primary

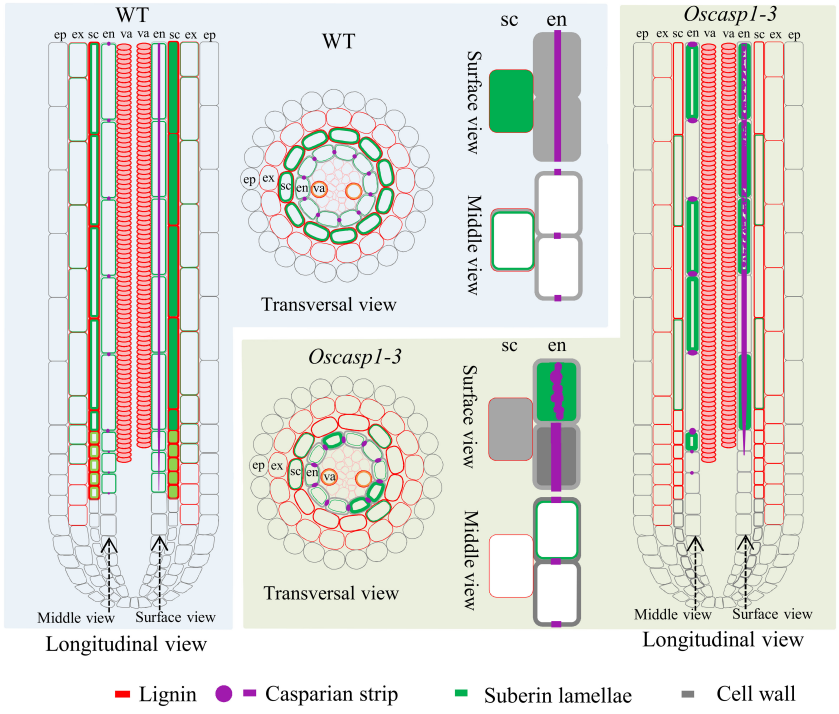

FIGURE 8
Schematic longitudinal and transversal views of SLRs and single cells showing characteristics of SLRs and the differences between WT and *Oscasp1-3* in rice. Lignin and suberin depositions in the endodermis and sclerenchyma are represented by red and green lines, respectively. CSs are represented by purple dots and lines, and cell walls are represented by grey lines. ep, epidermis; ex, exodermis; sc, sclerenchyma; en, endodermis; va, vascular tissue.

root and had a similar diameter and compared the cellular distance from the first cell at which diffusion barrier appears to the first fully expanded cell in SLRs. The result showed that the cellular distances of the *Oscasp1-3* and *Oscasp1-4* mutants were significantly longer than that of WTs (Figure 9). Compared with Figure 5, we observed a radical difference between the appearance of the first CS and the block of PI diffusion. The block of PI diffusion appeared much later (Figure 9) and could not be attributed to CS structure. Summarizing above results, CSs in rice roots could not block PI into steles.

The *Oscasp1-3* mutant displays defective ion homeostasis and different sensitivities to different nutrient stresses

Loss of OsCASP1 function changed suberin deposition in SLRs and probably altered the ion permeability of the mutant. We measured the content of 9 metal elements in leaves at the tillering stage, where a small number of dead cells visible to the naked eye appeared. The result showed that the *Oscasp1-3* mutant had significantly higher concentrations of iron, manganese, and sodium and lower concentrations of potassium and arsenic (Figure S14). The *OsCASP1* mutation altered ion uptake in the root, and the previous report has also indicated that the shoots of the *Oscasp1-1* mutant display defective nutrient homeostasis (Wang Z. et al., 2019). We speculated that the disorder of ion homeostasis in plants resulted in the mutant phenotype, and then we examined the growth of *Oscasp1-3* plants in nutrient-poor solution in a climate incubator and discovered that the mutant displayed distinct phenotypes under different stress conditions. There was no visible leaf cell death in the *Oscasp1-3* mutant in complete medium. The mutant was insensitive to the deficiency of phosphorous, iron, or nitrogen and to a high concentration of phosphorous or iron (data not shown), and there were slight differences in the leaves between *Oscasp1-3* and WT in medium without potassium, magnesium, or with aluminum (Figures 10A–D, G, and Figures S15A–C). Compared to the *Oscasp1-3* mutant, the WT exhibited more tillers and fewer and shorter roots in potassium-free medium; the WT showed earlier senescence of lower leaves and more tillers in medium without magnesium or with aluminum (Figures 10B–D, G and S15B, C); and the WT was earlier senescence to the medium with a low pH value (pH = 4.0) (Figures 10E, G, and Figure S15D). In addition, the mutant showed more curled and dry leaves in the medium with cadmium (Figures S15E) and was more sensitive to high concentrations of NaCl relative to the WT (Figures 10F–G).

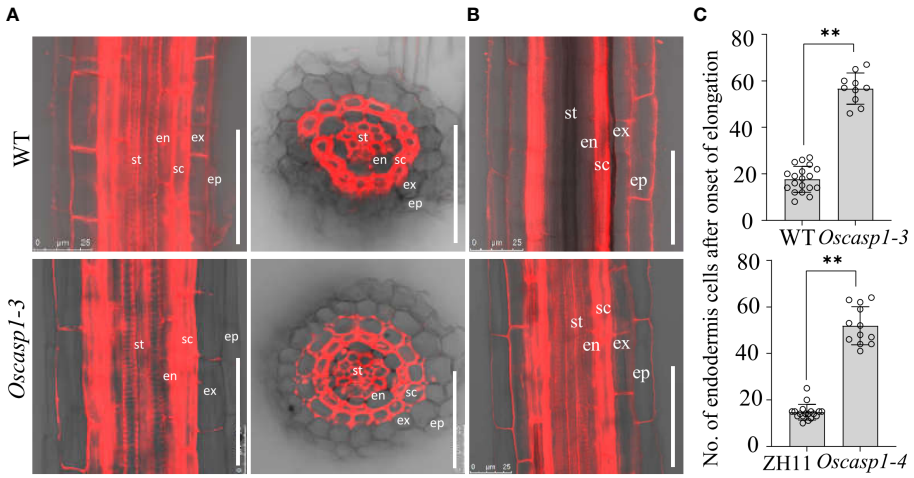

FIGURE 9
PI penetration in the *Oscasp1-3* mutant and WT roots. **(A)** Representative images of *Oscasp1-3* and WT SLRs showed the areas that lose barrier to PI in both of the mutant and WT. SLRs were incubated with 10 μg/ml PI for 10 minutes. **(B)** The area of WT SLR blocked PI penetration into stele. st, stele; en, endodermis; sc, sclerenchyma; ex, exodermis; ep, epidermis. Scale bar = 50 μm. **(C)** Quantification of PI penetration into the stele quantified as number of endodermal cells from the first fully expanded cell in wild type. Student's T-test was used for statistical analysis, and ** represents statistically significant difference (p value < 0.01); ns: no significance.

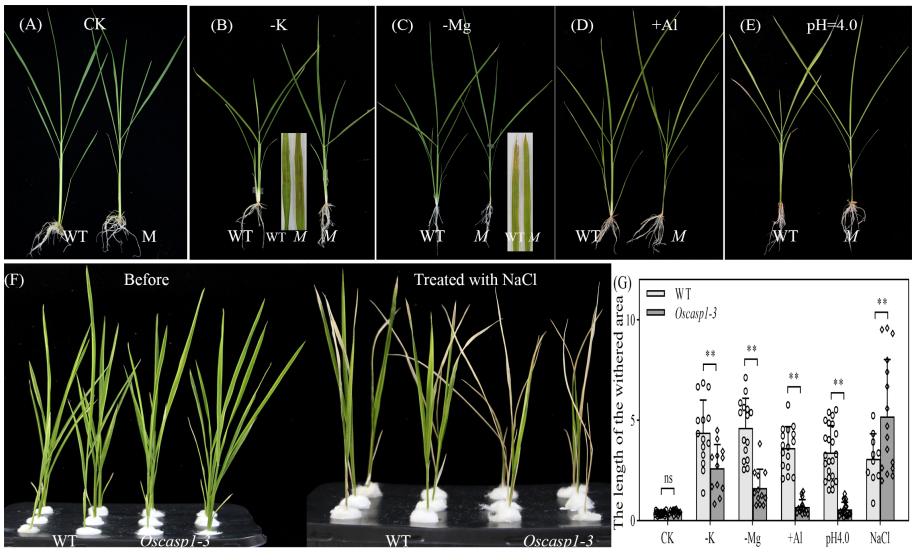

FIGURE 10
Phenotypes of WT and *Oscasp1-3* mutant plants grown in various media with elemental mineral imbalances. **(A)** In complete medium. **(B)** In medium without potassium. **(C)** In medium without magnesium. **(D)** In medium with 100 μM $AlCl_3$. **(E)** In medium with a low pH value (pH = 4.0). **(F)** In medium with 100 mM NaCl. **(G)** The length of the withered leaf area of these seedlings grown in various media. Student's T-test was used for statistical analysis, and ** represents statistically significant difference (p value < 0.01); ns: no significance. M: *Oscasp1-3*.

These results suggested that the *Oscasp1-3* mutant exhibited different sensitivity to different nutrient stresses, which could be relevant to the composition of mineral ions in the mutant plant.

Discussion

Characterization of lignin deposition of rice roots and the role of OsCASP1 in CS formation

Our study showed that the expression of *OsCASP1* gene is concentrated at the SLR tip and is strongly expressed after NaCl treatment especially in the steles (Figure 2). Its mutation delays CS formation (Figure 5) and leads to uneven lignin deposition in the endodermis (Figure 3) and ectopic suberin deposition in SLRs (Figure 6). Comparing with previous reports, our results differ in the following points (Wang Z. et al., 2019; Wang Z. et al., 2022). The first concerns the CS structure of the *Oscasp1* mutant in primary roots. We employed multiple approaches to observe CS structures of the primary roots and did not observe significant difference between the mutants and their corresponding WTs (Figures 3A, S6, S7, and S8A). Previous reports indicated that more CSs at 10 mm from apex and almost all CSs at 15 mm, and 20 mm from apex exhibit significantly broader and thicker bands in the *Oscasp1* mutant and that the "broad CS" is abnormal or defective (Wang Z. et al., 2019; Wang Z. et al., 2022). Unfortunately, we were not able to reproduce their results nor find more "broad CS" in the mutant (Figure S7). We also noticed that the pattern of lignin deposition revealed with Basic Fuchsin staining is different from that with berberine-aniline blue and phloroglucinol (Figures S6, S7). There is an area in the radial walls of endodermal cells that cannot be stained by Basic Fuchsin. In fact, it is difficult to determine where the CS is according to staining results. Wang Z. et al. (2019) thought that one of lignin bands is CS, but the evidence was insufficient (Wang Z. et al., 2019). In order to determine whether there is a CS difference between the *Oscasp1* mutant and WT, we used TEM to clearly observe structure of CS, which remains attached to the cell membrane after plasmolysis. We did not find difference between the mutants and their corresponding WTs, including between the *Oscasp1-1* mutant and Nipponbare used in the previous study (Wang Z. et al., 2019) (Figures 3A and S7). Summarizing the above results and previous reports, we speculate that the loss of OsCASP1 function enhances or accelerates lignin deposition (Figure S7A) (Wang Z. et al., 2019; Wang Z. et al., 2022). Furthermore, in addition to the radial wall, we observed lignin deposition in outer peripheral and stele-facing walls of endodermal cells and in the cell wall of cortical cells (Figure S7). The deposition pattern of lignin in rice roots is different from that in *Arabidopsis* roots.

The second concerns the localization of OsCASP1, which was found to specially accumulate in the CS-forming region of endodermal cells in rice roots by immunostaining with GFP antibody (Wang Z. et al., 2019; Wang Z. et al., 2022). This conclusion is different from our results (Figures 2 and S5). Carefully reading these reports, we found that the relevant experiments lacked negative controls. We repeated the experiment using Nipponbare (without *GFP* gene), observed cross-sections at 7 mm, 10 mm, and 20 mm from primary root tips, and found green fluorescence and red fluorescence at CS-forming region of endodermal cells (Figure S16). The green fluorescence could come from the autofluorescence of CSs, and the red fluorescence came from non-specific binding (Figure S16). The green fluorescent pattern is similar to that in the previous reports (Wang Z. et al., 2019; Wang Z. et al., 2022). Thus, it is necessary to add a negative control for immunostaining experiment in the previous study to eliminate false positives. Moreover, *OsMyb36a*, *OsMyb36b*, and *OsMyb36c* are strongly expressed in root tips like *OsCASP1* (Figures 2A and S5A), whose expression is not only concentrated in the endodermis. OsMyb36a, OsMyb36b, and OsMyb36c can bind to the promoter of *OsCASP1* and directly regulate its expression (Wang Z. et al., 2022). It is strange that Wang Z. et al. (2019, 2022) cannot detect the OsCASP1 accumulation in other tissues, such as steles and sclerenchyma. However, our results showed that the expression pattern of *OsCASP1* is more consistent with that of *OsMyb36a, OsMyb36b*, and *OsMyb36c* compared to the previous report (Wang Z. et al., 2022) Overexpression of *OsMyb36a* accelerates CS formation, whereas co-mutation of *OsMyb36a/b/c* delays CS formation in endodermis (Wang Z. et al., 2022). If the conclusion that OsCASP1 directly regulate CS formation is correct, the consistency of expression pattern between *OsCASP1* and *OsMyb36s* could better explain the conclusion that OsMYB36 modulates CS formation through regulating *OsCASP1* expression.

The third concerns PI penetration, which was used to detect the permeability of CS in *Arabidopsis* (Naseer et al., 2012; Hosmani et al., 2013; Barberon, 2017). However, our finding suggests that rice roots can hinder, but not prevent, the entry of PI into the stele (Figures 9A and S11, S13). Thus PI was not suitable for detecting CS integrity in rice root. The PI permeability of rice roots should be different from that of *Arabidopsis*.

Since thicker primary roots of rice seedlings are not suitable for whole-mount observation, we pay more attention to CS structure of SLRs. After treatment with ClearSee solution and staining with Basic Fuchsin and Calcofluor White, whole-mount observation of SLR can obtain clear CS structure. We discovered some abnormal CS bands and delayed CS formation in the mutant SLRs (Figures 3G, H, 5B, C). Compared with *Arabidopsis* roots, the first appearance of CS in rice is earlier than that in *Arabidopsis* (Figure 5C) (Naseer et al., 2012). Most abnormal CSs displayed uneven lignin deposition (Figures 3G, H), and strangely, abnormal CSs were mostly found in the region far from SLR tips. The lignin deposition in endodermis may be out

of control in the *Oscasp1* mutant. Combining the above results and previous reports (Wang Z. et al., 2019; Wang Z. et al., 2022), we propose that OsCASP1 can regulate CS formation, but whether OsCASP1 can form a scaffold with itself or other OsCASPs in CSD for CS biosynthesis needs more evidences.

The suberin deposition in the *Oscasp1* mutant SLRs

The recent report indicated that the loss of OsCASP1 function enhances suberin deposition in primary roots of the *Oscasp1* mutant by observing cross-sections. Unfortunately, the conclusion lacks statistical support (Wang Z. et al., 2019). We observed many cross-sections from different zones of many primary and large lateral roots and could not obtain consistent results to support the difference. Since suberin deposition of the endodermal cells is influenced by environmental factors and the location of the cells in roots (Barberon et al., 2016; Barberon, 2017), statistical analyses are necessary to determine the deposition pattern of suberin. However, it is difficult to quantify the onset of suberin accumulation and the difference between the *Oscasp1* mutant and WT based on cross-sectional results. Our study suggests that *Oscasp1* mutations result in heterogeneous enhancement of suberin deposition in the endodermis and loss of suberin deposition in the sclerenchyma, not only strong suberization through observing SLRs (Figures 4, 6). The deposition patterns of suberin in rice roots are different from that in *Arabidopsis* roots. Moreover, the plasticity of suberin is a major means of coping with nutrient stress by regulating their uptake or their retention in the vasculature (Barberon et al., 2016). Suberin deposition is induced by drought stress, salt treatment, and waterlogging condition and is important for growth under waterlogged conditions in rice (Krishnamurthy et al., 2009; Krishnamurthy et al., 2011; Ranathunge et al., 2011; Shiono et al., 2014). Thus, defective suberin lamellae in SLR could impair rice adaptation to growth environments.

Observation of SLRs treated with ClearSee solution accelerates progress in anatomical and developmental investigations

In *Arabidopsis*, the number of endodermal cells from the first fully expanded cell can be counted to quantitatively describe the formation of CS, the deposition of suberin, and permeability to PI using whole-mount method (Hosmani et al., 2013). *Arabidopsis* rootlets have a simple structure, including the epidermis, cortex (with only one cell layer), endodermis, and stele, and the autofluorescence of CS in the endodermis is strong and clearly visible (Roppoloet et al., 2011; Naseer et al., 2012). Rice rootlets are more complex than *Arabidopsis* and are not suitable for whole-mount observation. SLRs in rice have a simple structure too, consisting of epidermis, exodermis, sclerenchyma, endodermis, and stele (Rebouillat et al., 2009), in which lignin is deposited and displays autofluorescence except the epidermis (Figure S9). ClearSee solution significantly diminishes autofluorescence. In combination with confocal microscope, this treatment allows researcher to observe thicker tissues and improves image quality after the sample was stained with fluorescent dye.

To date, most knowledge about root structure and development has been gained through microtomy. However, the laborious nature of thin sectioning, the problem of obtaining the desired section plane, and the difficulty of obtaining complete series of sections limit the application of the technique. However, thick samples are often difficult to visualize without sectioning due to autofluorescence and tissue complexity. Here, we chose SLR as the study object and used the ClearSee technique to study CS formation and suberin deposition in SLRs, which reduces the time and cost of embedding/sectioning and difficulty of the research, and discovered that *Oscasp1* mutations resulted in delayed CS formation, abnormal lignin, and suberin deposition in SLRs. Comparing with previous reports, these findings deepens our understanding of OsCASP1-mediated CS formation and suberin deposition in rice roots.

OsCASP1 represents a novel regulative way of CASPs

The *OsCASP1* gene is highly expressed at the SLR tip, and its expression is highly induced by salt treatment especially in the steles, whereas *AtCASPs* are specially expressed in the endodermis (Roppolo et al., 2011). *AtCASPL* genes are expressed in tissues other than the endodermis, such as *AtCASPL2A1* in the lateral root tip, *AtCASPL5B1* in immature and differentiated trichomes in leaves, and *AtCASPL1F1* in anthers (Roppolo et al., 2014). *AtCASPL4C1* gene is widely expressed in a variety of organs and is cold-inducible, and the mutant shows elevated tolerance to cold stress (Yang et al., 2015). *AtCASPL1D2* is exclusively expressed in suberized endodermal cell and could regulate suberin deposition induced by NaCl stress (Champeyroux et al., 2019). These results suggest that AtCASPL proteins have various functions. OsCASP1 has a different function from AtCASPs and can appear similar to some AtCASPLs.

SLRs, in which lignin and suberin deposition are regulated by OsCASP1 (Figures 4, 6), are more sensitive to the perception of environmental conditions than other root types. The result gives a hint that OsCASP1 plays an important role in abiotic stress responses. The deposition patterns of lignin and suberin in rice roots, which are different from that of *Arabidopsis* roots, could be the reason why rice is adapted to the aquatic environment. The *Oscasp1* mutant is more sensitive to upland

condition (Wang Z. et al., 2019) and shows different tolerances to different nutrient stresses (Figures 10 and S15). These results suggest that OsCASP1 could play an important role in the adaptation to the growth conditions.

Data availability statement

The original contributions presented in the study are included in the article/Supplementary Material. Further inquiries can be directed to the corresponding author.

Author contributions

XS conceived and designed the experiments, wrote the manuscript, and took part in some experiments. HX completed the map-based cloning of *Oscasp1-3* gene. HX and QW did complementation test and CRISPR/Cas9 of OsCASP1. XY performed electron microscopy, lignin and suberin deposition analysis, and RT-qPCR. XY and QW performed histological analysis and hydroponic experiment. KL and YG performed field experiments and management. All authors contributed to the article and approved the submitted version.

Funding

This work was supported by grant from the National Natural Science Foundation of China (31571574).

Acknowledgments

We thank Dr. Jixing Xia of Guangxi University for providing the *Oscasp1-1* mutant and Dr. Fangyu Chen of College of Agriculture, Fujian Agriculture and Forestry University for helping in electron microscopy.

Conflict of interest

The authors declare that the research was conducted in the absence of any commercial or financial relationships that could be construed as a potential conflict of interest.

Publisher's note

All claims expressed in this article are solely those of the authors and do not necessarily represent those of their affiliated organizations, or those of the publisher, the editors and the reviewers. Any product that may be evaluated in this article, or claim that may be made by its manufacturer, is not guaranteed or endorsed by the publisher.

Supplementary material

The Supplementary Material for this article can be found online at: https://www.frontiersin.org/articles/10.3389/fpls.2022.1007300/full#supplementary-material

References

Alassimone, J., Roppolo, D., Geldner, N., and Vermeer, J. E. (2012). The endodermis–development and differentiation of the plant's inner skin. *Protoplasma.* 249, 433–443. doi: 10.1007/s00709-011-0302-5

Barberon, M. (2017). The endodermis as a checkpoint for nutrients. *New phytologist.* 213, 1604–1610. doi: 10.1111/nph.14140

Barberon, M., and Geldner, N. (2014). Radial transport of nutrients: the plant root as a polarized epithelium. *Plant Physiol.* 166, 528–537. doi: 10.1104/pp.114.246124

Barberon, M., Vermeer, J. E., De Bellis, D., Wang, P., Naseer, S., Andersen, T. G., et al. (2016). Adaptation of root function by nutrient-induced plasticity of endodermal differentiation. *Cell* 164, 447–459. doi: 10.1016/j.cell.2015.12.021

Beisson, F., Li, Y., Bonaventure, G., Pollard, M., and Ohlrogge, J. B. (2007). The acyltransferase GPAT5 is required for the synthesis of suberin in seed coat and root of arabidopsis. *Plant Cell* 19, 351–368. doi: 10.1105/tpc.106.048033

Brundrett, M. C., Enstone, D. E., and Peterson, C. (1988). A berberine-aniline blue fluorescent staining procedure for suberin,lignin and callose in plant tissue. *Protoplasma.* 146, 133–142.

Champeyroux, C., Bellati, J., Barberon, M., Rofidal, V., Maurel, C., and Santoni, V. (2019). Regulation of a plant aquaporin by a casparian strip membrane domain protein-like. *Plant Cell Environment.* 42, 1788–1801. doi: 10.1111/pce.13537

Compagnon, V., Diehl, P., Benveniste, I., Meyer, D., Schaller, H., Schreiber, L., et al. (2009). CYP86B1 is required for very long chain omega-hydroxyacid and alpha,omega-dicarboxylic acid synthesis in root and seed suberin polyester. *Plant Physiol.* 150, 1831–1843. doi: 10.1104/pp.109.141408

Doblas, V. G., Geldner, N., and Barberon, M. (2017a). The endodermis, a tightly controlled barrier for nutrients. *Curr. Opin. Plant Biol.* 39, 136–143. doi: 10.1016/j.pbi.2017.06.010

Doblas, V. G., Smakowska-Luzan, E., Fujita, S., Alassimone, J., Barberon, M., Madalinski, M., et al. (2017b). Root diffusion barrier control by a vasculature-derived peptide binding to the SGN3 receptor. *Science.* 355, 280–284. doi: 10.1126/science.aaj1562

Domergue, F., Vishwanath, S. J., Joubes, J., Ono, J., Lee, J. A., Bourdon, M., et al. (2010). Three arabidopsis fatty acyl-coenzyme a reductases, FAR1, FAR4, and FAR5, generate primary fatty alcohols associated with suberin deposition. *Plant Physiol.* 153, 1539–1554. doi: 10.1104/pp.110.158238

Fujita, S., De Bellis, D., Edel, K. H., Koster, P., Andersen, T. G., Schmid-Siegert, E., et al. (2020). SCHENGEN receptor module drives localized ROS production and lignification in plant roots. *EMBO J.* 39, e103894. doi: 10.15252/embj.2019103894

Hofer, R., Briesen, I., Beck, M., Pinot, F., Schreiber, L., and Franke, R. (2008). The arabidopsis cytochrome P450 CYP86A1 encodes a fatty acid omega-hydroxylase involved in suberin monomer biosynthesis. *J. Exp. Botany.* 59, 2347–2360. doi: 10.1093/jxb/ern101

Hosmani, P. S., Kamiya, T., Danku, J., Naseer, S., Geldner, N., Guerinot, M. L., et al. (2013). Dirigent domain-containing protein is part of the machinery required for formation of the lignin-based casparian strip in the root. *Proc. Natl. Acad. Sci. U.S.A.* 110, 14498–14503. doi: 10.1073/pnas.1308412110

Hubbe, M. A., Chandra, R. P., Dogu, D., and V., V. S. T. J. (2019). Analytical staining of cellulosic materials: A review. *BioResources* 14, 7387–7464. doi: 10.15376/biores.14.3.7387-7464

Hulskamp, M., Schwab, B., Grini, P., and Schwarz, H. (2010). Transmission electron microscopy (TEM) of plant tissues. *Cold Spring Harb. Protoc.* 2010, pdb prot4958. doi: 10.1101/pdb.prot4958

Kalmbach, L., Hematy, K., De Bellis, D., Barberon, M., Fujita, S., Ursache, R., et al. (2017). Transient cell-specific EXO70A1 activity in the CASP domain and Casparian strip localization. *Nat Plants* 3, 17058. doi: 10.1038/nplants.2017.58

Kolbeck, A., Marhavy, P., De Bellis, D., Li, B., Kamiya, T., Fujiwara, T., et al. (2022). CASP microdomain formation requires cross cell wall stabilization of domains and non-cell autonomous action of LOTR1. *eLife*. 11, e69602. doi: 10.7554/eLife.69602.

Kosma, D. K., Murmu, J., Razeq, F. M., Santos, P., Bourgault, R., Molina, I., et al. (2014). AtMYB41 activates ectopic suberin synthesis and assembly in multiple plant species and cell types. *Plant journal: Cell Mol. Biol.* 80, 216–229. doi: 10.1111/tpj.12624

Krishnamurthy, P., Ranathunge, K., Franke, R., Prakash, H. S., Schreiber, L., and Mathew, M. K. (2009). The role of root apoplastic transport barriers in salt tolerance of rice (Oryza sativa l.). *Planta.* 230, 119–134. doi: 10.1007/s00425-009-0930-6

Krishnamurthy, P., Ranathunge, K., Nayak, S., Schreiber, L., and Mathew, M. K. (2011). Root apoplastic barriers block na+ transport to shoots in rice (Oryza sativa l.). *J. Exp. botany.* 62, 4215–4228. doi: 10.1093/jxb/err135

Kumar, S., Stecher, G., Li, M., Knyaz, C., and Tamura, K. (2018). MEGA X: Molecular evolutionary genetics analysis across computing platforms. *Mol. Biol. Evol.* 35, 1547–1549. doi: 10.1093/molbev/msy096

Lee, S. B., Jung, S. J., Go, Y. S., Kim, H. U., Kim, J. K., Cho, H. J., et al. (2009). Two arabidopsis 3-ketoacyl CoA synthase genes, KCS20 and KCS2/DAISY, are functionally redundant in cuticular wax and root suberin biosynthesis, but differentially controlled by osmotic stress. *Plant journal: Cell Mol. Biol.* 60, 462–475. doi: 10.1111/j.1365-313X.2009.03973.x

Lee, Y., Rubio, M. C., Alassimone, J., and Geldner, N. (2013). A mechanism for localized lignin deposition in the endodermis. *Cell.* 153, 402–412. doi: 10.1016/j.cell.2013.02.045

Li, P., Yang, M., Chang, J., Wu, J., Zhong, F., Rahman, A., et al. (2018). Spatial expression and functional analysis of casparian strip regulatory genes in endodermis reveals the conserved mechanism in tomato. *Front. Plant Sci.* 9, 832. doi: 10.3389/fpls.2018.00832

Lux, A., Morita, S., Abe, J., and Ito, K. (2005). An improved method for clearing and staining free-hand sections and whole-mount samples. *Ann. Botany.* 96, 989–996. doi: 10.1093/aob/mci266

Molina, I., Li-Beisson, Y., Beisson, F., Ohlrogge, J. B., and Pollard, M. (2009). Identification of an arabidopsis feruloyl-coenzyme a transferase required for suberin synthesis. *Plant Physiol.* 151, 1317–1328. doi: 10.1104/pp.109.144907

Nakayama, T., Shinohara, H., Tanaka, M., Baba, K., Ogawa-Ohnishi, M., and Matsubayashi, Y. (2017). A peptide hormone required for casparian strip diffusion barrier formation in arabidopsis roots. *Science* 355, 284–286. doi: 10.1126/science.aai9057

Naseer, S., Lee, Y., Lapierre, C., Franke, R., Nawrath, C., and Geldner, N. (2012). Casparian strip diffusion barrier in arabidopsis is made of a lignin polymer without suberin. *Proc. Natl. Acad. Sci. U.S.A.* 109, 10101–10106. doi: 10.1073/pnas.1205726109

Okuda, S., Fujita, S., Moretti, A., Hohmann, U., Doblas, V. G., Ma, Y., et al. (2020). Molecular mechanism for the recognition of sequence-divergent CIF peptides by the plant receptor kinases GSO1/SGN3 and GSO2. *Proc. Natl. Acad. Sci. U.S.A.* 117, 2693–2703. doi: 10.1073/pnas.1911553117

Pradhan Mitra, P., and Loque, D. (2014). Histochemical staining of arabidopsis thaliana secondary cell wall elements. *J. Vis. Exp.* 87, 1–11. doi: 10.3791/51381

Ranathunge, K., Lin, J., Steudle, E., and Schreiber, L. (2011). Stagnant deoxygenated growth enhances root suberization and lignifications, but differentially affects water and NaCl permeabilities in rice (Oryza sativa l.) roots. *Plant Cell Environment.* 34, 1223–1240. doi: 10.1111/j.1365-3040.2011.02318.x

Rebouillat, J., Dievart, A., Verdeil, J. L., Escoute, J., Giese, G., Breitler, J. C., et al. (2009). Molecular genetics of rice root development. *Rice* 2, 15–34. doi: 10.1007/s12284-008-9016-5

Robbins, N. E.II, Trontin, C., Duan, L., and Dinneny, J. R. (2014). Beyond the barrier: Communication in the root through the endodermis. *Plant Physiol.* 166, 551–559. doi: 10.1104/pp.114.244871

Roppolo, D., Boeckmann, B., Pfister, A., Boutet, E., Rubio, M. C., Denervaud-Tendon, V., et al. (2014). Functional and evolutionary analysis of the CASPARIAN STRIP MEMBRANE DOMAIN PROTEIN family. *Plant Physiol.* 165, 1709–1722. doi: 10.1104/pp.114.239137

Roppolo, D., De Rybel, B., Denervaud Tendon, V., Pfister, A., Alassimone, J., Vermeer, J. E., et al. (2011). A novel protein family mediates casparian strip formation in the endodermis. *Nature* 473, 380–383. doi: 10.1038/nature10070

Shiono, K., Ando, M., Nishiuchi, S., Takahashi, H., Watanabe, K., Nakamura, M., et al. (2014). RCN1/OsABCG5, an ATP-binding cassette (ABC) transporter, is required for hypodermal suberization of roots in rice (Oryza sativa). *Plant journal: Cell Mol. Biol.* 80, 40–51. doi: 10.1111/tpj.12614

Shukla, V., Han, J. P., Cleard, F., Lefebvre-Legendre, L., Gully, K., Flis, P., et al. (2021). Suberin plasticity to developmental and exogenous cues is regulated by a set of MYB transcription factors. *Proc. Natl. Acad. Sci. U.S.A.* 118, 1–11. doi: 10.1073/pnas.2101730118

Ursache, R., Andersen, T. G., Marhavy, P., and Geldner, N. (2018). A protocol for combining fluorescent proteins with histological stains for diverse cell wall components. *Plant journal: Cell Mol. Biol.* 93, 399–412. doi: 10.1111/tpj.13784

Vermeer, J. E., von Wangenheim, D., Barberon, M., Lee, Y., Stelzer, E. H., Maizel, A., et al. (2014). A spatial accommodation by neighboring cells is required for organ initiation in Arabidopsis. *Science* 343 (6167), 178–183. doi: 10.1126/science.1245871

Wang, P., Calvo-Polanco, M., Reyt, G., Barberon, M., Champeyroux, C., Santoni, V., et al. (2019). Surveillance of cell wall diffusion barrier integrity modulates water and solute transport in plants. *Sci. Rep.* 9, 4227. doi: 10.1038/s41598-019-40588-5

Wang, Y., Cao, Y., Liang, X., Zhuang, J., Wang, X., Qin, F., et al. (2022). A dirigent family protein confers variation of casparian strip thickness and salt tolerance in maize. *Nat. Commun.* 13 (1), 2222. doi: 10.1038/s41467-022-29809-0

Wang, Z., Shi, M., Wei, Q., Chen, Z., Huang, J., and Xia, J. (2020). OsCASP1 forms complexes with itself and OsCASP2 in rice. *Plant Signaling behavior.* 15, 1706025. doi: 10.1080/15592324.2019.1706025

Wang, C., Wang, H., Li, P., Li, H., Xu, C., Cohen, H., et al. (2020). Developmental programs interact with abscisic acid to coordinate root suberization in arabidopsis. *Plant journal: Cell Mol. Biol.* 104, 241–251. doi: 10.1111/tpj.14920

Wang, Z., Yamaji, N., Huang, S., Zhang, X., Shi, M., Fu, S., et al. (2019). OsCASP1 is required for casparian strip formation at endodermal cells of rice roots for selective uptake of mineral elements. *Plant Cell* 31, 2636–2648. doi: 10.1105/tpc.19.00296

Wang, Z., Zhang, B., Chen, Z., Wu, M., Chao, D., Wei, Q., et al. (2022). Three OsMYB36 members redundantly regulate casparian strip formation at the root endodermis. *Plant Cell.* 34, 2948–2968. doi: 10.1093/plcell/koac140

Woolfson, K. N., Esfandiari, M., and Bernards, M. A. (2022). Suberin biosynthesis, assembly, and regulation. *Plants (Basel)* 11, 555. doi: 10.3390/plants11040555

Yadav, V., Molina, I., Ranathunge, K., Castillo, I. Q., Rothstein, S. J., and Reed, J. W. (2014). ABCG transporters are required for suberin and pollen wall extracellular barriers in arabidopsis. *Plant Cell.* 26, 3569–3588. doi: 10.1105/tpc.114.129049

Yang, J., Ding, C., Xu, B., Chen, C., Narsai, R., Whelan, J., et al. (2015). A casparian strip domain-like gene, CASPL, negatively alters growth and cold tolerance. *Sci. Rep.* 5, 14299. doi: 10.1038/srep14299

Frontiers in Plant Science

Cultivates the science of plant biology and its applications

The most cited plant science journal, which advances our understanding of plant biology for sustainable food security, functional ecosystems and human health.

Discover the latest Research Topics

See more →

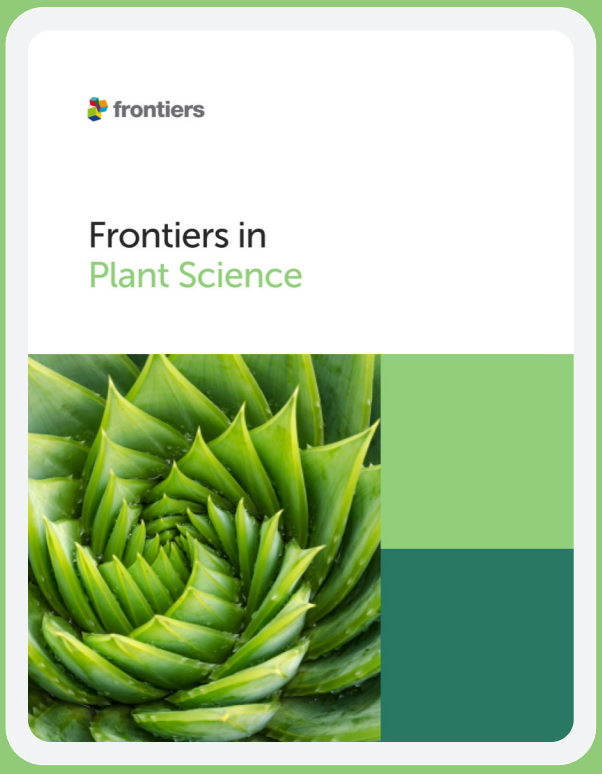

Frontiers

Avenue du Tribunal-Fédéral 34
1005 Lausanne, Switzerland
frontiersin.org

Contact us

+41 (0)21 510 17 00
frontiersin.org/about/contact